Unveiling the Physical Conditions in Star-Forming Galaxies at the Peak of Galaxy Assembly

Thesis by
Allison Leigh Strom

In Partial Fulfillment of the Requirements for the
Degree of
Doctor of Philosophy in Astrophysics

CALIFORNIA INSTITUTE OF TECHNOLOGY
Pasadena, California

2018
Defended July 26, 2017

Allison Leigh Strom
ORCID: 0000-0001-6369-1636

To those who feel a responsibility to awe,
but sometimes lose their way

ACKNOWLEDGEMENTS

Writing these two pages has taken me longer than writing all of the many pages that follow—and I am sure that most people who know me won't be surprised to hear that. If the last six years have taught me anything about myself, it is that I possess a highly-developed sense of perfectionism paired with an equally deep-seated lack of patience with myself. Of course, I am not alone in indulging in these twin vices; as I have made the journey from student to astronomer, I have watched fellow scientists (both coeval and not) wrestle with the same insecurities. And yet so many of the same people have been patient with me when I could not be patient with myself, have supported me when I could not remember why I wanted to be an astronomer at all, and have celebrated my victories with me, both large and small. These are the people without whom my life would have turned out very differently, and I will always be thankful for having known them. Even now, after countless drafts of these acknowledgements, I feel that words alone cannot express the depth of my gratitude—but I have tried my best.

Thank you foremost to my advisor, Chuck Steidel, who gave me the incredible opportunity to work on the project that became this thesis. He gave me the space to explore my own interests and then waited, perhaps in consternation, while I spent years "polishing the cannonball". His door was always open when I needed to ask a question about science or being a scientist, even when I had already asked the same question several times before. I feel fortunate that we were able to work so closely together while I was at Caltech and that I was able to learn the art of observational astronomy from him.

Thank you also to Gwen Rudie and Ryan Trainor, who welcomed me to the group and have provided invaluable guidance from the first term of graduate school through today (literally *today*). They have given selflessly of their time and energy more frequently than I can remember, and I count them among my closest friends and colleagues. I look forward to many more years of collaborating and promise I will (try to) write shorter sentences and shorter papers.

Thank you to Travis Rector, the very first astronomer I ever met and had the chance to work with. It is only because of him that I knew that I could grow up to be an astronomer too. In April 2005, he set me on this path when he took me for the first time to Kitt Peak—a place that still feels like home every time I round the corner of

the mountain road and see the telescopes waiting. I hope it always feels that way.

Thank you to the many other advisors I have been privileged to work with over the years, including Rajib Ganguly, Dave Sand, Aneta Siemiginowska, Jill Bechtold, and Buell Jannuzi. They stoked my interest in extragalactic astronomy, pushed me to try things I was afraid might not work, and never turned me away when I needed help.

Thank you to my mentors (and occasional life coaches) Max Pettini and Anneila Sargent, who shared their personal wisdom with me and made the second half of graduate school seem possible. Each has provided me with honest encouragement and served as a role model for the kind of astronomer I hope to be.

Thank you to my cohort, especially Mislav Baloković, Trevor David, Abhilash Mishra, Ben Montet, and Antonija Oklopčić. Together, we went on a number of (mis)adventures, both science-related and otherwise. They are all exceptional scientists and people, and I could not be prouder to be a part of their class.

Thank you to my friends, specifically those I met through the Graduate Student Council: Gina Duggan, Felicia Hunt, Alicia Lanz, and Jason Pollack. Because of them, I discovered an interest in and an aptitude for advocacy and policy-making that I hope to carry with me for a long time. The work we did together taught me that engaging with the *people* who do science is just as important as supporting the science itself.

And finally *thank you* always to my family who, among other things, have listened to me read aloud all of my applications—to college, to summer programs, to graduate schools, to postdoc fellowships—without complaint, even though we were usually on vacation. They have been and always will be the true constants in my life.

ABSTRACT

Galaxies at the peak of cosmic star formation ($z \sim 2-3$) exhibit significantly higher star formation rates and gas fractions at fixed stellar mass than nearby galaxies. These $z \sim 2-3$ galaxies are also distinct in terms of their nebular spectra, reflecting important differences not only in the physical conditions of their interstellar medium (e.g., electron density and gas-phase metallicity), but also in the details of their massive stellar populations. Jointly observing galaxies' H II regions, at rest-UV and rest-optical wavelengths, and massive stars, at rest-UV wavelengths, is central to constructing a framework for understanding the differences between $z \sim 2-3$ and $z \sim 0$ star-forming galaxies and also vital for self-consistently explaining the trends observed in the high-z population.

This thesis presents the main results from the near-infrared (NIR) component of the Keck Baryonic Structure Survey (KBSS), a targeted spectroscopic survey of $z \sim 2-3$ galaxies that uniquely combines observations in the rest-UV ($1000-2000$Å) and rest-optical ($3500-7500$Å) bandpasses. The NIR spectroscopic campaign conducted using Keck/MOSFIRE, described in Chapter 2, includes observations over 1200 high-z galaxies and represents one of the largest samples of high-quality rest-optical spectra of $z \sim 2-3$ galaxies ever assembled. These measurements offer new insights regarding the physical conditions in galaxies forming during one of the most active periods in the universe's history.

Chapter 3 describes the rest-optical spectra of ~ 380 KBSS galaxies at $z \simeq 2-2.7$ and shows that the primary difference between H II regions in $z \sim 2.3$ galaxies and those at $z \sim 0$ is an enhancement in the degree of nebular excitation. KBSS galaxies are also 10 times more massive than $z \sim 0$ galaxies with similar ionizing spectra and have higher gas-phase N and O abundances at fixed excitation. These results indicate the presence of harder ionizing radiation fields at fixed gas-phase enrichment relative to typical $z \sim 0$ galaxies, consistent with Fe-poor stellar population models that include massive binaries.

Chapter 4 builds on this analysis to develop a new technique for determining the physical conditions in individual high-z galaxies—independent of diagnostics tuned to local calibration samples. This method produces self-consistent measurements of the chemical enrichment and excitation conditions in ~ 150 galaxies at $z \simeq 2-2.7$.

Together, these results provide compelling evidence that the distinct chemical abundance patterns observed in $z \sim 2-3$ star-forming galaxies result from systematic differences in their star formation histories relative to galaxies with similar stellar masses today. The thesis concludes by considering the importance of accounting for differences in galaxies' past star formation when interpreting spectroscopic observations and briefly discusses opportunities for extending the framework for analyzing high-z galaxies presented here to future studies of star-forming galaxies throughout cosmic time.

PUBLISHED CONTENT AND CONTRIBUTIONS

Strom, A. L., Steidel, C. C., Rudie, G. C., et al., 2017,
"Nebular Emission Line Ratios in $z \simeq 2-3$ Star-forming Galaxies with KBSS-MOSFIRE: Exploring the Impact of Ionization, Excitation, and Nitrogen-to-Oxygen Ratio", The Astrophysical Journal, 836, 164
DOI:10.3847/1538-4357/836/2/164
ALS participated in the conception of the project, conducted the observations, developed the analysis software, reduced and analyzed the data, and wrote the paper.

TABLE OF CONTENTS

LIST OF ILLUSTRATIONS

LIST OF TABLES

Chapter 1

INTRODUCTION

The universe's history spans nearly 14 Gyr, but our ability to provide a detailed accounting of stars and galaxies throughout cosmic time has largely been limited to the current epoch, owing to the fact that nearby astronomical objects are bright enough to be easily observed in large numbers. Surveys of local galaxies reveal an impressive array of galaxy properties, including a diverse range of masses, star formation rates, morphologies, kinematics, and chemical enrichment (see Blanton & Moustakas, 2009, for a review), but the origin of such diversity remains uncertain. What causes some galaxies to finish forming stars and become "red and dead" elliptical galaxies (like M87, in the left panel in Figure 1.1), while others are still actively forming stars (like the Milky Way's neighbor, M31, in the right panel of Figure 1.1)? The elliptical galaxy M87 contains roughly twice as much mass in stars as M31, but knowing the mass of a galaxy—which is certainly correlated with

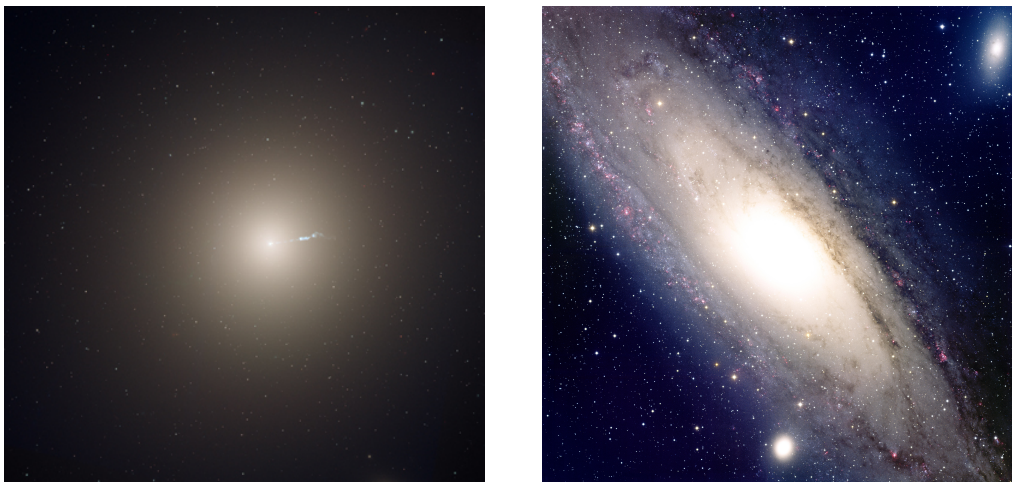

Figure 1.1: Two galaxies in the local universe, M87 (left panel, credit: P. Cote and E. Baltz, NASA/ESA/STScI/AURA) and the Andromeda Galaxy, or M31 (right panel, credit: T. A. Rector and B. A. Wolpa, NOAO/AURA/NSF). M87 is a giant elliptical galaxy in the Virgo cluster and one of the most massive nearby galaxies, although it is essentially done forming stars at the present time. In addition to the smooth profile of the stellar light, the radio jet powered by the supermassive black hole in the center of M87 is also visible in the image. In contrast, M31 is a disk-like galaxy and appears much bluer than M87 due to the presence of younger stars. The reddish features along the spiral arms of M31 are sites of active star formation, visible because of the strong Hα recombination emission from photoionized gas.

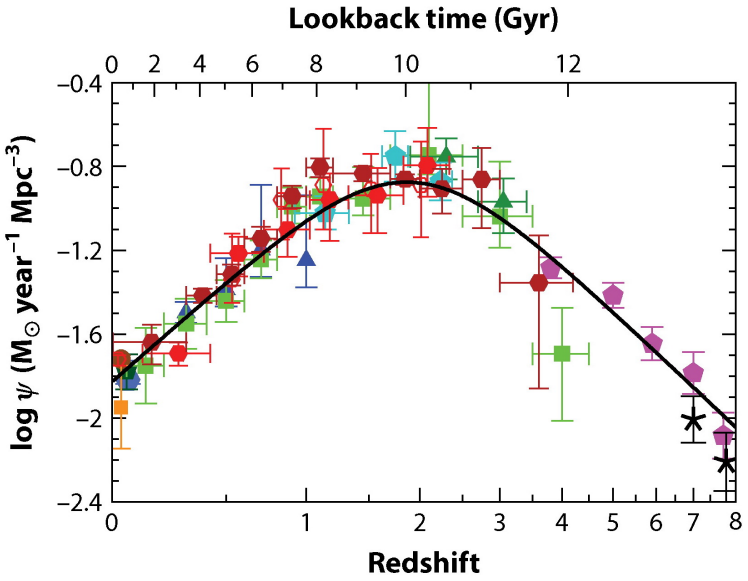

Figure 1.2: The cosmic star formation history of the universe, traced by rest-frame far-UV and infrared measurements drawn from a variety of sources (see Table 1 from Madau & Dickinson, 2014). The star formation rate density reaches a maximum between $1 \lesssim z \lesssim 3$, a period in the universe's history commonly referred to as the peak of galaxy assembly or "cosmic noon". Figure reproduced from Madau & Dickinson (2014).

many other observables, including the current star formation rate (SFR) and the chemical enrichment from previous generations of stars—is not sufficient to predict everything about it. Indeed, despite some other promising leads (including velocity dispersion, as proposed by Wake, van Dokkum & Franx, 2012), evidence for a single fundamental property that determines a galaxy's fate is inconclusive. It seems that, as is often the case in astronomy, the truth is more complicated.

It is possible to assemble at least a partial framework for understanding how present-day galaxies formed by leveraging the vast quantities of data available today and looking at trends across the population. Such trends are fossil evidence of the detailed astrophysics that dictated galaxy evolution at earlier times, when many galaxies formed a significant fraction of their stellar mass. We know from studies of the cosmic star formation history (e.g., Madau & Dickinson, 2014) that approximately 75% of stars in the universe were formed in the first half of its history (at $z > 1$), with the majority born in galaxies between $1 \lesssim z \lesssim 3$ (Figure 1.2). These redshifts correspond to lookback times of $\sim 8 - 12$ Gyr and represent the peak of galaxy assembly. This epoch is also an important period for the growth of supermassive black holes in the centers of galaxies, many of which were accreting at high rates as evidenced by the peak in quasar number density at the same redshifts (Richards

et al., 2006). Until recently, however, it has been challenging to study many $z > 1$ galaxies with detail similar to $z \sim 0$ galaxies, owing to the difficulties inherent in identifying high-z galaxies and—more importantly—obtaining the spectroscopic observations that yield information regarding their physical conditions.

1.1 H II Region Spectra as Astrophysical Probes

The strong emission lines of elements such as hydrogen, oxygen, nitrogen, and sulfur observed in the rest-optical (3600 – 7000Å) spectra of galaxies provide an essential toolkit for studying the detailed astrophysics of star-forming systems at all times. These lines originate primarily in galaxies' H II regions and correspond, directly or indirectly, to conditions in the ionized gas (including electron density, electron temperature, and gas chemistry), as well as the properties of the stars illuminating the gas, especially the shape of their ionizing spectra. The astrophysical basis for using nebular emission lines to measure these quantities as well as some of the most commonly-used diagnostics are reviewed below.

1.1.1 Electron Density

Atoms and ions with 7 or 15 electrons have np^3 configurations, with a $^4S_{3/2}$ ground state and the doublet $^2D_{3/2,5/2}$ as the first excited term. Ions that satisfy this criterion include both S^+ and O^+, which require energies of 10.36 eV and 13.61 eV, respectively, to be singly ionized and will therefore be present in typical H II regions. For S^+, the doublet occurs at 6718Å and 6732Å, and for O^+, the doublet occurs at 3727Å and 3729Å.

Because the $^2D_{3/2,5/2}$ states have very similar excitation energies but different critical densities ($n_{\rm crit} \equiv A_{ul}/q_{ul}$), the ratio of their line intensities depends strongly on electron density (n_e) and only weakly on the temperature of the gas. Further, because the transition probabilities for collisionally-excited lines of these metallic ions are very low, the lines are generally optically thin, and the line intensities are proportional to the line emissivities. In the low density limit ($n_e \sim 0$), every excitation to one of the higher states results in the spontaneous emission of a photon, and the ratio of line intensities is simply the ratio of the collision rates: Ω_{20}/Ω_{10}. At high densities, however, collisions dominate both excitation and de-excitation; the ratio of the level populations is then given by the ratio of their statistical weights, and the line ratio becomes $g_2 A_{21}/g_1 A_{10}$. The ratio [S II]λ6718/[S II]λ6732 therefore ranges from 1.5 – 0.43 (Tayal & Zatsarinny, 2010; Mendoza & Bautista, 2014), whereas [O II]λ3729/[O II]λ3727 spans 1.5 – 0.35 at the low- and high-density

limits, respectively (Kisielius et al., 2009).

Between the two extremes, the exact ratio of emission line strengths follows a form which is proportional to $n_e\,T^{-1/2}$. For [O II], the critical densities are both $\sim 10^3$ cm^{-3}, which means the line ratio is sensitive over the range $100 - 4000$ cm^{-3}, but [S II] continues to be sensitive up to $\sim 10^4$ cm^{-3}, because the $^2D_{3/2}$ level has $n_{\rm crit} = 1.5 \times 10^4$ cm^{-3}.

1.1.2 Electron Temperature

The most commonly-used probe of electron temperature (T_e) is line emission from atoms and ions with 6 electrons, which have a $2p^2$ configuration with ^{3}P as the ground state term and $^1D_2$ and $^1S_0$ as the first and second excited terms. Because the two excited levels are both populated by collisions but have different excitation energies, the ratio of line emission from these levels is highly sensitive to the kinetic temperature of electrons in the gas and remains independent of density for $n_e \ll n_{\rm crit}$:

$$\frac{I_{32}}{I_{21}} = \frac{n_3 \nu_{32} A_{32}}{n_2 \nu_{21} A_{21}} \propto e^{-E_{32}/kT_e}. \tag{1.1}$$

The only ions that have ionization potentials that make them likely to be found in H II regions *and* $^1S_0$ levels at low enough energies to be collisionally excited in gas at the typical temperatures found in H II regions ($\sim 10^4$ K) are O^{++} and N^+. Fortunately, the critical densities of all four transitions are high enough to make the ratios of [O III]$\lambda\lambda$5008,4960/[O III]λ4364 and [N II]$\lambda\lambda$6585,6549/[N II]λ5754 useful probes of temperature for $n_e \lesssim 10^5$ cm^{-3}. However, the expected strength of [O III]λ4364 is $\sim 30\%$ higher than [N II]λ5754 at a given T_e (Esteban et al., 2004), making [O III]λ4364 the more practical probe of temperature in the spectra of faint sources. Still, the expected flux in [O III]λ4364 is only $1 - 2\%$ that of [O III]λ5008 when $T_e \approx 10^4$ K and decreases in nebulae with lower T_e.

The temperature determined using the [O III] lines is not necessarily characteristic of the entire H II region, which may have a complicated ionization structure and a resulting temperature gradient. Ideally, a separate temperature can be estimated for regions of lower ionization using lines of [O II] (O^+ has a different electron configuration but one which is also sensitive to T_e) or [N II], but this is extremely difficult for faint or distant galaxies where [O III]λ4364 is already too weak to be detected in most individual galaxy spectra. Locally, $T_{\rm [OII]}$ can be related to $T_{\rm [OIII]}$ via H II region models (e.g. Garnett, 1992), but in cases where the ionization

parameters are large and/or star formation is dense (as expected in high-z galaxies), it is reasonable to assume $T_{[\mathrm{OII}]} \simeq T_{[\mathrm{OIII}]}$.

1.1.3 Gas-Phase Oxygen Abundance

In general, the overall metal content of gas in H II regions can be traced by the total abundance of oxygen (O/H), since oxygen is the most abundant heavy element in the universe. Broadly speaking, the calibrations used for determining O/H in galaxies and H II regions fall into three categories: (1) "direct" (T_e-based), (2) empirical, or (3) theoretical. The last two families of methods are often grouped together as "strong-line methods", since they rely on correlating the observed ratios of strong nebular emission lines with metallicities determined using the direct method or through comparisons with photoionization models.

1.1.3.1 Direct Method

Because metals are the primary coolants in the ISM, T_e should be tightly correlated with the metal content of the gas. Indeed, once T_e has been established using observations of the auroral [O III]λ4364 line, the total oxygen abundance for each ionization state can be calculated using the electron temperature and the ratio of the corresponding oxygen emission line(s) to one of the Balmer recombination lines (usually Hβ). For typical H II regions, both O^+ and O^{++} contribute significantly to the total oxygen abundance.

Although the direct method is considered the gold-standard for metallicity measurements, it has limited utility for oxygen-rich galaxies, as the auroral [O III]λ4364 line becomes progressively fainter at higher metallicities. The very long integrations necessary to obtain a precise measurement of the nebular-to-auroral line ratio for individual objects mean that obtaining direct method measurements for a large number of faint, distant, and/or metal-rich galaxies can be prohibitively expensive.

1.1.3.2 Empirical Strong-Line Methods

Given the challenges associated with T_e-based methods, it is more practical to estimate O/H using measurements of the strongest emission lines in galaxies' rest-optical spectra. As a result, there exist a number of strong-line calibrations relating T_e-based metallicities to the emission line ratios observed in the same objects. It is also possible to calibrate strong-line diagnostics using O/H measurements from photoionization models capable of reproducing the observed spectra of galaxies;

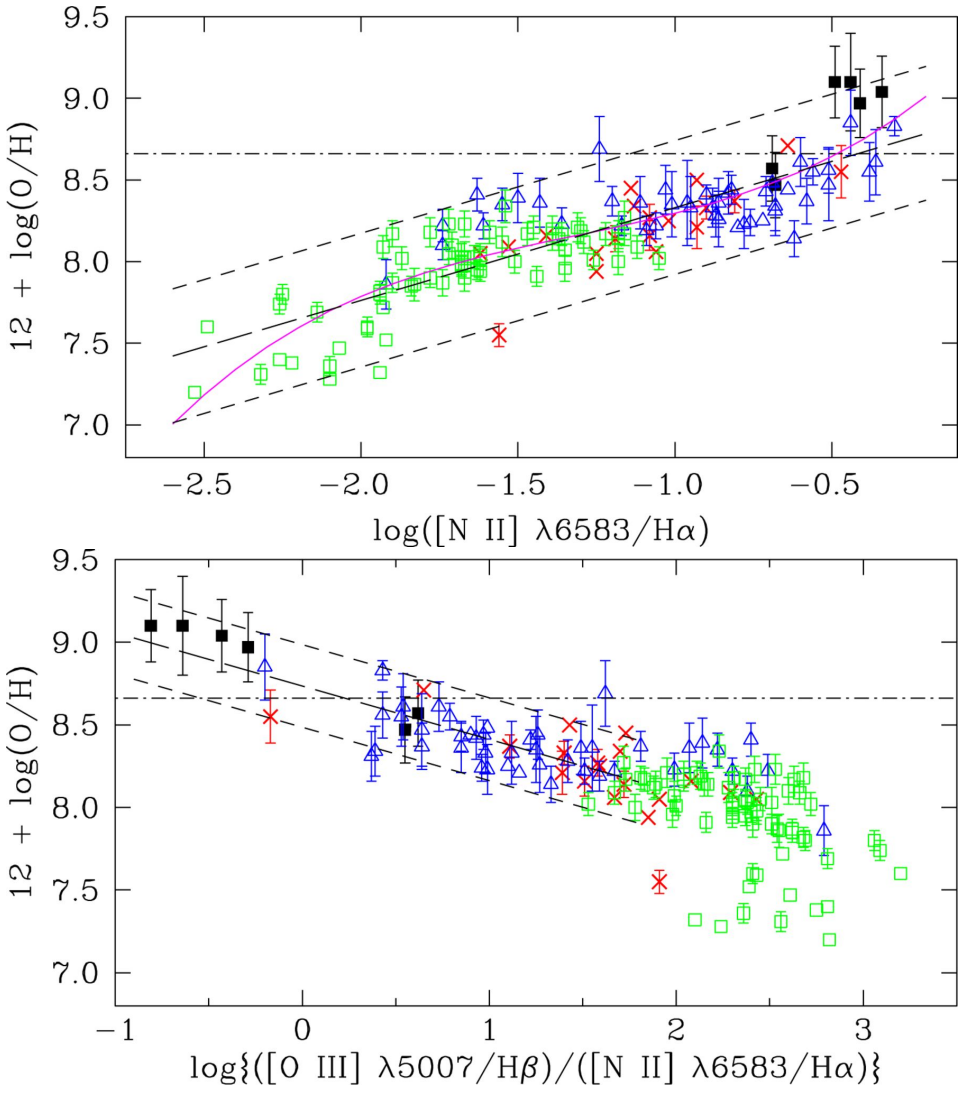

Figure 1.3: Oxygen abundance in extragalactic H II regions as a function of the N2 index (top panel) and O3N2 index (bottom panel). The long-dashed lines indicate the best-fit linear relationships between these quantities, as provided in the text. The short-dashed lines encompass 95% of the measurements in each panel. Figure reproduced from Pettini & Pagel (2004).

photoionization models are generally used to characterize high-metallicity objects, where estimates of T_e are no longer practical.

One of the first attempts at devising a strong-line calibration of O/H was by Jensen, Strom & Strom (1976), who considered [O III]λ5008/Hβ. Pagel et al. (1979) extended this work to include [O II] emission, in order to capture the contributions from both of the dominant ionization states of oxygen in typical H II regions. The so-called R23 index is defined as log[([O III]$\lambda\lambda$4949, 5008+[O II]$\lambda\lambda$3727, 3729)/Hβ] and, although less sensitive to differences in the ionization state of the gas than [O III]λ5008/Hβ, exhibits a double-valued behavior with O/H. Thus, most calibrations for R23 (including McGaugh, 1991; Pilyugin, 2003) break the degeneracy between the low-O/H and high-O/H "branches" by requiring additional data—often [O III]/[O II], which traces ionization, or [N II]λ6585/Hα, which itself traces O/H to some degree. Still, uncertainties in 12+log(O/H) estimated using R23 can be significant, ranging from $\sim$ 0.5 – 1 dex (Pettini et al., 2001; Skillman, Côté & Miller, 2003; Kennicutt, Bresolin & Garnett, 2003).

Two of the most common alternatives to R23 that circumvent these problems are the N2($\equiv$log([N II]λ6585/Hα)) and O3N2($\equiv$log([O III]λ5008/Hβ)-log([N II]λ6585/Hα)) indices. Both indices also have the advantage of being relatively insensitive to uncertainties in flux calibration and differential extinction due to dust. Pettini & Pagel (2004) provided the calibrations (shown in Figure 1.3 as the long-dashed lines) that are still frequently used today:

$$\begin{aligned} 12 + \log(\mathrm{O/H}) &= 8.90 + 0.57 \times \mathrm{N2} \\ 12 + \log(\mathrm{O/H}) &= 8.73 - 0.32 \times \mathrm{O3N2}. \end{aligned}$$

The N2 calibration has scatter of $\approx$ 0.18 dex, but tends to saturate at solar metallicities and above ($12 + \log(\mathrm{O/H})_\odot \geq 8.69$, Asplund et al., 2009), because [N II] becomes the dominant avenue for cooling and has increasing contributions from AGN- and shock-heated gas (Kewley & Dopita, 2002). The O3N2 calibration has somewhat lower scatter ($\approx$ 0.14 dex) and remains useful at metallicities where [N II] saturates, but is less reliable for $12 + \log(\mathrm{O/H}) \lesssim 8.0$, where O3N2 is no longer tightly correlated with T_e-based metallicity estimates.

Although strong-line diagnostics like those introduced here are attractive because they are easier to implement for large samples with fewer observations, there remains longstanding disagreement between the calibrations reported by different authors. Kewley & Ellison (2008) conducted a comprehensive comparison of 10 different

calibrations and found that the value of 12+log(O/H) reported for a given object can vary by up to 0.7 dex. In an attempt to address this issue, attempts have been made to "cross-calibrate" metallicity diagnostics (e.g., Kewley & Ellison, 2008; Maiolino et al., 2008), thereby forcing the O/H inferred using different indices to agree for the calibration sample (usually $z \sim 0$ galaxies).

1.2 Correlations Between Galaxy Properties and the "BPT" Diagram

The details of galaxy formation and evolution cause the physical conditions (including those discussed above) in nascent galaxies to be correlated with one another in specific ways, and these relationships will subsequently manifest as observed correlations between features in galaxies' spectra. Thus, by quantifying the observed trends between line ratios and uncovering their physical origin(s), we may be able to directly constrain theories of galaxy assembly.

The use of rest-optical nebular spectra to discern the properties of star-forming galaxies has a long history, extending at least as far back as the early 1970s. Much of this early work was conducted by astronomers at the California Institute of Technology (Caltech) and the Carnegie Observatories, including a survey of extragalactic H II regions in nearby spiral galaxies completed by Searle (1971). In that paper, Searle argues that while observations of the spectra of H II regions generally favor hot O stars ($T > 40000$ K) as the ionizing sources, the variations in the strong-line ratios with respect to one another within single galaxies and between galaxies indicate the presence of "systematic variations in *either* the composition of the gas *or* in the color temperature of the ionizing radiation fields" (emphasis his). Figure 1.4 shows the entire H II region sample, regardless of host galaxy, from Searle (1971) in Hα/[N II] vs. [O III]/Hβ space, where they occupy a single, distinct locus.

A decade later, Baldwin, Phillips & Terlevich (1981) relied on the existence of this H II region sequence to advocate using the line ratios observed in extragalactic objects' rest-optical spectra to distinguish between excitation mechanisms (e.g., hot O and B stars, planetary nebulae, shocks, or a power-law continuum from an active galactic nucleus, or AGN). Veilleux & Osterbrock (1987) refined the "BPT" technique and established the three diagnostic diagrams that are now commonly used to separate star-forming galaxies from AGN at $z \sim 0$: the [O III]λ5008/Hβ vs. [N II]λ6585/Hα (N2-BPT) diagram, the [O III]λ5008/Hβ vs. [S II]$\lambda\lambda$6718, 6732/Hα (S2-BPT) diagram, and the [O III]λ5008/Hβ vs. [O I]λ6301/Hα (O1-BPT) diagram. The authors focused primarily on the utility of

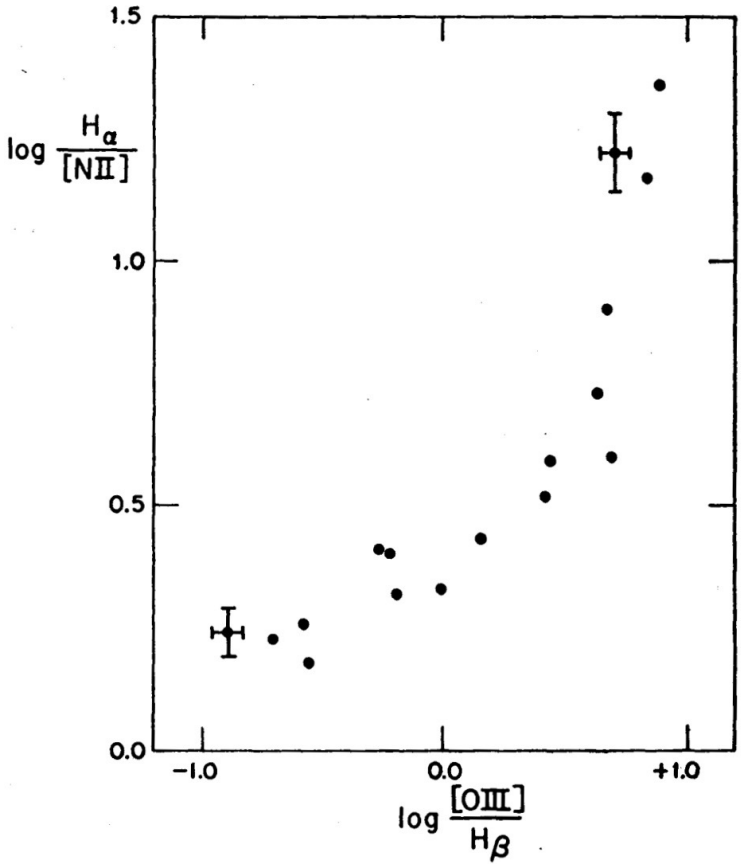

Figure 1.4: The rest-optical line ratios observed in a sample of H II regions found in nearby spiral galaxies. Notably, the locus in Hα/[N II] vs. [O III]/Hβ space is the same for all H II regions. This figure (reproduced from Searle, 1971, by permission of the AAS) is the first example of its kind in the literature, although the combination of these two line ratios is commonly referred to as "the BPT diagram" today, after Baldwin, Phillips & Terlevich (1981).

galaxies' rest-optical spectra for classification of the principal excitation mechanism, not for determining their physical conditions.

In the spirit of the original analysis by Searle (1971), more recent studies of large samples containing many thousands of nearby galaxies, such as the Sloan Digital Sky Survey (SDSS, York et al., 2000), have used observations of strong-line indices in concert with measurements of other galaxy properties to attempt to explain the physical origin of the tight galaxy locus in the classic line-ratio diagrams. Because of these efforts, we now know that the sequence of $z \sim 0$ star-forming galaxies in the N2-BPT diagram is associated with underlying correlations between stellar mass (M_*), specific star formation rate (sSFR≡SFR/M_*), ionization parameter (U), electron density (n_e), and metallicity (both O/H and N/O) (e.g., Kauffmann et al.,

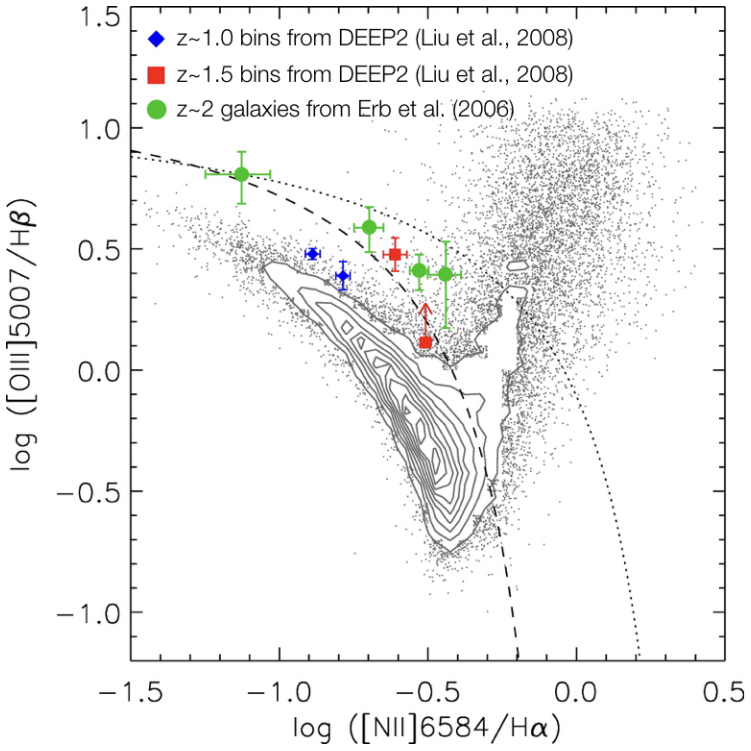

Figure 1.5: The N2-BPT diagram, showing the distribution of $z \sim 0$ galaxies from SDSS as grey contours and dots, compared to the line ratios measured from composite spectra of $z \sim 1$ galaxies (blue diamonds) and $z \sim 1.4$ galaxies (red squares) from the DEEP2 Galaxy Redshift Survey (Davis et al., 2003; Faber et al., 2007) and from the spectra of 4 individual $z \sim 2$ galaxies (green points) from Erb et al. (2006a). The dashed and dotted lines show the relations from Kauffmann et al. (2003) and Kewley et al. (2001), respectively, used to separate star-forming galaxies from AGN in the local universe. The line ratios observed in high-z galaxies place them above the majority SDSS galaxies (toward higher [O III]λ5008/Hβ), with many even found beyond the Kauffmann et al. (2003) curve. Figure adapted from (Liu et al., 2008) by permission of the AAS.

2003; Brinchmann, Pettini & Charlot, 2008; Masters, Faisst & Capak, 2016).

Although initial observations of galaxies at higher redshifts in the mid-2000s (Erb et al., 2006a; Liu et al., 2008) revealed a distinct offset between $z > 1$ and $z \sim 0$ galaxies in the N2-BPT diagram (Figure 1.5), small sample sizes and the lack of complete rest-optical spectra for high-z galaxies available at the time required interpreting such observations in the context of the paradigm used to explain present-day galaxies. Given the myriad physical reasons that might cause local galaxies to occupy the same region of the N2-BPT diagram, however, there was still significant uncertainty in the *true* origin of the offset of high-z galaxies; Liu et al. (2008) cite AGN activity, shocks, higher n_e, and higher U all as possible explanations.

There has been mounting evidence based on studies of other high-z galaxy properties

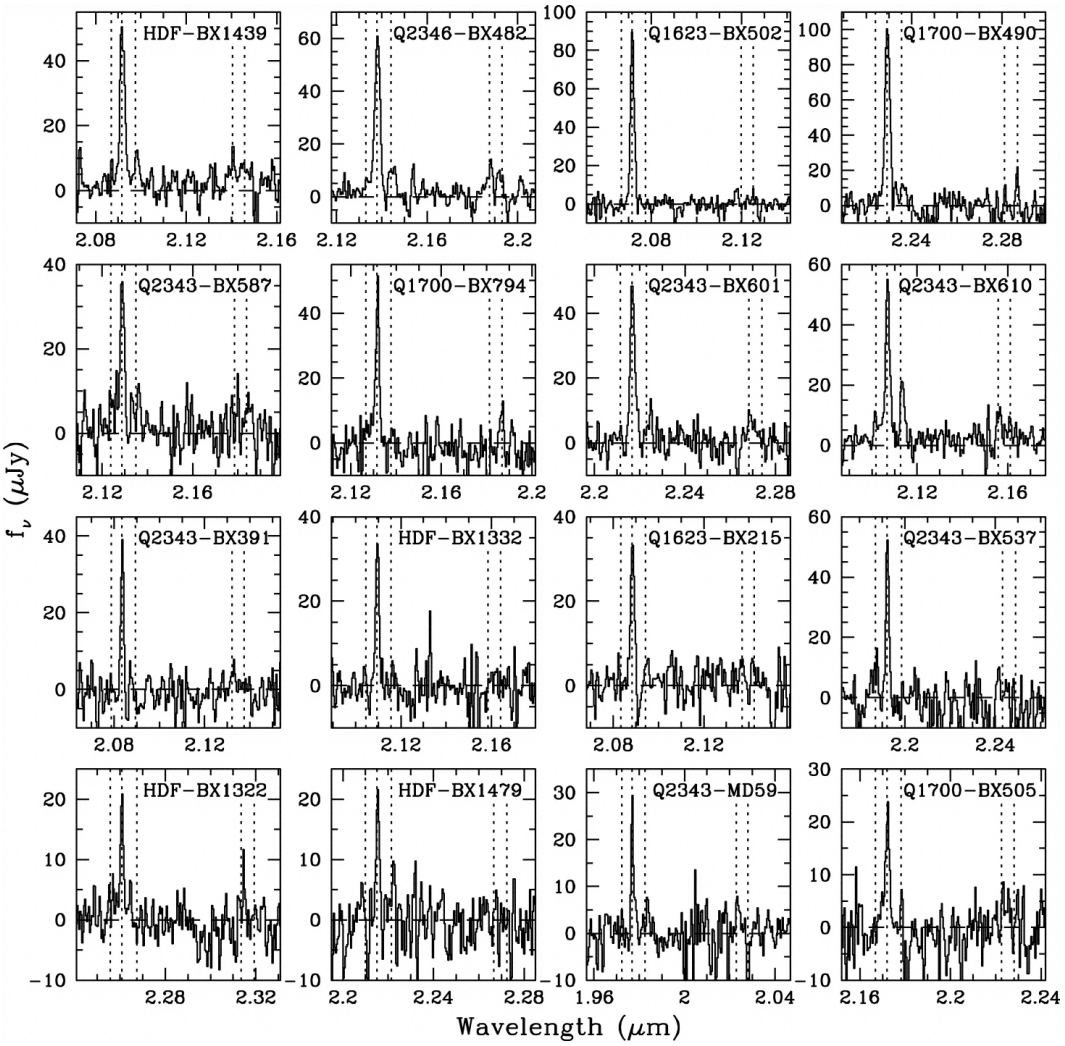

Figure 1.6: Representative K-band spectra of $z \sim 2$ galaxies obtained with NIRSPEC, showing the region around the Hα recombination line and the collisionally-excited [N II] and [S II] lines. Each row shows galaxies drawn from a different quartile in observed Hα flux, from the highest (top row) to the lowest (bottom row) quartiles. Figure reproduced by permission of the AAS from Erb et al. (2006c).

(see Shapley, 2011, for a review) that interpreting high-z observations in the context of local populations might be inappropriate and lead to misinterpretation of the observations. This concern is particularly relevant for $z \sim 2-3$ galaxies, which have higher SFRs at fixed M_* by at least a factor of 10 and cold gas masses higher by at least a factor of ~ 5, all within smaller volumes compared to local galaxies (e.g., Erb et al., 2006b; Law et al., 2012; Tacconi et al., 2013).

Despite these concerns, it has remained challenging to assemble statistical samples of $z \sim 2-3$ galaxies that can be studied independently of the local paradigm, because the strong rest-optical emission lines from their H II regions are shifted to near-

infrared (NIR) wavelengths ($1 - 2.5\mu$m), where limitations in detector technology and the lack of multi-object spectrographs have kept sample sizes comparatively small until recently. Some of the earliest seminal results pertaining to the rest-optical spectra of high-z galaxies come from the thesis work of Dawn K. Erb (published as Erb et al., 2006a; Erb et al., 2006b; Erb et al., 2006c), which was conducted at Caltech using the NIR spectrograph NIRSPEC (McLean et al., 1998) on the Keck I telescope to observe 114 galaxies at $z \sim 2$. Figure 1.6 shows the typical quality of the K-band spectra available for these galaxies. Although significant detections of multiple emission lines in individual galaxy spectra were rare, Erb (2006) investigated the stellar, gas, and dynamical mass budget of high-z galaxies and provided a measurement of the $z \sim 2$ mass-metallicity relation (MZR) that confirmed that early galaxies were less chemically-evolved at fixed stellar mass than their counterparts today.

Many of those results—especially the MZR from Erb et al. (2006a)—remained the benchmark for understanding high-z galaxies' rest-optical spectra for nearly a decade. Only in the last few years have the size and quality of spectroscopic samples of many individual (unlensed) $z \sim 2 - 3$ galaxies surpassed the sample from Erb (2006). This has been possible thanks to the most recent generation of multi-object NIR spectrographs, particularly the K-band Multi-Object Spectrograph on the VLT (KMOS, Sharples et al., 2013) and the Multi-Object Spectrometer for InfraRed Exploration on the Keck I telescope (MOSFIRE, McLean et al., 2012).

1.3 Outline of This Thesis

This thesis presents a detailed analysis of the rest-optical spectra of high-z star-forming galaxies selected from the Keck Baryonic Structure Survey (KBSS, Steidel, Rudie, Strom et al., 2014) and observed with MOSFIRE. These measurements represent one of the largest spectroscopic studies of high-z galaxies ever assembled and offer new insights regarding the physical conditions in galaxies forming during one of the most active periods in the universe's history. Chapter 2 introduces KBSS and the parts of the survey most salient to the work contained in this thesis, including a new method for selecting red, star-forming galaxies at $z \sim 1.5 - 2.5$ and a comparison between the KBSS sample and other ongoing NIR spectroscopic surveys of high-z galaxies. Chapter 3 describes the nebular spectroscopic properties of ~ 380 KBSS galaxies at $z \simeq 2 - 2.7$ observed with MOSFIRE, with an emphasis on understanding the differences between high-z galaxies and typical present-day galaxies. Chapter 4 builds on the analysis presented in Chapter 3 and the complementary

work by Steidel, Strom, et al. (2016) to develop a new technique for determining the physical conditions in *individual* high-z galaxies, independent of diagnostics tuned to local calibration samples. This method provides self-consistent measurements of the chemical enrichment and ionization/excitation conditions in $\sim$ 150 galaxies, resulting in the largest high-z sample with such measurements to date. Chapter 5 reviews the main conclusions of the thesis and discusses the implications for future studies of star-forming galaxies at the peak of galaxy assembly—and throughout cosmic time.

In addition to the results discussed in the following chapters, this work has also contributed to new discoveries regarding the nature of low-mass galaxies at the same redshifts (Erb et al., 2014; Trainor et al., 2015; Erb et al., 2016, Trainor, Strom, et al., 2016), facilitated more precise studies of the kinematics and metal content of the high-z circumgalactic medium (Turner et al., 2015; Turner et al., 2017), and aided in determining the ionizing photon budget in young galaxies at high redshift (Shapley, Steidel, Strom et al., 2016; Steidel et al., in prep.).

Chapter 2

THE KECK BARYONIC STRUCTURE SURVEY

The Keck Baryonic Structure Survey (KBSS, Steidel, Rudie, Strom et al., 2014) is a large, targeted spectroscopic survey designed to jointly probe galaxies *and* their gaseous environments at the peak of galaxy assembly at $z \sim 2-3$. The survey comprises 15 individual fields (totaling ~ 0.24 deg^2), each centered on one of the most luminous ($m_V \approx 15-17$) quasars in the sky, with $z_{\rm QSO} \sim 2.5-2.85$. Detailed information about the intergalactic medium (IGM) and circumgalactic medium (CGM) in these volumes comes from analysis of absorption line features in high-resolution, high-S/N spectroscopy of the central QSOs obtained with the High Resolution Echelle Spectrometer (HIRES, Vogt et al., 1994) on the Keck I telescope. Rudie et al. (2012), Turner et al. (2015), and Turner et al. (2017) provide results pertaining to the neutral hydrogen and metal content of the CGM based on data from KBSS. The galaxies themselves are selected from deep optical and near-infrared (NIR) imaging and subsequently followed up with spectroscopic observations of the rest-UV with the Low Resolution Imaging Spectrometer (LRIS, Oke et al., 1995; Steidel et al., 2004) and of the rest-optical with the Multi-Object Spectrometer For InfraRed Exploration (MOSFIRE, McLean et al., 2012), both on the Keck I telescope.

In addition to the physical motivation for studying galaxies at $z \sim 2-3$ discussed in Chapter 1, this redshift range also offers a number of practical advantages:

1. Potential galaxy targets both have a high spatial density on the sky and are still bright enough to be observed with $8-10$ meter telescopes from the ground,

2. Weak absorption lines from both metallic ions and HI can be observed in the spectra of the background QSOs, even when they fall shortward of the Lyα emission feature, and

3. Both the rest-frame far-UV ($1000-2000$Å) *and* rest-frame optical ($3500-7500$Å) portions of galaxies' spectra are accessible to ground-based telescopes.

The combination of these two bandpasses provides critical information about galaxies' massive stellar populations as well as the conditions in the surrounding star-forming regions. Furthermore, as galaxies during this epoch are actively exchanging baryonic material with the IGM and CGM via cosmological accretion and powerful outflows driven by star formation, supernovae, and active galactic nuclei (AGN), understanding their detailed astrophysics is central to uncovering the origin of the galaxy scaling relations observed across cosmic time.

Given the facilities currently available, the synergy arising from joint observations at rest-UV and rest-optical wavelengths is uniquely possible at these redshifts. The same exercise is significantly more difficult to perform for galaxies at lower redshifts, where galaxies' rest-UV spectra are observable only from space. For galaxies at earlier times, similar observations await the commissioning of space-based infrared spectrographs like the Near-Infrared Spectrograph (NIRSpec) and the Mid-Infrared Instrument (MIRI) on the *James Webb Space Telescope* (*JWST*), which will be able to observe the rest-optical spectra of many galaxies during the Epoch of Reionization ($z \gtrsim 6$) for the first time.

2.1 Imaging and Photometry

All of the KBSS fields have optical imaging in the U_n, G, and $\mathcal{R}$-bands as originally described by Steidel et al. (2003), which is used to select candidate galaxies for spectroscopic follow-up (Section 2.2). There is also substantial imaging at other wavelengths, which aids in the characterization of galaxies' spectral energy distributions (SEDs, Section 2.5.1), including data obtained with *Spitzer*/IRAC (typically including coverage in two channels per field) and *HST*/WFC3-IR (typically using the F140W and F160W filters). Table 2.1 provides a detailed overview of the photometric data available in each individual field.

The majority of these data were obtained prior to or separate from this thesis, with the exception of the deep NIR imaging obtained with MOSFIRE, which was completed as part of the instrument commissioning in Summer 2012 and during early science observations throughout 2012-13. These observations and the construction of the photometric catalogs used throughout the remainder of this work are described below.

2.1.1 Ground-based NIR Imaging

Early but incomplete NIR imaging in the KBSS fields was completed with the Wide Field Infrared Camera (WIRC, Wilson et al., 2003) at Palomar. In total, 8 (6) KBSS

Table 2.1: Summary of KBSS data

Field	z_{QSO}[1]	Area (arcmin^2)	N_{all}[2]	N_{UV}[3]	N_{neb}[4]	Photometric Data[5]
Q0100 + 130	2.721	43	189	137	90	$U_n, B, G, \mathcal{R}$, N4535, $Y, J, J2, J3, H1, H2, K_s$, 3.6 ,4.5, 5.8, 8.0, F140W, F160W
Q0105 + 163	2.652	40	164	131	69	$U_n, B, G, \mathcal{R}$, N4430, $Y, J, J2, J3, H1, H2, K_s$, 3.6, 4.5, F140W
Q0142 − 091	2.743	40	159	141	69	$U_n, B, G, \mathcal{R}$, N4535, $Y, J, J2, J3, H1, H2, K_s$, 3.6, 4.5, F140W, F160W
Q0207 − 003	2.872	40	163	123	69	$U_n, G, \mathcal{R}, Y, J, J2, J3, H1, H2, K_s$, 3.6, 4.5, F140W
Q0449 − 168	2.684	33	163	133	70	$U_n, G, \mathcal{R}, Y, J, J2, J3, H1, H2, K_s$, 3.6, 4.5, F105W, F140W, F160W
Q0821 + 312	2.616	40	156	119	69	$U_n, G, \mathcal{R}, J, K_s$, 3.6, 4.5, F140W
Q1009 + 295	2.652	37	169	134	68	$U_n, B, G, \mathcal{R}$, N4430, J, K_s, 3.6, 4.5, F140W, F160W
Q1217 + 499	2.704	35	150	119	48	$U_n, B, G, \mathcal{R}$, N4535, J, K_s 3.6, 4.5, F140W, F160W
Q1442 + 295	2.660	40	175	138	83	$U_n, B, G, \mathcal{R}$, N4535, J, K_s, 3.6, 4.5, F140W
Q1549 + 193	2.843	37	175	150	63	$U_n, G, V, \mathcal{R}$, N4670, $Y, J, J2, J3, H1, H2, K_s$, 3.6, 4.5, 5.6, 8.0, M24, F140W, F160W
Q1603 + 383	2.551	39	168	136	63	$U_n, B, G, \mathcal{R}$, N4325, J, K_s, 3.6, 4.5, F140W
Q1623 + 268	2.535	187	316	294	72	$U_n, G, \mathcal{R}, J, K_s$, 3.6, 4.5, 5.6, 8.0, M24, F140W, F160W
Q1700 + 643	2.751	127	251	211	96	$U_n, B, G, \mathcal{R}$, N4535, $Y, J, J2, J3, H1, H2, K_s$, 3.6, 4.5, 5.6, 8.0, M24, F140W, F160W
Q2206 − 199	2.573	41	153	136	49	$U_n, G, \mathcal{R}, Y, J, J2, J3, H1, H2, K_s$, 3.6, 4.5, F606W, F140W, F160W
Q2343 + 125	2.573	72	293	246	124	$U_n, B, G, \mathcal{R}$, N4325, $Y, J, J2, J3, H1, H2, K_s$, 3.6, 4.5, 5.8, 8.0, M24, F140W, F160W
Total:		860	2844	2348	1102	

[1] Redshift of central QSO for which $R \sim 40,000$, S/N $\sim$ 100 Keck/HIRES spectra (covering at least 3100-6000 Å) are available.

[2] Number of rest-UV color-selected galaxies with spectroscopic redshifts $1.5 < z < 3.5$ (from the rest-UV, rest-optical, or both).

[3] Number of rest-UV color-selected galaxies with rest-UV spectroscopic measurements $1.5 < z < 3.5$ (see Section 2.3).

[4] Number of rest-UV color-selected galaxies with rest-optical nebular spectroscopic measurements $1.5 < z < 3.5$ (see Section 2.4).

[5] Photometric bands observed; all cover the full field except HST/WFC3 bands, which generally covers only a central pointing. M24=Spitzer/MIPS 24μm; 3.6,4.5,5.6,8.0=Spitzer/IRAC 3.6μm, 4.5μm, 5.6μm, 8.0μm; F140W=HST/WFC3-IR F140W+grism; F160W=HST/WFC3-IR F160W (each pointing has 3-orbit depth); Y(J1),J2,J3,H1,H2=near-IR intermediate band filters; N4010, N4325, N4430, N4585, N4670 are custom narrow-band filters centered, respectively, at 4010, 4325, 4430, 4585, and 4670Å, with bandwidth $\simeq$ 80Å, designed for Lyα selection (c.f. Trainor et al., 2015).

fields were observed with WIRC using the K_s (J) filter, with total integration times of $\sim 8-12$ hr reaching a typical photometric depth of $K_{s,\mathrm{AB}} \approx 24.2$ ($J_{\mathrm{AB}} \approx 24.9$). Following the commissioning of MOSFIRE in June 2012, NIR imaging was obtained in 9 fields, under good to fair conditions with $\sim 0\farcs5 - 0\farcs7$ seeing. On average, the MOSFIRE images reach ~ 0.3 mag deeper than the WIRC data, even with typical exposure times of $\lesssim 1$ hour.

The MOSFIRE J and K_s images are constructed from a sequence of individual frames following a prescribed "box-9" dither pattern, with the offsets between dither positions and between dither sequences chosen to ensure adequate coverage of the footprint of the optical images in the same field (typically $6' \times 8'$). Integration times ranged between 7 and 10 s per exposure, where $8-10$ integrations were taken at each dither position and combined into a single coaveraged frame.

These data were reduced using a custom version of the *XDIMSUM* package in IRAF, which is designed specifically for accurately subtracting the high infrared sky background from sets of dithered images. The complete reduction method includes background sky-subtraction with *XDIMSUM*, generation of a combined bad pixel and cosmic ray rejection mask, subpixel registration of the individual frames, and construction of a final, exposure-time-weighted, stacked image with a corresponding exposure time map. The astrometry of the final stacked images was tied to the Sloan Digital Sky Survey (SDSS, York et al., 2000) DR6 (Adelman-McCarthy et al., 2008) objects in each field, and photometric zero points were calculated using unsaturated objects with J and K_s magnitudes from the 2MASS catalog (Skrutskie et al., 2006). Consistent photometric zero points were also re-derived for the WIRC imaging using the same procedure to ensure that the all of the KBSS NIR photometric data were on the same scale.

For 8 of the KBSS fields (including the 5 without J-band imaging from WIRC or MOSFIRE), observations in the intermediate bands $J1$ (Y), $J2$, $J3$, $H1$, and $H2$ were obtained by G. C. Rudie using the FourStar infrared camera (Persson et al., 2013) on Magellan in Fall 2013 under excellent conditions with $\sim 0\farcs4 - 0\farcs7$ seeing. These data were reduced with the publicly-available FourStar reduction package, FSRED, and zero points were determined based on the NIR color locus of stars compared to their photometry from the NEWFIRM Medium-Band Survey (NMBS, van Dokkum et al., 2009).

2.1.2 Photometric Catalogs

Photometric catalogs including measurements from the $\mathcal{R}$-band images and all available ground-based NIR images (from WIRC, MOSFIRE, and FourStar) were produced from versions that were pixel-registered to the corresponding $\mathcal{R}$ image in each field and Gaussian-smoothed to match the image with the largest point source function (PSF). Object detection and measurement were then performed with Source Extractor (SExtractor, Bertin & Arnouts, 1996) in dual-image mode, using the $\mathcal{R}$ images as the detection images. This method implicitly assumes that the aperture correction in each band is the same as in the $\mathcal{R}$-band. Objects in these catalogs were then matched to U_n and G measurements from previous work.

2.2 Galaxy Selection

2.2.1 Rest-UV Color Selection

The majority of KBSS galaxies are selected by their optical (rest-UV) colors, using a $U_nG\mathcal{R}$ color selection designed to identify star-forming galaxies at $z \simeq 1.5 - 3.5$ (Steidel et al., 2003; Adelberger et al., 2004; Steidel et al., 2004). High-z galaxies can be identified in this color space by looking for the signature of strong Lyman continuum absorption at rest-UV wavelengths (i.e., the canonical Lyman Break Galaxies, or LBGs, at $z \gtrsim 3$) or by sampling the relatively flat rest-UV spectra between the Lyman and Balmer breaks of galaxies at somewhat lower redshifts. The original $U_nG\mathcal{R}$ color selection windows were designed to take advantage of the high sensitivity, high spatial resolution, and large fields-of-view offered by optical imaging instruments on ground-based telescopes.

KBSS targets selected on the basis of their optical colors are labeled according to their expected redshifts. These groupings include "C/D" and "MD/M" objects, which are selected to be at redshifts $z \simeq 2.7 - 3.4$ and satisfy the following criteria:

$$U_n - G > G - \mathcal{R} + 1.0$$
$$G - \mathcal{R} \leq 1.2.$$

"BX" objects are selected to be at redshifts $2.0 \lesssim z \lesssim 2.6$ using the following criteria:

$$G - \mathcal{R} \geq -0.2$$
$$U_n - G \geq G - \mathcal{R} + 0.2$$
$$G - \mathcal{R} \leq 0.2(U_n - G) + 0.4$$
$$U_n - G \leq G - \mathcal{R} + 1.0.$$

Finally, "BM" objects are selected to be at redshifts $1.5 \lesssim z \lesssim 2.0$ and identified using the following criteria:

$$G - \mathcal{R} \geq -0.2$$
$$U_n - G \geq G - \mathcal{R} - 0.1$$
$$G - \mathcal{R} \leq 0.2(U_n - G) + 0.4$$
$$U_n - G \leq G - \mathcal{R} + 0.2.$$

In general, the $U_nG\mathcal{R}$ selection also imposes a magnitude limit of $\mathcal{R} \leq 25.5$, meant to increase the likelihood of successful spectroscopic follow-up. The properties of UV-faint objects ($\mathcal{R} > 25.5$) that otherwise satisfy the $U_nG\mathcal{R}$ criteria are discussed elsewhere (e.g., Reddy et al., 2005, Reddy et al., in prep.), but these galaxies represent only a small fraction of the total KBSS spectroscopic sample assembled to date. In total, the optical color selection criteria above yield 13,482 targets in the 15 KBSS fields.

Figure 2.1 illustrates $U_nG\mathcal{R}$ color space, alongside data for objects with $\mathcal{R} \leq 25.5$ in the Q0449 − 168 field. The hooked shape of the locus in color-color space is due to the transition between sampling the Balmer and 4000Å breaks in galaxies at $z < 1$ (to the lower right of the $U_nG\mathcal{R}$ windows) and observing the Lyman break in galaxies with $z \gtrsim 2.5$ (mostly in the yellow C/D and blue M/MD regions). Galaxies in the BM and BX windows (orange and green shaded regions, respectively) have relatively flat $G - \mathcal{R}$ colors, as neither the Balmer nor Lyman break is observable at these wavelengths, and only slightly redder $U_n - G$ colors due to a small amount of blanketing from the Lyα forest[1]. KBSS galaxies with spectroscopically-confirmed redshifts are identified by red squares in Figure 2.1, with $z_{\rm spec} = 1.44 - 3.57$.

2.2.2 Massive, Dusty Star-forming Galaxies: the RK Selection

Not every galaxy at the redshifts of interest will satisfy the color selection criteria originally adopted for KBSS, especially when photometric errors are significant compared to the size of the selection windows. Although many high-z galaxies that scatter out of one color-selection window will instead fall in an adjacent selection window, some galaxies whose true rest-UV colors satisfy the $U_nG\mathcal{R}$ color selection criteria will have observed colors that cause them to be excluded. This is of greatest concern for dusty, massive galaxies and quiescent galaxies of all masses, which

[1]The absence of any clear spectral break at these observed wavelengths is what led authors in the late 1990s and early 2000s to refer to the redshift range $z \sim 1.5 - 2.5$ as the "redshift desert".

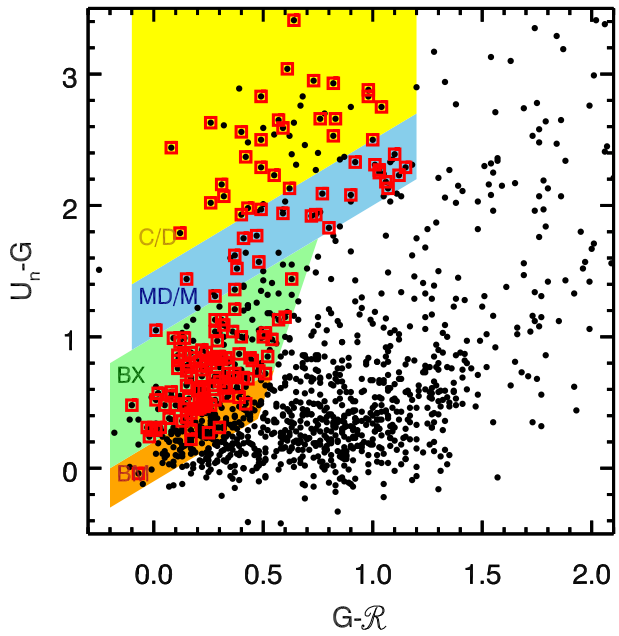

Figure 2.1: Optical colors for objects with $\mathcal{R} \leq 25.5$ in the Q0449 − 168 field. The original color selection windows from Steidel et al. (2003) and Adelberger et al. (2004) designed to identify star-forming galaxies at $z \simeq 2.7 - 3.4$ (C/D in yellow, MD/M in blue), $2.0 \lesssim z \lesssim 2.6$ (BX in green), and $1.5 \lesssim z \lesssim 2.0$ (BM in orange) are also shown. Galaxies with spectroscopically-confirmed redshifts are marked by red squares. The dense locus of sources to the lower right of the selection windows is populated largely by low-redshift ($z < 1$) contaminants (Adelberger et al., 2004), whose optical colors trace the Balmer and 4000Å breaks, rather than Lyman continuum absorption, as is the case with galaxies at $z \gtrsim 2.5$.

will be fainter and potentially more heavily reddened at rest-UV wavelengths than galaxies with larger amounts of unobscured star formation.

A number of NIR color selection criteria were devised to mitigate this bias by leveraging information about the rest-optical shape of high-z galaxies' spectra, as the presence of a strong Balmer break should allow galaxies to be selected regardless of the details of their rest-UV spectra. Franx et al. (2003) proposed to identify passively-evolving and/or heavily-reddened galaxies at $z \gtrsim 2$ on the basis of $J - K_s$ color, which is sensitive to both age and stellar mass because it traces the Balmer and 4000Å breaks to some degree. Objects with $(J - K_s)_{\rm Vega} > 2.3$ identified in this manner are referred to as distant red galaxies, or DRGs. Daddi et al. (2004) separately defined the quantity $BzK \equiv (z - K)_{\rm AB} - (B - z)_{\rm AB}$, which can be used to select $z \simeq 1.4 - 2.5$ galaxies that are likely to be star-forming ($BzK \geq -0.2$) and those that are passively-evolving ($BzK < -0.2$ and $(z - K)_{\rm AB} \geq 2.5$).

Reddy et al. (2005) compared optical and NIR techniques for selecting high-z galaxies and reported overlap at the 70% – 80% level between $z \sim 2$ $U_nG\mathcal{R}$-selected and BzK-selected galaxies in the GOODS-North field (Giavalisco et al., 2004) when the same maximum K_s-band limit was applied. The authors also found that many BzK objects missed by the $U_nG\mathcal{R}$ selection criteria fell within $\lesssim 0.2$ mag of the BX/BM selection windows, usually toward larger $G - \mathcal{R}$ colors. Similarly, $U_nG\mathcal{R}$-selected objects missed by the BzK selection were often very close to the star-forming BzK selection window in the $B - z$ vs. $z - K$ plane.

Motivated by the findings from Reddy et al. (2005) and a desire to be more complete in the selection of high stellar mass galaxies at $z \simeq 1.5 - 3.5$, we introduced two modifications to the original optical color selection windows. Although Franx et al. (2003) use $J - K_s$ color for their DRG selection, the 4000 Å and Balmer breaks are in fact still shifting through the J-band at these redshifts, making $\mathcal{R} - K_s$ color a better tracer of age and stellar mass (Shapley et al., 2005). Further, the use of $\mathcal{R} - K_s$ color does not additionally require deep J imaging, which must be significantly deeper than the corresponding K_s imaging in order to make use of a DRG-type selection. By combining the original $U_nG\mathcal{R}$ color selection criteria with a cut in $\mathcal{R} - K_s$ color, it is possible to efficiently select galaxies at the redshifts of interest that preferentially occupy the high end of the mass distribution. After some experimentation, we adopted a threshold of $(\mathcal{R} - K_s)_{\rm AB} \geq 2$ for identifying such galaxies.

To recover heavily-reddened or more moderately star-forming galaxies missed by the BX/BM criteria entirely, we coupled the $\mathcal{R} - K_s$ color cut with a new optical color selection window at redder $G-R$ colors. These criteria should identify galaxies in the same redshift range as BX/BM galaxies but which are scattered out of the traditional selection windows due to the effects of dust obscuration. This "RK" selection, shown as the red shaded region in Figure 2.2, imposes the following criteria:

$$\mathcal{R} \leq 25.5$$
$$G - \mathcal{R} \leq 1.2$$
$$U_n - G \geq G - \mathcal{R} - 0.1$$
$$G - \mathcal{R} > 0.2(U_n - G) + 0.4$$
$$U_n - G \leq G - \mathcal{R} + 1.0.$$

In total, the RK selection adds 417 galaxy candidates to the photometric KBSS sample, and we discuss the redshift distribution and other properties for those with

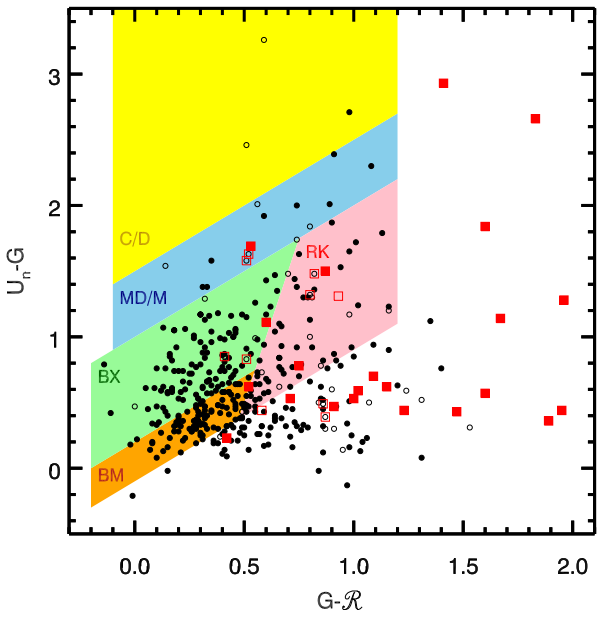

Figure 2.2: Optical color space, highlighting the original $U_nG\mathcal{R}$ color selection windows (yellow, blue, green, and orange shaded regions) as well as the new RK selection window (red shaded region), as described in the text. For comparison, objects in GOODS-N that satisfy the star-forming BzK galaxy selection (black circles) and DRG selection (red squares) are also shown; solid points represent objects with $\mathcal{R} \leq 25.5$ and open points signify objects with $\mathcal{R} > 25.5$. All objects shown also have $K_{s,\mathrm{AB}} < 22.85$. With the exception of objects that also coincide with the low-z locus at small $U_n - G$ colors, many of the NIR-selected galaxies missed by the original $U_nG\mathcal{R}$ windows fall in the RK region.

successful spectroscopic follow-up with MOSFIRE in Sections 2.4 and 2.5.1.

As illustrated in Figure 2.2 using $U_nG\mathcal{R}$ photometric data for objects in the GOODS-N field described by Reddy et al. (2006) and NIR data from the consolidated catalogs published by the 3D-HST survey (Skelton et al., 2014), the RK selection window also corresponds to the region in optical color space where many of the NIR-selected objects missed by the BX/BM selection criteria are found. The remainder of the missing BzK objects and DRGs overlap with the locus of low-z contaminants and are difficult to recover using optical colors alone. However, many of these photometric candidates are found to have $z < 1.5$ from spectroscopic follow-up (Figure 2.3), below the redshift range targeted by KBSS.

2.3 Optical Spectroscopy with LRIS

Prior to 2014, $\sim$ 2300 $U_nG\mathcal{R}$-selected star-forming galaxies in KBSS fields were observed with the blue arm of LRIS with the primary aim of determining redshifts for

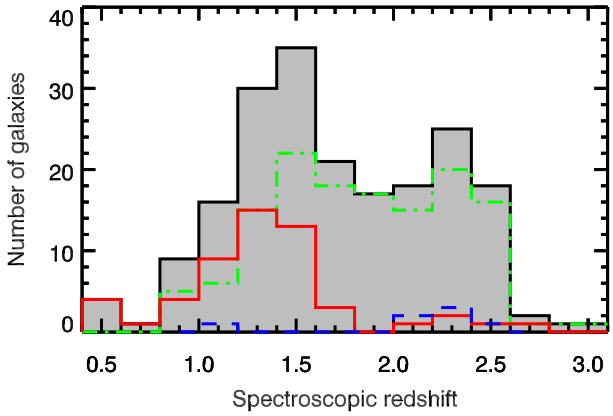

Figure 2.3: The distribution in spectroscopic redshift for star-forming BzK galaxies and DRGs in GOODS-N. The grey shaded histogram represents the distribution for all NIR-selected galaxies, with those that would also have been selected using the $U_nG\mathcal{R}$+RK criteria shown by the dot-dashed green histogram. The other colored outlines show the distributions for galaxies missed by all of the optical color selection criteria used by KBSS, separated by whether they satisfy the $U_nG\mathcal{R}$+RK color cuts but have $\mathcal{R} > 25.5$ (dashed blue histogram) or whether they have optical colors that fall outside of the selection windows entirely (solid red histogram). Galaxies in the latter category predominately have $z < 1.5$, below the redshift range targeted by KBSS (and comparable high-z spectroscopic surveys).

galaxies near the quasar sightlines. These observations were generally conducted in one of two configurations: (1) with the 400 line mm^{-1} grism and the d680 dichroic, covering $\simeq 3100-6000$Å, or (2) with the 600 line mm^{-1} grism and the d560 dichroic, covering $\simeq 3400-5600$Å. Individual galaxies were most commonly observed for a combined total of 1.5 hr on 1 or 2 masks, but some targets have exposure times of up to 7.5 hr. The LRIS observations and data reduction for this early campaign are described in more detail by Steidel et al. (2010) and Rudie et al. (2012).

The majority of the original LRIS sample have spectra suitable for measuring redshifts, but of insufficient quality for detailed analysis. To facilitate the joint investigation of galaxies' LRIS and MOSFIRE spectra, we began expanding the rest-UV sample to include uniform, deep ($\sim$ 10 hr) spectroscopic observations with LRIS for a large, representative sample of KBSS galaxies in Fall 2014, prioritizing those with multi-band nebular spectroscopy from MOSFIRE already in hand (Steidel, Strom, et al., 2016). These observations utilize both the blue side (with the 600 line mm^{-1} grism) and the red side (with the 600 line mm^{-1} grating), with the d500 dichroic or, more commonly, the d560 dichroic. As of January 2017, the deep LRIS component of KBSS includes observations of 226 galaxies in 9 of the KBSS fields,

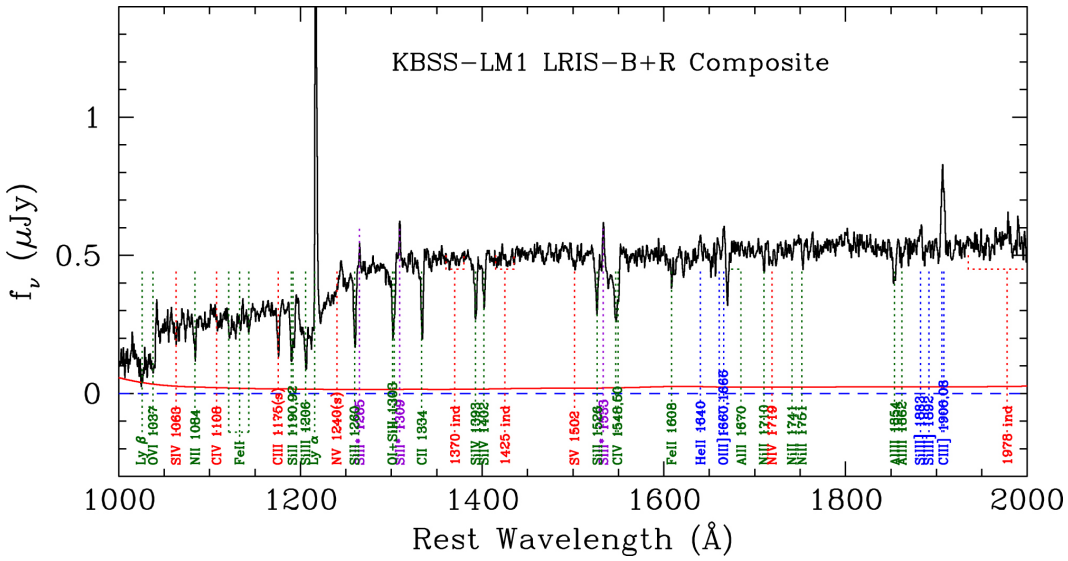

Figure 2.4: The rest-UV composite spectrum of 30 $z \simeq 2-2.7$ KBSS galaxies with deep spectroscopic observations from the post-2014 LRIS campaign. Most of the fluctuations in the stack reflect real spectroscopic features, including stellar absorption features (labeled in red), interstellar absorption features (labeled in green), nebular emission lines (labeled in blue), and fine structure emission lines (labeled in purple). Measurements of these emission and absorption features can be used independently and in combination with observations of rest-optical spectra to constrain the properties of the galaxies' gas and stars. Figure from Steidel, Strom, et al. (2016).

157 of which have corresponding MOSFIRE observations.

Although the work presented in this thesis primarily concerns the rest-optical spectroscopy of high-z galaxies, such studies both inform and are informed by knowledge of the same galaxies' rest-UV spectra. Figure 2.4, reproduced from Steidel, Strom et al. (2016), shows a rest-UV composite spectrum constructed using the pilot LRIS observations of 30 KBSS galaxies with $z \simeq 2-2.7$ from the Q1442 and Q2343 fields. The most prominent emission line is Lyα near 1216Å[2], but the composite also highlights the wealth of other spectral features that reveal information about the massive stellar populations (via photospheric absorption lines), the bulk motion of gas inside the galaxy (probed by the interstellar absorption lines), and the H II regions (using the nebular emission lines) in high-z galaxies. These observations complement those that can be made at rest-optical wavelengths, where a larger set of nebular emission lines provide more insight into the detailed physical conditions

[2]The peak of the observed Lyα line is not always coincident with 1216Å due to resonant scattering, which produces an overall shift toward longer wavelengths. For a more thorough discussion of this issue, readers are directed to the work of Pettini et al. (2001) and also Trainor et al. (2015), who discuss the Lyα morphologies of Lyα-emissioned-selected galaxies in KBSS in detail.

of gas in galaxies' star-forming regions (as discussed in Chapter 1) and additional, albeit indirect, constraints on the properties of the youngest and most massive stars.

2.4 Near-Infrared Spectroscopy with MOSFIRE

2.4.1 Observing Strategy

The MOSFIRE component of KBSS (KBSS-MOSFIRE) was designed to address multiple science goals simultaneously, which required revisiting galaxies for observation more than once, depending their contributions to specific science cases. There were three primary objectives, listed below in order of increasing observing time typically required to achieve them:

1. To measure systemic redshifts for as many galaxies as possible, prioritizing those near the bright quasar in the center of each survey field. These measurements reduce redshift uncertainties and are crucial for improving studies of gas content and kinematics in the CGM (e.g. Rudie et al., 2012; Turner et al., 2015; Turner et al., 2017), quantifying outflow kinematics via the strong interstellar absorption lines observed in galaxies' rest-UV spectra (Steidel et al., 2010), and investigating the Lyα properties of high-z star-forming galaxies (e.g., Trainor et al., 2015).

2. To assemble a statistical sample of galaxies with high-S/N measurements of the strong rest-optical nebular emission lines, including Hα, [N II]λ6585, [O III]λ5008, Hβ, and [O II]$\lambda\lambda$3727,3729. Collectively, these lines allow the ISM conditions in individual high-z galaxies to be studied in detail (which is the subject of the work presented in Chapters 3 and 4).

3. To obtain deep, high-quality spectroscopy for a specially-selected subset of galaxies at $z = 2.36 - 2.57$, where the electron temperature-sensitive [O III]λ4364 line falls in H-band and can be used to inform empirical and photoionization model-based inferences of gas-phase metallicity.

Most targets were initially placed on masks designed for observations in H- and/or K-band and observed for $1.5-2$ hr. When these observations yielded a nebular redshift, galaxies were either down-weighted if only a subset of the diagnostic lines were observable or put on subsequent masks until the strongest lines (Hα, [N II]λ6585, [O III]λ5008, Hβ, and [O II]$\lambda\lambda$3727,3729) were measured at $> 5\sigma$. Often, the same mask configurations were used for observations in J-, H-,and K-band. Galaxies

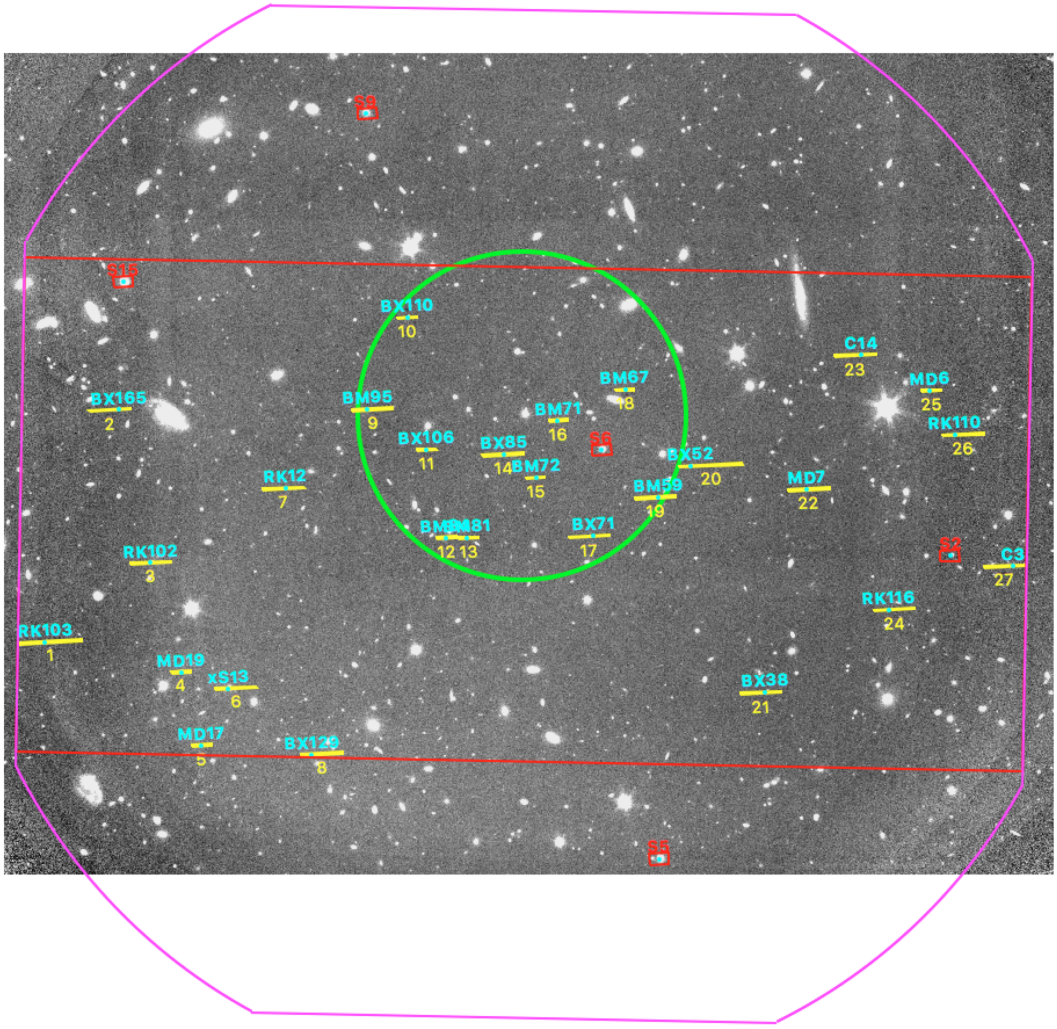

Figure 2.5: The MOSFIRE configuration for the mask "Q0449close1", shown relative to the K_s image obtained with MOSFIRE and reduced as described in the text. The magenta outline illustrates the MOSFIRE field-of-view, with the red rectangle showing the allowed real estate for slits. Slits assigned to science targets are shown in yellow, with alignment star boxes shown in red. The green circle has a radius of $60''$ and is centered on the bright central quasar Q0449 – 168, highlighting the range in projected distance where observations of foreground galaxies were prioritized according to the first survey goal, intended to address the study of $z \sim 2 - 3$ galaxies' CGM.

for which [O III]λ4364 is accessible continued to be assigned to masks until they reached 8 – 10 hr of total integration in H-band, the estimated exposure time required to reach the expected flux level of the auroral line (1×10^{-18} erg/s/cm^2).

A typical KBSS-MOSFIRE mask (Figure 2.5) contained $\sim$ 30 targets: 10 – 15 high-priority galaxies, 15 – 20 "filler" targets, and 1 bright star used for estimating the seeing and zero-pointing the flux calibration for the mask. Because of the dense

spatial sampling of the KBSS fields, multiple slit-mask configurations were usually required to obtain observations of all high-priority targets in a given field, although we attempted to re-observe galaxies at the same position angle to eliminate concerns about combining spectra taken at different position angles.

Observations were taken as a sequence of 30×120s exposures in J and H (or 20×180s in K), with an ABAB dither pattern and an offset of $3''$ between dither positions. These exposure times are short enough to allow for extremely good background subtraction and help minimize the effects of the rapidly-changing bright OH emission lines.

2.4.2 Data Reduction and Analysis

The data were reduced using the publicly-available data-reduction pipeline[3] (DRP) written by N. P. Konidaris in collaboration with C. C. Steidel and other members of the MOSFIRE instrument team. The DRP produces a flat-fielded, background-subtracted, and rectified stack for each slit, reduced to vacuum wavelengths using a wavelength solution determined from the OH emission lines (or a combination of OH emission lines and Ne arc lamp spectra in K-band). The two-dimensional (2D) pipeline products are then flux-calibrated and corrected for telluric absorption using wide- and narrow-slit observations of A0V stars and shifted to account for the heliocentric velocity at the start of each exposure sequence.

The 2D spectrograms are analyzed using *MOSPEC*, an interactive software tool developed as part of this thesis specifically for visualizing, fitting, and extracting one-dimensional (1D) spectra from MOSFIRE observations. The development and use of *MOSPEC* is discussed at greater length in Chapter 3 and Appendix A, but the default usage for the analysis of the NIR spectroscopy of KBSS galaxies is reviewed here. Where possible, 1D science spectra and corresponding error spectra were extracted from each individual 2D spectrogram using boxcar extraction apertures (determined by the user, with a median value of 10 pixels or $1\farcs80$, corresponding to 14.8 kpc at $z = 2.3$). The location of the target on the slit was then measured, either from the peak of a 2D Gaussian fit to a strong emission line or from the middle of the extraction aperture. The measured slit positions of objects varied by up to a few pixels relative to the predicted positions due to small errors in mask alignment and/or tracking. To account for these differences, separate MOSFIRE observations of the same object were first shifted to align the measured positions

[3] `http://www2.keck.hawaii.edu/inst/mosfire/drp.html`

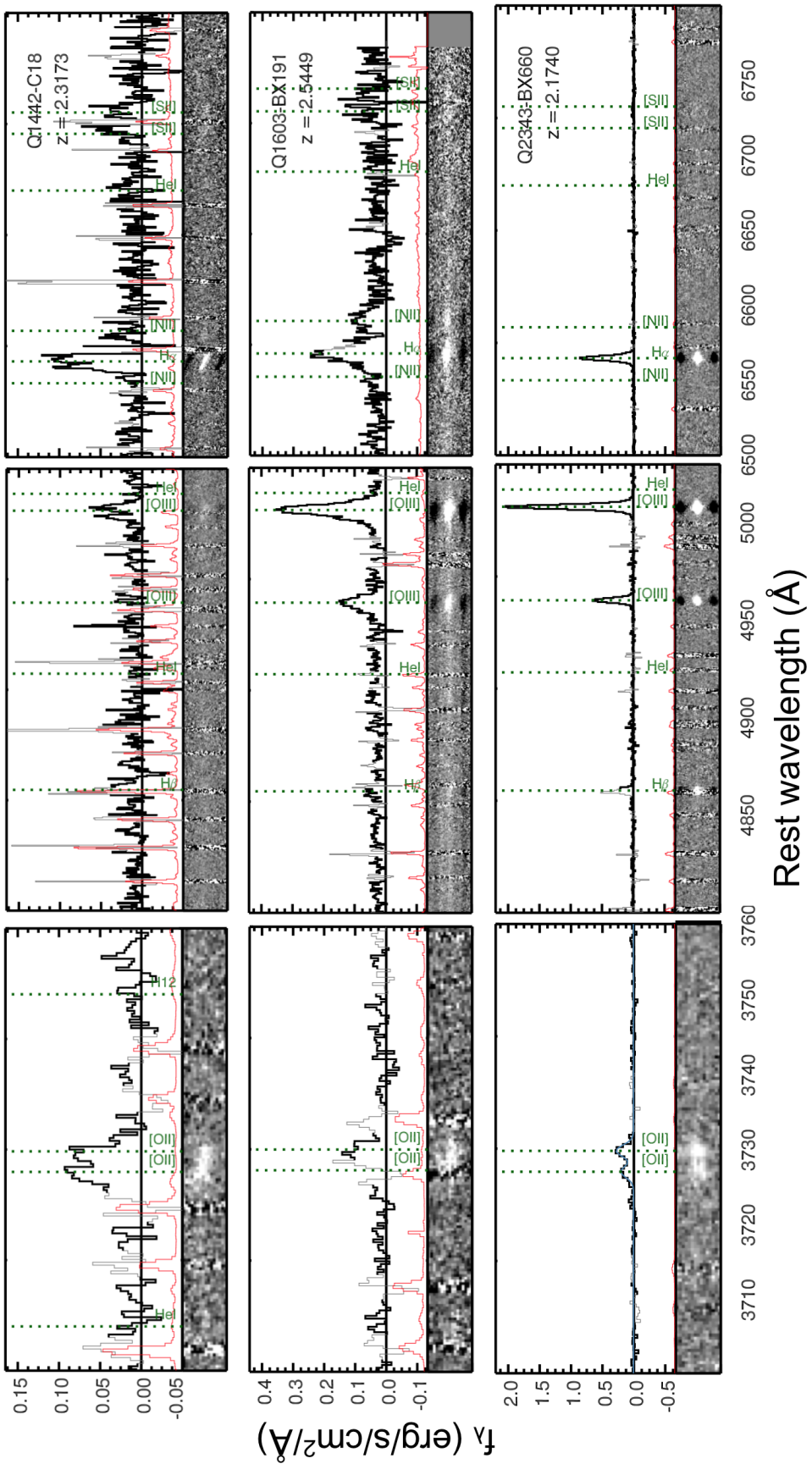

Figure 2.6: MOSFIRE spectroscopy of KBSS galaxies, showing the rest-optical wavelength range accessible in the J-band (left column), H-band (center column), and K-band (right column). The 2D spectrograms are shown at the bottom of each panel, with the extracted 1D spectrum from *MOSPEC* plotted above in black and the corresponding 1σ error spectrum shown in red. Regions near strong OH sky lines have been colored grey. The rest-optical emission lines fit by *MOSPEC*, including many of the strong lines commonly observed in individual galaxy spectra, are labeled in green, and the systemic redshift measured from the combination of these lines is shown in the upper right corner of the K-band spectrum for each galaxy.

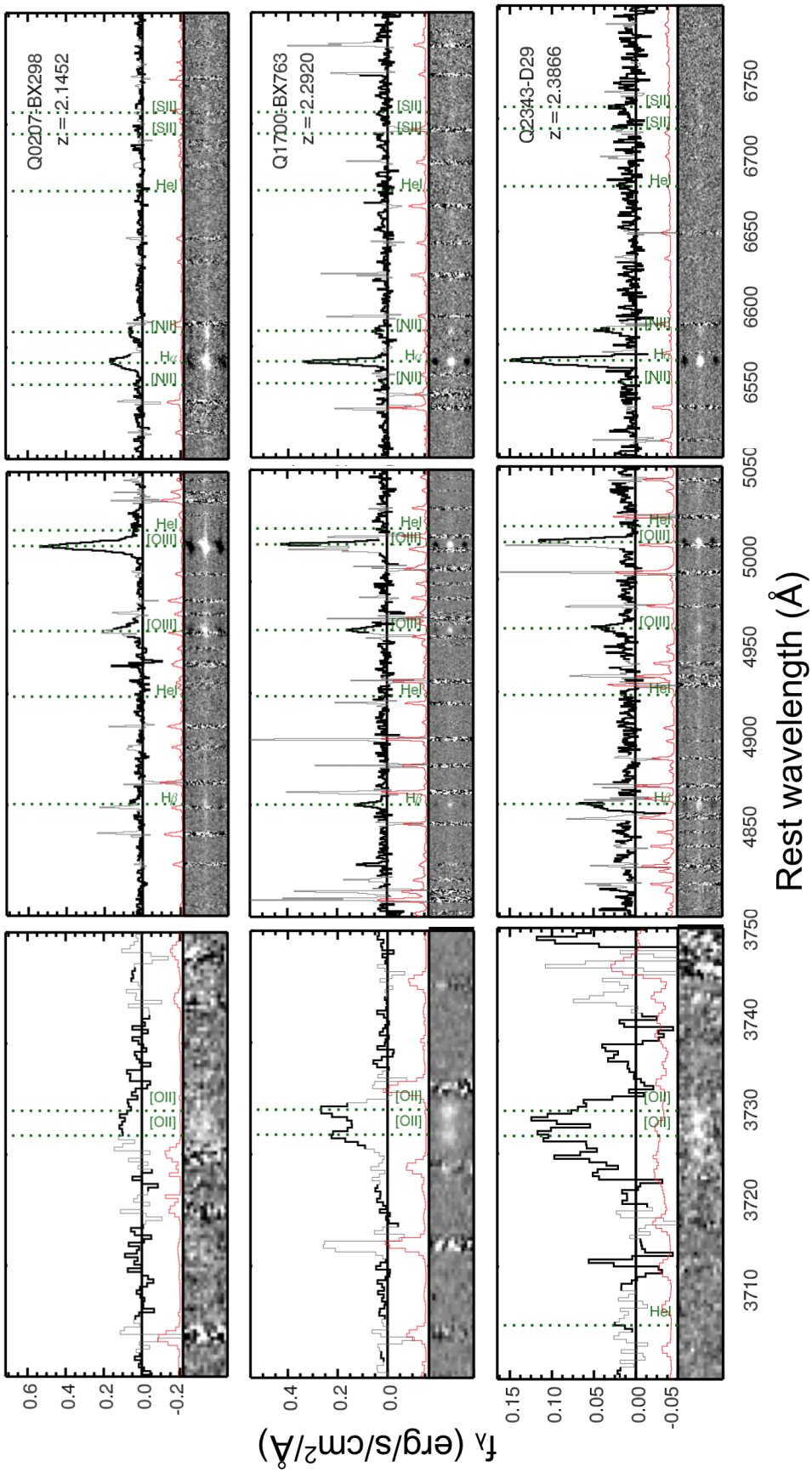

Figure 2.6 (continued)

and subsequently combined using inverse-variance weighting to produce the 2D spectra from which the final 1D spectroscopic products and catalog measurements were derived. Figure 2.6 shows the quality of the data typically available for individual galaxies.

Nebular redshifts, line widths, and total emission line fluxes (of a user-supplied list of emission lines) are measured as part of the extraction process, using information about the systemic redshift and velocity profile determined from the brightest lines to constrain measurements of fainter features. In most cases ($\sim 90\%$ of galaxies), the continuum is estimated using a reddened high-resolution stellar population synthesis model that matches the full SED of the galaxy, which self-consistently accounts for the effects of age and dust extinction on the underlying stellar continuum and automatically includes the stellar Balmer absorption features.

The emission lines in the continuum-subtracted spectrum are fit using Gaussian profiles with a single redshift (z) and observed velocity width (σ, in km s^{-1}) allowed in each band, but these parameters may differ between bands (i.e., we separately record z and σ measured from all of the emission lines in a galaxy's K-band spectrum, but separate values for z and σ measured from the same galaxy's H-band spectrum). As noted by Steidel, Rudie, Strom et al. (2014) and Strom et al. (2017), the Gaussian approximation typically agrees with the directly-integrated flux of isolated lines at the few percent level.

Figure 2.7 shows the optical colors (top panel) and redshift distribution (bottom panel) for the KBSS-MOSFIRE galaxy sample discussed in this thesis. The majority of galaxies with MOSFIRE spectroscopy have optical colors that place them in the BX selection window (green shaded region) and have $1.9 \lesssim z \lesssim 2.7$ (dark blue histogram), which is the redshift range that allows the greatest number of the strong rest-optical emission lines to be observed for individual objects. The bottom panel also highlights the distribution in nebular redshift for galaxies identified using the new RK selection. Of the 100 spectroscopically-confirmed RK objects, 69 have $z < 1.9$, 30 have $1.9 \lesssim z \lesssim 2.7$, and only 1 has $z > 2.75$ (Q2206-RK116 at $z = 3.12$).

2.4.3 Slit Corrections and Cross-band Calibration

The overall image quality for MOSFIRE data is monitored using observations of a bright comparison star placed on a slit on each mask, which are also used to estimate typical slit losses for spatially-unresolved objects by comparing the spec-

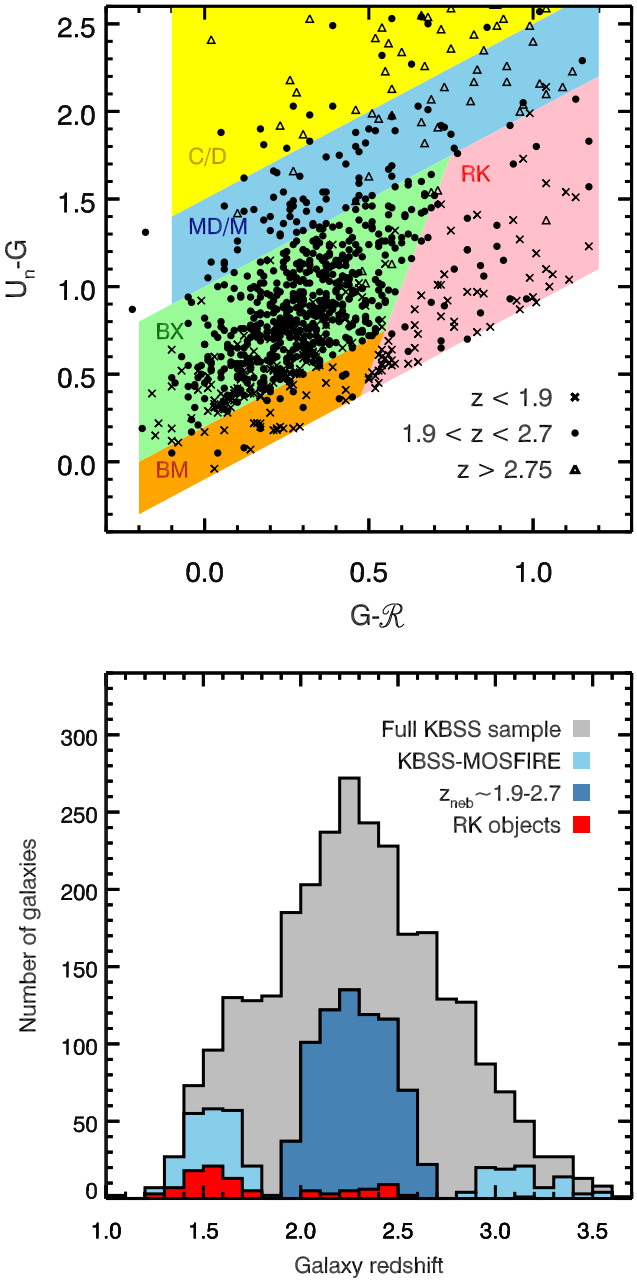

Figure 2.7: *Top:* The optical color selection windows used for selecting KBSS targets, with the black symbols showing the locations of spectroscopically-confirmed galaxies (symbol shape indicates the nebular redshift range). *Bottom:* The redshift distribution for KBSS galaxies, showing the comparison between the larger LRIS-observed sample (grey histogram) and the MOSFIRE component of the survey (blue histograms). The majority of MOSFIRE follow-up has concentrated on galaxies at $z \simeq 1.9 - 2.7$ (dark blue histogram), although observations of galaxies identified using the new RK selection tend to have $z \lesssim 1.9$.

trum of the star in each NIR band with its broadband photometry[4]. Under typical conditions (with seeing between $0\farcs5 - 0\farcs7$), most science targets are unresolved or only marginally resolved. Still, a number of issues can cause the relative slit-losses for individual sources observed with MOSFIRE to differ from both the comparison star and one another. Small errors in mask alignment will result in different losses for objects assigned to slits on the top half of the mask than for objects placed in slits on the lower half of the mask. Delays in tracking the rotation of high-elevation fields and consequences of "slit drift", which arises from the combination of differential atmospheric refraction and the differential flexure of the guider field relative to the science field[5], further complicate the calculation of slit losses for individual objects. Because these issues affect each slit differently, the correction calculated for the bright comparison star will not necessarily capture the true correction for objects in other slits on the same mask.

To address this issue, we developed a method for optimizing the correction factors for individual objects to ensure the most accurate slit loss estimates possible (Strom et al., 2017). These corrections are also critical for knowing the relative scaling that should be applied to measurements of lines observed in different NIR bands—including Hα and Hβ, which are in turn used to determine dust extinction corrections for other emission lines. Our method relies on the assertion that the emission lines measured from a galaxy's spectrum should have the same flux in every observation at the same position angle (i.e., the flux of Hα measured for Galaxy A from Spectrum X should be the same as the Hα flux measured for Galaxy A in Spectrum Y). Following from this reasonable assumption, we are able to leverage measurements of the strong emission lines in every galaxy's J-, H-,and K spectra (typically Hα, [O III]λ5008, or the sum of the [O II]$\lambda\lambda 3727, 3729$ doublet) to determine the combination of correction factors for each mask configuration that minimizes the scatter between independent measurements of those lines for individual galaxies. Because individual mask configurations have some, but not complete, overlap with other masks observed in the same NIR band, this method optimizes the results for the ensemble of masks. The result is a set of band-specific correction factors that are representative of all objects on a given mask and are directly applied in cases where a galaxy is observed only once. To account for the remaining differences between objects on a mask, which was the original motivation for this method, line

[4]Early MOSFIRE observations in KBSS fields did not include slit stars, but we are able to account for this using the method described in this section.

[5]Both components of this issue have been resolved as of May 2017.

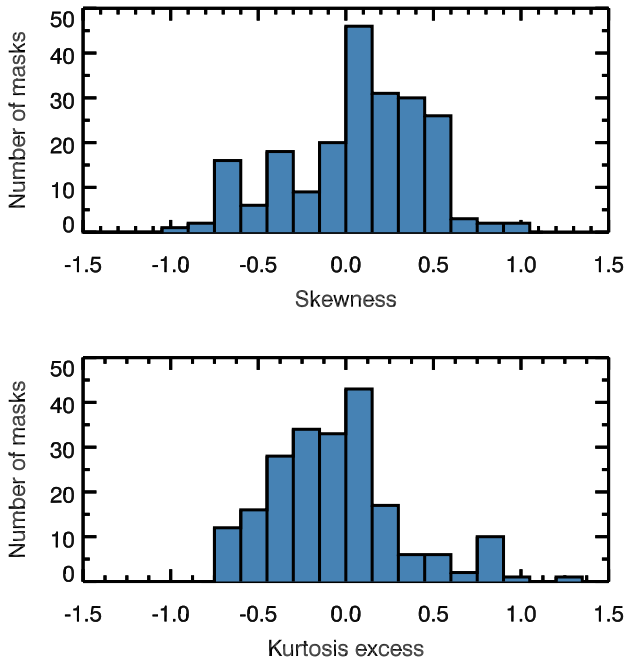

Figure 2.8: Distributions of posterior PDF skewness (top panel) and kurtosis excess (bottom panel) for the correction factors for the 213 KBSS-MOSFIRE masks considered in Strom et al. (2017). Although the skewness distribution peaks near $S = 0$ (corresponding to a symmetric PDF), at least 60% of the mask correction factor posteriors exhibit significant skewness ($|S| > 0.2$). In general, most mask correction factor posteriors appear to have more power in their tails compared to a normal distribution ($K < 0$).

fluxes from an object's 2D weighted average spectrum are corrected to match the weighted average of the corrected line flux measurements from the separate 2D spectral observations that compose the weighted average spectrum.

The results of our cross-calibration method are described further in Chapter 3, but we briefly note one additional benefit of determining correction factors in this manner. Because the mask correction factors are estimated using a Markov Chain Monte Carlo (MCMC) routine, we are also able to characterize the posterior probability distribution function (PDF) for each correction factor and estimate the level of uncertainty in our cross-band calibrations.

We quantify the typical shape of the PDFs using the second and third moments of the mean: skewness and kurtosis excess. Skewness is defined as

$$S = \frac{1}{N} \sum \left(\frac{x - \mu}{\sigma} \right)^3, \tag{2.1}$$

where μ is the mean and σ is the standard deviation. For symmetric populations, $S = 0$; S is positive for right-skewed distributions (tail to the right) and negative for

left-skewed distributions (tail to the left). The distribution in skewness for the 213 KBSS-MOSFIRE mask correction factors from Strom et al. (2017) is shown in the top panel of Figure 2.8. The bottom panel shows the distribution in kurtosis excess, defined as

$$K = \frac{1}{N} \sum \left(\frac{x - \mu}{\sigma} \right)^4 - 3. \tag{2.2}$$

Normal distributions have zero kurtosis excess ($K = 0$), regardless of the value of μ or σ, with "peakier" distributions having positive values of K and flatter distributions exhibiting negative values. The minimum kurtosis excess is -2, corresponding to a Bernoulli distribution with $p = 0.5$, like a coin toss.

Although the mask correction factor PDFs are about equally negatively and positively skewed, $\sim 60\%$ of masks have $|S| > 0.2$ and can be considered significantly skewed. This degree of asymmetry precludes the use of a simple mean, and so we adopt the middle of the highest posterior density interval (HDI) containing 68% of the posterior as the characteristic value for a given mask correction. As we report in Strom et al. (2017), these results lead to an overall median slit correction of 2.03, with a median uncertainty on the slit correction of 8%.

2.4.4 Composite Spectra

It is often useful to combine 1D spectra of individual galaxies in order to measure faint features that are not commonly detected with high significance on a case-by-case basis. Figure 2.4 demonstrated the usefulness of composite spectra in studying the rest-UV properties of high-z galaxies, and the exploration of galaxies' rest-optical spectra benefits similarly—if not more so, due to the absence of significant continuum emission in individual rest-optical galaxy spectra with typical exposure times of a few hours.

One of the challenges inherent in constructing rest-optical composite spectra for high-z galaxy samples is the bright, rapidly-changing emission from the Earth's atmosphere, primarily observed as strong OH emission lines and thermal blackbody emission, especially at the long-wavelength end of the K-band. In general, it is difficult to derive any meaningful information about the spectrum of the science target at wavelengths coinciding with the OH emission lines, which *MOSPEC* accounts for by fitting all of the emission lines in a galaxy's spectrum simultaneously; since not all of the lines will be contaminated by regions of high noise due to OH emission, the emission from features that fall near sky lines can still be estimated for individual galaxies. In contrast, the quality of composite spectra is greatly enhanced

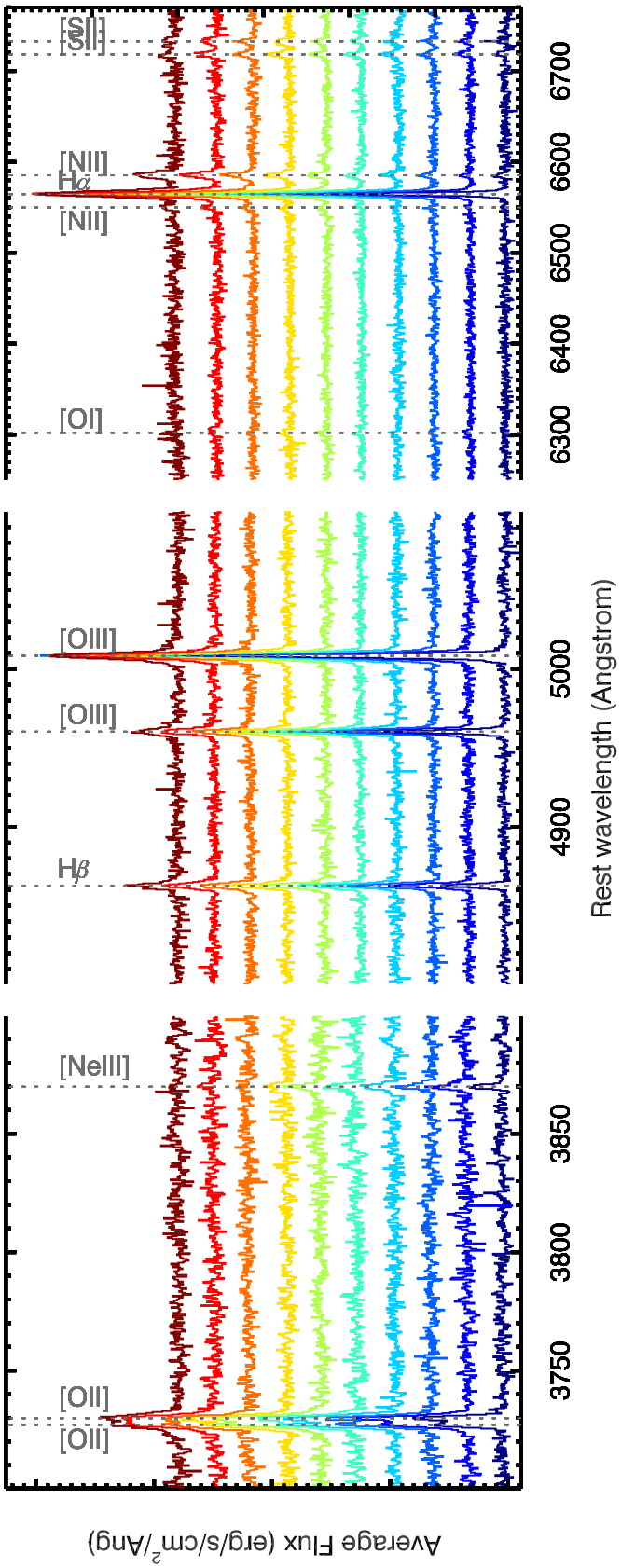

Figure 2.9: Portions of the rest-optical bandpass for 10 composite spectra constructed using MOSFIRE observations of $z \simeq 2 - 2.7$ KBSS galaxies in bins of $\mathcal{R} - K_s$ color (which is correlated with M_*). The color of the stack reflects increasing $\mathcal{R} - K_s$ color, from blue to red. For clarity, the spectra have been vertically offset relative to one another, with the reddest galaxy stack at the top. The strong nebular emission lines used to infer quantities such as electron density, ionization state, and gas-phase oxygen abundance from the spectra of individual objects are labeled. It is immediately obvious that the appearance of the rest-optical spectrum is correlated strongly with $\mathcal{R} - K_s$ color: redder galaxies tend to have broader line widths, higher continuum flux, lower ratios of [O III]/Hβ (indicating lower levels of nebular excitation), and higher ratios of [N II]/Hα (indicating higher oxygen abundances, higher nitrogen-to-oxygen ratios, AGN activity, or a combination of all three). Understanding the contributions of various astrophysical effects to the rest-optical nebular spectra of high-z galaxies is the focus on Chapters 3 and 4.

by automatically excluding regions near the OH lines. We perform this task by applying a mask to each spectrum—based on the absolute deviation from the model fit for each pixel in the 1D spectrum relative to the noise in the same pixel—before including it in the stack. As this masking procedure eliminates the majority of outliers, composite spectra can be calculated by simply averaging the unmasked portions of the constituent galaxies' spectra.

Figure 2.9 presents composite spectra constructed in this manner for galaxies with $z \simeq 2-2.7$ as a function of $\mathcal{R}-K_s$ color. Each composite reveals more detail than is available in individual galaxy spectra, including the semi-strong [Ne III]λ3869 and [O I]λ6302 lines. Composite spectra also allow trends in galaxies' spectroscopic properties to be visualized more clearly. As shown in Figure 2.9, for example, redder galaxies (near the top) tend to have broader lines (indicating larger dynamical masses), higher continuum flux (reflecting a larger population of older stars), and significantly different ratios of [O III]/Hβ and [N II]/Hα than galaxies with smaller $\mathcal{R}-K_s$ colors (near the bottom). Understanding the characteristic properties of high-z galaxies through the lens of their rest-optical spectra and exploring how these properties vary across the galaxy population are the foci of the work presented in Chapters 3 and 4.

2.5 Bulk Galaxy Properties

2.5.1 Stellar Masses

Stellar masses (M_*) for KBSS galaxies are estimated by comparing stellar population synthesis models with the broad- and intermediate-band photometry available for each individual galaxy, which spans rest-UV through rest-infrared wavelengths as listed in Table 2.1. The methodology we use is described in detail by Reddy et al. (2012), but the most important features are as follows. Model SEDs at a variety of stellar population ages are assembled assuming constant-star formation histories for all galaxies, then redshifted, reddened, and attenuated for IGM absorption blueward of 1216Å. The grid of models is then scaled to match the observed photometry, with the best-fit model determined by minimizing the χ^2 relative to the observations. The model with the lowest χ^2 yields the best-fit age and reddening, parameterized by $E(B\text{-}V)_{cont}$, and the required normalization provides the best-fit M_* and star-formation rate (SFR). The SED fit parameters reported throughout this work employ solar metallicity models from Bruzual & Charlot (2003), the Calzetti et al. (2000) extinction curve, and a Chabrier (2003) stellar initial mass function (IMF).

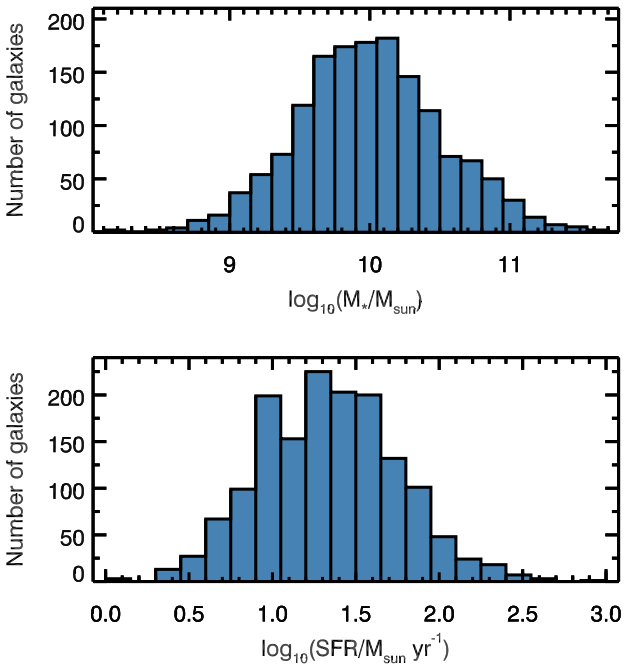

Figure 2.10: Distributions in M_* and SFR estimated from SED fitting only for the sample of $z \simeq 2-2.7$ galaxies discussed throughout this thesis. The median $M_* = 9.65 \times 10^9$ $M_\odot$ and the median SFR = 22.0 $M_\odot$ yr^{-1}.

The optical photometry has been corrected for the effect of Lyα emission and/or absorption, and the NIR photometry (F140W, F160W, $J1$, $J2$, $J3$, J, $H1$, $H2$, H, and K_s) has been corrected for contamination from the strongest nebular emission lines using the catalog of slit-loss-corrected line flux measurements from this thesis, made using *MOSPEC*. Whereas this was previously only possible for the small number of KBSS galaxies with Hα measurements from Erb et al. (2006c), corrections are now possible for the entire KBSS-MOSFIRE sample, and we consider contributions from [O II]$\lambda\lambda$3727,3729, Hβ, [O III]$\lambda\lambda$4960,5008, and Hα. Together these features contribute the majority of the nebular emission (in discrete lines) at rest-optical wavelengths. Accounting for this contamination prevents SED fitting methods from overestimating the continuum level longward of the Balmer break and subsequently overestimating galaxies' M_* (c.f. Schenker et al., 2013; Stark et al., 2013).

Figure 2.10 shows the results from the SED fitting procedure described above for the subsample of KBSS galaxies with redshifts $1.9 \lesssim z \lesssim 2.7$, measured either from rest-UV or rest-optical spectroscopy. The median M_* is 9.65×10^9 $M_\odot$ and the median SFR is 22.0 $M_\odot$ yr^{-1}. Although parameters from SED fitting are always degenerate at some level, M_* is usually the most robustly estimated, with typical

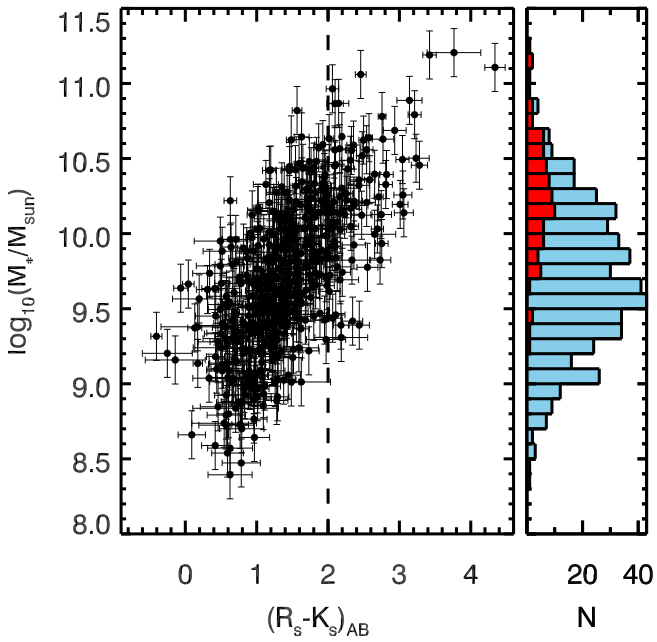

Figure 2.11: Stellar masses inferred from SED fitting are strongly correlated $\mathcal{R} - K_s$ color. This trend is unsurprising, as $\mathcal{R} - K_s$ color serves a crude measure of the depth of the Balmer break for $z \sim 1 - 3$ galaxies. The vertical dashed line illustrates the $(\mathcal{R} - K_s)_{\rm AB} \geq 2$ cut imposed for selecting red star-forming galaxy candidates (Section 2.2.2), which results in a sample that is significantly more massive than typical rest-UV color-selected galaxies. The flanking histogram shows the distribution in M_* for the full sample in blue, with the $(\mathcal{R} - K_s)_{\rm AB} \geq 2$ subsample shown in red. For red galaxies, $\langle \log(M_*/M_\odot) \rangle_{\rm red} = 10.3$, compared to $\langle \log(M_*/M_\odot) \rangle = 9.7$ for the full sample.

uncertainties in $\log(M_*/M_\odot)$ of $\pm 0.1 - 0.2$ dex and a median uncertainty of 0.16 dex (Shapley et al., 2005; Erb et al., 2006b).

Figure 2.11 shows the SED-inferred M_* for KBSS galaxies as a function of $\mathcal{R} - K_s$ color. This correlation has been discussed elsewhere (including by Shapley et al., 2005) and is not altogether surprising, but it reinforces the utility of $\mathcal{R} - K_s$ as a way of identifying massive high-z star-forming galaxies as suggested in Section 2.2. For KBSS galaxies with $(\mathcal{R} - K_s)$AB ≥ 2, $\langle \log(M_*/M_\odot) \rangle_{\rm red} = 10.3$, compared to $\langle \log(M_*/M_\odot) \rangle = 9.7$ for the full sample.

2.5.2 Star-formation Rates

Rather than rely solely on the SFRs from SED fitting, which are naturally correlated with other fit parameters such as age and stellar mass, the SFR estimates favored for KBSS galaxies are obtained from measurements of the Hα recombination line. Emission in recombination lines like Hα is simply reprocessed light from stars

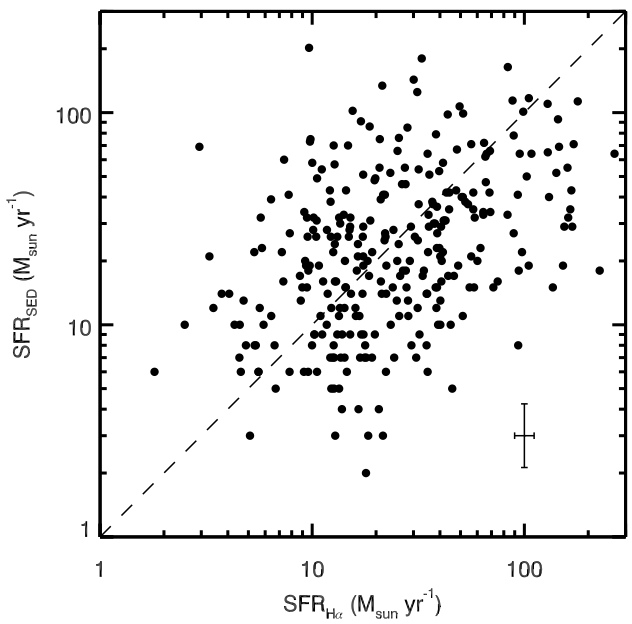

Figure 2.12: A comparison between SFRs inferred from Hα measurements and SED fitting for KBSS-MOSFIRE galaxies at $z \sim 2$. The comparison highlights the large scatter between these two inferences, which may arise due to inconsistencies in the conversion between Hα and SFR, uncertainties in the shape of the IMF, and/or ambiguity regarding the best choice of extinction curve used to correct for dust extinction. Typical measurement errors are illustrated in the lower left corner.

shortward of the ionizing limit of neutral hydrogen at 912Å. Since most of the ionizing flux in galaxies comes from stars with $M_* > 10\,M_\odot$ and lifetimes < 20 Myr, such a diagnostic essentially probes the instantaneous SFR without any assumption about the previous star-formation history.

To account for dust extinction toward star-forming regions and the resulting diminution in observed Hα flux, we compare the observed Balmer decrement (Hα/Hβ) with the expected "Case B" value of 2.86 (Osterbrock, 1989). Adopting the Galactic extinction law from Cardelli, Clayton & Mathis (1989), the typical range in extinction along the line-of-sight to H II regions in $z \sim 2$ KBSS galaxies is E(B-V)$_{\rm neb} = 0.14 - 0.46$, corresponding to $A(\mathrm{H}\alpha) = 0.35 - 1.17$ mag.

After correcting for dust attenuation, we apply the calibration from Kennicutt (1998), adapted to a Chabrier IMF:

$$\mathrm{SFR}(\mathrm{M}_\odot\ \mathrm{yr}^{-1}) = \frac{7.9 \times 10^{-42}}{1.8} L(\mathrm{H}\alpha)\ (\mathrm{erg\ s}^{-1}). \tag{2.3}$$

Figure 2.12 compares SFRs estimated in this manner with those resulting from the

SED fitting for 207 $z \sim 2$ KBSS galaxies with a $> 5\sigma$ measurement of the Balmer decrement. This limit is imposed to ensure a robust estimate of dust extinction.

The comparison in Figure 2.12 shows relatively large scatter between the two inferences, even accounting for measurement errors. This disagreement, especially in individual cases, has contributions from several different sources. We note, however, that although the exact shape of the ionizing spectrum of massive stars remains uncertain, the conversion from Hα luminosity to SFR relies primarily on the *number* of ionizing photons and not the specific shape of the ionizing spectrum[6]. Uncertainties in terms of IMF variations (including differences in shape and the upper mass cut-off) and the effect of dust extinction contribute more significantly to the final uncertainty on the inferred SFR. For example, there is evidence that extinction along the line-of-sight to H II regions may be larger than the extinction of the stellar continuum (e.g., Calzetti et al., 2000; Price et al., 2014). This issue complicates comparisons between estimates of SFR and $E(B-V)_{cont}$ from SED fitting with SFR and $E(B-V)_{neb}$ obtained from the nebular spectrum alone and casts doubt on the common practice of using a scaled value of $E(B-V)_{cont}$ to correct nebular line measurements for attenuation due to dust. Our use of the Cardelli extinction law, which describes line-of-sight attenuation, to correct the nebular spectra of KBSS-MOSFIRE galaxies avoids the uncertainty regarding any scaling between nebular and continuum extinction. A more thorough investigation of dust extinction observed in KBSS galaxies using a combination of rest-UV and rest-optical observations is the subject of a forthcoming paper (Theios, Steidel, Strom et al., in prep.).

2.6 Sample Completeness

In Section 2.2, we discussed some of the challenges associated with selecting high-z galaxies using optical color criteria. Although color selection techniques benefit from requiring relatively few data to implement, the redshift selection function resulting from any combination of selection criteria is often broad. Many surveys conducted over the last decade—and, indeed, many surveys being planned for future facilities—attempt to leverage the rich multi-wavelength photometric data now available in many fields to estimate galaxies' redshifts more precisely using SED fitting. Although, in principle, this exercise can be performed for any field where SED

[6]It is critically important to ensure self-consistency between the conversion from Hα and the ionizing flux predicted for the stellar population models used in SED fitting. The conversion between SFR and Hα luminosity changes by factors of up to 2-3, between the calibration from Kennicutt (1998) and the Fe-poor binary models introduced in Chapters 3 and 4.

fitting is used to estimate M_*, in practice it operates most effectively when there is substantial imaging in intermediate- and narrow-band filters. Such data allow spectral breaks (especially the Balmer break) to be more easily isolated, yielding photometric redshift estimates that are both more precise *and* more accurate.

Accurate photometric redshift estimates allow targets for spectroscopic follow-up to be selected more carefully. In the case of NIR follow-up with an instrument like MOSFIRE, there are certain redshift ranges (e.g., $1.75 \lesssim z \lesssim 1.9$) where no strong nebular emission lines are accessible through the atmospheric transmission windows that ultimately dictate the *J*-, *H*-,and *K*-bands; galaxy candidates with photometric redshifts in such ranges could be avoided, leading to higher survey efficiency. If photometric redshifts can be confidently determined for all galaxies, it would also be possible to identify a "mass-complete" sample by prioritizing galaxies at the redshifts of interest down to some M_* threshold. This is the goal of other ongoing high-z galaxy surveys, like the MOSFIRE Deep Evolution Field survey (MOSDEF, Kriek et al., 2015; Shapley et al., 2015).

Such samples would make make comparisons with surveys of galaxies at other epochs more straightforward and separately facilitate unbiased studies of galaxy scaling relations related to M_*. However, even galaxies with the same M_* will have a variety of SEDs, depending on the details of their star-formation histories. Since photometric redshift estimates rely heavily on prior knowledge of the range of possible spectral shapes, galaxies with different star-formation histories may be recovered with varying degrees of success, leading to a sample that is not actually mass-complete—especially if the distribution of star-formation histories across M_* is not well-understood.

Despite our best efforts, all galaxy selection techniques remain subject to bias. As these biases will subsequently influence the final galaxy sample assembled by any survey, understanding the differences in sample selection between surveys is critical for interpreting any differences in their conclusions. A detailed quantitative comparison of the KBSS sample selection with surveys that rely on photometric redshift selection is the focus of ongoing work (Strom et al., in prep.). However, this section provides an overview of the issues most germane to understanding the completeness of KBSS, including a discussion of which objects may still be missing from or underrepresented in the survey, even after accounting for galaxies identified by the RK selection (Section 2.2.2).

2.6.1 Comparison with Photometric Redshift-Selected Samples in GOODS-N

As in Section 2.2, we choose to compare the $U_nG\mathcal{R}$+RK selection used for KBSS with other selection techniques using the data available in GOODS-N. The 3D-HST catalogs assembled in this field and other legacy fields (including the COSMOS and AEGIS fields) form the basis of the sample selection for MOSDEF, as described by Kriek et al. (2015). MOSDEF is the most comparable survey to KBSS, as it targets $1.5 \lesssim z \lesssim 3.5$ galaxies with a range of M_* for follow-up in the J-, H-,and K-bands, also using MOSFIRE. The KMOS^{3D} survey (Wisnioski et al., 2015), which also makes use of the 3D-HST catalogs, focuses primarily on K-band integral-field spectroscopy of more massive galaxies using the K-band Multi-Object Spectrograph on the VLT (KMOS, Sharples et al., 2013).

The top panel of Figure 2.13 shows the optical colors for galaxies in GOODS-N with $2.09 \leq z_{\rm phot} \leq 2.61$ and $H_{\rm AB} \leq 24.5$, a selection which mimics the target selection used by MOSDEF[7]. These selection criteria result in a comparison sample of 345 objects. Of these, $\sim 83\%$ have optical colors consistent with the $U_nG\mathcal{R}$+RK selection criteria and $\sim 62\%$ satisfy both the color cuts and have $\mathcal{R} \leq 25.5$.

We contrast these results with the comparison based on the currently-available spectroscopic data releases from MOSDEF[8] (bottom panel of Figure 2.13). There are 70 galaxies in GOODS-N with nebular redshifts from MOSFIRE observations obtained as part of the MOSDEF survey and significant detections of their optical colors. Of these, $\sim 89\%$ have colors that place them in the $U_nG\mathcal{R}$+RK selection windows, and $\sim 77\%$ also have $\mathcal{R} \leq 25.5$. There are 9 galaxies with MOSDEF observations that satisfy the RK selection criteria, representing $\sim 13\%$ of the comparison sample.

It is useful to consider the properties of $z \sim 2$ galaxies that are selected on the basis of their photo-z estimates but would be missed by a rest-UV color selection. Figure 2.14 shows the distributions in M_*, SFR, and specific SFR (sSFR = SFR/M_*) for the photo-z-selected objects from GOODS-N shown in the top panel of Figure 2.13. The coloring indicates whether objects satisfy the $U_nG\mathcal{R}$+RK selection criteria (grey histograms) or would have been missed by a survey like KBSS (red hatched histograms). Although the total sample spans a similar range in M_* and SFR as

[7] In order to maximize the success of MOSFIRE observations of candidate galaxies, MOSDEF prioritized objects with spectroscopic redshifts in the literature, including $U_nG\mathcal{R}$-selected galaxies from Reddy et al. (2006). Because the final selection of spectroscopic targets relied on more than photo-z and H-band magnitude, a true comparison between MOSDEF and KBSS must be conducted in collaboration with members of both survey teams, an effort planned for Fall 2017.

[8] `http://mosdef.astro.berkeley.edu/for-scientists/data-releases/`

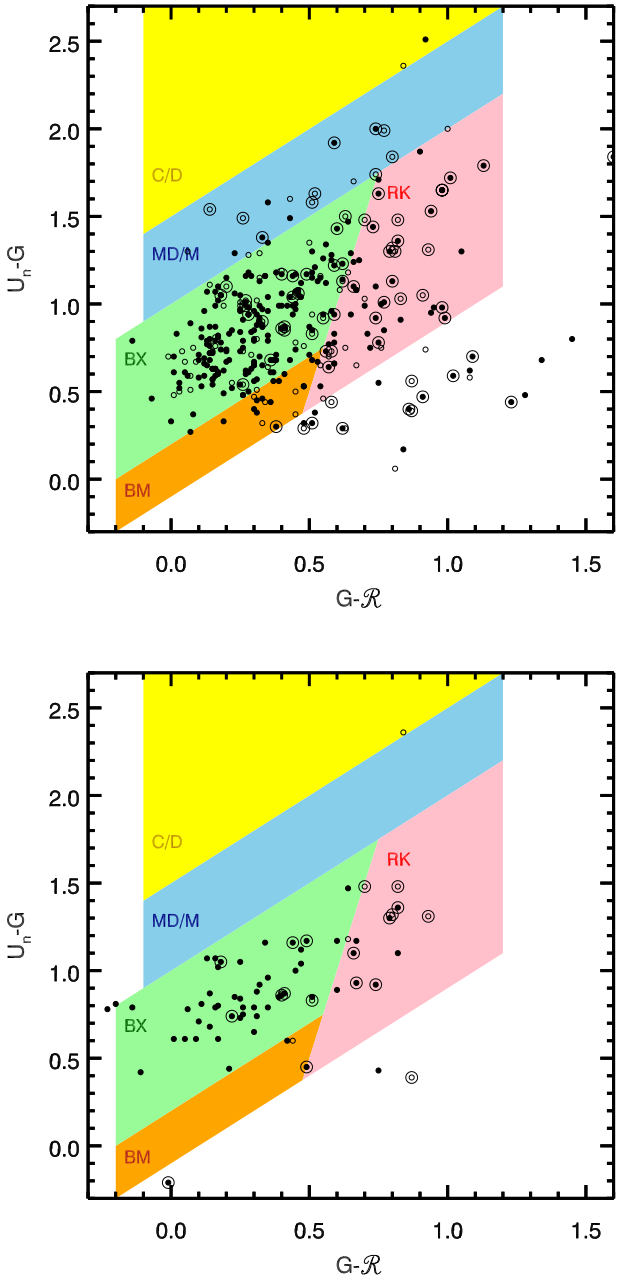

Figure 2.13: The optical color selection windows described in Section 2.2 and shown in Figure 2.7, with a photometric redshift-selected sample from the 3D-HST catalog for GOODS-N (top) and the spectroscopically-confirmed sample from MOSDEF in GOODS-N (bottom). Both panels focus on galaxies with $z_{\rm phot}$ or $z_{\rm spec}$ in the range $z = 2.09 - 2.61$. Solid points represent objects with $\mathcal{R} \leq 25.5$, whereas open point are objects with $\mathcal{R} > 25.5$. Points surrounded by a larger circle have $(\mathcal{R} - K_s)_{\rm AB} \geq 2$. Of the objects shown in both panels, $\sim$ 62% of the photometric redshift sample (top panel) would would have been $U_nG\mathcal{R}$+RK-selected and $\sim$ 77% of the spectroscopically-confirmed sample (bottom panel) would have been $U_nG\mathcal{R}$+RK-selected.

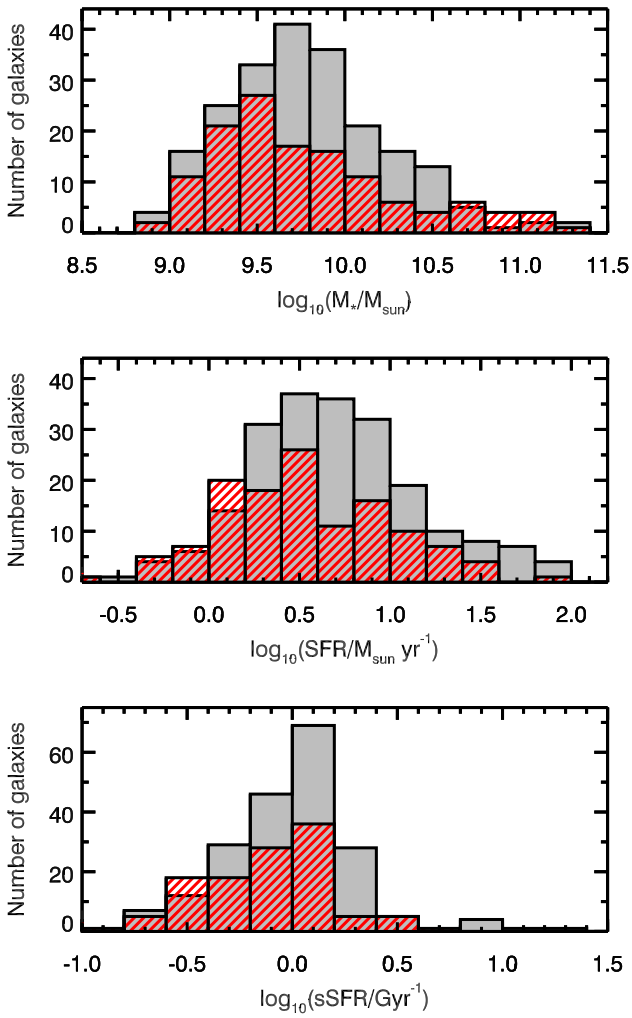

Figure 2.14: The M_*, SFR, and sSFR distributions for all objects in GOODS-N with $2.09 \leq z_{\rm phot} \leq 2.61$ and $H_{\rm AB} \leq 24.5$, colored according to whether they satisfy the $U_nG\mathcal{R}$+RK criteria used by KBSS (grey histograms) or whether they would have been missed (red hatched histograms), either because of differences in their optical colors or because they are rest-UV-faint. A comparison between these subsamples suggests that optical-color-selected samples like KBSS may be biased against the highest mass galaxies and galaxies with low SFR and/or sSFR in general.

that observed for KBSS galaxies (Figure 2.10), it is clear that most of the objects missed by the KBSS color selection criteria have overall lower SFRs and sSFRs. A two-sample Kolmogorov-Smirnov test indicates that the distributions in sSFR for the two subsamples are significantly different at the 3σ level ($p = 0.003$). It is also notable that by relying on optical color selection alone (even with the RK selection), KBSS may be missing approximately half of $z \sim 2$ galaxies with the highest M_* ($\gtrsim 10^{10.5}$ $M_\odot$).

2.6.2 Recovering Young High-z Galaxies

We can account for at least some of the difference in completeness of a $U_nG\mathcal{R}$+RK selection in the two panels of Figure 2.13 by acknowledging that some fraction of objects with $z_{\rm phot}$ estimates will have true $z_{\rm spec}$ measurements that are significantly different. Indeed, $\sim 26\%$ of the photo-z-selected sample shown in the top panel of Figure 2.13 with spectroscopic redshifts from the literature have $z_{\rm spec}$ outside the desired range, extending down to $z_{\rm spec} \approx 0.5$.

Given the non-negligible rate of large photo-z errors found for GOODS-N objects, it is unavoidable that—in addition to including galaxies with unwanted $z_{\rm spec}$—a photo-z selection may also exclude a non-negligible number of galaxies whose $z_{\rm phot}$ estimates incorrectly place them outside the selection window. Figure 2.15 compares $z_{\rm phot}$ from the 3D-HST catalogs (Skelton et al., 2014) with $z_{\rm spec}$ for galaxies with $2.09 \leq z_{\rm spec} \leq 2.61$. The spectroscopic redshift measurements are drawn from a variety of sources, including directly from LRIS spectra of rest-UV color-selected galaxies in GOODS-N (Reddy et al., 2006) and the MOSDEF data releases (see also the references in Skelton et al., 2014, who compiled $z_{\rm spec}$ for objects in 3D-HST fields). If galaxies satisfy the $U_nG\mathcal{R}$+RK selection criteria, they are represented by solid points; if not, they are drawn as open squares.

It is notable that of the 147 galaxies shown in Figure 2.15, $\sim 21\%$ have $z_{\rm phot}$ measurements that place them outside the $z_{\rm phot}$ range corresponding to the cut imposed in $z_{\rm spec}$, illustrated by the horizontal shaded region from $2.09 \leq z_{\rm phot} \leq 2.61$. Many of these objects are catastrophic failures, with the difference between $z_{\rm phot}$ and $z_{\rm spec}$ exceeding several sigma. Such objects would not have been selected by a photo-z selection alone, although $\sim 65\%$ of the photo-z "failures" (red points and squares in Figure 2.15) satisfy the rest-UV color selection used by KBSS.

This sample of galaxies is particularly interesting, as it may account for the differences observed between the characteristic nebular line ratios (specifically [O III]/Hβ

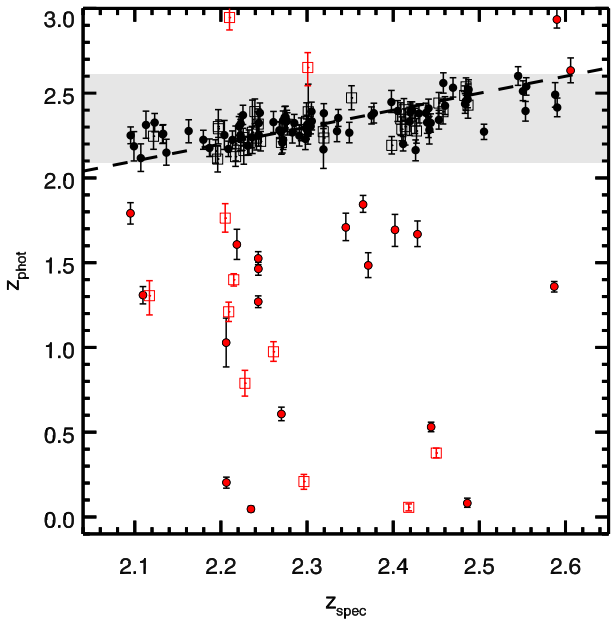

Figure 2.15: A comparison between $z_{\rm phot}$ and $z_{\rm spec}$ for 147 galaxies in GOODS-N with $z_{\rm spec} = 2.09 - 2.61$, showing objects that satisfy the $U_nG\mathcal{R}$+RK selection (solid points) and those selected in other ways (open squares). The peak of photometric redshift probability distribution function from 3D-HST (Skelton et al., 2014) has been taken as $z_{\rm phot}$, with the error bars indicating the upper- and lower-limits of the 68% confidence interval. The grey shaded region represents the $z \sim 2$ photo-z selection window targeted by MOSDEF. Galaxies whose $z_{\rm phot}$ estimates place them outside the $z \sim 2$ selection window have been marked in red ($\sim 21\%$ of the total sample shown).

and [N II]]/Hα) of $z \sim 2$ galaxies from KBSS-MOSFIRE and MOSDEF (e.g. Steidel et al., 2014; Shapley et al., 2015; Sanders et al., 2016; Strom et al., 2017). These differences indicate that galaxies similar to a subsample of high-excitation KBSS-MOSFIRE objects are underrepresented in the MOSDEF survey, which contributes to conflicting interpretations of high-z galaxies' rest-optical spectroscopic properties. As discussed at greater length in Chapter 3, these KBSS-MOSFIRE galaxies have smaller $\mathcal{R} - K_s$ colors, lower M_*, higher sSFR, and younger ages than the full KBSS-MOSFIRE sample.

We test the idea that MOSDEF (and other surveys that rely on photo-z selection) may not efficiently target these younger, relatively unevolved galaxies in Figure 2.16, which shows the absolute difference between $z_{\rm phot}$ and $z_{\rm spec}$ as a function of $\mathcal{R} - K_s$ color for all galaxies in the MOSDEF data releases with $2.09 \leq z_{\rm spec} \leq 2.61$; galaxies with $z_{\rm phot}$ outside the desired range are colored red. The incidence of erroneous photo-z estimates decreases rapidly as $\mathcal{R} - K_s$ color (and, thus, Balmer

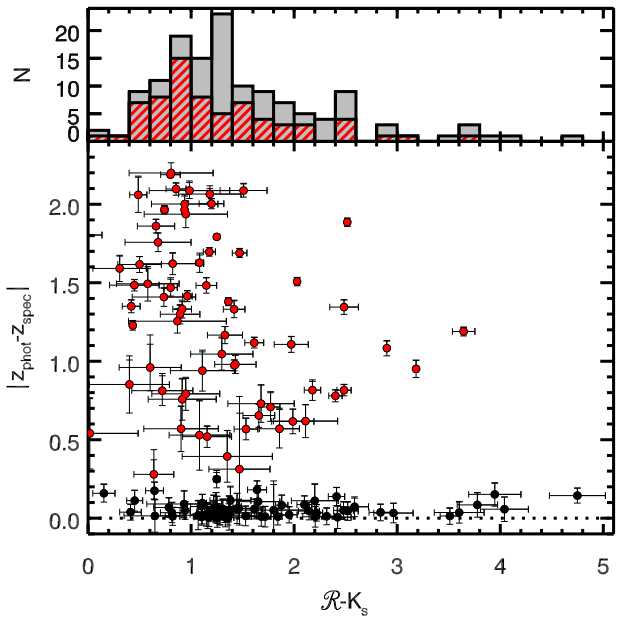

Figure 2.16: The difference between $z_{\rm phot}$ and $z_{\rm spec}$ as a function of $\mathcal{R} - K_s$ color for all spectroscopically-confirmed galaxies in the public MOSDEF data releases, with $z_{\rm spec} = 2.09 - 2.61$. Galaxies whose $z_{\rm phot}$ fall outside the targeted window are shown as red points and represent 51% of the total sample. The upper envelope in $|z_{\rm phot} - z_{\rm spec}|$ decreases dramatically toward redder $\mathcal{R} - K_s$ colors, which correspond to larger Balmer breaks in $z \sim 2$ galaxies. Particularly notable is the relative paucity of objects with $(\mathcal{R} - K_s)_{\rm AB} < 1$ and good agreement between $z_{\rm phot}$ and $z_{\rm spec}$, suggesting that a photo-z selection may preferentially exclude $z \sim 2$ galaxies with shallow Balmer breaks. The distributions in $\mathcal{R} - K_s$ for galaxies that would have been selected using their photo-z alone (grey histogram) and those that represent photo-z "failures" (red hatched histogram) are shown at the top.

break depth) increases. For $\mathcal{R} - K_s < 1$, however, the majority of galaxies have $z_{\rm phot}$ estimates significantly different from their true $z_{\rm spec}$. Such objects are not uncommon at high-z and represent $\sim 30\%$ of $z \sim 2$ KBSS-MOSFIRE galaxies.

The results presented in this section highlight the complementary strengths and weaknesses of common high-z galaxy selection techniques. Very massive galaxies and quiescent (low-sSFR) galaxies at all masses appear to be underrepresented in rest-UV color-selected samples like KBSS compared to photo-z-selected samples. In turn, photo-z-selection recovers younger galaxies with shallow Balmer breaks (which likely have the highest sSFRs) less efficiently than KBSS. A complete understanding of the universe during the epoch of peak galaxy assembly will require leveraging observations of galaxies identified in a variety of ways in order to achieve the most representative sample of galaxies. Systematically comparing the relative advantages and disadvantages of galaxy selection techniques will also help guide

sample selection for future large galaxy surveys, such as those that will be conducted at higher redshifts using the *James Webb Space Telescope* (*JWST*) and those that will target galaxies at somewhat lower redshift, as being planned for the Prime Focus Spectrograph (PFS, Tamura & PFS Collaboration, 2016) on Subaru.

Chapter 3

NEBULAR EMISSION LINE RATIOS IN $Z \sim 2-3$ STAR-FORMING GALAXIES WITH KBSS-MOSFIRE: EXPLORING THE IMPACT OF IONIZATION, EXCITATION, AND NITROGEN-TO-OXYGEN RATIO

Strom, A. L., Steidel, C. C., Rudie, G. C., et al., 2017, ApJ, 836, 164, 164

ABSTRACT

We present a detailed study of the rest-optical (3600 – 7000Å) nebular spectra of $\sim$ 380 star-forming galaxies at $z \sim 2-3$ obtained with Keck/MOSFIRE as part of the Keck Baryonic Structure Survey (KBSS). The KBSS-MOSFIRE sample is representative of star-forming galaxies at these redshifts, with stellar masses $M_* = 10^9 - 10^{11.5} M_\odot$ and star formation rates SFR= 3 – 1000 $M_\odot$ yr^{-1}. We focus on robust measurements of many strong diagnostic emission lines for individual galaxies: [O II]$\lambda\lambda$3727,3729, [Ne III]λ3869, Hβ, [O III]$\lambda\lambda$4960,5008, [N II]$\lambda\lambda$6549, 6585, Hα, and [S II]$\lambda\lambda$6718,6732. Comparisons with observations of typical local galaxies from the Sloan Digital Sky Survey (SDSS) and between subsamples of KBSS-MOSFIRE show that high-redshift galaxies exhibit a number of significant differences in addition to the well-known offset in log([O III]λ5008/Hβ) and log([N II]λ6585/Hα). We argue that the primary difference between H II regions in $z \sim 2.3$ galaxies and those at $z \sim 0$ is an enhancement in the degree of nebular excitation, as measured by [O III]/Hβ and R23 $\equiv$ log[([O III]$\lambda\lambda$4960, 5008+[O II]$\lambda\lambda$3727, 3729)/Hβ]. At the same time, KBSS-MOSFIRE galaxies are $\sim$ 10 times more massive than $z \sim 0$ galaxies with similar ionizing spectra and have higher N/O (likely accompanied by higher O/H) at fixed excitation. These results indicate the presence of harder ionizing radiation fields at fixed N/O and O/H relative to typical $z \sim 0$ galaxies, consistent with Fe-poor stellar population models that include massive binaries, and highlight a population of massive, high-specific star formation rate galaxies at high redshift with systematically different star formation histories than galaxies of similar stellar mass today.

3.1 Introduction

The strong emission lines of elements such as hydrogen, oxygen, and nitrogen observed in the rest-optical (3600 – 7000Å) spectra of galaxies come primarily from the H II regions surrounding massive O and B stars. Thus, attempts to characterize this emission ultimately reveal information regarding the properties of both the massive stars *and* the ionized gas immediately surrounding them. Furthermore, we know from studies of individual H II regions in the Milky Way and nearby galaxies that changes in the nebular spectrum are tightly correlated with one another, manifesting the underlying correlations between the physical properties of the ionized regions—including electron density, electron temperature, gas chemistry, and ionization parameter—that determine the strength of emission lines.

Studies conducted using integrated-light spectra of large samples of nearby galaxies, such as the Sloan Digital Sky Survey (SDSS, York et al., 2000), reveal similar behavior in galaxies spanning a wide range in stellar mass and star formation rate, with star-forming galaxies occupying a tight locus in many parameter spaces. For example, low-z star-forming galaxies form a relatively narrow sequence in the log([O III]λ5008/Hβ) vs. log([N II]λ6585/Hα) plane (hereafter the N2-BPT diagram), extending from high [O III]/Hβ and low [N II]/Hα to low [O III]/Hβ and high [N II]/Hα as gas-phase metallicity increases and the level of ionization decreases. The position of objects in the N2-BPT plane can therefore be used as a tool for distinguishing galaxies powered by young stars from galaxies with significantly harder ionizing radiation fields (such as those produced by active galactic nuclei, or AGN). The very hard ionizing spectrum of AGN produces enhanced collisional line emission in an extended partially-ionized region, resulting in a diffuse "plume" that extends to both high [O III]/Hβ and high [N II]/Hα in the N2-BPT plane.

The use of line ratios to distinguish between sources of ionizing radiation was first proposed by Baldwin, Phillips & Terlevich, 1981, but Veilleux & Osterbrock, 1987 introduced the version of the N2-BPT diagram commonly used today (along with two other diagnostic diagrams using [S II]$\lambda\lambda$6718,6733/Hα and [O I]λ6300/Hα instead of [N II]λ6585/Hα). Kewley et al. (2001) and Kauffmann et al. (2003) separately provided classification curves that are now frequently used to separate $z \sim 0$ star-forming galaxies from AGN in the N2-BPT plane; the former relied on predictions from photoionization models, but the latter specifically considered the importance of correlations between the physical conditions in star-forming galaxies, particularly between metallicity and ionization parameter.

Advances in our knowledge of the conditions (and the important correlations between them) in galaxies at earlier epochs—specifically $z \sim 2-3$, when both cosmic star formation (e.g., Madau et al., 1996; Hopkins & Beacom, 2006; Reddy et al., 2008; Madau & Dickinson, 2014) and supermassive black hole accretion reached their peak values (Richards et al., 2006)—have been slower to arrive, due in large part to limitations in the sensitivity and multiplexing capabilities of near-infrared spectrographs on 8 − 10 m class telescopes. Still, early observations of small samples of high-redshift galaxies (e.g., Shapley et al., 2005; Erb et al., 2006a; Liu et al., 2008) suggested that the situation at high-z might be radically different, with galaxies exhibiting lower gas-phase oxygen abundance at fixed stellar mass and nebular line ratios inconsistent with observations of the majority of local galaxies. Since the commissioning of efficient multi-object near-infrared spectrographs like the K-band Multi-Object Spectrograph on the VLT (KMOS, Sharples et al., 2013) and the Multi-Object Spectrometer for InfraRed Exploration on the Keck I telescope (MOSFIRE, McLean et al., 2012), the number of $z \sim 2-3$ galaxies with high-quality rest-optical spectra has increased dramatically (Steidel et al., 2014; Kriek et al., 2015; Wisnioski et al., 2015). The results from galaxy surveys using these instruments have confirmed that, while high-redshift star-forming galaxies also occupy a relatively tight locus in the N2-BPT diagnostic diagram, they show a clear offset toward higher [O III]λ5008/Hβ at a given [N II]λ6585/Hα compared to their low-redshift counterparts (Masters et al., 2014; Steidel et al., 2014; Shapley et al., 2015).

Systematic differences between typical star-forming galaxies in the local universe and those present during the peak epoch of galaxy growth are not surprising—on average $z \sim 2$ galaxies have higher star formation rates at fixed mass by at least a factor of 10 and cold gas masses higher by at least a factor of ~ 5, all in smaller volumes compared to local galaxies (e.g., Erb et al., 2006b; Law et al., 2012; Tacconi et al., 2013). However, understanding the physical cause of the differences in their nebular spectra has proven both challenging and controversial (c.f. Masters et al., 2014; Steidel et al., 2014; Sanders et al., 2016; Masters, Faisst & Capak, 2016), with much of the difficulty stemming from the diversity (and degeneracy) of possible explanations. The differences between nebular diagnostics observed at $z \sim 2$ relative to $z \sim 0$ can be attributed to differences in the underlying stellar populations (e.g., EUV ionizing spectrum, main sequence lifetime, metallicity, binarity, rotation) and/or differences in the conditions of the interstellar medium (ISM; e.g., density, temperature, metallicity).

From our analysis of the initial KBSS-MOSFIRE sample of ~ 200 $z \simeq 2.3$ galaxies in Steidel et al. (2014, hereafter S14), we concluded that the high-redshift locus of galaxies in the N2-BPT plane is most easily explained by a harder stellar ionizing radiation field than applies to galaxies occupying the low-redshift sequence, accompanied by slightly elevated ranges in ionization parameter $U(\equiv n_\gamma/n_H)$ and electron density (n_e). In S14, we noted that the systematic offset of high-z galaxies relative to star-forming galaxies in the low-redshift universe in the N2-BPT plane cautions against using the common "strong-line" metallicity relations (generally calibrated using galaxy and H II region samples at $z \sim 0$) for high-redshift galaxies, since the calibrations are designed to reproduce the local N2-BPT sequence. Additionally, an important consequence of the high excitation of the $z \sim 2.3$ KBSS-MOSFIRE sample is that the strong-line ratios become relatively insensitive to the ionized gas-phase oxygen abundance (often what one intends to measure) and more dependent on the spectral shape of the integrated ionizing radiation field produced by massive stars.

In S14, we also investigated the effect of differences in nitrogen-to-oxygen abundance ratio on the rest-optical nebular spectra of high-z galaxies, but ultimately found that systematically different values of N/O between $z \sim 2.3$ and $z \sim 0$ galaxies were not required to reproduce the observed N2-BPT offset using the photoionization models presented in that paper. Other recent work based on independent (but smaller) galaxy samples at similar redshifts (Masters et al., 2014; Shapley et al., 2015; Cowie, Barger & Songaila, 2016; Sanders et al., 2016; Masters, Faisst & Capak, 2016) has argued that high-redshift objects have higher N/O at a given O/H—i.e., that the N2-BPT offset is primarily a shift toward higher [N II]/Hα and is confined to lower-mass galaxies in those samples. The primary basis for this assertion was that an offset of the BPT locus is observed in [N II]/Hα but not in [S II]/Hα. However, the behavior of N/O versus O/H for many individual galaxies at high redshift has yet to be established.

Although much can be learned from rest-optical nebular spectra regarding the properties of the ISM and massive stars, it is not clear that the physical factors most important for determining the location of typical local star-forming galaxies in the nebular diagnostic diagrams are the same as those at $z \sim 2$. The work presented in this chapter leverages measurements from the rest-optical spectra of an expanded sample of $\langle z \rangle = 2.3$ KBSS-MOSFIRE galaxies to characterize the properties of high-z galaxies in terms of their stellar masses, star formation rates, ionization

and excitation conditions, electron densities, and the variation in N/O as a function of O/H. We will show that the seemingly discrepant behavior in the N2-BPT and S2-BPT diagrams (and other diagnostic line ratios) is expected in the context of physically-motivated photoionization models anchored by observations of the rest-UV spectra of the same galaxies (Steidel et al., 2016, hereafter S16).

The remainder of this chapter is structured as follows: Section 3.2 describes the Keck Baryonic Structure Survey, the near-infrared spectroscopic observations, and the detailed spectral fitting of the data. Section 3.3 reports the measurements of strong-line ratios from the nebular spectra of KBSS-MOSFIRE galaxies; Section 3.4 examines the properties of $z \sim 2.3$ galaxies as a function of their offset from the $z \sim 0$ relation in the N2-BPT diagram, Section 3.5 presents the N/O measurements and their correlation with galaxy properties, and Section 3.6 describes the inferences that can be made by comparing a subset of the photoionization models from S16 with the observed line ratios and inferred abundance ratios. Finally, Section 3.7 revisits the nature of the BPT "offset" in the context of the KBSS-MOSFIRE results. The conclusions are summarized in Section 3.8.

We assume a ΛCDM cosmology when necessary, with $H_0 = 70\,\mathrm{km\,s^{-1}\,Mpc^{-1}}$, $\Omega_\Lambda = 0.7$, and $\Omega_\mathrm{m} = 0.3$. Stellar masses and star formation rates are reported assuming a Chabrier (2003) stellar initial mass function (IMF). When a solar metallicity scale is needed for comparison, we adopt $12+\log(\mathrm{O/H})_\odot = 8.69$, $\log(\mathrm{N/O})_\odot = -0.86$, and $Z_\odot = 0.0142$ (Asplund et al., 2009). Specific spectral features are referred to using their vacuum wavelengths.

3.2 The Keck Baryonic Structure Survey

The Keck Baryonic Structure Survey (KBSS, Rudie et al., 2012; Steidel et al., 2014) is a large, targeted spectroscopic survey designed to jointly probe galaxies and their gaseous environments at the peak of galaxy assembly, $z \sim 2-3$. The survey comprises 15 independent fields, with a total survey area of 0.24 deg^2. The galaxies themselves are selected from deep optical and near-infrared (NIR) imaging and subsequently followed up with spectroscopic observations in the rest-UV with the Low Resolution Imaging Spectrometer (LRIS, Oke et al., 1995; Steidel et al., 2004) and, since 2012 April, in the rest-optical with the Multi-Object Spectrometer For InfraRed Exploration (MOSFIRE, McLean et al., 2012; Steidel et al., 2014).

In addition to the physical motivation for studying galaxies at $z \sim 2-3$, this redshift range also offers important practical advantages: many of the strong rest-optical

(3600 – 7000Å) nebular emission lines originating in the galaxies' H II regions are well-positioned with respect to the J, H, and K band atmospheric windows. Additionally, the rest-frame far-ultraviolet (1000 – 2000Å) spectra of the same galaxies are accessible to ground-based telescopes, which is critically important for complementary studies of their massive stellar populations, which is one of the main goals of our recent work in S16 and is discussed briefly in Section 3.6.

3.2.1 Photometry and Sample Selection

The photometric data available in the KBSS fields have been described in detail elsewhere (e.g., by Steidel et al., 2004; Reddy et al., 2012; Steidel et al., 2014). To summarize, all of the survey regions have optical imaging in the U_n, G, and $\mathcal{R}$ bands, as well as broad-band NIR imaging in J and K_s. For 14 fields, imaging was also obtained using *Spitzer*/IRAC (typically including coverage in two channels per field); 10 fields have at least one deep pointing obtained using *Hubble*/WFC3-IR F160W. Intermediate-band NIR imaging in $J1$, $J2$, $J3$, $H1$, and $H2$ was collected using Magellan-FourStar (Persson et al., 2013) for 8 fields accessible from the southern hemisphere.

The majority of KBSS galaxies are selected by their rest-UV colors, based on a $U_nG\mathcal{R}$ color selection designed to identify Lyman Break Galaxy analogues at $z \simeq 2 - 2.7$ (Adelberger et al., 2004; Steidel et al., 2004). However, this rest-UV color selection may be biased against massive galaxies and galaxies whose UV continua are heavily reddened due to extinction by dust ($E(B-V)_{\rm cont} > 0.3$). Fortunately, these biases can be mitigated by using information about the combined rest-UV and rest-optical shape of the galaxies' spectra. The 4000 Å and Balmer breaks, which probe both age and stellar mass, lie within the J band at $z \sim 2.3$ but are still well-traced by $\mathcal{R} - K_s$ color. Therefore, combining a $U_nG\mathcal{R}$ color selection with a $(\mathcal{R} - K_s)_{\rm AB} > 2$ color cut preferentially selects galaxies at the redshifts of interest that occupy the high end of the stellar mass distribution. We also extend the optical color selection to include sources with redder $U_nG\mathcal{R}$ colors and simultaneously impose a $\mathcal{R} - K_s$ cut, in order to identify galaxies which may be at similar redshifts but are scattered out of the Steidel et al. (2004) selection windows due to the effects of substantial reddening by dust.

A more detailed description of this sample of galaxies—referred to as "RK" objects—can be found elsewhere in this thesis, but Figure 3.1 offers a visual illustration of the color selection windows described here. With the inclusion of RK

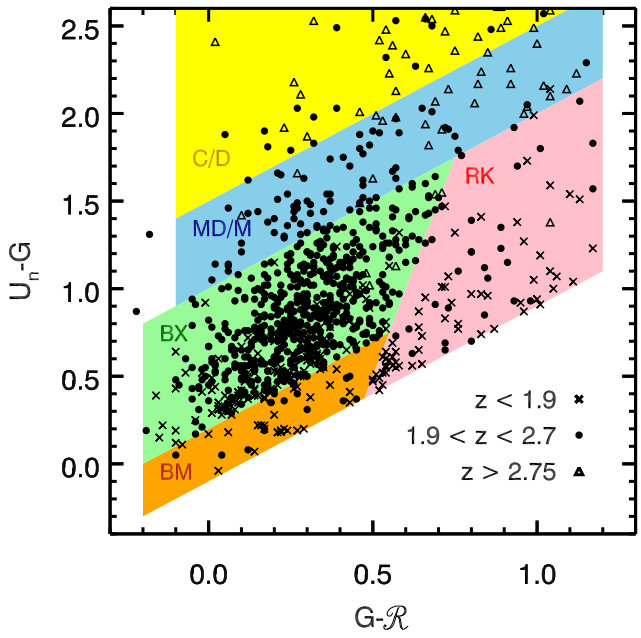

Figure 3.1: The optical color selection windows from Steidel et al. (2004) used to identify candidate star-forming galaxies with $z \simeq 2.0 - 2.7$ ("BX" in green) and $z \simeq 2.7 - 3.4$ ("MD/M" and "C/D" in blue and yellow, respectively); the grey region indicates the new "RK" color selection at redder $G - \mathcal{R}$ colors. Black symbols represent spectroscopically-confirmed galaxies in KBSS-MOSFIRE sample, with the symbol shape indicating the nebular redshift.

objects, the KBSS targets sources throughout the full rest-UV color space occupied by high-z galaxies. Although the sample only includes galaxies with $\mathcal{R} < 25.5$ ($\mathcal{R}$ samples the rest-frame at $\sim$ 2100Å), the color selection allows for galaxies with significantly fainter rest-frame FUV emission to be selected, down to an AB magnitude of 26.7 in G band ($\lambda_e \sim 1500$Å at $z \sim 2.3$).

3.2.2 NIR Spectroscopic Observations

S14 introduced the NIR spectroscopic observations of KBSS galaxies with MOSFIRE, and readers are referred to Section 2 of that paper for details related to data acquisition and reduction. One particularly salient aspect of the KBSS-MOSFIRE observing strategy is that, due to the dense spatial sampling of the KBSS fields, multiple slitmask configurations in each band are usually required to obtain observations of all high-priority targets in a given field. Because galaxies remain on masks until the strongest lines (Hα, [N II]λ6585, [O III]λ5008 Hβ, and [O II]$\lambda\lambda$3727,3729) are measured with S/N > 5, an individual galaxy is often observed at least 2 times in a single band. Section 3.2.4 describes the method used to correct observations

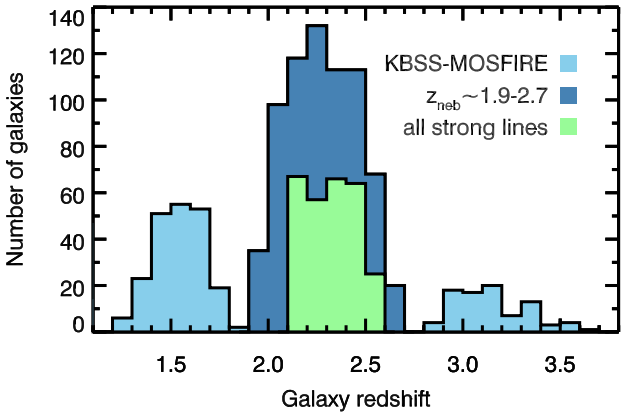

Figure 3.2: The redshift distribution of spectroscopically-confirmed KBSS-MOSFIRE galaxies, as of 2016 May. The blue histograms represent galaxies with confirmed nebular redshifts from MOSFIRE observations (1060 total). Of these, 733 are known to be at $1.9 \leq z \leq 2.7$ and have MOSFIRE observations covering at least one atmospheric band (dark blue). The subsample with good signal-to-noise detections of strong rest-optical emission lines in J, H, and K band is shown in green (279 galaxies).

of KBSS-MOSFIRE galaxies for slit losses, which takes advantage of the multiple observations of individual galaxies that result from this survey strategy.

As of 2016 May, 1060 KBSS galaxies have been confirmed spectroscopically with observations from MOSFIRE (Figure 3.2); of these, 733 are in the primary targeted redshift range $1.9 \lesssim z \lesssim 2.7$, with the remainder split roughly 2:1 between $1.3 \lesssim z \lesssim 1.7$ and $z \gtrsim 2.9$. The majority of the $z \sim 2.3$ galaxies have been observed in at least two NIR bands, and 279 have high-quality observations in J, H, and K band, providing good S/N measurements of most of the strong rest-optical emission lines: [O II]$\lambda\lambda$3727,3729, [Ne III]λ3869 in J band; Hβ, [O III]$\lambda\lambda$4960,5008 in H band; [N II]$\lambda\lambda$6549, 6585, Hα, [S II]$\lambda\lambda$6718,6732 in K band.

3.2.3 1D Spectral Extraction and Emission-line Fitting with *MOSPEC*

The two-dimensional (2D) spectrograms produced by the MOSFIRE data reduction pipeline[1] are flux-calibrated and corrected for telluric absorption using wide- and narrow-slit observations of A0V stars and then shifted to account for the heliocentric velocity at the start of each exposure sequence. Separate MOSFIRE observations of the same object are combined using inverse-variance weighting to produce the final 2D spectrograms from which 1D spectra are extracted.

[1] `http://www2.keck.hawaii.edu/inst/mosfire/drp.html`

One-dimensional (1D) spectra are extracted from the 2D spectrograms using *MOSPEC*, an interactive analysis tool developed in IDL specifically for MOSFIRE spectroscopy of faint emission-line galaxies. By default, *MOSPEC* uses a boxcar extraction aperture (determined by the user, with a median value of 10 pixels or 1.″80, corresponding to 14.8 kpc at $z = 2.3$). Other extraction algorithms, including optimal extraction, were tested and found not to significantly impact the measured line fluxes or their significance.

As part of the extraction process, the 1D spectrum is simultaneously fit for the redshift, line width, and fluxes of a user-specified list of emission lines. The continuum level is estimated using a reddened high-resolution stellar population synthesis model (from Bruzual & Charlot, 2003) that best matches the full spectral energy distribution (SED) of the galaxy and is scaled to match the median level of the observed spectrum excluding regions < 5Å from strong emission lines. This method self-consistently accounts for the effects of age and dust extinction on the underlying stellar continuum. If this method is not possible (most frequently due to very faint continua), *MOSPEC* uses a linear fit to the continuum, again excluding regions around strong emission lines. These two estimates agree well for most galaxies, although the model-continuum method has the advantage of including the stellar Balmer absorption features.

The correction for absorption in Hα and Hβ for individual objects is determined by fitting the galaxy spectrum with a modified SED model continuum that linearly interpolates between the continuum on either side of regions around Balmer features and comparing the result with measurements from the full fit that includes stellar absorption features. For the $\sim 13\%$ of the sample where a stellar continuum model could not be used to automatically correct the measured line fluxes, we assume a multiplicative correction of $C_{\mathrm{H}\beta} = 1.06$, the median of the measured corrections. No correction is applied to Hα (although, formally, the median measured correction is $C_{\mathrm{H}\alpha} = 1.01$).

The emission lines are fit using Gaussian profiles with a single redshift (z) and observed velocity width (σ, in $\mathrm{km\,s^{-1}}$) in a given band (i.e., all lines in the K band spectrum are fit with a single z and σ, but these may differ from the parameters measured in J or H band). For objects with observations covering H and K band, $\langle|\Delta z_{H-K}|\rangle = 2 \times 10^{-4}$ ($\Delta v \approx 18$ km/s) and $\langle\frac{|\Delta\sigma_{H-K}|}{\sigma_H}\rangle = 0.22$. For 19% of galaxies with observations covering J band, the redshift was fixed to match the redshift observed in H or K band to ensure an accurate measurement of the

[O II] doublet ratio in cases where the lines are only partially resolved; for all other objects, $\langle|\Delta z_{K-J}|\rangle = 4 \times 10^{-4}$ and $\langle|\Delta z_{H-J}|\rangle = 4 \times 10^{-4}$. Except for emission lines with particularly high signal-to-noise (S/N $\sim$ 50), the Gaussian approximation agrees with the directly integrated flux (summed over a range $\pm 3\sigma$ as defined by the fitted velocity width) at the few percent level. The ratios of the nebular [O III]$\lambda\lambda$4959,5008 and [N II]$\lambda\lambda$6549,6585 doublets are fixed at 1:3 and the ratios of the density-sensitive [O II]$\lambda\lambda$3727,3729 and [S II]$\lambda\lambda$6718,6732 doublets are restricted to be within 20% of the range of physically allowed values, which is $0.43 - 1.5$ for [S II]λ6718/[S II]λ6732 (Tayal & Zatsarinny, 2010; Mendoza & Bautista, 2014) and $0.35 - 1.5$ for [O II]λ3729/[O II]λ3727 (Kisielius et al., 2009). The 1σ errors on all measurements account for uncertainties in the fit parameters as well as covariance between parameters.

3.2.4 Slit-Loss Corrections

Because some rest-frame optical diagnostics rely on ratios of emission lines widely separated in wavelength, it is important to ensure that the relative flux-calibration between the NIR atmospheric bands is correct for individual objects. For example, without such cross-calibration, extinction corrections using the Balmer decrement are impossible, as Hβ falls in H band and Hα falls in K band for galaxies at $z \simeq 2 - 2.7$.

The overall atmospheric transparency and image quality for each MOSFIRE mask are monitored using concurrent observations of a bright star placed in a dedicated slit (with all slit widths = $0\farcs7$), and an initial guess at the slit-loss correction factor for observations from that mask is determined by comparing the measured flux of the star with its broadband photometry. At the typical seeing (between $0\farcs5 - 0\farcs7$), most science targets are unresolved or only marginally resolved. However, there are still several factors which can affect throughput of sources differently depending on their physical size and location on the mask, including minor glitches in tracking the rotation of high-elevation pointings and "slit drift" due to the combined effects of differential atmospheric refraction and differential flexure of the guider field relative to the science field. Consequently, it is important to optimize the mask correction factors for all objects on a given mask in a given atmospheric band, rather than rely exclusively on the correction determined using observations of the bright comparison star.

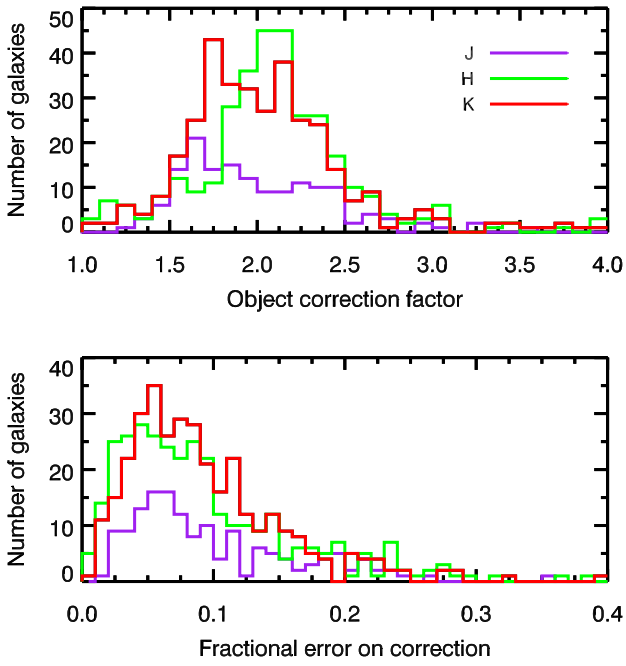

Figure 3.3: The distributions of individual object slit correction (top panel) and fractional error on the correction (bottom panel) broken down by NIR atmospheric band for 826 measurements of $z \sim 2.3$ KBSS-MOSFIRE galaxies. Overall, the median slit correction is 2.03, with a median uncertainty of 8%.

Optimal mask correction factors are calculated for all individual masks (213 total) using a Markov Chain Monte Carlo (MCMC) routine. The MCMC routine searches parameter space for the combination of individual mask correction factors that minimizes the scatter between independent measurements of strong lines (typically Hα, [O III]λ5008, or the sum of the [O II]$\lambda\lambda$3727, 3729 doublet) in galaxies' spectra, as many galaxies are observed more than once in a given band. The routine uses the comparison star measurements to construct priors on the mask corrections, which are allowed to sample a range from 1 to 3.5, chosen empirically to coincide with the range of corrections observed for the comparison stars. In cases where an individual mask includes observations of more than one bright star, the preliminary correction factors are compared to ensure good agreement. Outlier rejection is performed on a mask-by-mask basis prior to initializing the chain by censoring individual galaxies that require an anomalously high or low correction factor relative to other galaxies on the same mask. The principal advantage of using this method to solve for the mask correction factors in parallel is that it provides a quantitative measure of how well or how poorly a single mask correction factor performs for all objects observed on a mask and provides the means to flag masks with unreliable correction factors

based on the shape of the posterior distribution.

On average, the posteriors for the mask corrections are positively skewed, and $\sim 60\%$ of masks exhibit a significant degree of skewness (positive or negative). As a result, the characteristic value for a given mask correction is taken to be the center of the 68% highest posterior density interval rather than the mean value, with the width of the interval representing the uncertainty in the mask correction determination.

For galaxies observed on a single mask, the optimal mask correction is used to correct the measured line fluxes. When a galaxy has been observed more than once, line fluxes from the 2D weighted average spectrum are corrected to match the weighted average of the corrected line flux measurements from the constituent 2D spectral observations; the scatter around the average is the reported uncertainty on the individual object slit correction. The statistics of the 826 individual measurements of galaxies and their uncertainties are presented in Figure 3.3; the median slit-loss correction factor is 2.03, with a median uncertainty of 8%.

3.2.5 Stellar Masses and Star-formation Rates

Stellar mass (M_*) estimates for galaxies in the KBSS-MOSFIRE sample are inferred from reddened stellar population synthesis models fit to broadband photometry, as described by Reddy et al. (2012) and S14. The SED fitting employs solar metallicity models from Bruzual & Charlot (2003), a Chabrier (2003) IMF, the Calzetti et al. (2000) attenuation curve, and constant star formation histories for all galaxies, with a minimum allowed age of 50 Myr. This age is a dynamically-reasonable minimum imposed to prevent best-fit solutions with unrealistically young ages, as discussed by Reddy et al. (2012). Typical uncertainties in $\log(M_*/M_\odot)$ are estimated to be $\pm 0.1 - 0.2$ dex, with a median uncertainty of 0.16 dex (Shapley et al., 2005; Erb et al., 2006b).

Because star formation rate (SFR) estimates from SED fitting are naturally correlated with other fit parameters such as age and M_*, the SFRs used for analysis of the KBSS-MOSFIRE sample in this chapter are obtained from dust-corrected measurements of the Hα recombination line using the relation from Kennicutt (1998) and assuming a Chabrier (2003) IMF. Shivaei et al. (2016) reported that for $z \sim 2$ galaxies from the MOSFIRE Deep Evolution Field survey (MOSDEF, Kriek et al., 2015), Hα-based estimates of SFR are consistent with those estimated from the full panchromatic SED (including UV and far-IR photometry). Dust extinction toward star-forming regions is estimated by comparing the Balmer decrement ($H\alpha/H\beta$) with the expected Case

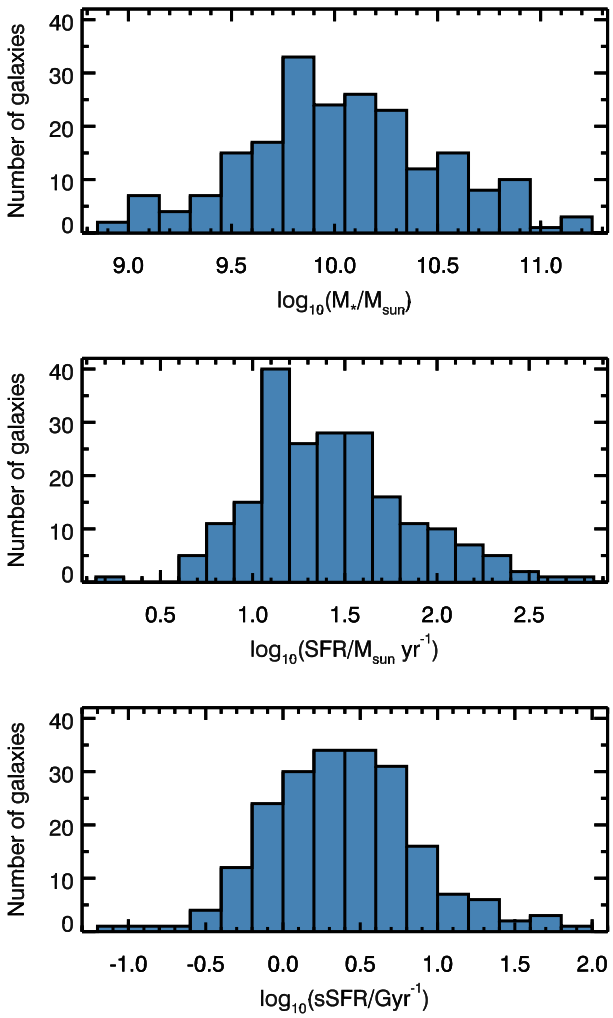

Figure 3.4: Stellar mass, star formation rate, and specific star formation rate distributions for 207 $z \sim 2.3$ KBSS-MOSFIRE galaxies with S/N > 5 Balmer decrement measurements. Stellar masses are determined from SED fits, and SFRs are calculated from dust-corrected Hα emission line measurements. The median stellar mass is 1.0×10^{10} $M_\odot$, and the median SFR is 24 $M_\odot$ yr^{-1}, with a median sSFR of 2.4 Gyr^{-1}.

Table 3.1: KBSS-MOSFIRE samples used for line-ratio analysis

subsample	N	$\langle z \rangle$	M_*[1] ($M_\odot$)	SFR[1] ($M_\odot$ yr^{-1})	Emission Line Criteria	Notes
N2-BPT	377	2.31	1.09×10^{10}	23.6	H$\alpha \geq 5\sigma$, Hβ, [O III]λ5008 $\geq 3\sigma$, [N II]λ6585 observed	[2,3]
S2-BPT	370	2.30	1.13×10^{10}	23.5	H$\alpha \geq 5\sigma$, Hβ, [O III]λ5008 $\geq 3\sigma$, [S II]$\lambda\lambda$6718, 6733 observed	[3]
O32-R23	171	2.35	9.49×10^{9}	22.9	H$\alpha \geq 5\sigma$, Hβ, [O III]λ5008, [O II]$\lambda\lambda$3727, 3729 $\geq 3\sigma$	[3,4]
N/O	151	2.34	9.94×10^{9}	23.5	H$\alpha \geq 5\sigma$, Hβ, [O II]$\lambda\lambda$3727, 3729 $\geq 3\sigma$, [N II]λ6585 observed	[3,4]
Ne3O2	69	2.33	7.14×10^{9}	22.6	H$\alpha \geq 5\sigma$, Hβ, [O III]λ5008, [O II]$\lambda\lambda$3727, 3729, [Ne III]λ3869 $\geq 3\sigma$,	[3,4]

[1] Median values

[2] S14 used H$\alpha \geq 5\sigma$, H$\beta \geq 3\sigma$, [O III]λ5008 $\geq 5\sigma$, [N II]λ6585 observed, taken as an upper limit when the S/N < 2

[3] We adopt 2σ upper limits for emission lines without a listed S/N threshold and $< 2\sigma$ significance

[4] Emission line errors incorporate uncertainties in the slit-loss corrections, and the Balmer decrement must have S/N > 5

B value of 2.86 (Osterbrock, 1989). Galaxies with Balmer decrements < 2.86 are assumed to have zero extinction, with ∼ 46% of such galaxies exhibiting Balmer decrements consistent with the nominal Case B value within 3σ. Adopting the Galactic extinction curve from Cardelli, Clayton & Mathis (1989) for galaxies with $H\alpha/\mathrm{H}\beta \geq 2.86$, the interquartile range for extinction along the line-of-sight to H II regions in the full sample of $z \sim 2.3$ KBSS-MOSFIRE galaxies is $E(B-V)_{\mathrm{neb}} = 0.06 - 0.47$, with a median value of 0.25 and a corresponding median $A_{\mathrm{H}\alpha} = 0.63$ mag.

The distributions of M_*, Hα-based SFR, and specific star formation rate (sSFR≡SFR/M_*) for 207 $z \sim 2.3$ KBSS-MOSFIRE galaxies with S/N > 5 Balmer decrement measurements are presented in Figure 3.4. Table 3.1 provides an overview of the sample statistics for the subsamples of KBSS-MOSFIRE galaxies discussed in the following sections and notes the corresponding emission line selection criteria. In cases where extinction corrections are necessary, we require the measurement of Hα/Hβ to have S/N > 5, including the uncertainty from the relative slit corrections. This S/N cut is well-motivated by the fact that extinction corrections for individual emission lines scale non-linearly with the measured value of the Balmer decrement, going approximately as $(\mathrm{H}\alpha/\mathrm{H}\beta)^{k_\lambda}$, where k_λ is the value of the reddening curve at a specific wavelength ($k_{\mathrm{H}\alpha} = 2.52$ for the Cardelli, Clayton & Mathis 1989 extinction curve). Thus, even relatively small uncertainties in the Balmer decrement translate to much larger uncertainties in the corrected line ratio.

3.3 Nebular Emission Line Ratios

3.3.1 The N2- and S2-BPT Diagrams

Figure 3.5 shows the location of 377 KBSS-MOSFIRE galaxies with $1.9 < z < 2.7$ ($\langle z \rangle = 2.3$) in the N2-BPT plane, including only those galaxies where Hα is detected at > 5σ and Hβ and [O III]λ5008 are detected at > 3σ (light green points). Galaxies with [N II]λ6585 measurements with S/N < 2 are assigned 2σ upper limits (dark green triangles), accounting for ∼ 36% of the sample. As we originally reported in S14 for a smaller sample, KBSS-MOSFIRE galaxies occupy a region of the N2-BPT plane almost entirely distinct from the majority of local galaxies, represented by SDSS-DR8 (in greyscale, Aihara et al., 2011).

The SDSS comparison sample employed in this chapter takes emission line measurements and ancillary physical parameters from the MPA-JHU catalogs[2] (c.f.

[2] https://www.sdss3.org/dr10/spectro/galaxy_mpajhu.php

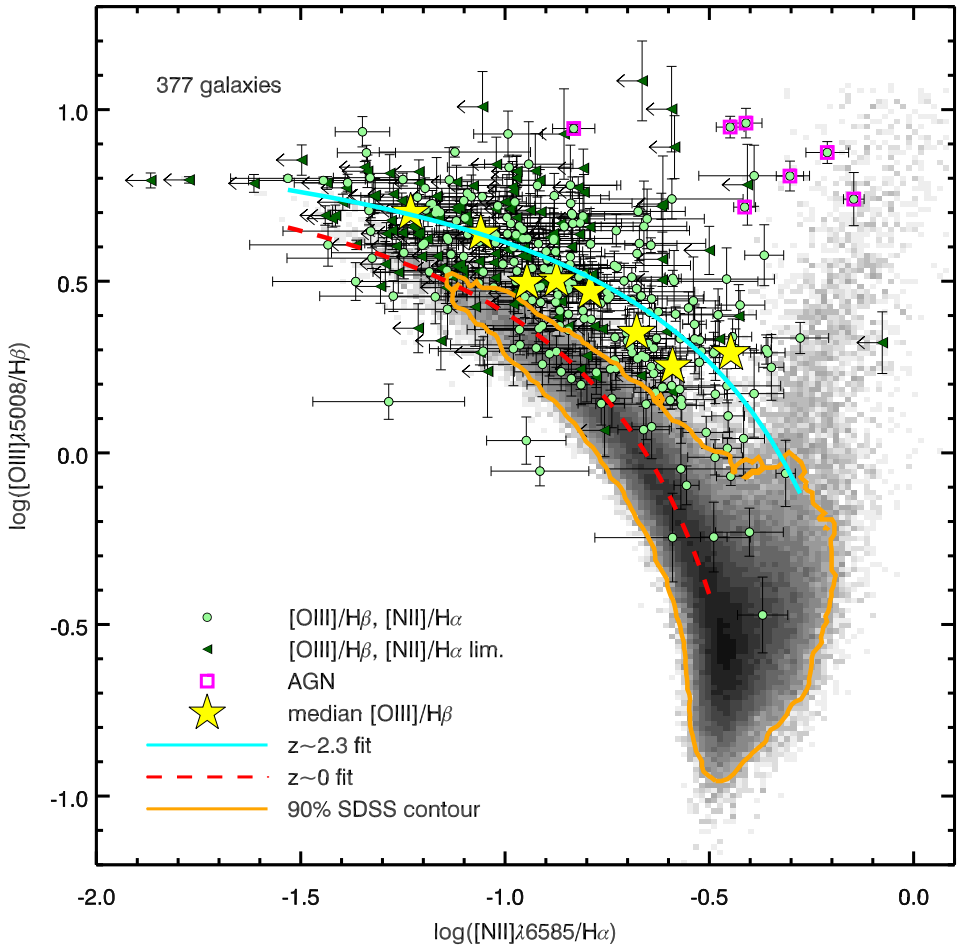

Figure 3.5: KBSS-MOSFIRE galaxies in the N2-BPT plane, compared with local galaxies from SDSS (in greyscale, with the orange contour enclosing 90% of the total sample). KBSS-MOSFIRE galaxies with $> 2\sigma$ detections of [N II]λ6585 are plotted in light green, with 2σ upper limits shown instead as dark green triangles. Magenta squares denote objects identified as AGN/QSOs. The ridge-line of the high-z locus occurs far outside the 90% SDSS contour, demonstrated not only by the location of the median log([O III]λ5008/Hβ) values in equal-number bins of log([N II]λ6585/Hα) (yellow stars, see also Table 3.2) but also by the formal fit to the distribution of KBSS-MOSFIRE galaxies (cyan curve). The $z \sim 0$ locus is represented by the red dashed curve.

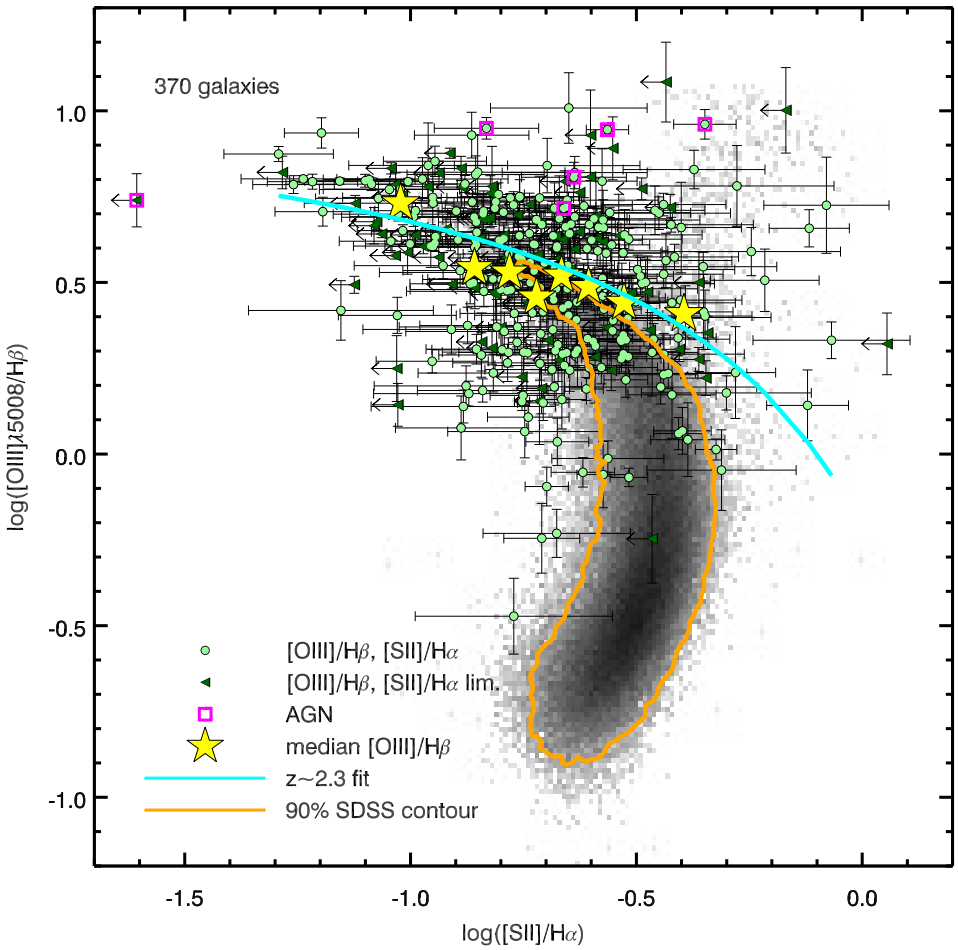

Figure 3.6: The S2-BPT diagram displayed in the same manner as Figure 3.5. Note that while $z \sim 2.3$ galaxies are noticeably offset relative to the $z \sim 0$ sample in the N2-BPT diagram, a similar offset is not observed in the S2-BPT plane. Instead, the log([O III]/Hβ) medians (yellow stars, Table 3.2) and the fit to the KBSS-MOSFIRE locus (cyan curve) coincide with the upper envelope of the orange contour, which encloses 90% of SDSS galaxies.

Sections 4.3.1 and 4.3.2 of Aihara et al., 2011) and has been selected to be similar to KBSS-MOSFIRE in terms of detection properties. The SDSS comparison galaxies have $0.04 \leq z \leq 0.1$ (to avoid severe aperture effects), $> 50\sigma$ measurements of Hα, and a "reliable" flag signaling good results from the MPA-JHU pipeline. Stellar masses, SFRs, and sSFRs are reported using the median estimates of the PDFs for the "total" values.

Although the existence of an offset in the N2-BPT plane has been widely reported for other samples of high-redshift galaxies (Masters et al., 2014; Shapley et al., 2015; Sanders et al., 2016), the degree to which the KBSS-MOSFIRE sample differs from typical local galaxies is quite remarkable. Nearly all KBSS-MOSFIRE galaxies have larger values of log([O III]/Hβ) at fixed log([N II]/Hα) than typical SDSS galaxies in the N2-BPT diagram (represented by the 90% of $z \sim 0$ galaxies enclosed by the orange contour in Figure 3.5). Furthermore, the ridge-line of the $z \sim 2.3$ sample with $> 2\sigma$ detections of [N II]λ6585, traced by median values of log([O III]/Hβ) in equal-number bins of log([N II]/Hα) (yellow stars, Table 3.2), falls well outside the same contour.

The N2-BPT locus can be described analytically using the following functional form:

$$\log([\text{O III}]/\text{H}\beta) = \frac{p_0}{\log([\text{N II}]/\text{H}\alpha) + p_1} + p_2. \tag{3.1}$$

However, because the fit parameters are degenerate, interpreting them is difficult. To be consistent with the literature, we fit the KBSS-MOSFIRE locus with p_0 fixed to the value reported by Kewley et al. (2001) for the N2-BPT extreme starburst classification line ($p_0 = 0.61$). We determine the best-fit curve describing the KBSS-MOSFIRE N2-BPT locus (cyan curve in Figure 3.5) using the IDL routine *MPFIT* (Markwardt, 2009), with the following result:

$$\log([\text{O III}]/\text{H}\beta) = \frac{0.61}{\log([\text{N II}]/\text{H}\alpha) - 0.22} + 1.12. \tag{3.2}$$

The intrinsic scatter relative to the best-fit curve is 0.18 dex, estimated from the amount of additional uncertainty required to achieve $\chi^2/\text{DOF}= 1$ after accounting for individual measurement errors. Galaxies with upper limits on [N II] and objects identified as AGN (magenta squares; see also Section 3.3.2) are excluded from the fit.

We determine the $z \sim 0$ locus for the SDSS comparison sample using the same form (red dashed line), including only star-forming galaxies identified using the

Table 3.2: Median line ratios in the N2-BPT and S2-BPT diagrams

N2-BPT		S2-BPT	
log[N II]/Hα	log[O III]/Hβ	log[S II]/Hα	log[O III]/Hβ
-1.23	0.70	-1.02	0.73
-1.06	0.64	-0.86	0.54
-0.95	0.50	-0.78	0.53
-0.87	0.50	-0.72	0.46
-0.79	0.47	-0.67	0.52
-0.68	0.35	-0.61	0.49
-0.59	0.25	-0.53	0.44
-0.45	0.29	-0.39	0.41

Note: The above values of log[O III]/Hβ are the medians in equal-number bins of log[N II]/Hα and log[S II]/Hα, where only galaxies with $> 2\sigma$ detections of [N II]λ6585 or [S II]$\lambda\lambda$6718, 6732 have been included. The reported values of log[N II]/Hα and log[S II]/Hα are the median values of those quantities in each bin.

Kauffmann et al. (2003) selection. When p_1 and p_2 are fixed separately, we find that the observed offset between the $z \sim 0$ N2-BPT locus and the KBSS-MOSFIRE ridge-line can be described by a shift of either

$$\begin{aligned} \Delta \log([\text{O III}]/\text{H}\beta) &= 0.26 \text{ dex or} \\ \Delta \log([\text{N II}]/\text{H}\alpha) &= 0.37 \text{ dex.} \end{aligned}$$

Even when p_0 is treated as a free parameter, the amplitudes of these shifts are similar, so long as the same p_0 is adopted for both the low-z SDSS and high-z KBSS-MOSFIRE samples.

The difference between $z \sim 0$ and $z \sim 2.3$ galaxies observed in the S2-BPT diagram (Figure 3.6) is less notable than in the N2-BPT plane, a result that was previously shown by Masters et al. (2014) for stacked spectra and by Shapley et al. (2015) and Sanders et al. (2016) for individual high-z galaxies from the MOSDEF survey. The KBSS-MOSFIRE galaxies appear to trace the high [O III]/Hβ tail of SDSS, although with larger scatter due to measurement errors. The best fit to the S2-BPT locus (cyan curve in Figure 3.6) with $p_0 = 0.72$ (Kewley et al., 2001) grazes the upper edge of the distribution of local galaxies, taking the form

$$\log([\text{O III}]/\text{H}\beta) = \frac{0.72}{\log([\text{S II}]/\text{H}\alpha) - 0.53} + 1.15, \tag{3.3}$$

with an intrinsic scatter of 0.22 dex. Note that the median values of log([O III]/Hβ) in equal-number bins of log([S II]/Hα) (yellow stars) also lie close to the upper envelope of the orange contour enclosing 90% of SDSS galaxies.

As we will discuss in Section 3.5.3, the same behavior persists when one compares the $z \sim 2.3$ KBSS-MOSFIRE sample with SDSS galaxies that have similar ionization and excitation properties: the KBSS-MOSFIRE sample exhibits a substantial offset relative to SDSS in the N2-BPT plane, but virtually no separation is observed in the S2-BPT diagram. In Section 3.6, we show that the same self-consistent photoionization models can explain the observations in both cases.

3.3.2 AGN Contamination

Given the differences observed in the N2-BPT diagram between $z \sim 2.3$ galaxies and local star-forming galaxies, it is important to understand the risk of AGN contamination, which could lead to misinterpretation of the results described above. Although the BPT diagrams are used to separate star-forming galaxies and AGN at low-z, a similar application at high redshift is less straightforward. Kewley et al., 2013 used photoionization models to explore differences in the BPT plane at higher redshifts and noted that the distinct "branches" seen in the N2-BPT diagram become less discernible with changes in ISM conditions and AGN properties. From observations alone, the problem is also clear: the majority of $z \sim 2.3$ KBSS galaxies fall in the region of the N2-BPT diagram (Figure 3.5) generally reserved for "composite" objects—those that show signs of AGN activity as well as ongoing star formation—at $z \sim 0$.

We considered this issue in some detail in S14, but summarize it again here. KBSS galaxies are flagged as AGN or QSOs if (1) their rest-UV (LRIS) spectrum shows significant emission in high ionization lines (such as C IVλ1549, C III]λ1908, N Vλ1240; Hainline et al. 2011) or (2) a combination of their rest-optical emission-line ratios and line widths suggest the presence of an AGN. These objects (7 in total) generally fall near the upper envelope of log([O III]/Hβ) observed for KBSS galaxies and in the upper half of the stellar mass range sampled by the survey; they are excluded from fits to the galaxy sample (including those reported in Section 3.3.1) and from analyses that require extinction corrections.

3.3.3 The Stellar Mass-Excitation Relation

Similar to the offset observed in the N2-BPT plane, the behavior of [O III]/Hβ with respect to M_* (referred to as the MEx, Juneau et al., 2011) highlights dramatic

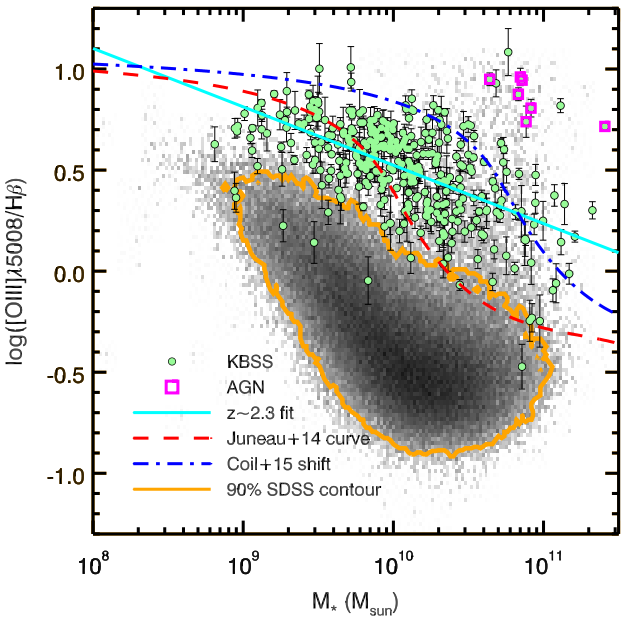

Figure 3.7: The mass-excitation relation (MEx) for 365 KBSS-MOSFIRE galaxies with M_* estimates (green) and SDSS galaxies (greyscale), with the division between star-forming/composite galaxies and AGN in the local universe from Juneau et al. (2014) illustrated by the red dashed curve. The dot-dashed blue curve represents the shift proposed by Coil et al. (2015) to separate $z \sim 2$ star-forming galaxies from AGN. KBSS-MOSFIRE galaxies identified as AGN are denoted by magenta squares. The correlation between [O III]λ5008/Hβ and M_* is one of the strongest observed for the KBSS-MOSFIRE sample (with the best-fit linear relation shown by the cyan line) and also highlights one of the largest differences between $z \sim 2.3$ galaxies and those at $z \sim 0$.

differences between $z \sim 2.3$ KBSS-MOSFIRE galaxies and local galaxies from SDSS. Figure 3.7 shows the M_*-excitation relation for both samples.

As for local galaxies (greyscale in Figure 3.7), $z \sim 2.3$ KBSS-MOSFIRE galaxies (green points) exhibit a significant inverse correlation between [O III]/Hβ and M_*, with a Spearman correlation coefficient of $\rho = -0.47$ and $p = 1.4 \times 10^{-21}$. However, the distribution of the $z \sim 2.3$ sample is almost entirely disjoint with respect to the majority of SDSS galaxies (enclosed by the 90% contour in orange), with 82% of KBSS-MOSFIRE objects falling above the updated curve from Juneau et al. (2014) used to divide star-forming/composite galaxies from AGN in the local universe (red dashed curve in Figure 3.7). This empirical division was calibrated using $z \sim 0.1$ SDSS galaxies and designed to function as an alternative method of distinguishing between AGN and star-forming (or composite) galaxies when not all of the BPT lines are available. Figure 3.7 also shows that AGN in the KBSS-MOSFIRE sample

are offset to even higher [O III]/Hβ than the majority of the $z \sim 2.3$ galaxies at fixed M_*, although there are $z \sim 0$ AGN from SDSS that occupy the same region of parameter space. These results are largely consistent with those reported by Coil et al. (2015), who explicitly tested the success of the MEx in identifying $z \sim 2$ AGN using observations from the MOSDEF survey. In order to construct a diagnostic that more accurately distinguishes between high-z star-forming galaxies and AGN, Coil et al. (2015) proposed shifting the MEx division by $\Delta \log(M_*/M_\odot) = 0.75$, as illustrated by the dot-dashed blue curve in Figure 3.7; to cleanly separate AGN from star-forming galaxies in the current KBSS-MOSFIRE sample, an even larger shift ($\gtrsim 1.0$ dex) would be required.

We calculate a linear fit to the locus of $z \sim 2.3$ KBSS-MOSFIRE star-forming galaxies in Figure 3.7 using the *MPFITEXY* IDL routine[3] (Williams, Bureau & Cappellari, 2010), and it has the form:

$$\log([\text{O III}]/\text{H}\beta) = 0.52 - 0.29 \times [\log(M_*/M_\odot) - 10], \tag{3.4}$$

with $\sigma_{\rm RMS} = 0.19$ dex scatter about the best-fit relation and an implied intrinsic scatter of $\sigma_{\rm int} = 0.17$ dex. The correlation between excitation, as probed by [O III]/Hβ, and M_* is therefore one of the tightest correlations between the nebular spectrum and a global galaxy property.

Compared to SDSS, KBSS-MOSFIRE galaxies exhibit an offset of up to 0.8 dex toward higher log([O III]/Hβ) at fixed M_*. The largest separation occurs at the high mass end of the M_* distribution, where there are few local analogs to KBSS-MOSFIRE galaxies. Although some of the offset likely results from decreased gas-phase oxygen abundances in high-z H II regions (e.g., Pettini & Pagel, 2004; Maiolino et al., 2008), we show in the following sections that the higher values of [O III]/Hβ observed in $z \sim 2.3$ galaxies reflect differences in the typical shape of the ionizing radiation field in galaxies at fixed M_* as a function of redshift.

3.3.4 Ionization and Excitation: O32 and R23

We also consider the behavior of O32 and R23; the definitions for both indices as used in this chapter can be found in Table 3.3, together with other strong-line indices. O32 is often employed as a proxy for ionization (Penston et al., 1990) and can be used to calculate the ionization parameter ($U \equiv n_\gamma/n_H$, the dimensionless ratio of the number density of incident H-ionizing photons to the number density of hydrogen

[3] `http://purl.org/mike/MPFITEXY`

Table 3.3: Definitions for strong-line indices

index	definition
N2	log([N II]λ6585/Hα)
O3N2	log([O III]λ5008/Hβ)− log([N II]λ6585/Hα)
R23	log[([O III]$\lambda\lambda$4960, 5008+[O II]$\lambda\lambda$3727, 3729)/Hβ]
O32	log([O III]$\lambda\lambda$4960, 5008/[O II]$\lambda\lambda$3727, 3729)
N2O2	log([N II]λ6585/[O II]$\lambda\lambda$3727, 3729)
N2S2	log([N II]λ6585/[S II]$\lambda\lambda$6718, 6732)
Ne3O2	log([Ne III]λ3869/[O II]$\lambda\lambda$3727, 3729)

Note: The $\lambda\lambda$ notation refers to the sum of both lines.

atoms in the gas) given an assumed ionizing spectrum. R23 is used to estimate oxygen abundance (e.g., Pagel et al., 1979; McGaugh, 1991; Kewley & Dopita, 2002), although because of its double-valued nature, an additional parameter (like N2 or O3N2) must be used to break the degeneracy. R23 may also be used as probe of the overall degree of excitation in H II regions with moderate gas-phase metallicity, as it compares the emission from two collisionally-excited metallic ions (O^+ and O^{++}) with the emission from a recombination line of hydrogen, thus providing a rough constraint on the amount of kinetic energy in the gas relative to the number of ionizing photons in a similar manner to the line ratios used in the BPT diagrams.

The clear advantage of indices like O32 and R23 over the BPT ratios is that they include only one element (oxygen) in addition to hydrogen and should be insensitive to differences in the abundance ratio patterns of $z \sim 0$ and $z \sim 2.3$ galaxies (or, indeed, between any two populations). Moreover, unlike [O III]/Hβ, which is sensitive to changes in both the kinetic energy of the gas and U, R23 and O32 offer relatively independent probes of excitation and ionization, respectively. However, because both O32 and R23 require nebular extinction corrections, the indices can only be determined for $z \sim 2.3$ galaxies with observations in J, H, and K band.

Figure 3.8 shows $z \sim 2.3$ KBSS-MOSFIRE galaxies in the O32-R23 plane, compared with galaxies from SDSS. The lefthand panel shows the observed ratios, corrected for relative slit losses but not for dust extinction, while the righthand panel shows the line ratios corrected for differential extinction due to dust as described above in Section 3.2.5. The KBSS-MOSFIRE galaxies are largely coincident with the high-O32, high-R23 tail of SDSS (similar to the S2-BPT plane, Figure 3.6), although this region of parameter space is relatively sparsely populated by $z \sim 0$ galaxies overall, with the majority of the SDSS sample exhibiting much lower values

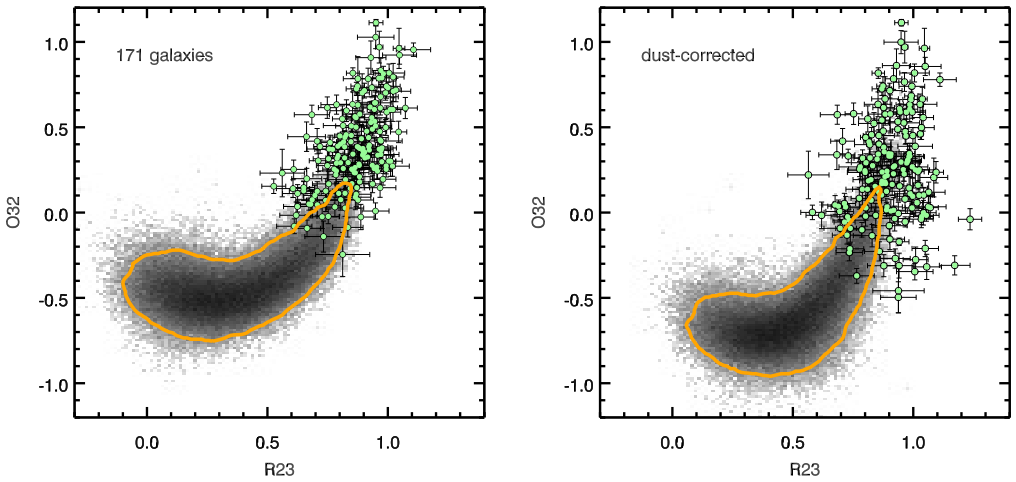

Figure 3.8: *Left:* The distribution of the O32 and R23 indices for KBSS-MOSFIRE galaxies (excluding AGN), using line fluxes that have not been corrected for dust extinction, compared with the locus of $z \sim 0$ SDSS galaxies in greyscale (the orange contour encloses 90% of the sample). Here, in contrast to earlier figures, the SDSS sample contains only star-forming galaxies, separated from AGN by the curve from Kauffmann et al. (2003). *Right:* The same parameter space as the lefthand panel, but with line ratios that have been corrected for dust extinction. As in the S2-BPT diagram, KBSS-MOSFIRE galaxies largely follow the trend established by typical local galaxies, despite overlapping with only the most extreme tail of SDSS.

of both indices; similar results were also reported for $z \sim 2$ MOSDEF galaxies by Shapley et al. (2015).

This agreement reflects fundamental similarities between the most extreme SDSS galaxies and KBSS-MOSFIRE galaxies. At low gas-phase O/H, R23 increases with metallicity as the number of oxygen atoms increases; at high gas-phase O/H, R23 declines again, because the oxygen present in the gas functions as an efficient cooling pathway, reducing the gas temperature and thus the number of collisionally-excited oxygen ions. Thus, R23 reaches a maximum value at intermediate O/H, with the value of R23 at the turnaround depending sensitively on the hardness of the incident radiation field at fixed gas-phase O/H: a harder ionizing photon distribution will result in greater kinetic energy per ionized electron than a softer distribution. Because there is a maximum degree of hardness for the spectra of massive stars set by stellar evolutionary processes, there is a corresponding maximum R23 achievable for star-forming galaxies, reflected in the upper envelope at R23 $\sim$ 1 for both samples in the righthand panel of Figure 3.8.

Thus, although there exist SDSS galaxies occupying the same high-O32, high-R23

region of parameter space as the majority of $z \sim 2.3$ galaxies, both samples must be characterized by large ionization parameters and the combination of hard ionizing radiation fields and moderate gas-phase O/H needed to produce values of R23 near the turnaround. We test this assumption in Section 3.5.3 and Section 3.6.2 and evaluate the utility of the combination of O32 and R23 for determining gas-phase oxygen abundance at high redshift.

3.4 Physical Characteristics of the Most Offset Galaxies in the $z \sim 2.3$ N2-BPT Plane

In addition to comparing typical $z \sim 2.3$ galaxies with those commonly seen in the local universe (such as star-forming galaxies from SDSS), comparisons between high-redshift samples with different properties are also important. The latter is necessary to understand whether the physical process(es) driving the differences observed between typical galaxies at different epochs are also responsible for the diversity of galaxy properties observed at a single epoch. To facilitate this exercise, we divide the $z \sim 2.3$ KBSS-MOSFIRE galaxies into two subsamples on the basis of their position in the N2-BPT plane. High-redshift samples show the greatest deviations relative to SDSS galaxies in this parameter space and we might therefore expect to identify correlated differences in other line ratios and physical properties between subsamples identified in such a manner.

For the purposes of this comparison, galaxies with log([O III]/Hβ) ratios that fall above the $z \sim 2.3$ N2-BPT ridge-line (Equation 3.2, cyan curve in Figure 3.5) are designated the "large-offset" subsample, and those below the ridge-line form the "small-offset" subsample; AGN are excluded from both. Figure 3.9 shows the location of these two subsamples in the N2-BPT plane (where they are selected) and the S2-BPT plane. Galaxies with low-significance ($< 2\sigma$) detections of [N II] or [S II] are identified by darker-colored triangles at the position of their 2σ upper limits. Note that if a more stringent selection is applied, such that galaxies must lie $> 3\sigma$ away from the ridge-line in log([O III]/Hβ) in order to be classified as large-offset or small-offset, the nature of the results discussed below remains unchanged.

3.4.1 BPT Offsets

The loci of small-offset galaxies (orange curve in Figure 3.9) and large-offset galaxies (cyan curve) in the N2-BPT and S2-BPT planes are independently fit using the method and functional form described in Section 3.3.1. As before, objects with upper limits on [N II] or [S II] are not included in determining the fits. The results

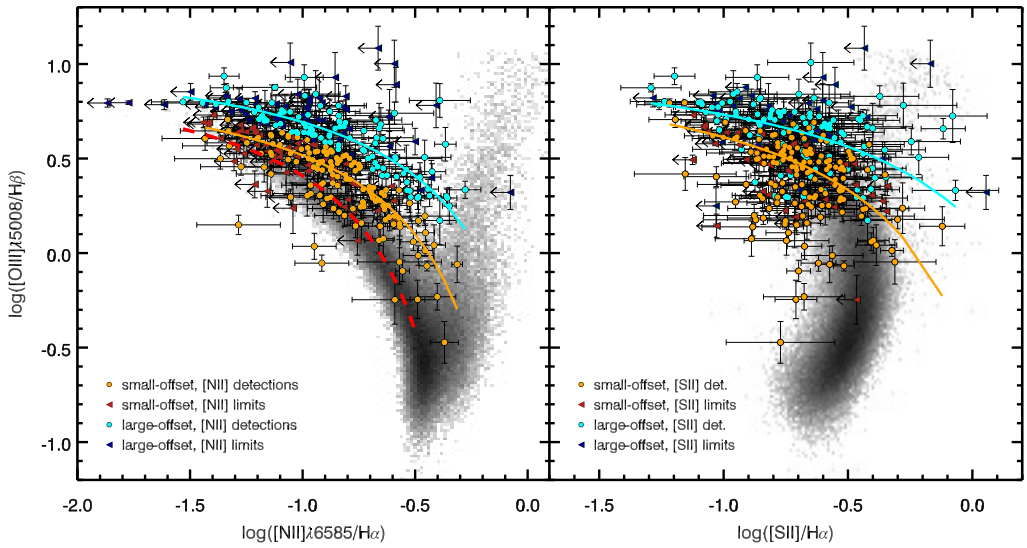

Figure 3.9: The N2-BPT (left) and S2-BPT (right) diagrams, showing the location of $z \sim 2.3$ KBSS-MOSFIRE galaxies color-coded on the basis of their location in the N2-BPT plane. Those falling above the KBSS ridge-line (Equation 3.2, cyan curve in Figure 3.5) are referred to as the "large-offset" subsample (cyan/navy points), and those falling below the ridge-line are instead referred to as "small-offset" galaxies (orange/red points). For reference, the $z \sim 0$ N2-BPT locus from Figure 3.5 is shown in red, and separate fits to the loci of both the small- and large-offset subsamples are illustrated by the solid orange and cyan curves, respectively. A comparison between the $z \sim 2.3$ loci reveals a significant shift even with respect to one another: up to $\Delta\log([\mathrm{O\ III}]/\mathrm{H}\beta) = 0.19$ dex or $\Delta\log([\mathrm{N\ II}]/\mathrm{H}\alpha) = 0.34$ dex. In the S2-BPT plane, a shift of $\Delta\log([\mathrm{O\ III}]/\mathrm{H}\beta) = 0.16$ dex or $\Delta\log([\mathrm{S\ II}]/\mathrm{H}\alpha) = 0.36$ dex would be required to bring the two loci into agreement. AGN in the KBSS-MOSFIRE sample have been excluded from both panels.

for both BPT diagrams are summarized in Table 3.4.

Even the locus of small-offset KBSS-MOSFIRE galaxies remains noticeably different from typical SDSS galaxies in the N2-BPT plane, as shown by the offset of orange curve relative to the $z \sim 0$ locus (red dashed curve) in the lefthand panel of Figure 3.9. The additional separation between the small-offset and large-offset loci is consistent with an offset of either

$$\begin{aligned} \Delta\log([\mathrm{O\ III}]/\mathrm{H}\beta)_{\mathrm{N2}} &= 0.19 \text{ dex or} \\ \Delta\log([\mathrm{N\ II}]/\mathrm{H}\alpha)_{\mathrm{N2}} &= 0.34 \text{ dex,} \end{aligned}$$

if the shift is restricted to one axis.

The two subsamples are also clearly differentiated in the S2-BPT diagram (righthand panel of Figure 3.9), with large-offset galaxies exhibiting systematically higher

Table 3.4: Best-fit parameters for BPT ridgelines

	p_0	p_1	p_2
SDSS N2-BPT	0.61	0.09	1.08
KBSS-MOSFIRE N2-BPT	0.61	-0.22	1.12
KBSS-MOSFIRE small-offset (N2)	0.61	-0.14	1.05
KBSS-MOSFIRE large-offset (N2)	0.61	-0.31	1.16
KBSS-MOSFIRE S2-BPT	0.72	-0.53	1.15
KBSS-MOSFIRE small-offset (S2)	0.72	-0.41	1.12
KBSS-MOSFIRE large-offset (S2)	0.72	-0.73	1.15

log([O III]/Hβ) at fixed log([S II]/Hα) compared with the small-offset subsample. If only one fit parameter is allowed to vary, the separation between the two loci is equivalent to either

$$\begin{aligned} \Delta \log([\text{O III}]/\text{H}\beta)_{\text{S2}} &= 0.16 \text{ dex or} \\ \Delta \log([\text{S II}]/\text{H}\alpha)_{\text{S2}} &= 0.36 \text{ dex.} \end{aligned}$$

This significant displacement between the subsample loci in the S2-BPT diagram is intriguing because of its implications for the physical origin of the offset in the N2-BPT plane. Assuming the offset between the small-offset and large-offset subsamples in the N2-BPT plane is entirely a horizontal displacement toward higher log([N II]/Hα) resulting from an enhancement in N/O at fixed O/H implies $\Delta \log([\text{O III}]/\text{H}\beta) \approx 0$. Provided all other abundance ratios (particularly S/O) are similar between small- and large-offset galaxies, $\Delta \log([\text{S II}]/\text{H}\alpha)$ should also be close to zero. The assumption of similar S/O abundances among the two subsamples is reasonable, as sulfur and oxygen are both alpha process elements released primarily by Type II SNe.

Consequently, the two ridge-lines in the righthand panel of Figure 3.9 ought to lie coincident with one another if the offset between the subsamples were due primarily to differences in N/O at fixed O/H. Indeed, when Sanders et al. (2016) performed the same exercise using galaxies from the MOSDEF survey, they found that high-z galaxies separated on the basis of their offset from local galaxies in the N2-BPT diagram are well-mixed in the S2-BPT and O32-R23 planes. The authors interpret this result as evidence in favor of elevated N/O at fixed O/H in $z \sim 2.3$ galaxies, but such an explanation is inconsistent with the results shown for the KBSS-MOSFIRE subsamples in Figure 3.9.

While some horizontal separation between the KBSS-MOSFIRE S2-BPT loci might occur if a larger amount of [S II] emission originated from diffuse ionized gas in large-offset galaxies than in small-offset galaxies, the contribution from such gas would need to be substantial to account for the 0.36 dex difference in log([S II]/Hα) at fixed log([O III]/Hβ) between the subsamples. Instead, it is likely that the clear separation between the two loci corresponds to important differences in the shape and/or normalization of the ionizing radiation in small- and large-offset galaxies, and similar differences may be important between $z \sim 0$ and $z \sim 2.3$ galaxies. In Section 3.5.3, we test whether such differences can account for the entirety of the offset observed between KBSS-MOSFIRE and SDSS in the N2-BPT diagram.

3.4.2 Galaxy Properties

We can also compare the global properties of galaxies as a function of their N2-BPT offset. In general, large-offset galaxies have significantly lower M_* than small-offset galaxies, despite having nearly identical distributions in SFR (see Figure 3.10). The separation as a function of M_* is consistent with the results reported by Shapley et al. (2015) for $z \sim 2$ MOSDEF galaxies, but the resulting separation in sSFR for KBSS-MOSFIRE galaxies is especially notable. This difference highlights the fact that recent star formation has contributed a larger fraction of the integrated stellar mass of large-offset galaxies than for small-offset galaxies. For comparison, the distributions of M_*, SFR, and sSFR for the SDSS galaxies are shown in grey in Figure 3.10. Interestingly, the SDSS, small-offset KBSS-MOSFIRE, and large-offset KBSS-MOSFIRE samples appear to form a sequence in sSFR that mirrors their separation in N2-BPT diagram (from least to most offset).

The importance of recent star formation is also apparent in the behavior of [O III]/Hβ—which we have already shown is significantly higher for KBSS-MOSFIRE galaxies compared with SDSS and serves as a measure of excitation—as a function of sSFR, which is shown in Figure 3.11. Unlike M_*-excitation space (Figure 3.7), KBSS-MOSFIRE galaxies appear to follow the sSFR-excitation trend established by local galaxies in SDSS, with large-offset galaxies exhibiting the highest sSFRs and ratios of [O III]/Hβ. Dickey et al. (2016) found the same trend for a sample of $z \sim 2$ star-forming galaxies from the 3D-*HST* survey.

The interquartile range in M_* for SDSS galaxies with sSFR > 2 Gyr^{-1} ($\sim 1\%$ of the total sample) is $\log(M_*/M_\odot) = 8.40 - 9.06$, while high sSFRs are found in significantly more massive $z \sim 2.3$ galaxies. KBSS-MOSFIRE galaxies with

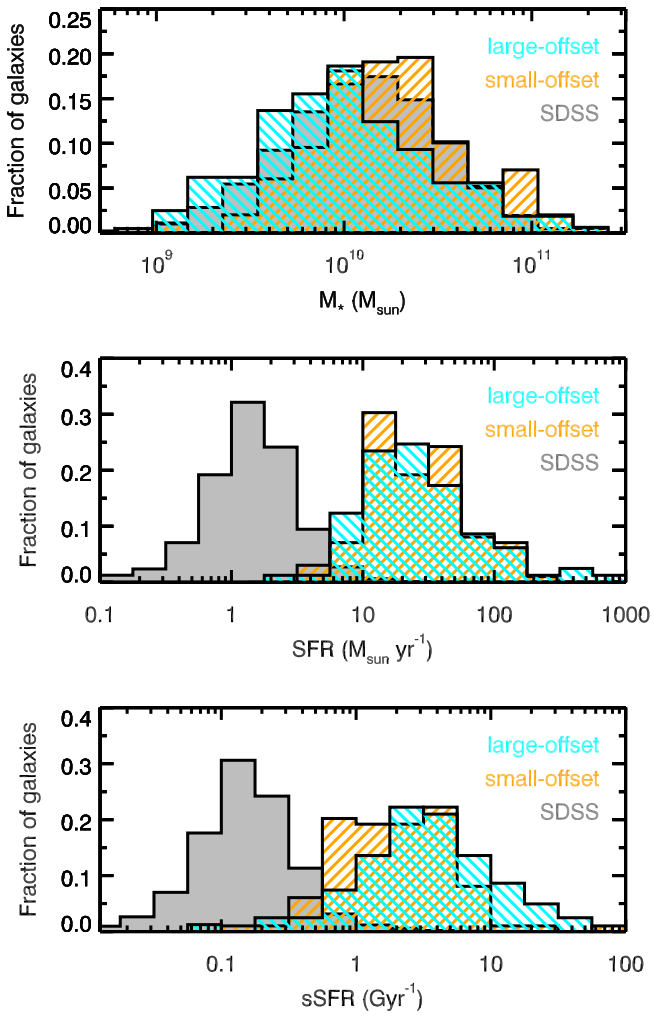

Figure 3.10: The distributions of M_*, SFR, and sSFR for SDSS galaxies (in grey) and the KBSS-MOSFIRE subsamples divided by the degree of their N2-BPT offset. Although the two $z \sim 2.3$ subsamples have very similar distributions in SFR, they exhibit clear differences in M_* and sSFR. All KBSS-MOSFIRE galaxies have substantially higher SFRs and sSFRs than SDSS galaxies.

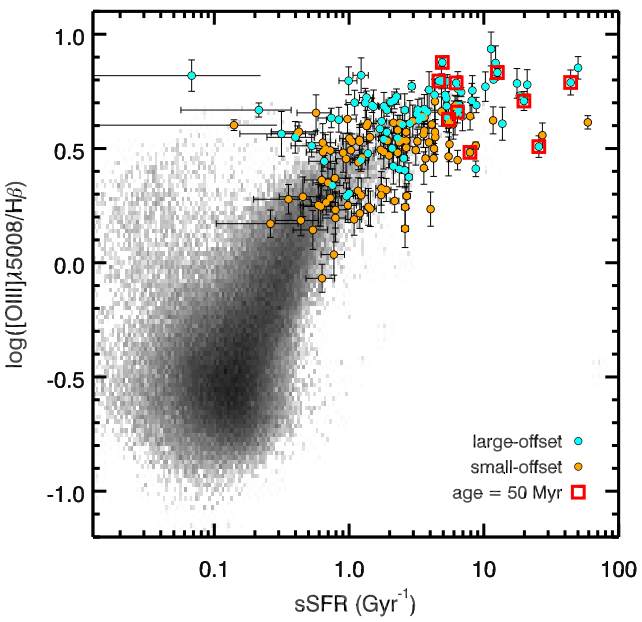

Figure 3.11: The sSFR-excitation relation for SDSS (in greyscale) and KBSS-MOSFIRE galaxies, with the $z \sim 2.3$ galaxies color-coded by the degree of their N2-BPT offset (large-offset galaxies in cyan, small-offset galaxies in orange; see lefthand panel of Figure 3.9). KBSS-MOSFIRE galaxies with an imposed minimum age of 50 Myr from SED fitting are identified by red squares; this sample of galaxies is discussed at greater length in Section 3.4.3 and Figures 3.12 and 3.13. All of the KBSS-MOSFIRE galaxies overlap only with SDSS galaxies with the highest log([O III]/Hβ) and sSFR. However, both $z \sim 2.3$ and $z \sim 0$ samples appear to form a single excitation sequence.

sSFR> 2 Gyr^{-1} represent $\sim 57\%$ of the $z \sim 2.3$ sample and are ~ 10 times more massive than high-sSFR $z \sim 0$ SDSS galaxies on average, with an interquartile range in $\log(M_*/M_\odot) = 9.59 - 10.11$. If the offset of the two $z \sim 2.3$ subsamples with respect to one another (and with respect to $z \sim 0$) is tied to sSFR, the implication is that the physical cause of the observed differences between samples is also correlated with the relative importance of recent star formation in galaxies at fixed M_*. This highlights the importance of the details of star formation history generally, as the high sSFRs seen in KBSS-MOSFIRE galaxies become increasingly difficult to sustain in older, massive galaxies and/or galaxies that have begun to deplete their gas supply. Consequently, galaxies with the most extreme sSFRs are likely to have rising star formation histories or intense bursts of recent star formation, conditions that are seemingly commonplace at $z \simeq 2 - 2.7$ (e.g., Reddy et al., 2012) but rare in the local universe.

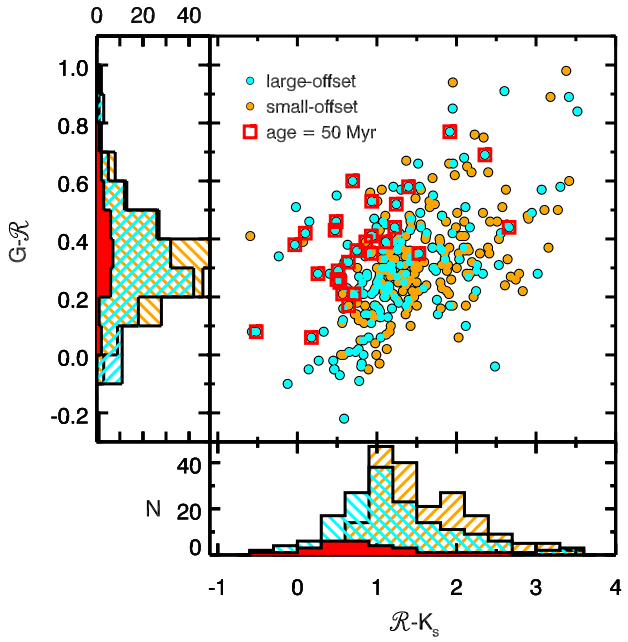

Figure 3.12: The distribution of $\mathcal{R} - K_s$ and $G - \mathcal{R}$ color for the two subsamples of KBSS galaxies, flanked by 1D histograms to highlight the differences. The large-offset galaxies (cyan) have generally bluer colors than their small-offset counterparts (orange), with fewer small-offset galaxies exhibiting blue optical-NIR colors ($\mathcal{R} - K_s \leq 1$). Galaxies with an imposed minimum age of 50 Myr (which are identified by red squares and are among the quartile of galaxies most offset from the $z \sim 0$ locus) have the bluest $\mathcal{R} - K_s$ colors, which suggests that the maturity of the stellar population is inversely correlated with the degree of offset from SDSS galaxies in the N2-BPT diagram.

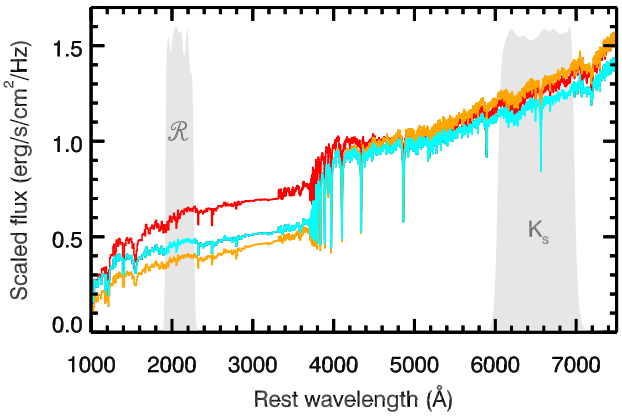

Figure 3.13: Typical SEDs for subsamples of KBSS-MOSFIRE galaxies (small-offset galaxies in orange, large-offset galaxies in cyan, and minimum-age galaxies in red), showing how differences in global spectral shape correlate with the degree of offset in the N2-BPT plane.

3.4.3 SED Shapes

The KBSS-MOSFIRE subsamples also exhibit significant differences in the characteristic shape of their SEDs, with a larger fraction ($\sim$ 40%) of large-offset galaxies appearing blue in the rest-optical ($(\mathcal{R} - K_s)_{\rm AB} \leq 1$) than small-offset galaxies ($\sim$ 19%). Figure 3.12 presents the distributions of both $\mathcal{R} - K_s$ and $G - \mathcal{R}$ color for the two subsamples; despite a statistically significant difference in $\mathcal{R} - K_s$, the $G - \mathcal{R}$ distributions are nearly identical.

Because $\mathcal{R} - K_s$ color probes the depth of the Balmer and 4000Å breaks, it traces both age and stellar mass (e.g., Shapley et al., 2005), which is part of the motivation for the RK selection described in Section 3.2.1. The bluer colors of the large-offset galaxies are therefore consistent with their smaller overall M_* (Figure 3.10). Additionally, although age estimates from SED fitting are not very robust in an absolute sense, 15% of large-offset galaxies have SEDs that are best fit by a constant star formation history with an age of 50 Myr, compared to only 3% of small-offset galaxies; as discussed in Section 3.2.5, this age is a minimum imposed to avoid unrealistically young inferred ages. In total, 17/28 (61%) "minimum-age" galaxies (identified by red squares in Figure 3.11 and Figure 3.12) fall above even the large-offset N2-BPT locus (cyan curve in Figure 3.9) and are therefore among the quartile exhibiting the most dramatic offset with respect to SDSS galaxies.

Figure 3.13 shows the average SED model for small-offset (orange) and large-offset (cyan) galaxies alongside the SED model characteristic of minimum-age galaxies (red), illustrating both the similarities in shape in the rest-UV and the differences across the Balmer break and at rest-optical wavelengths. The SEDs have been constructed by averaging the reddened high-resolution best-fit stellar population synthesis models from Bruzual & Charlot (2003), after scaling each to match between 4500 – 4600Å; the continuum extinction for small- and large-offset galaxies is roughly similar, with $\langle E(B-V)\rangle_{\rm small} = 0.18$ and $\langle E(B-V)\rangle_{\rm large} = 0.16$. The templates shown in Figure 3.13 do not include nebular continuum emission, which will further diminish the stellar Balmer break.

The over-representation of minimum-age systems with blue $\mathcal{R} - K_s$ colors among the most offset galaxies suggests that selection techniques that rely on the presence of a significant Balmer break may not reliably identify such galaxies. Conversely, the fact that small- and large-offset KBSS-MOSFIRE galaxies show no obvious separation in their rest-UV colors—despite differences in their rest-optical colors and nebular emission line properties—suggests that the selection techniques described

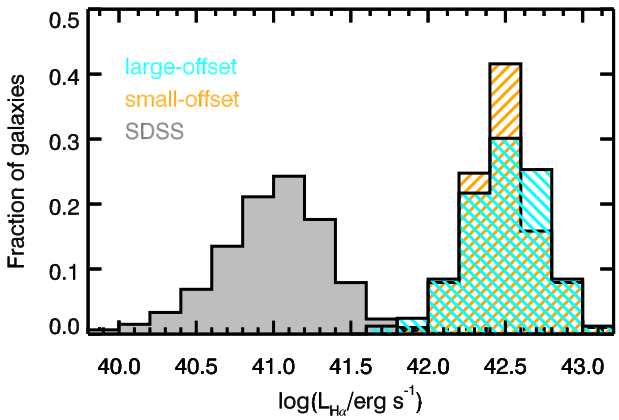

Figure 3.14: Histograms of Hα luminosity for SDSS galaxies and KBSS-MOSFIRE galaxies, divided on the basis of their N2-BPT offset into large- and small-offset subsamples. Although a Balmer luminosity selection in SDSS mimics the N2-BPT offset observed for $z \sim 2.3$ galaxies, the same behavior is not observed for KBSS-MOSFIRE galaxies, with the two samples having statistically consistent distributions.

in Section 3.2.1 are not strongly biased in favor of large-offset galaxies; in fact, the RK selection described in Section 3.2.1 will prefer galaxies with larger Balmer breaks, like the small-offset galaxies.

3.4.4 Balmer Emission Line Luminosity

Juneau et al. (2014) showed that a Balmer emission line luminosity selection applied to SDSS galaxies could result in a sample that exhibits an N2-BPT offset of similar magnitude to that reported for $z \sim 2$ galaxies. More recently, Cowie, Barger & Songaila (2016) suggested that Balmer line luminosity may be an efficient way of identifying low-redshift analogs of typical $z \sim 2$ galaxies. Given these results, the magnitude of the N2-BPT offset observed in KBSS-MOSFIRE could be artificially inflated if the sample were biased toward galaxies with the highest Balmer luminosities. It is interesting therefore to consider whether large-offset galaxies are overrepresented in KBSS-MOSFIRE due to such observational biases.

Figure 3.14 shows the distribution of observed Hα luminosity, uncorrected for dust extinction, for the small- and large-offset KBSS-MOSFIRE subsamples, as well as that for the full SDSS comparison sample. For SDSS galaxies, $L_{\mathrm{H}\alpha}$ has been corrected for aperture effects using the ratio of the total inferred SFR to the SFR measured from the fiber. All KBSS-MOSFIRE galaxies exhibit significantly higher line luminosities than typical $z \sim 0$ galaxies, but the $z \sim 2.3$ subsamples are statistically consistent with being drawn from the same parent population as

each other ($p = 0.55$ from a two-sample Kolmogorov-Smirnoff test). Moreover, when the full KBSS-MOSFIRE sample is divided by Hα luminosity, fits to the N2-BPT loci do not show a significant offset with respect to one another in either log([O III]/Hβ) or log([N II]/Hα). Together, these results suggest that observational biases do not significantly impact the degree of the observed N2-BPT offset and that Hα luminosity is not strongly correlated with the location of $z \sim 2.3$ galaxies in the N2-BPT plane. In fact, the observing strategy outlined in Section 3.2.1 mitigates this kind of incompleteness, as observations of individual galaxies are repeated until the strongest lines (including Hα) are significantly detected.

3.4.5 Electron Density

Finally, we consider differences between the large- and small-offset samples in terms of the electron density (n_e) in their H II regions. Sanders et al. (2016) offered a thorough discussion of electron density estimates for $z \sim 2$ star-forming galaxies using observations from the MOSDEF survey, noting that electron densities inferred from both the [O II]$\lambda\lambda$3727, 3729 and [S II]$\lambda\lambda$6718, 6732 doublets are an order of magnitude higher for $z \sim 2$ galaxies in their sample relative to a comparison sample from SDSS. At the same time, a number of studies have demonstrated that galaxies with higher electron densities ($n_e \sim 10^2$ cm^{-3}) exhibit higher log([N II]/Hα) and log([O III]/Hβ) than typical SDSS galaxies (e.g. Brinchmann, Pettini & Charlot, 2008; Liu et al., 2008; Yuan, Kewley & Sanders, 2010), often associated with higher inferred ionization parameters and differences in ISM pressure (Lehnert et al., 2009; Kewley et al., 2013). One may therefore expect large-offset KBSS-MOSFIRE galaxies to exhibit higher electron densities than small-offset galaxies.

To estimate n_e for the KBSS-MOSFIRE subsamples, we rely on inferences from spectral stacks, in order to consistently account for individual galaxies with lower S/N observations of the density-sensitive [O II] doublet. Galaxies from the small- and large-offset subsamples were corrected for slit losses then averaged separately, masking regions contaminated by OH emission lines. The spectral region near the [O II] doublet is shown in Figure 3.15, where the J band stacks have been scaled by the peak flux in the [O II]λ3729 line for ease of comparison.

For the small-offset composite, $I(3729)/I(3727) = 1.13 \pm 0.03$, and for the large-offset composite, $I(3729)/I(3727) = 1.14 \pm 0.04$. Using the diagnostic relation

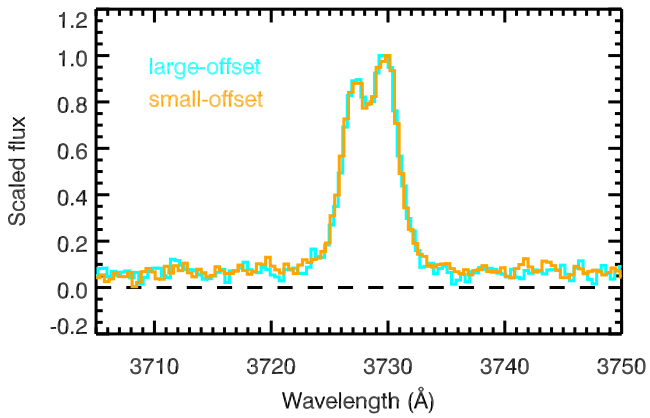

Figure 3.15: The [O II]$\lambda\lambda$3727, 3729 doublet, commonly used to infer n_e in the emitting gas, as observed in stacks of small- and large-offset KBSS-MOSFIRE galaxies. That the n_e estimates for both composites are consistent with one another (values for each subsample are listed in the text) suggests that electron density—and, by extension, ISM pressure—do not play an important role in determining the location of $z \sim 2.3$ galaxies in the N2-BPT plane.

from Sanders et al. (2016), which assumes $T_e = 10^4$ K, these values correspond to

$$n_{e,\mathrm{small}} = 281^{+43}_{-39}\ \mathrm{cm}^{-3}$$
$$n_{e,\mathrm{large}} = 267^{+48}_{-43}\ \mathrm{cm}^{-3}.$$

These values are consistent with one another within measurement uncertainties and also with the median value reported by Sanders et al. (2016) for MOSDEF galaxies using the [O II] diagnostic ($n_{e,\mathrm{MOSDEF}} = 225\ \mathrm{cm}^{-3}$).

The similarity between the electron density estimates for the two KBSS-MOSFIRE subsamples suggests that n_e is not strongly correlated with the physical process(es) that determine the position of $z \sim 2.3$ galaxies in the N2-BPT diagram, in contrast to observations of galaxies in the local universe.

3.5 Nitrogen-to-Oxygen Abundance Ratios

Nitrogen is formed as part of the CNO cycle in intermediate mass and massive stars, both as a primary and secondary element. Primary nitrogen production is regulated by the C, N, and O created within stars formed out of relatively metal-poor gas, whereas secondary production is seeded by the C, N, and O initially present in stars (as the result of prior enrichment of the ISM). This double nature is reflected by the well-documented behavior of the N/O abundance ratio as a function of O/H for samples of galaxies and H II regions (e.g., Diaz & Tosi, 1986; van Zee, Salzer

& Haynes, 1998), where N/O remains at a constant value ($\log(\mathrm{N/O}) \approx -1.5$) for low values of 12+log(O/H) ($\lesssim 8.0$), but rapidly increases with increasing oxygen abundance at higher values of O/H.

The precise relationship between N/O and O/H is a matter of some debate in the literature, depending sensitively on the choice of sample and method of measurement, making it difficult to place the N/O reported for individual sources or small samples in context. At $z \sim 0$, many studies rely on measurements from the spectra of individual compact galaxies or local H II regions (e.g., Pérez-Montero & Contini, 2009; Pilyugin, Grebel & Mattsson, 2012) or from composite spectra of relatively metal-poor galaxies (Andrews & Martini, 2013), but the typical value of N/O at a given measured value of O/H can vary by up to 0.5 dex. As we discussed in S14, the differences between such studies may be dominated by differences in the method used to measure O/H. It has been argued separately that scatter in the N/O-O/H relation is due instead to the effects of pristine gas inflow (e.g., Köppen & Hensler, 2005), which could lower O/H while leaving N/O largely unaffected, particularly if much of the nitrogen is formed in intermediate mass stars that take longer to return their nucleosynthetic products to the ISM.

In Section 3.4.1, we briefly addressed the idea that the N2-BPT offset observed for $z \sim 2.3$ galaxies could be due primarily to an enhancement in N/O relative to typical local galaxies with the same gas-phase oxygen abundance (as proposed by, e.g., Masters et al., 2014; Shapley et al., 2015; Cowie, Barger & Songaila, 2016; Sanders et al., 2016; Masters, Faisst & Capak, 2016). If found to be present in high-redshift galaxies, such systematic deviations in N/O would have serious implications for calibrations linking nebular emission line ratios that include nitrogen lines (e.g., [N II]λ6585) to oxygen abundance. Strong-line abundance calibrations rely on the implicit assumption that N/O varies similarly with O/H for both the calibration sample and the objects of interest, and many photoionization models likewise impose a prior on the value of N/O expected at a given O/H.

From an astrophysical perspective, it is also a concern that there is presently no consensus regarding the physical process(es) that might result in enhanced N/O for the majority of high-redshift galaxies. Although Masters et al. (2014) favored the existence of a large population of Wolf-Rayet stars as one possible explanation, the lifetimes of such stars are short, meaning that the effect would be limited to systems with extremely young ages (as discussed by Shapley et al., 2015). More recently, Masters, Faisst & Capak, 2016 have suggested that the existence of a

redshift-invariant or slowly-evolving N/O-M_* relation, when combined with the strong evolution toward lower O/H at fixed M_* observed at $z > 1$ (e.g., Erb et al., 2006a; Wuyts et al., 2014; Steidel et al., 2014; Sanders et al., 2015), might more plausibly explain a systematic increase in N/O at fixed O/H for high-redshift galaxies.

The Masters, Faisst & Capak (2016) study relied on a detailed analysis of $\sim 100,000$ star-forming galaxies from SDSS-DR12 and compared the behavior of $z \sim 0$ galaxies with the results from stacked spectra from the FMOS-COSMOS survey at $z \sim 1.6$ reported by Kashino et al. (2017). However, to fairly evaluate the likelihood of the proposed explanations, observations of a statistical sample of individual $z \sim 2$ galaxies are necessary. In this section, we present the first efforts to explicitly examine N/O for such a sample, using observations of the $z \sim 2.3$ KBSS-MOSFIRE sample to investigate the behavior of N/O as a function of other measured galaxy properties.

3.5.1 Strong-line Abundance Calibration using N2O2

For ionized gas, the most reliable measurements of O/H and N/H—and thus N/O—are derived from the measurement of electron temperature (T_e), which is often described as the "direct" method. Unfortunately, these measurements are extremely challenging even for galaxies in the local universe, as the auroral emission lines necessary for measuring T_e of both singly- and doubly-ionized species are relatively weak compared to their nebular counterparts and become more difficult to measure for objects with increasing gas-phase abundance. The situation is even worse for distant objects, including star-forming galaxies at high redshift.

The most practical alternative is to rely on strong-line indices known to exhibit tight correlations with intrinsic O/H and N/O. For oxygen abundance, two of the most widely-used indices are N2 and O3N2 (Table 3.3). For N/O, N2O2 and N2S2 (also defined in Table 3.3) are the most common choices. One of the most serious outstanding challenges to using strong-line calibrations for these indices is knowing whether or not they are reliable for sources that differ from those used to establish the original calibration between emission line ratio and metallicity. The existence of the strong N2-BPT offset cautions against the application of locally-calibrated relations for N2 and O3N2 at high redshift, as they will inevitably return inconsistent estimates of 12+log(O/H) with respect to one another for objects that are offset from the $z \sim 0$ locus. Studies of local objects have also shown that a factor of $\sim 2-3$ enhancement in N/O at fixed O/H (measured using the direct method) is not recovered when both

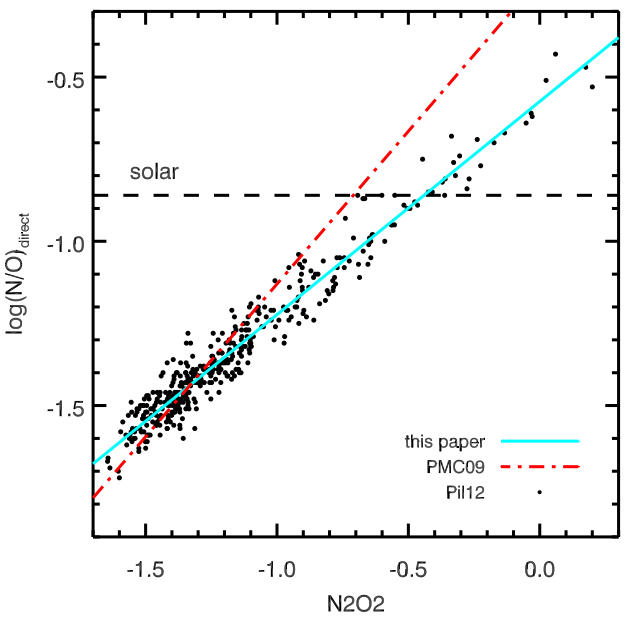

Figure 3.16: The observed N2O2 index and T_e-based N/O measurements for the extragalactic H II regions from Pilyugin, Grebel & Mattsson (2012). The best-fit linear relation is shown in cyan. The relation from Pérez-Montero & Contini (2009) is shown by the dashed red line for comparison.

N/O and O/H are estimated using strong-line methods, because O/H is overestimated for such objects (Pilyugin, Vílchez & Thuan, 2010). Furthermore, as we previously discussed in S14, photoionization models suggest that many of the strong-line ratios are more strongly correlated with the details of the ionizing radiation field than gas-phase oxygen abundance, particularly for high-excitation nebulae.

In contrast, the calibration for N/O using N2O2 relies primarily on the assumption that, due to the similarity in the ionization potentials for O and N, the relative ionization correction factors (ICFs) are also similar and, thus, $\log(\mathrm{N/O}) \simeq \log(\mathrm{N^+/O^+})$. This makes N2O2 considerably less sensitive to changes in the ionization parameter and/or the shape of the ionizing radiation than O3N2 or N2.

We employ a new calibration for N/O derived using a sample of extragalactic H II regions compiled by Pilyugin, Grebel & Mattsson (2012, hereafter Pil12). The 414 sources described therein have direct method measurements of both nitrogen and oxygen abundance as well as measurements of [O II]$\lambda\lambda$3727,3729, Hβ, [O III]$\lambda\lambda$4960,5008, [N II]$\lambda\lambda$6549, 6585, Hα, and [S II]$\lambda\lambda$6718,6732. In most cases, the electron temperature was measured directly for only one ion (and thus only one temperature zone); since the authors adopt a two-zone model, the temper-

ature in the second zone is determined using the relations from Campbell, Terlevich & Melnick (1986) and Garnett (1992).

Figure 3.16 shows the N2O2 and N/O measurements for the Pil12 sample and the corresponding calibration used in this chapter (in cyan). For reference, the calibration from Pérez-Montero & Contini (2009, PMC09) is shown in red, highlighting the differences that can arise from the choice of calibration sample, particularly when both individual H II regions and entire galaxies are considered, as is the case with Pérez-Montero & Contini (2009). For the new calibration, we have fit to the entire range in N/O, since the spread in observed N2O2 is nearly identical for KBSS-MOSFIRE and the Pil12 sample. The resulting relation is

$$\log(\mathrm{N/O}) = 0.65 \times \mathrm{N2O2} - 0.57, \tag{3.5}$$

with an accompanying RMS scatter about the best-fit relation of $\sigma_{\mathrm{RMS}} = 0.05$ dex. Adopting the PMC09 calibration instead of Equation 3.5 would imply values of log(N/O) larger by up to ~ 0.3 dex.

The use of N2S2 as an alternative to N2O2 presents many practical advantages, as it requires observations in only one NIR band, and thus needs fewer observations, no cross-band calibration, and is much less sensitive to relative extinction due to dust. However, the mapping of N2S2 to N/O relies on the expectation that S/O remains constant and, therefore, that sulfur may be used as a proxy for oxygen. Because the ionization potentials of O (13.62 eV) and S (10.4 eV) differ significantly, though, [S II]-emitting gas may not be entirely spatially coincident with the region where the [O II] emission originates and could lie well outside of the H-ionizing region. Thus, despite the advantages of requiring observations in only one NIR window and no extinction correction, we rely exclusively on the N2O2 index in this chapter.

3.5.2 Correlation with Galaxy Properties

We infer N/O for 151 galaxies in the $z \sim 2.3$ KBSS-MOSFIRE sample using Equation 3.5. Galaxies were included in the sample if they had a $\geq 3\sigma$ detection of the combined [O II]$\lambda\lambda 3726, 3729$ doublet and Hβ, a $\geq 5\sigma$ detection of Hα, and a robust measurement of the Balmer decrement (as described in Section 3.2.5); objects with $< 2\sigma$ detections of [N II] were assigned 2σ upper limits.

Figure 3.17 shows the N/O-M_* relation for $z \sim 2.3$ KBSS-MOSFIRE galaxies compared with $z \sim 0$ SDSS galaxies. As for local galaxies, the KBSS-MOSFIRE sample exhibits a positive correlation between N/O and M_* (with Spearman correlation co-

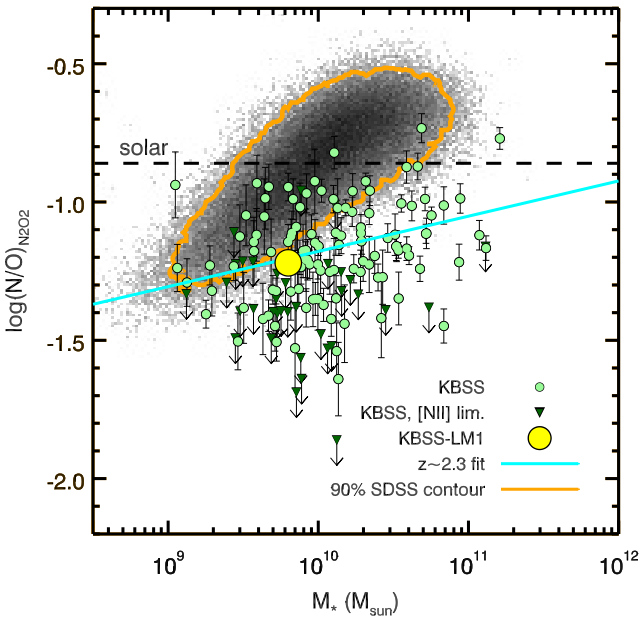

Figure 3.17: N/O measurements for KBSS-MOSFIRE galaxies (excluding AGN) as a function of M_*, plotted alongside the $z \sim 0$ SDSS sample (with the orange contour enclosing 90% of the local galaxies). KBSS-MOSFIRE galaxies exhibit significantly lower N/O at fixed M_* relative to SDSS galaxies, which show a strong positive correlation between both parameters. The more moderate positive correlation observed for the $z \sim 2.3$ KBSS-MOSFIRE galaxies can be approximated by a linear relation (Equation 3.6), which is shown in cyan. The location of the Steidel et al. (2016) composite spectrum in this parameter space is represented by the large yellow point, showing that it is fully consistent with the $z \sim 2.3$ relation.

efficient $\rho = 0.24$ and $p = 0.01$). The best-fit linear relation describing the sample is

$$\log(\mathrm{N/O}) = -1.18 + 0.13 \times [\log(M_*/M_\odot) - 10], \tag{3.6}$$

which has $\sigma_{\mathrm{RMS}} = 0.17$ dex.

The $z \sim 2.3$ locus is noticeably offset relative to typical SDSS galaxies (enclosed by the orange contour) at fixed M_*. At low stellar masses, the difference between the two samples is small, but becomes larger with increasing M_*, reaching an offset of ~ 0.5 dex toward lower log(N/O) at $M_* \sim 10^{11} M_\odot$; if the $z \sim 0$ locus is also approximated by a linear relation, the average separation between $10^9 - 10^{11} M_\odot$ is ~ 0.32 dex in log(N/O). This is a much larger shift than that observed (albeit using N2S2) for the $z \sim 1.6$ FMOS-COSMOS stacks from Kashino et al. (2017). Moreover, those authors reported the largest differences relative to SDSS at low stellar masses ($M_* \sim 10^{9.5}$), the opposite of the trend seen here for KBSS-MOSFIRE

galaxies.

Clearly, the N/O-M_* relation evolves significantly between $z \sim 0$ and $z \sim 2.3$. However, high-z galaxies would still exhibit higher values of N/O at fixed O/H relative to $z \sim 0$ galaxies if the N/O-M_* relation evolves more slowly than the O/H M_*-metallicity relation (MZR). Although it remains difficult to measure O/H independently of N for many individual high-z galaxies, there is some evidence to suggest that the redshift evolution of the N/O-M_* relation and the MZR are comparable: S14 showed that oxygen abundances measured using the O3N2 index exhibit the least bias and scatter relative to the direct method for individual KBSS-MOSFIRE galaxies with T_e-based measurements and that when O3N2 is used to estimate O/H, $z \sim 2.3$ galaxies exhibit a 0.32 dex offset toward lower 12+log(O/H) at fixed M_* relative to SDSS. Furthermore, in S16, we reported a direct, T_e-based O/H abundance for a stack of KBSS galaxies and N/O independently inferred using both photoionization modeling and the strong-line calibration from Equation 3.5. These measurements show that the KBSS stack, which is representative of the full KBSS-MOSFIRE sample discussed here (c.f. the yellow point in Figure 3.17), is consistent with the N/O-O/H relation observed for the sample of H II regions from Pil12 (see Figure 16 of Steidel et al. 2016).

Taken together, these results suggest that the N/O-O/H relation is redshift-invariant. Confirming the universality of the N/O-O/H relation must await independent measurements of N/O and O/H for a large sample, and we discuss the possibility of obtaining such measurements for KBSS-MOSFIRE galaxies in Section 3.6.3. For now, we consider the behavior of N2O2 as a function of O3N2 for the KBSS-MOSFIRE galaxies (green) and the Pil12 sample (orange) in Figure 3.18. The best-fit linear relation describing the KBSS-MOSFIRE locus (cyan line) also traces the behavior of the Pil12 sample in terms of observed line ratios. Indeed, there is virtually no separation in either N2O2 or O3N2 between the samples, except for O3N2 > 2.5, where there are no KBSS-MOSFIRE galaxies. The reason for the lack of $z \sim 2.3$ galaxies in that region of parameter space is easily understood as a selection effect in the KBSS-MOSFIRE sample; high values of O3N2 correspond to low values of 12+log(O/H), and at such low metallicities, the strength of both oxygen and nitrogen emission lines begins to decline below practical detection limits.

We can establish a calibration mapping O/H to O3N2 for the Pil12 sample as we did

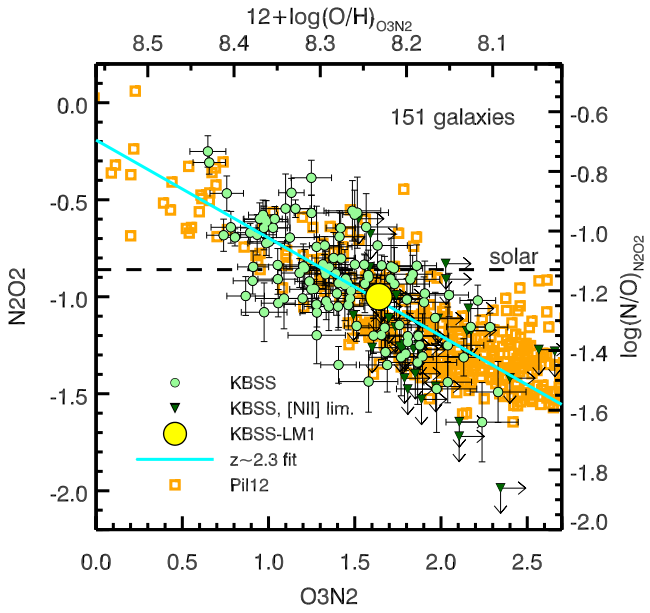

Figure 3.18: N2O2 as a function of O3N2 for both $z \sim 2.3$ KBSS-MOSFIRE galaxies (green points, with 2σ upper limits in [N II] shown as dark green triangles) and extragalactic H II regions from Pil12 (orange squares). Both samples behave similarly and exhibit comparable degrees of scatter in this observed line ratio space. For comparison, the location of the composite spectrum of KBSS galaxies from S16, which shows no enhancement in N/O at fixed O/H relative to the Pil12 sample, is shown by the large yellow point. The best-fit linear relation for the full KBSS-MOSFIRE sample is shown in cyan; if interpreted as a N/O-O/H relation using log(N/O) derived from N2O2 (see right axis, Equation 3.5) and estimates of 12+log(O/H) from O3N2 (see top axis, Equation 3.7), this relation is fully consistent with the T_e-based N/O-O/H relation observed for the Pilyugin, Grebel & Mattsson (2012) sample.

for N/O and N2O2 in Section 3.5.1, resulting in the following linear relation[4]:

$$12 + \log(\mathrm{O/H}) = 8.56 - 0.20 \times \mathrm{O3N2};\ \sigma_{\mathrm{RMS}} = 0.08\ \mathrm{dex}. \tag{3.7}$$

Such a calibration will disguise a potential enhancement in N/O at fixed O/H, but if we assume that the N/O-O/H relation is indeed the same at all redshifts, the linear fit to the $z \sim 2.3$ KBSS-MOSFIRE locus in Figure 3.18 can then be described as

$$\log(\mathrm{N/O}) = -1.29 + 1.64 \times [(12 + \log(\mathrm{O/H})_{\mathrm{O3N2}}) - 8.2]. \tag{3.8}$$

This relation is slightly steeper but statistically consistent with a linear relation determined using only T_e-based measurements of N/O and O/H for the Pil12 sample. Because of this similarity, we use Equation 3.8 in Section 3.6.2, but note that

[4]We include only H II regions with 12+log(O/H)> 8.0 in determining the calibration.

the results presented there would be the same if we used a fit to the T_e-based measurements from Pil12.

3.5.3 N/O at Fixed Ionization and Excitation

We have already discussed the likelihood that SDSS galaxies occupying the same region of parameter space in the O32-R23 plane possess similar ionization and excitation properties as neighboring KBSS-MOSFIRE galaxies. This claim was based on the nature of the O32 and R23 indices: sources with maximal R23 are expected to have similar (moderate) oxygen abundances, so that O32 independently tracks ionization parameter, with higher values of O32 corresponding to higher degrees of ionization. The value of R23 at fixed U and O/H is likewise set by the shape of the ionizing spectrum, as we reasoned in Section 3.3.4 and show explicitly in Section 3.6 below.

However, given the obvious discrepancy between typical values of O32 and R23 for $z \sim 0$ and $z \sim 2.3$ galaxies (Figure 3.8) and the similarly dramatic separation in [O III]/Hβ (Figures 3.7 and 3.11) it is necessary to test whether differences in the shape and normalization of the ionizing spectrum account for all (or most) of the differences observed between the nebular properties of $z \sim 0$ and $z \sim 2.3$ galaxies, including the N2-BPT offset. To make a fair comparison between KBSS-MOSFIRE and SDSS, it is imperative to select a sample of SDSS galaxies in a way that matches the high-redshift distribution of these quantities. Because high-ionization, high-excitation galaxies are common at $z \sim 2.3$ yet relatively rare at $z \sim 0$, imposing a simple cut in both line ratios will sample only the tail of local galaxies and lead to significantly different distributions in O32 and R23 (and, therefore, ionization and excitation) for the low- and high-redshift samples.

Instead, we identify a SDSS "twin" for each of the 150 $z \sim 2.3$ KBSS-MOSFIRE galaxies with $> 5\sigma$ measurements of Hα, $> 3\sigma$ measurements of Hβ, [O III], and [O II], and $> 5\sigma$ significance measurements of the Balmer decrement (see Figure 3.19). For each KBSS-MOSFIRE galaxy (identified by green points with error bars), the closest SDSS galaxy in the O32-R23 diagram within 2σ measurement uncertainties is selected (represented by open orange squares). To ensure a unique comparison sample, the next closest SDSS galaxy is chosen in cases where a single SDSS galaxy is the closest "twin" for more than one KBSS-MOSFIRE galaxy. There are 17 KBSS-MOSFIRE galaxies without a SDSS galaxy within 2σ measurement uncertainties, due largely to the absence of SDSS galaxies with very

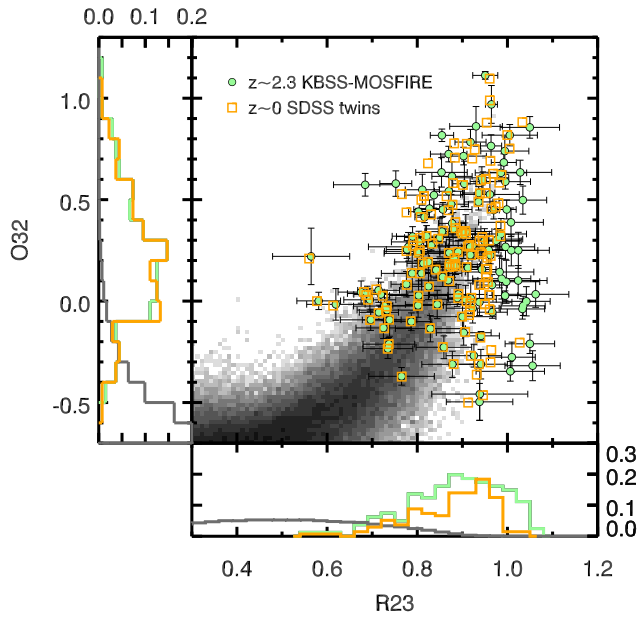

Figure 3.19: The distribution of $z \sim 2.3$ KBSS-MOSFIRE galaxies and $z \sim 0$ SDSS twins in the O32-R23 plane. Each SDSS comparison galaxy (shown by the open orange squares) is chosen based on proximity to a KBSS-MOSFIRE galaxy (represented by the green points with error bars) in both parameters. This selection technique ensures that the distributions of R23 and O32 are statistically consistent for the two samples, as can be seen in the flanking histograms of both line ratios. For comparison, the distributions of O32 and R23 for the full SDSS sample are shown in grey.

large values of R23 at fixed O32; KBSS-MOSFIRE galaxies without SDSS twins were removed from the sample described here and excluded from the analysis in this section. The resulting distributions of O32 and R23 for the KBSS-MOSFIRE sample and the SDSS twins are shown in the flanking panels of Figure 3.19 and are statistically consistent with being drawn from the same parent distributions of these quantities. For comparison, the distributions of O32 and R23 for the full SDSS sample are shown in grey.

We consider the nebular and chemical properties of KBSS-MOSFIRE galaxies and the SDSS twins in Figure 3.20. The upper panels show the distribution of both samples in the N2-BPT and S2-BPT planes. Even for galaxies matched in O32 and R23, there is a large offset between the KBSS-MOSFIRE galaxies and their SDSS twins in the N2-BPT plane whereas there is no apparent separation in the S2-BPT plane, consistent with the behavior observed for the full samples of $z \sim 0$ and $z \sim 2.3$ galaxies presented in Section 3.3.1. Notably, the SDSS twins fall largely above the ridge-line of the full SDSS sample (red dashed line), such that the offset

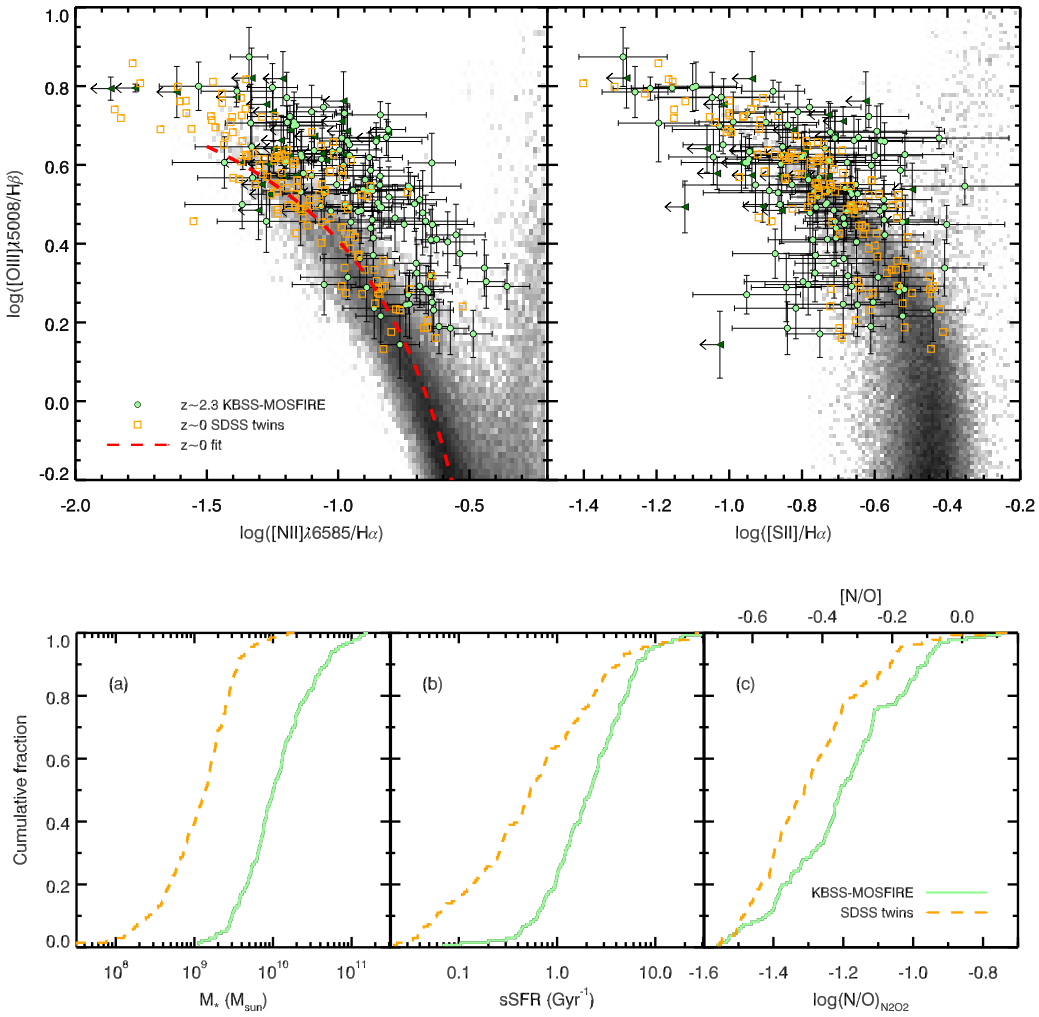

Figure 3.20: A comparison of the nebular, physical, and chemical properties of $z \sim 2.3$ KBSS-MOSFIRE galaxies and their $z \sim 0$ SDSS twins matched in O32 and R23, as described in the text and shown in Figure 3.19. The upper row illustrates the differences in the N2- and S2-BPT diagrams, which are consistent with the results described in Section 3.3.1: in the N2-BPT plane, there is a strong offset observed between KBSS-MOSFIRE galaxies (green points with error bars, 2σ upper limits in [N II] drawn as dark green triangles) and the SDSS twins (open orange squares), with no significant separation in the S2-BPT plane (here the dark green triangles represent 2σ upper limits in [S II]). The bottom panels show differences in the physical properties of KBSS-MOSFIRE galaxies (solid green curves) and SDSS twins (dashed orange curves); from left to right: M_*, sSFR, and N/O determined from N2O2 (Equation 3.5). The ~ 0.10 dex higher values of log(N/O) observed in KBSS-MOSFIRE galaxies fall short of accounting for the horizontal displacement of $z \sim 2.3$ galaxies relative to SDSS in Figure 3.5 and are much lower than would be expected if the N/O-M_* relation were redshift-invariant.

between the orange squares and green points in the upper left panel of Figure 3.20 is almost entirely horizontal. The median horizontal offset of KBSS-MOSFIRE galaxies relative to their SDSS twins is equivalent to a 0.18 dex shift toward higher log([N II]/Hα), whereas the median $\Delta \log$ [O III]/Hβ $<$ 0.01 dex. This result is largely in agreement with Shapley et al. (2015), who reported an offset in the N2-BPT plane for low-mass ($M_* < 10^{10.11} M_\odot$) MOSDEF galaxies relative to SDSS galaxies matched in O32 and R23. Contrary to the MOSDEF results, however, both low- and high-mass KBSS-MOSFIRE galaxies are offset with respect to their SDSS twins, with median offsets in log([N II]/Hα) of 0.17 dex for $M_* < 10^{10.11} M_\odot$ and 0.19 dex for $M_* \geq 10^{10.11} M_\odot$.

KBSS-MOSFIRE galaxies are also $\sim$ 10 times more massive than SDSS galaxies matched in O32 and R23 (see panel (a) in the bottom row of Figure 3.20). While SDSS twins have higher sSFRs than the majority of SDSS galaxies (Figure 3.10), panel (b) shows that KBSS-MOSFIRE galaxies still have 0.58 dex higher sSFRs on average. Panel (c) in the bottom row of Figure 3.20 presents the distribution of N/O for both samples, showing that the $z \sim 2.3$ KBSS-MOSFIRE galaxies have higher N/O than their SDSS twins ($p = 1.1 \times 10^{-5}$ that they are drawn from the same distribution), with a median difference of 0.10 dex. These results are broadly consistent with the trends observed for all SDSS galaxies (Masters, Faisst & Capak, 2016); however, based on the difference in M_* observed between KBSS-MOSFIRE galaxies and the SDSS twins, the $z \sim 2.3$ galaxies should exhibit N/O close to solar (log(N/O)= -0.86, [N/O]= 0.0) if the N/O-M_* is redshift-invariant as the authors propose. Additionally, the observed difference in N/O falls markedly short of the 0.37 dex enhancement in N/O that would be required to explain the separation between the $z \sim 0$ and $z \sim 2.3$ N2-BPT loci in Figure 3.5 if the difference were entirely in log([N II]/Hα).

Although we do not report O/H measurements for individual KBSS-MOSFIRE galaxies here, we note that 0.10 dex higher N/O would correspond to only a 0.06 dex difference in O/H if $z \sim 2.3$ galaxies follow the N/O-O/H relation in Equation 3.8. As we will show in the next section, such a difference in O/H would not be readily apparent in S2-BPT and O32-R23 diagnostic diagrams, as those nebular line ratios are relatively insensitive to changes in O/H in high-excitation nebulae, particularly at moderate gas-phase metallicities.

3.6 Photoionization Models

Many inferences regarding the properties of high-z H II regions can be made by comparing observations of their nebular spectra with carefully-chosen samples of analogous objects, usually low-redshift sources whose characteristic physical conditions are more easily established due to the availability of higher S/N data and/or large sample sizes; we employed this technique in Section 3.5 to infer the distribution of N/O in the $z \sim 2.3$ KBSS-MOSFIRE sample. Still, there remain limitations to using calibrations based on comparison samples that may differ systematically in some key parameter—including the inability to construct suitable calibrations for characteristics that depend on several correlated variables, like ionization parameter (U).

Photoionization models predict the nebular spectrum produced by a specific combination of input ionizing spectrum, ionization parameter, chemical abundance pattern, and physical conditions in the emitting gas (e.g., electron density). A common shortcoming of photoionization model comparisons, however, is that the large number of free parameters makes it difficult to infer physically meaningful results from the agreement between a given model grid and the data. Ideally, some of the inputs to the photoionization model can be fixed using independent measurements, leaving only a small number of parameters to vary; in this case, the agreement between a specific set of photoionization models and the data constrains the allowed range of those parameters.

One of the strengths of conducting a survey of $z \sim 2-3$ galaxies is the ability to simultaneously obtain spectra in the rest-UV and rest-optical wavebands. Together, observations of both spectral windows provide probes of the massive stars and the surrounding gas that is being ionized and heated by radiation from the same stars. In S16, we described the results from a campaign of deep rest-UV spectroscopic follow-up of KBSS galaxies with MOSFIRE spectroscopy, specifically focusing on demonstrating the ability to account simultaneously for the observed stellar FUV spectrum and the UV-optical nebular spectrum using a set of physically-motivated photoionization models. The models used here represent a small subset of those described in that paper, where we discussed them in detail; for completeness, we briefly summarize the salient features.

We use Cloudy (v13.02, Ferland et al., 2013) to predict the nebular spectrum of the irradiated gas given an incident radiation field with a fixed spectral shape. The models assume a plane-parallel geometry where the intensity of the radiation field

is parametrized by the ionization parameter $U(\equiv n_\gamma/n_H)$. For ionized gas, n_H is roughly equivalent to the electron density (n_e) and is assumed to be 300 cm^{-3} based on measurements of the density-sensitive [O II] and [S II] doublets from the rest-optical composite spectrum of 30 KBSS-MOSFIRE galaxies (S16). This value is also consistent with the densities reported in S14 for a early sample of KBSS-MOSFIRE galaxies and with the stacked spectra of the small-offset and large-offset subsamples presented in Section 3.4.5. Because n_H is fixed, U may be interpreted as the normalization of the ionizing radiation field.

Our earlier work (S14) relied on similar models, but eschewed a specific choice of spectral synthesis model, instead using blackbodies to parametrize the shape of the input ionizing spectrum. Here, we employ stellar population models from the most recent version of "Binary Population and Spectral Synthesis" (BPASSv2; Stanway, Eldridge & Becker, 2016, Eldridge et al. in prep.). The most important aspect of BPASSv2 relative to other stellar population synthesis codes is the inclusion of interacting massive binary stars, which has the net effect of boosting the overall ionizing flux and producing a significantly harder ionizing spectrum for models with continuous star formation histories, particularly at low stellar metallicity. We adopt the default IMF for BPASSv2, with an IMF slope of -2.35 over the range $0.5 \leq \mathrm{M}_*/\mathrm{M}_\odot \leq 300$.[5]

The metallicity of the gas ($Z_{\rm neb}$) is allowed to vary independently and is not required to match the stellar metallicity (Z_*) of the input population synthesis model, where Z_* is the fraction of metals by mass and $Z_\odot = 0.0142$ (Asplund et al., 2009). Although the metallicity of the gas near young, massive stars should closely trace the stellar metallicity, decoupling $Z_{\rm neb}$ from Z_* reflects the understanding that high-redshift galaxies may not exhibit solar abundance ratios, particularly between elements synthesized by stars of different masses (as is the case for O/Fe). We specifically highlight O/Fe because the cooling of hot, ionized gas (and thus many features in the nebular spectrum) is regulated largely by the abundance of O, whereas the shape of the ionizing spectrum is instead determined by the abundance of Fe, which accounts for much of the total opacity in stellar atmospheres and, in turn, governs mass loss rates. As we discussed in S16, this means that since Z_* effectively traces the Fe abundance in stars, a combination of low Z_* and moderate $Z_{\rm neb}$ in high-z galaxies does not require the stellar O/H to differ from O/H in the gas—because O/Fe may be enhanced relative to $(\mathrm{O/Fe})_\odot$ by up to a factor of ~ 5.5 (Nomoto et al., 2006).

[5] We discuss the effects of restricting the BPASSv2 IMF to a maximum of 100 $\mathrm{M}_\odot$ in S16, which do not impact any of the results presented here.

In the case of the composite spectrum of 30 KBSS galaxies from S16, we demonstrated that the UV-optical nebular properties were consistent with $Z_{\rm neb}/Z_{\odot} = 0.5$, while the shape of the rest-UV spectrum was globally best fit by population synthesis models with $Z_*/Z_{\odot} \approx 0.1$. Together, these results imply O/Fe$\simeq 4-5$(O/Fe)$_{\odot}$, consistent with the Nomoto et al. (2006) yields for low-$Z_{\star}$ core-collapse SNe. Since we are now interested in comparing the model predictions with observations of the *ensemble* of $z \sim 2.3$ KBSS-MOSFIRE galaxies, we consider two separate models with $Z_*/Z_{\odot} = 0.07$ (BPASSv2-z001) and $Z_*/Z_{\odot} = 0.28$ (BPASSv2-z004) in order to account for a range in the Fe content of massive stars in high-z galaxies. As we will show in Section 3.6.2.1, significantly higher values of $Z_*(\gtrsim 0.5\ Z_{\odot})$ can be ruled out for the majority of $z \sim 2.3$ galaxies by comparison with their nebular spectra alone.

3.6.1 Ionization Parameter

When the input ionizing spectrum is fixed, the photoionization model predictions are restricted to a surface in line ratio space, with each point on the surface defined by a unique combination of U and $Z_{\rm neb}$. The space occupied by the photoionization model surface can be compared with line ratio measurements from the full $z \sim 2.3$ KBSS-MOSFIRE sample to understand the allowed range in both parameters and also how they are correlated with one another across the galaxy population.

Inconveniently, the photoionization model surface "folds over" in many 2D line ratio spaces, requiring constraints from many individual line ratios to break the degeneracy between combinations of U and $Z_{\rm neb}$ that result in at least some of the same observed line ratios. Fortunately, O32 and Ne3O2 (see Table 3.3) are substantially more sensitive to changes in U than changes in $Z_{\rm neb}$, and we use measurements of these line ratios to independently constrain the likely values of ionization parameter.

Figure 3.21 illustrates how the predicted value of the O32 index varies as a function of $\log(U)$, assuming $Z_*/Z_{\odot} = 0.07$ (red points) or $Z_*/Z_{\odot} = 0.28$ (blue squares); the nebular oxygen abundance is assumed to be $Z_{\rm neb}/Z_{\odot} = 0.5$ in both cases. The 68% highest density interval (HDI, the narrowest range that includes 68% of the sample) for O32 in the KBSS-MOSFIRE sample is indicated by the vertical extent of the shaded region, with a median O32 = 0.24. Using the predictions from the models, the corresponding ranges in $\log(U)$ needed to reproduce the observed range in O32

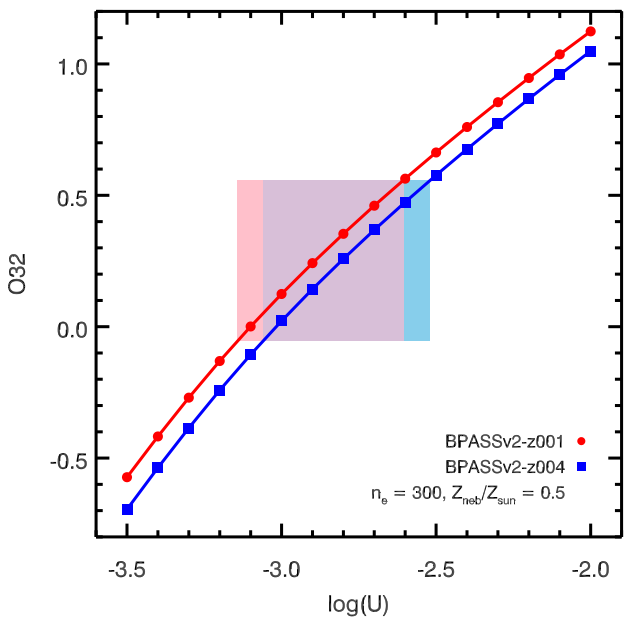

Figure 3.21: O32 as a function of $\log(U)$ for BPASSv2 models with $Z_*/Z_\odot = 0.07$ (red points) and $Z_*/Z_\odot = 0.28$ (blue squares). The metallicity of the gas is assumed to be $Z_{\rm neb}/Z_\odot = 0.5$ in both cases. The vertical extent of the shaded region denotes the 68% HDI in O32 for the KBSS-MOSFIRE sample; the width of the shaded region shows the corresponding intervals in $\log(U)$ for the models (values provided in the text).

are

$$\log(U)_{\rm z001,68\%} = [-3.14, -2.61]$$
$$\log(U)_{\rm z004,68\%} = [-3.06, -2.52].$$

Note that the inferences made assuming $Z_*/Z_\odot = 0.28$ are shifted toward higher $\log(U)$ by ~ 0.08 dex. This trend extends to higher Z_* as well, such that higher values of U are required to produce the same value of O32 as Z_* increases. This trend—highlighting the trade-off between ionization parameter and hardness of the ionizing radiation field—is discussed more generally by Sanders et al. (2016).

The Ne3O2 index serves as a powerful cross-check on ionization parameters determined using O32, as it is significantly less affected by differential extinction due to dust, does not require any cross-band calibration, and provides an additional constraint on the shape of incident ionizing radiation. As with O32, however, the translation from Ne3O2 to U depends sensitively on the details of the photoionization model, particularly on the choice of ionizing spectrum. In brief, because the ionization potential of Ne^+ (40.96 eV) is larger than that of O^+ (35.12 eV), which is

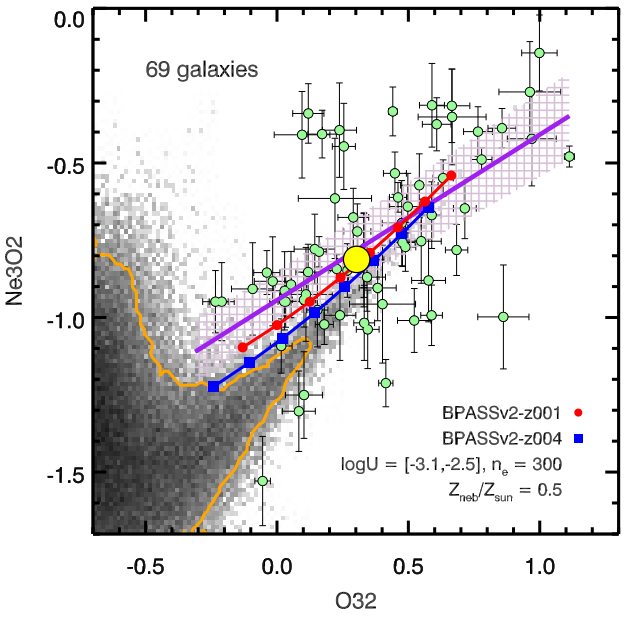

Figure 3.22: The distribution of Ne3O2 vs. O32 for KBSS-MOSFIRE (green points with error bars) and SDSS (in greyscale) galaxies, with the orange contour enclosing 90% of the $z \sim 0$ sample; the location of the S16 stack is identified by the large yellow point. The solid purple line shows the fit to the KBSS-MOSFIRE sample, with the 1σ errors in the fit parameters represented by the hatched purple region. The nebular line ratio predictions for BPASSv2 models with $Z_*/Z_\odot = 0.07$ (red points) and $Z_*/Z_\odot = 0.28$ (blue squares) are shown for $Z_{\rm neb}/Z_\odot = 0.5$ and $\log(U) = [-3.1, -2.5]$, with the lowest values of $\log(U)$ corresponding to low O32 and Ne3O2.

the probe of high-ionization emission in the O32 index, the Ne3O2 index responds to changes in the shape of the EUV stellar spectrum at higher energies than O32. Thus, Ne3O2 is predicted to increase relative to O32 with increasing hardness of the ionizing spectrum.

Figure 3.22 shows both indices, Ne3O2 and O32, for $z \sim 0$ SDSS galaxies (in greyscale, 90% contour in orange) and the $z \sim 2.3$ KBSS-MOSFIRE sample selected as outlined in Table 3.1 (green points with error bars). The linear fit to the data, accounting for errors in both line indices, is shown by the solid purple line, with the 1σ uncertainty in the fit parameters represented by the hatched purple region.

For comparison, the nebular line ratio predictions from the $Z_*/Z_\odot = 0.07$ (red points) and $Z_*/Z_\odot = 0.28$ (blue squares) models shown in Figure 3.21 are also included in Figure 3.22, with $\log(U)$ limited to the range identified using O32 measurements alone. The $Z_*/Z_\odot = 0.07$ model predicts slightly higher values of Ne3O2 at fixed O32 than the $Z_*/Z_\odot = 0.28$ model, but both agree well with the

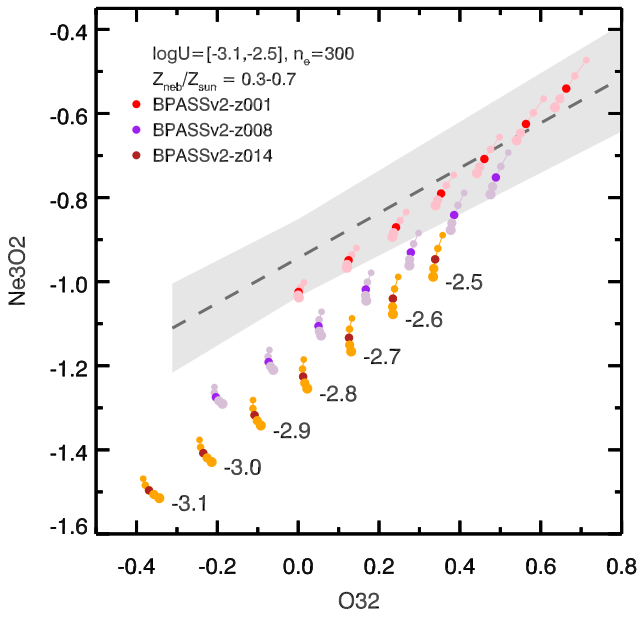

Figure 3.23: Photoionization model predictions for Ne3O2 and O32 for a range of Z_* and $Z_{\rm neb}$. Each color reflects a different stellar metallicity: $Z_*/Z_\odot = 0.07$ (red), $Z_*/Z_\odot = 0.56$ (purple), and $Z_*/Z_\odot = 1.0$ (orange). The gas-phase metallicity sequence at each $\log(U)$ is represented by the connected points, with the increasing size of the symbol reflecting an increase in $Z_{\rm neb}/Z_\odot$ from 0.3 – 0.7; the grid points with $Z_{\rm neb}/Z_\odot = 0.5$ are identified by darker-colored symbols. For comparison, the locus of $z \sim 2.3$ galaxies is represented by the grey line and shaded region, which is identical to the hatched region in Figure 3.22.

ridgeline of $z \sim 2.3$ galaxies.

Although we have thus far assumed a single gas-phase metallicity, the inferred range of $\log(U)$ is not particularly sensitive to $Z_{\rm neb}$. Figure 3.23 shows the effect of changing $Z_{\rm neb}$ on the predicted line indices for three separate stellar metallicities: $Z_*/Z_\odot = 0.07$ (red), $Z_*/Z_\odot = 0.56$ (purple), or $Z_*/Z_\odot = 1.0$ (orange). For each value of $\log(U)$, the sequence in $Z_{\rm neb}$ is illustrated by a series of connected points, with increasing symbol size reflecting larger values of $Z_{\rm neb}$; grid points with $Z_{\rm neb}/Z_\odot = 0.5$ are identified by darker-colored symbols. Regardless of Z_*, the differences in the predicted line indices are substantially larger for changes in U than for changes in $Z_{\rm neb}$, particularly at low ionization parameters. At high U, the effect of decreasing $Z_{\rm neb}$ is more pronounced, but degenerate with changes in U.

However, the choice of Z_* does have a noticeable impact on the model predictions for Ne3O2 and O32. Figure 3.23 shows that increasing $Z_*/Z_\odot$ from 0.07 to 0.56 decreases the predicted value of Ne3O2 by ~ 0.4 dex at every value of $\log(U)$; the

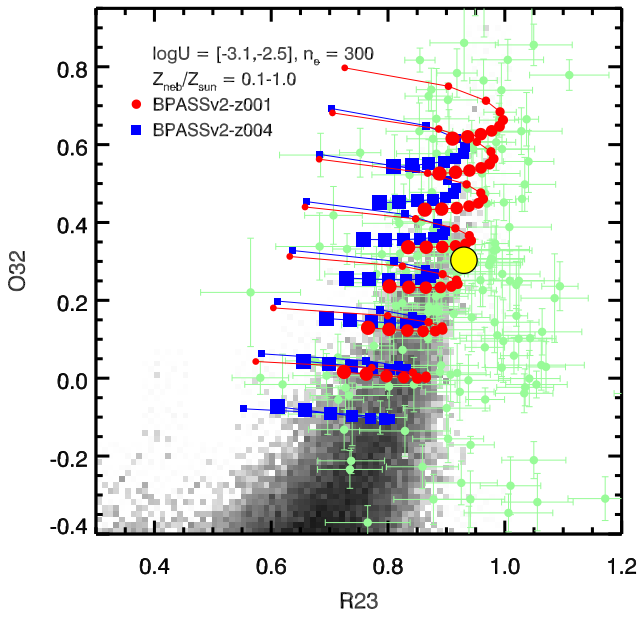

Figure 3.24: A comparison between the photoionization model predictions for O32 and R23 and the location of $z \sim 2.3$ KBSS-MOSFIRE and $z \sim 0$ SDSS galaxies, with the location of the S16 stack identified by the large yellow point. A range of ionization parameters and gas-phase metallicities are considered, with the $Z_{\rm neb}$ sequence at each value of U connected by a line; the increasing size of the points reflects increasing $Z_{\rm neb}/Z_{\odot}$ from $0.1 - 1.0$. At fixed O32 and $Z_{\rm neb}$, the only way to increase the maximum value of R23 is to change the shape of the ionizing radiation, here parametrized by Z_{*}.

corresponding decrease in O32 is ~ 0.3 dex. Although it is possible to reproduce separate values of Ne3O2 or O32 with other combinations of Z_{*}, $Z_{\rm neb}$, and U, the model assuming $Z_{*}/Z_{\odot} = 0.07$ (red points) is best able to match the *combinations* of Ne3O2 and O32 observed in KBSS-MOSFIRE galaxies, represented by grey shaded region in Figure 3.23.

3.6.2 Comparison with Other Nebular Diagnostics

3.6.2.1 The O32-R23 Diagram

Figure 3.24 compares predictions for O32 and R23 from the photoionization models with observations of the KBSS-MOSFIRE and SDSS galaxies; the sample of KBSS-MOSFIRE galaxies is identical to the sample introduced in Section 3.3.4 and is represented by the green points with error bars. The allowed range in ionization parameter has been set by the results from the previous section and matches the values shown in Figure 3.22, but we now consider a range in gas-phase metallicity: $Z_{\rm neb}/Z_{\odot} = 0.1 - 1.0$.

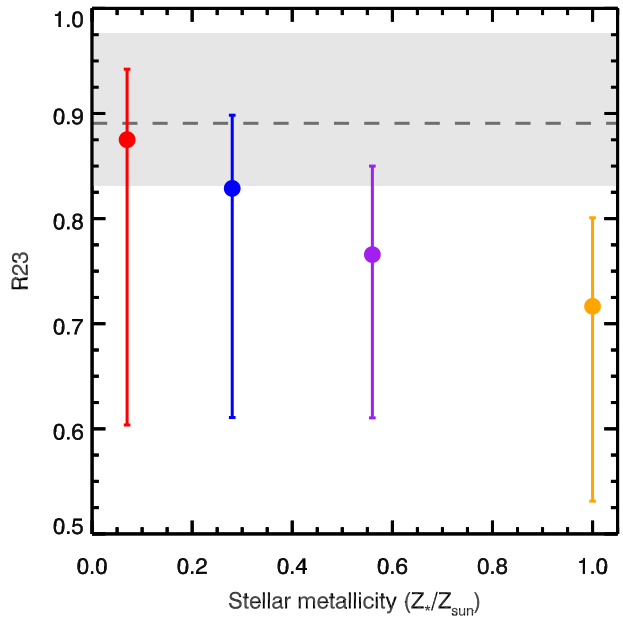

Figure 3.25: The range of predicted R23 indices from BPASSv2 models with a range of Z_* compared to the interquartile range observed in $z \sim 2.3$ KBSS-MOSFIRE galaxies with O32 ratios within 2σ of the median, O32= $0.10 - 0.40$ (horizontal grey band, with the median R23 shown by the dashed line). The colored points represent the median R23 value predicted for all combinations of $Z_{\rm neb}$ and U at fixed Z_* for grid points with equivalent O32 ratios; the error bars show the minimum and maximum R23 predicted for the same grid points. Notably, models assuming $Z_*/Z_\odot \gtrsim 0.5$ predict peak values of R23 that are too low to match the majority of $z \sim 2.3$ galaxies, suggesting high Z_* is not typical in this sample.

The metallicity sequences for both models are shown by the series of connected points in Figure 3.24 and are nearly horizontal, with changes in $Z_{\rm neb}$ (reflected by the symbol size) resulting in motion to the left or right (in R23). Independently, changes in U move points vertically (in O32). Thus, extending models with fixed Z_* to higher values of U and/or lower $Z_{\rm neb}$ cannot produce the high values of R23 at high O32 that are characteristic of both the $z \sim 2.3$ KBSS-MOSFIRE sample and the extreme tail of SDSS. Models with the lowest gas-phase metallicities (the smallest red points and blue squares) are among the most discrepant with respect to the data; only grid points with $Z_{\rm neb}/Z_\odot \approx 0.3 - 0.9$ can match the line indices observed for the majority of galaxies, but the location of individual objects will be equally (or more) sensitive to changes in U and Z_*.

These results present severe challenges to using the combination of O32 and R23 as a metallicity determination method for objects in this region of parameter space. Because of the narrow high-ionization sequence at both $z \sim 0$ and $z \sim 2.3$ and

the double-valued nature of the R23 index, galaxies with different $Z_{\rm neb}$ but similar values of U may exhibit similar values of R23 at fixed O32 and thus be spatially coincident in Figure 3.24. As discussed in Section 3.5.3, the difference in N/O between SDSS twins (identified in the O32-R23 diagram) and KBSS-MOSFIRE galaxies imply that $z \sim 2.3$ galaxies have 0.06 dex higher 12+log(O/H) than $z \sim 0$ galaxies with the same ionizing spectral shape. Thus, if a KBSS-MOSFIRE galaxy has $Z_{\rm neb}/Z_{\odot} = 0.5$, its $z \sim 0$ twin should have $Z_{\rm neb}/Z_{\odot} = 0.44$, and the insensitivity of O32 and R23 to $Z_{\rm neb}$ (particularly near the turnaround in R23) will render them virtually indistinguishable in Figure 3.24. An apparent metallicity sequence in the O32-R23 plane could arise due to an anti-correlation between ionization parameter and O/H, as proposed by Sanders et al. (2016), but the relationship between those parameters may not be redshift-invariant and is sensitive to the shape of the incident ionizing radiation. Because the shape of the EUV radiation is regulated largely by the Fe content of massive stars (Z_*), it can differ greatly for galaxies with the same O/H ($Z_{\rm neb}$) if they have different values of O/Fe.

The O32-R23 diagram serves as a much more sensitive diagnostic of the shape and normalization of the ionizing radiation fields in H II regions and galaxies, in part because it is so insensitive to $Z_{\rm neb}$ for objects with high values of both indices. Figure 3.25 compares the interquartile range of R23 for $z \sim 2.3$ KBSS-MOSFIRE galaxies with O32 ratios within 2σ of the median, O32 = 0.10 − 0.40 (represented by the horizontal grey band) with R23 predictions from photoionization models spanning $Z_*/Z_{\odot} = 0.07 - 1.0$. The colored points represent the median R23 value for all model grid points ($Z_{\rm neb}/Z_{\odot} = 0.1 - 1.0$ and log(U)=[-3.5,-2.0]) with O32 = 0.10 – 0.40 at each Z_*; the error bars show the minimum and maximum R23 values. For $Z_*/Z_{\odot} \gtrsim 0.5$, even the maximum value of R23 in this range of O32 is too low to match the majority of $z \sim 2.3$ galaxies, which suggests that the ionizing spectra in most KBSS-MOSFIRE galaxies are consistent with low-Z_* BPASSv2 models. It is important to note that the actual constraint imposed by the comparison of the data with the model predictions is on the *shape* of the stellar population EUV SED in the 1-4 Ryd range, and the implementation of low-metallicity binaries in BPASSv2 is simply one realistic way of achieving that spectral shape.

3.6.2.2 The BPT Diagrams

We now return to the BPT diagrams, using constraints from the rest-UV spectral analysis presented in S16 combined with the analysis presented earlier in this chapter.

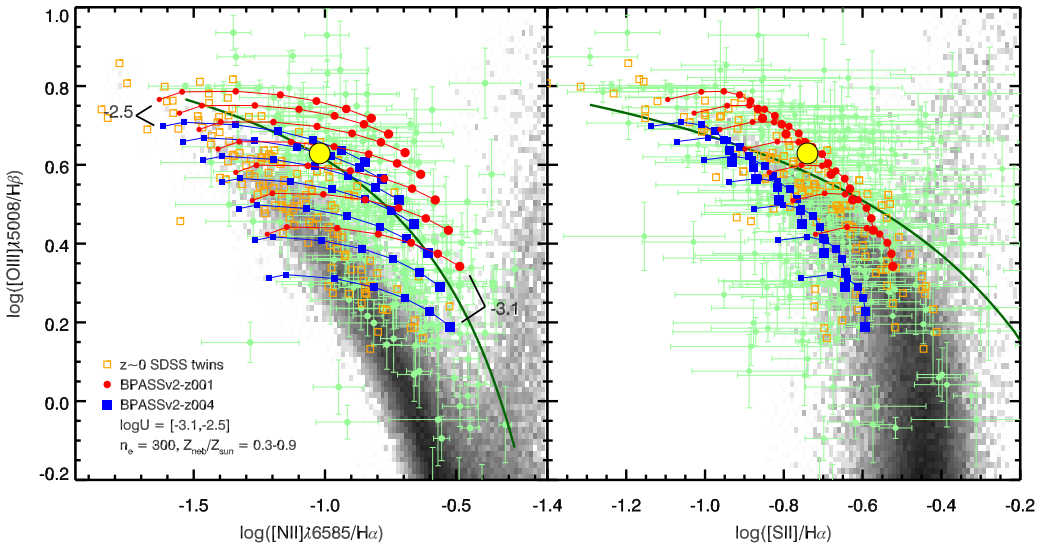

Figure 3.26: A comparison between the range of nebular emission-line ratios predicted by the photoionization models described in the text and those observed in $z \sim 2.3$ KBSS-MOSFIRE galaxies (represented by the green points with error bars, with the ridge-line shown by the solid green curve and the location of the S16 stack identified by the large yellow point). The model predictions are presented in the same manner as Figure 3.24, with the $Z_{\rm neb}$ sequence at each value of U connected by a line; the size of the point reflects the level of gas-phase enrichment, which has been restricted to $Z_{\rm neb}/Z_{\odot} = 0.3 - 0.9$. The model predictions agree well with the full range of observations in both panels and support the results from Section 3.5.3: $z \sim 2.3$ galaxies and SDSS twins (matched in O32 and R23, Figure 3.19) are consistent with having the same relatively hard ionizing spectra, but KBSS-MOSFIRE galaxies require higher $Z_{\rm neb}$ to explain their nebular line ratios. The most offset $z \sim 2.3$ galaxies in the N2-BPT are consistent with values of $Z_{\rm neb}$ that make them indistinguishable from the SDSS locus in the S2-BPT plane, meaning that an offset in [N II]/Hα with no corresponding offset in [S II]/Hα is a prediction of the models.

To summarize, we adopt

$$\begin{aligned} n_e &= 300\mathrm{cm}^{-3} \\ \log(U) &= [-3.1, -2.5] \\ Z_*/Z_{\odot} &= 0.07 - 0.28 \\ Z_{\rm neb}/Z_{\odot} &= 0.3 - 0.9 \end{aligned}$$

as the optimal combination of parameters capable of reproducing the nebular properties of $z \sim 2.3$ KBSS-MOSFIRE galaxies.

The relation between N/O and O/H in the photoionization models is motivated by the agreement between the Pil12 sample and KBSS-MOSFIRE galaxies shown in Section 3.5.2. As shown in Figure 3.18, however, the apparent N/O-O/H relation for

the KBSS-MOSFIRE sample would imply super-solar values of N/O at solar O/H, a feature common to many empirical relations for N/O-O/H. Evidence suggests that this discrepancy arises from the tendency of direct T_e-based abundances to underestimate the true nebular O/H, in part because the highest temperature regions of nebulae will contribute more to the total flux in collisionally-excited lines than cooler regions. We discussed this topic in detail in Section 8.1.2 of S16, but we refer to one specific example from the literature here: Esteban et al. (2014) found that direct-method oxygen abundances based on measurements of collisionally-excited lines from the H II regions of nearby galaxies were 0.24 ± 0.02 dex lower than the oxygen abundances determined from measurements of nebular recombination lines. Recombination line methods are less temperature-sensitive and often agree better with stellar abundances when gas-phase and stellar abundances are measured for the same systems. Motivated by this significant difference, we introduce a +0.23 dex shift in 12+log(O/H) to Equation 3.8, which forces the relation to produce $(\mathrm{N/O})_\odot$ at $(\mathrm{O/H})_\odot$. The final relation used in the photoionization models is then

$$\begin{aligned} \log(\mathrm{N/O}) &= 1.68 \times \log(Z_{\mathrm{neb}}/Z_\odot) - 0.86; Z_{\mathrm{neb}}/Z_\odot > 0.4 \\ \log(\mathrm{N/O}) &= -1.5; Z_{\mathrm{neb}}/Z_\odot \leq 0.4 \end{aligned} \tag{3.9}$$

Figure 3.26 shows the range of line ratios observed in KBSS-MOSFIRE galaxies in the N2-BPT and S2-BPT planes compared with predictions from the photoionization models. The best-fit loci for the KBSS-MOSFIRE sample are represented by the dark green curves, with the KBSS-MOSFIRE sample plotted as light green points with error bars. The models are illustrated in a similar manner to Figure 3.24, where the metallicity sequence at each value of $\log(U)$ is connected by a line and the size of the point reflects the value of $Z_{\mathrm{neb}}/Z_\odot$.

Foremost, we note that the model predictions agree well with the range of KBSS-MOSFIRE observations in both diagrams, as they have for the other combinations of line indices presented in this section. The ability of the BPASSv2 models to self-consistently reproduce many of the commonly-used strong rest-optical emission line ratios across the $z \sim 2.3$ sample is encouraging. It also confirms that the radiation fields in the majority of high-redshift galaxies must at least resemble the spectra produced by stellar populations with $Z_*/Z_\odot = 0.07 - 0.28$ that include massive binaries.

In contrast to the locus of $z \sim 2.3$ galaxies in the O32-R23 diagram, which provides only weak constraints on the likely range of Z_{neb}, the left panel of Figure 3.26 shows

that moderately-high $Z_{\rm neb}$ is required to reproduce the high values of log([N II]/Hα) observed at fixed log([O III]/Hβ). However, despite exhibiting an offset relative to the locus of SDSS galaxies in the N2-BPT diagram, the photoionization model predictions for $Z_{\rm neb}/Z_{\odot} \approx 0.6 - 0.9$ overlay the high-[O III]/Hβ tail of SDSS in the S2-BPT diagram—as observed for the KBSS-MOSFIRE galaxies. The strong offset of $z \sim 2.3$ galaxies relative to SDSS in the N2-BPT diagram with little to no corresponding offset in the S2-BPT plane is actually a prediction of photoionization models that include hard ionizing radiation from relatively low-Z_* stars and relatively high-$Z_{\rm neb}$ gas.

We may also use observations of SDSS galaxies in the N2- and S2-BPT diagrams to constrain the combination of photoionization model parameters that would successfully describe $z \sim 0$ galaxies with the highest ratios of [O III]/Hβ, such as the SDSS twins introduced in Section 3.5.3. The location of the SDSS twins in the O32-R23 diagram (Figure 3.19) provides a compelling argument that the shape and normalization of their ionizing radiation fields (and, thus, Z_* and U) are similar to those observed in KBSS-MOSFIRE galaxies and that predictions from the same BPASSv2 models are appropriate. In the left panel of Figure 3.26, the SDSS twins are identified by open orange squares and most closely matched by models with $Z_{\rm neb}/Z_{\odot} \approx 0.3 - 0.5$; the same model parameters also provide good agreement with observations of the SDSS twins in the S2-BPT diagram. That SDSS galaxies matched in O32 and R23 appear to have lower $Z_{\rm neb}$ than KBSS-MOSFIRE galaxies (which require $Z_{\rm neb}/Z_{\odot}$ up to ≈ 0.9) is compatible with the significantly different distributions of N/O for the SDSS twins and KBSS-MOSFIRE galaxies (panel (c) in Figure 3.20) and the N/O-O/H relation from Equation 3.8.

3.6.3 O/H Constraints from Photoionization Models

The discussion in this section explicitly highlights the separate impact that gas chemistry (including both N/O and O/H) and the shape and normalization of the ionizing radiation (parametrized by Z_* and U) have on the nebular spectra of H II regions. Although the combination of O32 and R23 is relatively insensitive to gas-phase oxygen abundance in high-excitation nebulae (like those in $z \sim 2.3$ galaxies and in the SDSS twins), the O32-R23 diagram is especially powerful for constraining the shape of the EUV radiation field because the line indices trace ionization parameter and excitation almost independently.

Conversely, the location of galaxies in the N2-BPT diagram depends sensitively

on almost every parameter of interest—gas-phase oxygen abundance, N/O, ionization parameter, and the shape of the ionizing radiation field—making it difficult to disentangle the contributions of each. Fortunately, surveys like KBSS-MOSFIRE allow us to leverage observations of $z \sim 2.3$ galaxies in a multidimensional nebular line ratio space to constrain these quantities *for individual galaxies* through comparisons with photoionization models, without requiring a recalibration of the relationship between O/H and the strong-line indices. The utility of this method has already been demonstrated for composite spectra by S16, where the oxygen abundance could be measured directly using T_e, and independent constraints on the most likely input ionizing radiation field were available from comparisons between stellar population models and the rest-UV spectrum. The agreement between the BPASSv2 models and the extent of the full KBSS-MOSFIRE sample in multiple parameter spaces suggests that similar families of models may be applied directly to observations of individual galaxies, which is the focus of the work presented in Chapter 4. Self-consistent measurements of O/H, N/O, and U for a large sample of $z \sim 2.3$ galaxies will allow us to directly investigate the N/O-O/H relation and the correlation between metallicity and U.

3.7 What Causes the $z \sim 2.3$ BPT Offset?

Returning to the question that has been the subject of much scientific debate over the last few years—"What causes the BPT offset?"—we are now better equipped to determine which mechanism or combination of mechanisms is likely to be primarily responsible, both for explaining the differences between samples of galaxies at $z \sim 0$ and $z \sim 2.3$ and between galaxies at the same redshift. We have already shown that the offset of $z \sim 2.3$ galaxies with respect to SDSS in the N2 BPT plane cannot be attributed only to selection and observational biases (Figures 3.12 and 3.14). In this section, we use the combined analysis of the rest-optical spectra of KBSS-MOSFIRE galaxies to evaluate the relative importance of some of the most frequently proposed physical explanations.

Ubiquitous AGN activity. Like $z \sim 2$ galaxies from other surveys, the KBSS-MOSFIRE sample occupies a region in the N2-BPT diagram that is populated almost exclusively by AGN or composite galaxies at $z \sim 0$ (Figure 3.5). Additionally, the values of log([O III]/Hβ) observed in the $z \sim 2.3$ galaxies are ~ 0.8 dex higher than local star-forming galaxies at fixed M_* and, thus, similar to local AGN (Figure 3.7). However, there is no evidence of AGN activity in the rest-UV spectra of most KBSS-MOSFIRE galaxies with complementary LRIS observations (see S14); very

high values of log([N II]/Hα) or large rest-optical line widths are also rare. In total, only 7/377 KBSS-MOSFIRE galaxies with measurements that place them on the N2-BPT diagram are identified as AGN or QSOs (Section 3.3.2). Although the supermassive black holes in these galaxies are almost certainly accreting gas, the resulting effect on the total nebular spectrum is sub-dominant with respect to ongoing star formation.

Higher electron density. In the local universe, n_e is correlated with the location of galaxies in the N2-BPT plane (Brinchmann, Pettini & Charlot, 2008; Liu et al., 2008; Yuan, Kewley & Sanders, 2010). Because the characteristic n_e observed in high-redshift galaxies is 10 times higher than galaxies at $z \sim 0$, with typical values of $\approx 200 - 300$ cm^{-3} at $z \sim 2.3$ (e.g., Steidel et al., 2014; Sanders et al., 2016), it is important to quantitatively assess whether this difference is sufficient to explain the observed N2-BPT offset. As shown in Figure 3.15, however, measurements of the density-sensitive [O II] doublets for small- and large-offset KBSS-MOSFIRE galaxies (Figure 3.9) are nearly identical. Given that the inferred electron densities for both subsamples are consistent within errors, we conclude that a difference in n_e cannot account for the still significant offset between the small- and large-offset N2-BPT loci and, thus, is unlikely to be the primary driver of the overall $z \sim 2.3$ offset.

Enhanced N/O at fixed O/H. Several authors have interpreted the strong offset of high-z galaxies in the N2-BPT plane (and lack of corresponding offset in the S2-BPT and O32-R23 diagrams) as evidence for larger N/O at fixed O/H (including Masters et al., 2014; Shapley et al., 2015; Cowie, Barger & Songaila, 2016; Sanders et al., 2016; Masters, Faisst & Capak, 2016), an explanation that naturally results in larger values of log([N II]/Hα) while leaving line ratios not including N unaffected. This enhancement, if it exists, should also be reflected in the correlation between N/O and other galaxy properties (such as M_*), particularly given the strong, but evolving correlation between O/H and M_* observed at all redshifts.

We showed in Figure 3.17 that, at fixed M_*, $z \sim 2.3$ KBSS-MOSFIRE galaxies exhibit values of log(N/O) that are lower by an average of ~ 0.32 dex relative to SDSS galaxies. Galaxies at $z \sim 2.3$ also have lower 12+log(O/H) than SDSS galaxies by a comparable amount (Steidel et al., 2014; Wuyts et al., 2014; Sanders et al., 2015), suggesting that there is a relatively constant N/O-O/H relation for all galaxies. Additional evidence in support of this interpretation comes from the comparison of the composite UV-optical nebular spectrum from S16 with a sample

of $z \sim 0$ H II regions from Pilyugin, Grebel & Mattsson (2012), with the $z \sim 2.3$ stack exhibiting N/O at fixed O/H consistent with the local relation.

KBSS-MOSFIRE galaxies do show 0.10 dex larger values of log(N/O) with respect to SDSS galaxies matched in O32 and R23 (as described in Section 3.5.3), consistent with the results reported by Shapley et al. (2015) for $z \sim 2$ MOSDEF galaxies, but we argue that samples matched in O32 and R23 are more likely to share ionizing radiation fields than gas-phase oxygen abundance. Assuming the N/O-O/H relation from Equation 3.8, this difference in N/O would accompany a 0.06 dex difference in 12+log(O/H), which would not be readily apparent from the locations of galaxies in the O32-R23 diagram (Figure 3.24). We note that, even if the higher N/O measurements represent an enhancement at fixed O/H, it can account for $< 55\%$ of the 0.37 dex horizontal displacement of the $z \sim 2.3$ locus with respect to the $z \sim 0$ locus in Figure 3.5. Thus, even if high-z galaxies were moderately N/O-enhanced, an additional mechanism (such as harder ionizing radiation fields) would still be required to explain the differences between $z \sim 2.3$ and $z \sim 0$.

Hard ionizing spectra of Fe-poor massive binaries. The analysis in Section 3.6 uses predictions from a subset of the photoionization models we considered in S16 to constrain the likely combination of U and $Z_{\rm neb}$ in the ensemble of KBSS-MOSFIRE observations. Adopting two BPASSv2 models with $Z_*/Z_\odot = 0.07$ and $Z_*/Z_\odot = 0.28$, we find that the line ratios observed in $z \sim 2.3$ galaxies are consistent with $\log(U) = [-3.1, -2.5]$ and $Z_{\rm neb}/Z_\odot \approx 0.3 - 0.9$. We are not able to place direct constraints on O/Fe in individual galaxies in the manner of S16, but we note that the upper range in $Z_{\rm neb}/Z_*$ obtained from comparisons with the full KBSS-MOSFIRE sample broadly agrees with the O/Fe reported for the composite spectra ($\simeq 4 - 5(\mathrm{O/Fe})_\odot$).

We argue, as we did in S14 and S16, that the primary cause of the differences observed between typical galaxies at high redshift and galaxies in the local universe is the degree of nebular excitation, with $z \sim 2.3$ galaxies exhibiting significantly higher values of [O III]/Hβ and R23 relative to the majority of $z \sim 0$ galaxies. These line ratios—especially the high values of R23 observed at high O32 in KBSS-MOSFIRE galaxies—can be explained by hard ionizing radiation fields, such as those produced by Fe-poor stellar populations that include massive binaries. Yet, when compared with SDSS galaxies with similar nebular excitation (like the SDSS twins from Section 3.5.3), KBSS-MOSFIRE galaxies are still substantially offset

to higher log([N II]/Hα) at fixed log([O III]/Hβ) due to larger values of N/O (and, likely, O/H). Thus, $z \sim 2.3$ galaxies must contain harder ionizing radiation fields *at fixed gas-phase N/O and O/H* to explain the N2-BPT offset relative to the locus of typical $z \sim 0$ galaxies.

3.7.1 Implications for Local Analogs

These results are a natural consequence of systematic differences in star formation history between high-redshift star-forming galaxies and galaxies occupying the low-redshift locus. As we reasoned in S16, the ISM in galaxies with roughly constant SFR and stellar population ages $\lesssim$ 1 Gyr will reflect enrichment primarily from core-collapse SNe, with the resulting super-solar O/Fe abundances responsible for harder ionizing spectra (from Fe-poor stars) at a given O/H compared to galaxies with lower O/Fe. If the characteristic star formation histories of galaxies were SFR increasing with time (as might be more common at high redshift; Reddy et al., 2012; Steidel et al., 2016), high values of O/Fe could easily be maintained for longer than 1 Gyr. This is possible because, to first order, the enrichment rate of O is proportional to the current SFR, whereas the rate of enrichment of Fe (which comes primarily from Type Ia SNe) is proportional to the SFR 1 Gyr earlier. Thus, given typical inferred ages of a few hundred Myr (Reddy et al., 2012), most $z \sim 2.3$ galaxies should be forming stars that are relatively α-enhanced (and O-enhanced), consistent with core-collapse SNe yields.

Specific star formation rate serves as a crude, but easily-measured probe of the overall star formation histories of galaxies. By definition, young stars make up a larger fraction of the stellar populations in galaxies with high sSFRs, and 1/sSFR is roughly equivalent to the age of the stellar population (assuming a constant SFR). Thus, galaxies with sSFR $>$ 1 Gyr^{-1} will have a substantial fraction of stars that formed from gas enriched almost entirely by Type II SNe. The median sSFR for the KBSS-MOSFIRE sample is 2.4 Gyr^{-1}, corresponding to a timescale of $\sim$ 400 Myr, substantially less than the 1 Gyr timescale for the onset of Type Ia SNe; moreover, as we showed in Section 3.4.2, nearly 60% of KBSS-MOSFIRE galaxies have sSFR $>$ 2 Gyr^{-1}, corresponding to timescales $<$ 500 Myr, with only $\sim$ 20% having sSFR $<$ 1 Gyr^{-1}. In contrast, only $\sim$ 1% of SDSS galaxies have sSFR $>$ 2 Gyr^{-1}, and such galaxies also have $\sim$ 10 times smaller M_* compared to high-sSFR KBSS-MOSFIRE galaxies. For the majority of SDSS galaxies, sSFR $\sim$ 0.1 Gyr^{-1}; at these low sSFRs, the youngest stars represent a small contribution to the overall M_*, and their O/Fe abundances will closely reflect the end state of the galaxy's chemical

evolution.

It is clear that sSFR can be used to identify galaxies whose nebular properties are similar in some ways to typical galaxies at $z \sim 2.3$. However, the KBSS-MOSFIRE galaxies that are *most* offset from the SDSS star-forming sequence in the N2-BPT diagram represent an interesting population without exact analogs in the local universe: galaxies at $z \sim 0$ with similar ionizing spectra are ~ 10 times less massive than typical $z \sim 2.3$ galaxies and have significantly lower N/O and O/H, but $z \sim 0$ galaxies with similar M_* or gas-phase metallicity will have substantially softer ionizing radiation fields. The absence of a suitable comparison sample—with both high levels of nebular excitation (high [O III]/Hβ and R23) *and* high gas-phase metallicity—limits the utility of $z \sim 0$ analogs for studying the conditions in $z \sim 2.3$ systems significantly offset in the N2-BPT plane. Specifically, it raises concerns about using extreme $z \sim 0$ galaxies (like the SDSS twins) to construct an empirical strong-line metallicity calibration intended to be used at $z \gtrsim 2$. Any study using calibrations based on nebular line ratios that are sensitive to both gas-phase chemistry and the shape and normalization of the ionizing radiation field must take care to understand the impact of differences between the calibration and test samples.

3.8 Summary

We have presented a detailed analysis of the rest-optical (3600 – 7000Å) spectra of ~ 380 $z \sim 2-3$ star-forming galaxies drawn from the MOSFIRE component of the Keck Baryonic Structure Survey. Combining multiwavelength photometric observations and SED fitting with robust measurements of many of the commonly-used strong nebular emission lines, we have shown that:

- KBSS-MOSFIRE galaxies at $z \sim 2.3$ exhibit a clear offset in the N2-BPT diagram relative to typical galaxies in the local universe, represented by SDSS (Figure 3.5). If one assumes the difference is along only one axis, the magnitude of this offset is $\Delta \log([\text{N II}]/\text{H}\alpha) = 0.37$ dex or $\Delta \log([\text{O III}]/\text{H}\beta) = 0.26$ dex.

- The same high-z galaxies have nebular properties consistent with the high-excitation tail of the $z \sim 0$ galaxy distribution in the S2-BPT (Figure 3.6) and O32-R23 (Figure 3.8) diagnostic diagrams.

- The offset of $z \sim 2.3$ galaxies relative to the $z \sim 0$ N2-BPT locus is inversely correlated with M_* and positively correlated with sSFR. Likewise, sSFR is

also strongly correlated with the degree of excitation (as probed by [O III]/Hβ and R23) for all galaxies (Figure 3.11).

- Many of the most offset $z \sim 2.3$ KBSS-MOSFIRE galaxies have blue optical-NIR colors ($\mathcal{R} - K_s \leq 1$), high sSFRs (~ 7 Gyr^{-1}), and are best-fit by young (50 Myr) stellar population ages, assuming constant or increasing star formation histories (Figures 3.11, 3.12, and 3.13).

- KBSS-MOSFIRE galaxies at $z \sim 2.3$ have 0.10 dex higher N/O than SDSS galaxies matched in O32 and R23 (panel (c) in Figure 3.20). If galaxies at all redshifts exhibit the same N/O-O/H relation (as we argue in Section 3.5.2), a 0.10 dex increase in log(N/O) corresponds to a 0.06 dex increase in 12+log(O/H). Such a small change in O/H would have only a minor effect on the observed locations of galaxies in the O32-R23 and S2-BPT diagrams.

- Observations of most $z \sim 2.3$ KBSS-MOSFIRE galaxies are consistent with photoionization models that use a binary population synthesis model (BPASSv2) with stellar metallicity $Z_*/Z_\odot = 0.07 - 0.28$ (Figure 3.25), gas-phase metallicity $Z_{\rm neb}/Z_\odot \approx 0.3 - 0.9$, and ionization parameter $\log(U) = [-3.1, -2.5]$ (Figure 3.26). These models reproduce the large observed shift with respect to local star-forming galaxies in the N2-BPT diagram, but result in no appreciable offset between the predicted line ratios for $z \sim 2.3$ galaxies and the local sequence in the S2-BPT plane; thus, this apparent discrepancy can be explained without needing to invoke elevated N/O at fixed O/H.

From these results, we conclude that the principal cause of the "BPT offset" is an increase in the hardness of the ionizing radiation at fixed N/O and O/H, consistent with the EUV spectra produced by Fe-poor stellar populations that include massive binaries.

Chapter 4

MEASURING THE PHYSICAL CONDITIONS IN HIGH-REDSHIFT GALAXIES: INSIGHTS FROM KBSS-MOSFIRE

4.1 Introduction

Advancing our understanding of galaxy assembly is one of the key goals of modern astrophysics. However, progress is often difficult, as galaxies form and evolve under the influence of a variety of competing baryonic processes, the effects of which are difficult to disentangle. Gaseous inflows supply the raw material for star formation and the growth of supermassive black holes. The resulting powerful stellar winds, supernova explosions, and feedback from active galactic nuclei (AGN) are all thought to contribute to galaxy-scale outflows, which are relatively uncommon in nearby galaxies, but known to be nearly ubiquitous in the early universe. The details of these processes and their relative importance throughout cosmic time leave imprints on nascent galaxies, resulting in the scaling relations and chemical abundance patterns observed across galaxy populations.

Efforts by several groups over the last few years have extended our understanding of galaxies' physical conditions to the peak of galaxy assembly ($z \simeq 1-3$; e.g., Madau & Dickinson, 2014), using new spectroscopic observations of large numbers of typical galaxies to study their gas and stars in detail (e.g., Masters et al., 2014; Sanders et al., 2015; Shapley et al., 2015; Steidel et al., 2014; Steidel et al., 2016; Strom et al., 2017). Many of these studies have focused on measurements from galaxies' rest-optical (3600 – 7000Å) nebular spectra, which can now be observed for large samples of individual objects, owing to sensitive multi-object near-infrared (NIR) spectrographs like the Multi-Object Spectrometer For InfraRed Exploration (MOSFIRE, McLean et al., 2012; Steidel et al., 2014) and the *K*-band Multi-Object Spectrograph (KMOS, Sharples et al., 2013). However, despite the headway made in characterizing galaxies during this crucial epoch, significant tension remains regarding how best to infer high-z galaxies' physical conditions from easily-observable quantities, such as the strong emission lines of hydrogen, oxygen, and nitrogen present in their H II region spectra.

It is tempting to simply build on the large body of work that has decrypted the spectra

of galaxies in the local universe (e.g., Kauffmann et al., 2003; Brinchmann, Pettini & Charlot, 2008; Masters, Faisst & Capak, 2016), often relying on the sample of $z \sim 0$ star-forming galaxies from the Sloan Digital Sky Survey (SDSS, York et al., 2000) to explore trends in physical conditions and construct diagnostics for quantities like oxygen abundance (O/H) that can then be applied to observations of other, high-redshift samples. Yet it is well-established that star-forming galaxies at $z \simeq 1-3$ differ from typical $z \sim 0$ star-forming galaxies in a number of key ways that make directly transferring this paradigm to the study of high-z galaxies problematic: $z \sim 2-3$ galaxies have 10 times higher star-formation rates (e.g., Erb et al., 2006b) and gas masses (Tacconi et al., 2013) at fixed stellar mass, significantly smaller physical sizes (Law et al., 2012), and are relatively young (characteristic ages of a few hundred Myr) with rising star-formation histories (Reddy et al., 2012). Recent work from surveys like the Keck Baryonic Structure Survey (KBSS, Steidel et al., 2014; Steidel et al., 2016; Strom et al., 2017), the MOSFIRE Deep Evolution Field survey (MOSDEF, Kriek et al., 2015; Shapley et al., 2015), and the KMOS^{3D} survey (Wisnioski et al., 2015) have also revealed a number of important differences in terms of the nebular spectra of high-z galaxies, with perhaps the most well-known being the offset in the log([O III]λ5008/Hβ) vs. log([N II]λ6585/Hα) plane (the so-called N2-BPT diagram, after Baldwin, Phillips & Terlevich 1981, but popularized by Veilleux & Osterbrock 1987). This offset has been attributed to a variety of astrophysical differences, including enhanced N/O at fixed O/H in high-z galaxies (Masters et al., 2014; Shapley et al., 2015; Sanders et al., 2016), higher ionization parameters (e.g. Kewley et al., 2015; Bian et al., 2016; Kashino et al., 2017), and harder ionizing radiation fields (Steidel et al., 2014; Steidel et al., 2016; Strom et al., 2017), although the true origin of the offset is likely due to a combination of effects for individual galaxies.

Since strong-line diagnostics operate by relying on the underlying correlations between the quantity of interest (often gas-phase O/H) and other astrophysical conditions (e.g., ionization state, ionizing photon distribution) that also influence the observables, it is imperative to consider how these quantities are different in typical high-z galaxies relative to present-day galaxies *and* how they may vary among high-z galaxies. In Steidel et al. (2016, hereafter S16) we sought to directly address this issue by combining observations of the rest-UV spectra of high-z galaxies' massive stellar populations with observations of the ionized gas surrounding the same stars, as probed by their rest-UV-optical nebular spectra. We compared a composite rest-UV-optical spectrum of 30 star-forming galaxies from KBSS with stellar population

models and photoionization model predictions and showed that only models which simultaneously include iron-poor massive star binaries and moderate oxygen enrichment in the gas can reconcile all of the observational constraints, even accounting for somewhat higher ionization parameters and electron densities than observed in typical $z \sim 0$ galaxies. In Strom et al. (2017, hereafter S17), we found that this abundance pattern—low Fe/H and moderate-to-high O/H—is also necessary to explain the behavior of *individual* $z \simeq 2-2.7$ KBSS galaxies and the behavior of the high-z star-forming galaxy locus in multiple 2D line-ratio spaces, including the N2-BPT diagram, the S2-BPT diagram (which trades [S II]6718, 6732 for [N II]λ6585), and the O32-R23 diagram[1] (which is sensitive to changes in ionization and excitation).

In this chapter, we expand on the analysis from S16 and S17 and present a new method for self-consistently determining gas-phase oxygen abundance (O/H), nitrogen-to-oxygen ratio (N/O), and ionization parameter (U) in individual high-z galaxies, utilizing measurements of the nebular emission lines in their rest-optical spectra and photoionization models motivated by observations of the same high-z galaxies. The sample used here is described in Section 4.2, followed by a description of the photoionization model method in Section 4.3. The results of this analysis are used to determine new strong-line diagnostics for U, N/O, and O/H in Section 4.4, which are presented alongside our guidance regarding the best method for determining these quantities using emission line measurements. New constraints on relationships between physical conditions in high-z galaxies' H II regions (including the N/O-O/H relation) are presented in Section 4.5. We conclude with a summary of our results in Section 4.6.

Throughout the chapter, we adopt the solar metallicity scale from Asplund et al. (2009), with $Z_\odot = 0.0142$, 12+log(Fe/H)$_\odot$ = 7.50, 12 + log(O/H)$_\odot$ = 8.69, and log(N/O)$_\odot = -0.86$. When necessary, we assume a ΛCDM cosmology: $H_0 = 70$ km s^{-1} Mpc^{-1}, $\Omega_\Lambda = 0.7$, and $\Omega_\mathrm{m} = 0.3$. Finally, specific spectral features are referred to using their vacuum wavelengths.

4.2 Sample Description

The sample of galaxies we consider for analysis is drawn from KBSS, which is a large, spectroscopic galaxy survey conducted in 15 fields centered on bright quasars and is explicitly designed to study the galaxy-gas correlation during the peak of cosmic star formation (Rudie et al., 2012). Extensive imaging and spectroscopic

[1] O32=log([O III]$\lambda\lambda$4960, 5008/[O II]$\lambda\lambda$3727, 3729) and R23=log[([O III]$\lambda\lambda$4960, 5008 + [O II]$\lambda\lambda$3727, 3729)/Hβ].

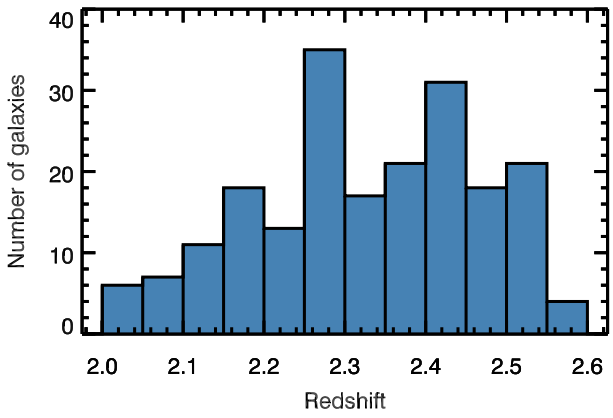

Figure 4.1: The distribution in nebular redshift for the sample of 203 galaxies discussed in this chapter, which has $\langle z \rangle = 2.3$.

campaigns have been conducted in all of the KBSS fields, including deep broad-band and medium-band optical-IR imaging[2], as well as spectroscopy obtained using the Low Resolution Imaging Spectrometer (LRIS, Oke et al., 1995; Steidel et al., 2004) at optical wavelengths and MOSFIRE in the NIR bands. The acquisition and reduction of the photometric and spectroscopic data have been described elsewhere (e.g., by Steidel et al., 2003; Reddy et al., 2012; Steidel et al., 2014), with additional details related to the rest-optical spectroscopic analysis (including cross-band calibration between NIR bands) provided by Strom et al. (2017).

For this chapter, we have selected the subsample of $z \simeq 2 - 2.7$ KBSS galaxies with nebular redshifts measured from MOSFIRE spectra ($\langle z \rangle = 2.3$, Figure 4.1) and spectral coverage of the regions near Hα, Hβ, [O III]λ5008, and [N II]λ6585 (i.e., the lines used in the N2-BPT diagram). Although not required for inclusion in the sample, measurements of [O II]$\lambda\lambda$3727, 3729, [O III]λ4364, [S II]$\lambda\lambda$6718, 6732 and [Ne III]λ3869 are incorporated when present. Objects are included regardless of the signal-to-noise ratio (SNR) for a single given line measurement, but we restrict the sample to those galaxies with SNR > 5 measurements of the Balmer decrement (Hα/Hβ), which we use to correct for dust attentuation. This requirement is imposed to ensure a fair comparison with the line flux predictions from photoionization models, which represent the nebular spectrum as it would appear if unattenuated by dust along the line-of-sight. We also exclude galaxies where there is evidence of

[2]All fields have imaging in U_n, G, $\mathcal{R}$, J, and K_s from the ground, as well as data from *Hubble*/WFC3-IR F140W and *Spitzer*/IRAC at 3.6μm and 4.5μm. 10 fields have at least one deep pointing obtained using *Hubble*/WFC3-IR F160W, and 8 fields have NIR imaging in $J1$, $J2$, $J3$, $H1$, and $H2$ collected using Magellan-FourStar (Persson et al., 2013).

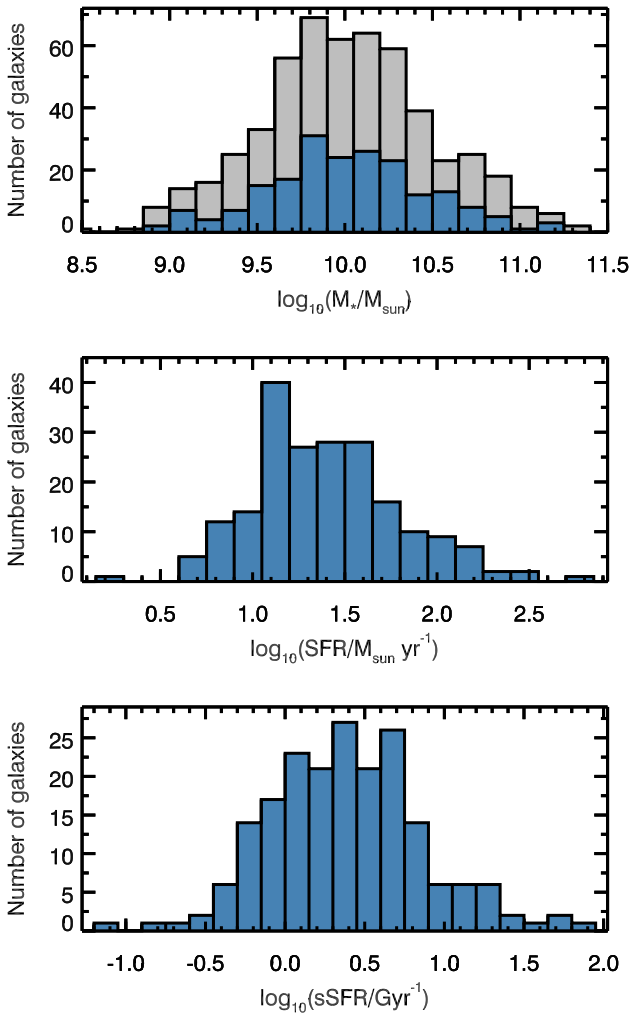

Figure 4.2: The bulk galaxy properties (M_*, SFR, and sSFR) for the KBSS sample used for the analysis presented in this chapter. The sample spans over two decades in all three parameters and is representative of the larger KBSS sample, with median $M_* = 9.5\times10^9\,M_\odot$, median SFR $= 23\,M_\odot\,yr^{-1}$, and median sSFR $= 2.5\,Gyr^{-1}$. For comparison, the distribution in M_* for all $z \simeq 2-2.7$ KBSS galaxies is shown in grey in the top panel, and a two-sample Kolmogorov-Smirnov (KS) test indicates that the distributions are consistent with one another ($p = 0.95$).

significant AGN activity (Steidel et al., 2014; Strom et al., 2017), as these galaxies will not be well-matched by photoionization model predictions made using ionizing radiation fields from purely stellar sources. In total, 203 galaxies satisfy these criteria and compose the sample discussed in the remainder of the chapter.

Figure 4.2 shows the stellar mass (M_*), star-formation rate (SFR), and specific star-formation rate (sSFR $=$ SFR$/M_*$) distributions for the sample (blue histograms), with the full sample of $z \simeq 2-2.7$ KBSS galaxies with M_* estimates shown for

comparison in the top panel (grey histogram). Stellar masses are measured as in Steidel et al. (2014) and S17, using the methodology described by Reddy et al. (2012). SFRs are determined using extinction-corrected Hα measurements, where we have adopted the Galactic extinction curve from Cardelli, Clayton & Mathis (1989). Values for M_*, SFR, and sSFR are reported assuming a Chabrier (2003) stellar initial mass function (IMF). The sample considered in this chapter spans a large range in all three bulk galaxy properties, with median $M_* = 9.51 \times 10^9$ $M_\odot$, median SFR = 22.8 $M_\odot$ yr^{-1}, and median sSFR = 2.45 Gyr^{-1}.

4.3 Model-Based Measurements of O/H, N/O and U

4.3.1 Photoionization Model Grid

As in S16 and S17, we use Cloudy (v13.02, Ferland et al., 2013) to predict the nebular spectrum originating from gas irradiated by a given stellar population radiation field, with the ultimate goal of generating predicted emission line fluxes as a function of *all* of the physical parameters of interest, $f_{\rm line}(Z_*, U, Z_{\rm neb}, {\rm N/O})$. In all cases, we adopt a plane parallel geometry and $n_H = 300$ cm^{-3}, with the latter motivated by measurements of electron density, n_e, in $\langle z \rangle = 2.3$ KBSS galaxies (S16, S17)[3]. Dust grains are included assuming the "Orion" mixture provided as part of Cloudy and with a dust-to-gas ratio that scales linearly with the metallicity of the gas, $Z_{\rm neb}$.

We use stellar population synthesis models from "Binary Population and Spectral Synthesis" (BPASSv2; Stanway, Eldridge & Becker, 2016, Eldridge et al. in prep.) as the input ionizing spectra, which set the *shape* of the ionizing radiation field. To capture the range of stellar populations that may exist in the parent sample of high-z star-forming galaxies, we employ models from BPASSv2 with constant star-formation histories and $Z_* = [0.001, 0.002, 0.003, 0.004, 0.006, 0.008, 0.010, 0.014]$ ($Z_*/Z_\odot \approx 0.07 - 1.00$). We use a single age of 100 Myr for all stellar population models, consistent with the characteristic ages of star-forming galaxies at $z \sim 2$ (e.g. Reddy et al., 2012); the assumption of a fixed age does not significantly impact the photoionization model predictions, as the BPASSv2 models reach equilibrium at UV wavelengths after a few $\times 10^7$ yr. Variations in the *intensity* of the radiation field are parameterized by the ionization parameter $U (\equiv n_\gamma/n_H$, the dimensionless ratio of the number density of incident ionizing photons to the number density of neutral hydrogen). Because we adopt a single n_H, differences in U reflect differences in the normalization of the radiation field.

[3] In ionized gas, $n_H \approx n_e$.

The metallicity of the gas, $Z_{\rm neb}$, is allowed to vary independently of Z_*, and spans $Z_{\rm neb}/Z_\odot = 0.1 - 2.0$. As discussed in greater detail elsewhere (including S16; S17), $Z_{\rm neb}$ primarily reflects the abundance of O (which is the most abundant heavy element in H II regions, thus regulating gas cooling and many features of the nebular spectrum), whereas Z_* traces Fe abundance (which provides the majority of opacity in stellar atmospheres and is critical for determining the details of the stellar wind). While we expect the gas and stars to have the same O/H and Fe/H as one another, decoupling $Z_{\rm neb}$ and Z_* allows us to explicitly explore the presence of non-solar O/Fe in both the gas and stars in high-z galaxies. Given the high sSFRs observed in these galaxies and young inferred ages, enrichment from core-collapse supernovae (CCSNe) will dominate relative to contributions from Type Ia SNe, making it likely that super-solar O/Fe is in fact more typical than $(\mathrm{O/Fe})_\odot$ at high redshift. In the future, we look forward to incorporating stellar population synthesis models with non-solar values of O/Fe—thus allowing a single value of Z to be adopted for both the gas and stars—but without access to such models at the current time, varying $Z_{\rm neb}$ and Z_* independently is the simplest way to mimic the super-solar O/Fe required to match the observations of typical high-z galaxies' nebular spectra (S16).

Finally, we allow N/O to vary independently of both $Z_{\rm neb}$ and Z_*, with a minimum $\log(\mathrm{N/O}) = -1.8$ ($[\mathrm{N/O}] = -0.94$). In the local universe, the N/O measured in H II regions and star-forming galaxies is known to correlate with the overall O/H (e.g., van Zee, Salzer & Haynes, 1998), exhibiting a low, constant value ($\log(\mathrm{N/O}) \approx -1.5$) at $12 + \log(\mathrm{O/H}) \lesssim 8.0$ and increasing with increasing O/H past this critical level of enrichment. Although the nucleosynthetic origin of N remains largely uncertain, this behavior is often interpreted as a transition between "primary" and "secondary" production of N (e.g., Edmunds & Pagel, 1978; Vila Costas & Edmunds, 1993). Notably, among a compilation of local extragalactic H II regions from Pilyugin, Grebel & Mattsson (2012, hereafter Pil12), there is a factor of $\sim 2 - 3$ scatter in N/O at *fixed* O/H, particularly near the transition metallicity ($12 + \log(\mathrm{O/H}) \approx 8.0$). Methods that adopt (explicitly or implicitly) a single relation with no scatter between N/O and O/H marginalize over this intrinsic physical scatter, which affects the accuracy of the inferred O/H. Some methods, like HII-CHI-MISTRY (Pérez-Montero, 2014), do allow for some scatter in N/O at fixed O/H, but still impose a prior that prevents any enrichment in N/O greater than that observed in the calibration sample. Because we are interested in quantifying the the relationship between N/O and O/H among high-z galaxies, including the degree of intrinsic scatter, we opt to allow any value of $\log(\mathrm{N/O}) \geq -1.8$.

Although varying other physical conditions (including n_H) can also affect the resulting nebular spectrum, the effect of such differences within the range observed in the KBSS sample (where most galaxies are consistent with $n_e = 300$ cm^{-3}) is significantly smaller than the effects of altering the shape and/or normalization of the ionizing radiation field (i.e., varying Z_* and/or U) or the chemical abundance pattern in the gas (i.e., varying $Z_{\rm neb}$ or N/O). Thus, in summary, we assemble a four-dimensional parent photoionization model grid, spanning the following parameter space:

$$Z_*/Z_\odot \approx [0.07, 1.00], \text{ from BPASSv2}$$
$$Z_{\rm neb}/Z_\odot = [0.1, 2.0], \text{ every 0.1 dex}$$
$$\log(U) = [-3.5, -1.5], \text{ every 0.1 dex}$$
$$\log(\text{N/O}) \geq -1.8$$

4.3.2 MCMC Method

We do not know *a priori* the degeneracies among Z_*, U, $Z_{\rm neb}$, and N/O, in terms of determining the observed nebular spectra of high-z galaxies, and it is possible that the correlations found in low-z samples may not hold at higher redshifts. Indeed, two of the main goals of this work are to: (1) quantitatively determine these quantities in individual high-z galaxies, discussed in this section, and (2) evaluate the presence of any intrinsic correlations between these parameters among the high-z galaxy population, discussed in Section 4.5. Given the relatively large size of the total parameter space outlined above and the expectation that the posterior probability density functions (PDFs) for the parameters may not be normally distributed, we choose to explore parameter space using a Markov Chain Monte Carlo (MCMC) technique. Such a method allows us to efficiently determine the combinations of Z_*, U, $Z_{\rm neb}$, and N/O that are consistent with the entire observed rest-optical nebular spectra of individual objects, as well as quantify the correlations between inferred parameters.

We initialize the chain at the photoionization model grid point that best matches the combination of emission lines measured from a galaxy's spectrum. The MCMC sampler then explores log parameter space, using a proposal algorithm that incorporates two step sizes to allow for efficient local sampling as well as exploration of widely-separated peaks in the PDF. In general, flat priors are adopted within the boundaries of the parent photoionization model grid, with one additional constraint:

$$0.0 < \log(Z_{\rm neb}/Z_*) < 0.73.$$

Given our assumption that $Z_{\rm neb}$ traces O/H and Z_* traces Fe/H, limits on $\log(Z_{\rm neb}/Z_*)$ in our model reflect limits on [O/Fe], which are informed by stellar nucleosynthesis and galactic chemical evolution models. The upper limit we impose on $\log(Z_{\rm neb}/Z_*)$ corresponds to the highest [O/Fe] expected for the Salpeter IMF-averaged yields from Fe-poor ($Z_* = 0.001$) CCSNe (Nomoto et al., 2006). The lower limit is equivalent to [O/Fe] = 0.0, which is the default implicitly assumed by most stellar population synthesis models and, by extension, most photoionization model methods for determining physical conditions in galaxies. Since high-z galaxies are typically young and rapidly star-forming, the true value of [O/Fe]—and, thus, $\log(Z_{\rm neb}/Z_*)$—likely falls in this range for most objects.

If the proposed step is not coincident with a grid point in the parent photoionization model grid, the predicted emission line fluxes are calculated via trilinear interpolation of the grid in Z_*, U, and $Z_{\rm neb}$ and subsequently scaling the model [N II]λ6585 flux based on the proposed value of log(N/O). For example, log(N/O) = −0.86 ([N/O] = 0) corresponds to a scale factor of 1, whereas log(N/O) = −1.5 ([N/O] = −0.64) corresponds to a scale factor of 0.23 relative to the default [N II]λ6585 flux from our parent photoionization model grid, which assumes solar N/O[4].

Because the photoionization model line intensities are reported relative to Hβ, we convert the observed line fluxes onto the same scale by first correcting all of the line measurements for differential reddening due to dust and then dividing by the flux in Hβ. Although a Balmer decrement of 2.86 is widely adopted as the fiducial value for Case B recombination (Osterbrock, 1989), the exact value is sensitive to both n_e and the electron temperature, T_e (and, thus, the shape of the ionizing radiation field). To remain self-consistent, we adopt a Case B value for the Balmer decrement based on the predicted Hα flux (in units of Hβ) at every proposed step, which ranges from $2.85 - 3.14$ in the parent photoionization model grid. In all cases, the line-of-sight extinction curve from Cardelli, Clayton & Mathis (1989) is used to correct the line fluxes, but because many commonly-used extinction curves have a similar shape at rest-optical wavelengths, our results do not change significantly if we adopt an SMC extinction curve.

Our MCMC method is able to account for low-SNR measurements of emission lines in the same manner as more significant detections, and thus no limits are used. If

[4]Assuming a constant value of N/O in Cloudy does not have a significant impact on the structure of the nebula.

a measured line flux is formally negative (as measured using the custom spectral analysis tool *MOSPEC*S17), the expectation value for the line flux is assumed to be zero, with a corresponding error $\sigma_{f/\mathrm{H}\beta} = \sigma_f / f_{\mathrm{H}\beta}$.

Convergence of the MCMC to the posterior is evaluated using the potential scale reduction factor, $\hat{R}$ (also known as the Gelman-Rubin diagnostic, Gelman & Rubin, 1992), using equal-length segments of the chain to compare the dispersion within the chain to the dispersion between portions of the chain. When the chain segments look very similar to one another, $\hat{R}$ will trend from higher values toward 1. When $\hat{R} < 1.05$ for all four model parameters, we assume approximate convergence has been achieved. For the majority of galaxies in the chapter sample, the MCMC converges within $20,000$ iterations.

4.3.3 MCMC Results

Figures 4.3 and 4.4 show the MCMC results for two individual galaxies in the KBSS sample, highlighting the range of possible outcomes. The results for Q1442-BX160 contain a single preferred solution, with pairwise 2D posteriors that resemble bivariate Gaussian distributions. In contrast, the joint posterior PDF for Q1009-BX218 reveals two distinct solutions and notably non-normal marginalized posteriors.

Approximately $\sim 61\%$ of objects, including Q1009-BX218, have 2 or more peaks in the marginalized posterior for at least one model parameter. Nevertheless the distribution of probability between multiple peaks still allows for a single solution to be preferred in many cases. This is true for Q1009-BX218, where the 68% highest density interval (HDI, the narrowest range that includes 68% of the distribution) contains a single dominant peak in $\log(Z_{\mathrm{neb}}/Z_{\odot})$ and $\log(Z_*/Z_{\odot})$.

We adopt the following criteria for identifying "bound" marginalized posteriors, which are those posterior distributions from which a preferred model parameter can be estimated: the 68% HDI must contain either a single peak or, if 2 or more peaks are present, there cannot exist a local minimum in the posterior PDF with lower probability than the probability at the edge of the 68% HDI. For bound posteriors, we adopt the maximum *a posteriori* (MAP) estimate as the inferred value for the model parameter. The MAP estimate is taken to be the peak value of the Gaussian-smoothed histogram representing the marginalized posterior. The asymmetric errors on this estimate are determined by calculating the 68% HDI for the same posterior. In total, 103 galaxies have bound posteriors and, thus, MAP estimates for $\log(Z_{\mathrm{neb}}/Z_{\odot})$, log(N/O), $\log(U)$, and $\log(Z_*/Z_{\odot})$.

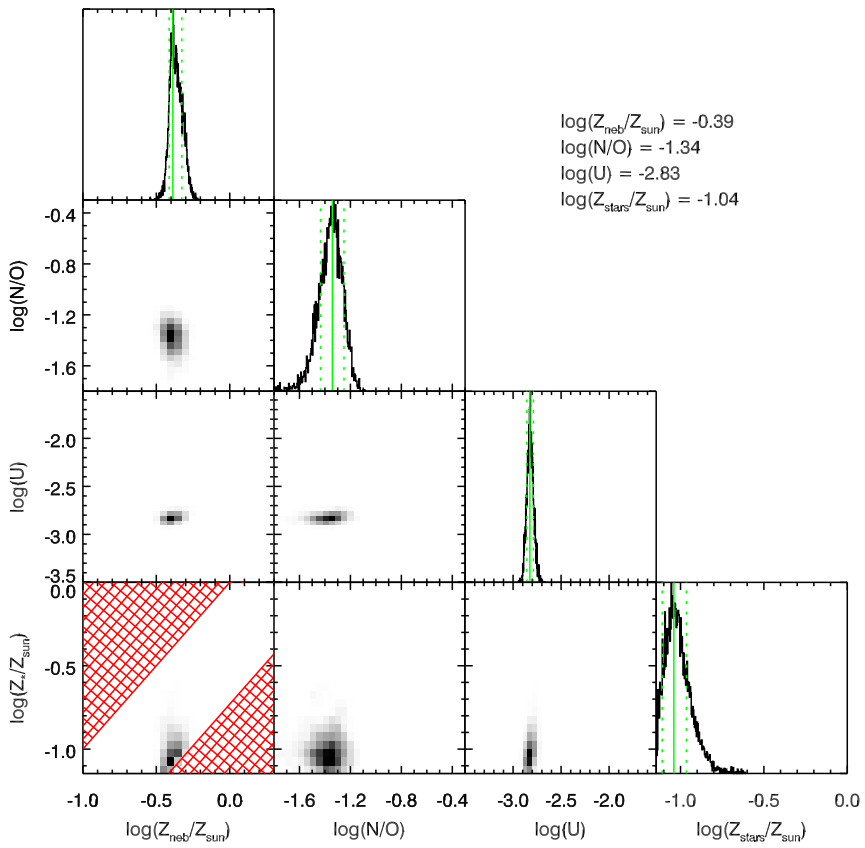

Figure 4.3: The posterior PDFs for $\log(Z_{\rm neb}/Z_\odot)$, log(N/O), $\log(U)$, and $\log(Z_*/Z_\odot)$ for Q1442-BX160, as estimated from the MCMC routine. The displayed range reflects the bounds on the parameters, which are listed in the text. The red shaded region in the panel showing the 2D pairwise posterior for $\log(Z_*/Z_\odot)$ and $\log(Z_{\rm neb}/Z_\odot)$ reflect disallowed regions of parameter space with $\log(Z_{\rm neb}/Z_*) < 0.0$ or $\log(Z_{\rm neb}/Z_*) > 0.73$. The solid green lines show the locations of the MAP estimates for the marginalized posteriors, with the dashed green lines reflecting the 68% highest posterior density interval. The MAP estimates for each parameter are printed above the figure. Q1442-BX160 is an example of an object with bound, single-peaked posteriors in all four parameters, where the parameter estimation is relatively straightforward.

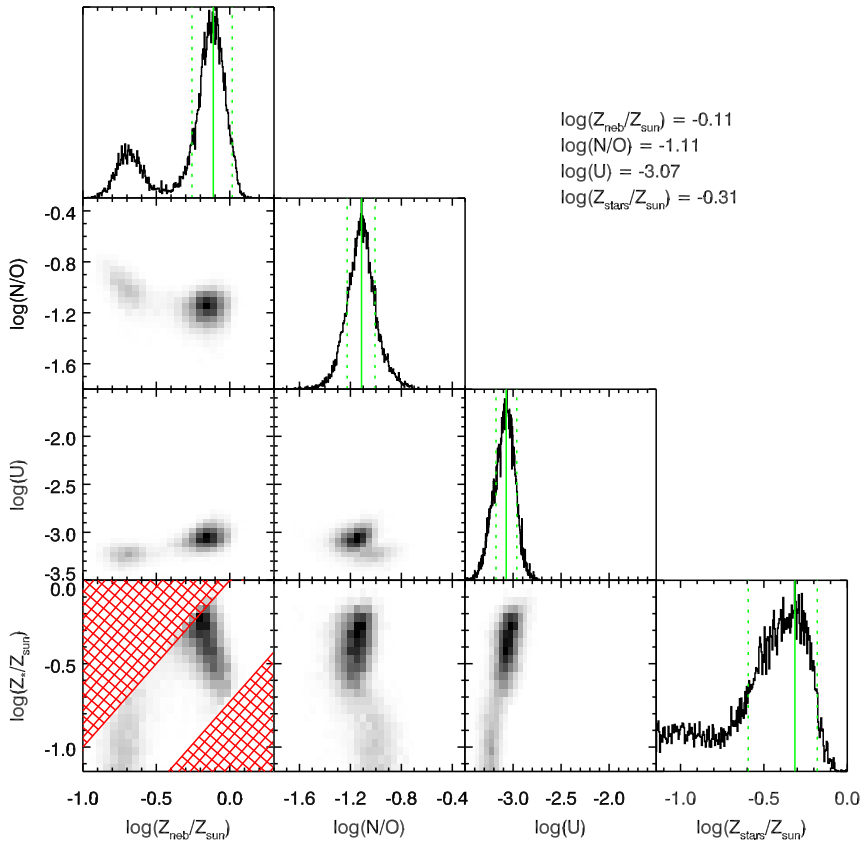

Figure 4.4: The posterior PDFs for Q1009-BX218, shown in the same manner as Figure 4.3. Q1009-BX218 highlights the case where the multi-dimensional posterior is double-peaked, because of degeneracies in the photoionization model grid. This is reflected in both the 2D posteriors and marginalized posteriors for single parameters. Nevertheless, because one solution is significantly more likely, it is possible to infer $\log(Z_{\rm neb}/Z_{\odot})$, log(N/O), $\log(U)$, and $\log(Z_{*}/Z_{\odot})$, as described in the text and shown by the solid green lines.

We separately consider cases where one edge of the 68% HDI coincides with the edge of the parent photoionization model grid for a given parameter. If so, we assume that the posterior reflects a limit and record the opposite edge of the 68% HDI as an upper or lower limit in that parameter, corresponding to a 2σ limit. Table 4.1 provides a more detailed summary of the MCMC results, including the number of galaxies with limits on a given parameter.

Figure 4.5 shows the distributions in inferred $\log(Z_{\rm neb}/Z_{\odot})$, log(N/O), $\log(U)$, and $\log(Z_{*}/Z_{\odot})$ for KBSS galaxies with bound posteriors in all four model parameters. The upper right panel, showing the distribution of log(N/O), also includes the contribution to each histogram bin from galaxies with upper limits on log(N/O) but bound posteriors in the other three model parameters (grey portion of the histogram);

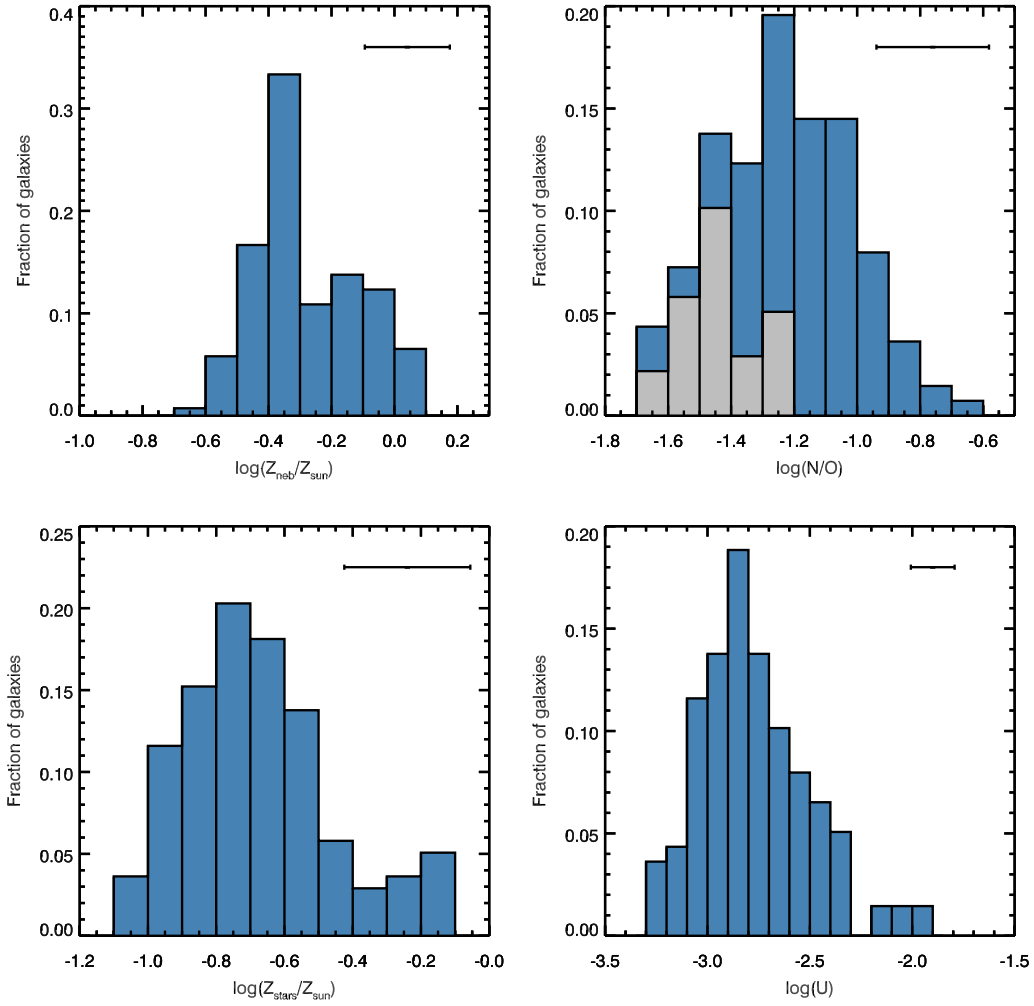

Figure 4.5: Distributions in model-inferred $\log(Z_{\rm neb}/Z_{\odot})$, log(N/O), $\log(Z_{*}/Z_{\odot})$, and $\log(U)$ for KBSS galaxies, showing for the first time self-consistent estimates of the physical conditions in a large sample of individual high-z galaxies. The contribution from galaxies with upper limits on log(N/O) is shown as the grey portion of the histogram in the upper right panel. For reference, the average error (Δ_{68}) for each parameter is shown in the upper right corner of each panel. These results are consistent in many respects with previous estimates of these parameters, including the range of $\log(U)$ we reported for KBSS galaxies in S17, but also offer new insights into the range of physical characteristics common in $\langle z \rangle = 2.3$ galaxies.

Table 4.1: MCMC results for $z \simeq 2 - 2.7$ KBSS-MOSFIRE galaxies

Sample	$N_{\rm gal}$
Galaxies used in the photoionization model analysis	203
Galaxies with bound PDFs for all parameters	103
Galaxies with bound PDFs for all but N/O	36
Galaxies with bound $\log(Z_{\rm neb}/Z_\odot)$ PDF	173
Galaxies with bound log(N/O) PDF	155
Galaxies with bound $\log(U)$ PDF	193
Galaxies with bound $\log(Z_*/Z_\odot)$ PDF	157
Galaxies with 2+ peaks in $\log(Z_{\rm neb}/Z_\odot)$	55
Galaxies with 2+ peaks in log(N/O)	5
Galaxies with 2+ peaks in $\log(U)$	11
Galaxies with 2+ peaks in $\log(Z_*/Z_\odot)$	53
Galaxies with an upper limit on log(N/O)	47
Galaxies with an upper limit on $\log(Z_*/Z_\odot)$	22
Galaxies with a lower limit on $\log(Z_*/Z_\odot)$	1

Note: A marginalized PDF is considered bound when the 68% highest posterior density interval (1) does not bracket a local minimum with lower probability than the probability at the interval boundaries and (2) does not abut the edge of the sampled range in the parameter (i.e., the PDF represents a limit).

we discuss this subsample in more detail below. The interquartile ranges in the model parameters for this subsample are

$$\begin{aligned} \log(Z_{\rm neb}/Z_\odot)_{50} &= [-0.40, -0.14] \\ \log({\rm N/O})_{50} &= [-1.41, -1.08] \\ \log(U)_{50} &= [-2.97, -2.61] \\ \log(Z_*/Z_\odot)_{50} &= [-0.84, -0.54]. \end{aligned}$$

These characteristic ranges agree well with inferences of these parameters by other means. In particular, the range of interred $\log(U)$ is in excellent agreement with the range we previously reported for individual KBSS galaxies in S17, using a more limited photoionization model approach.

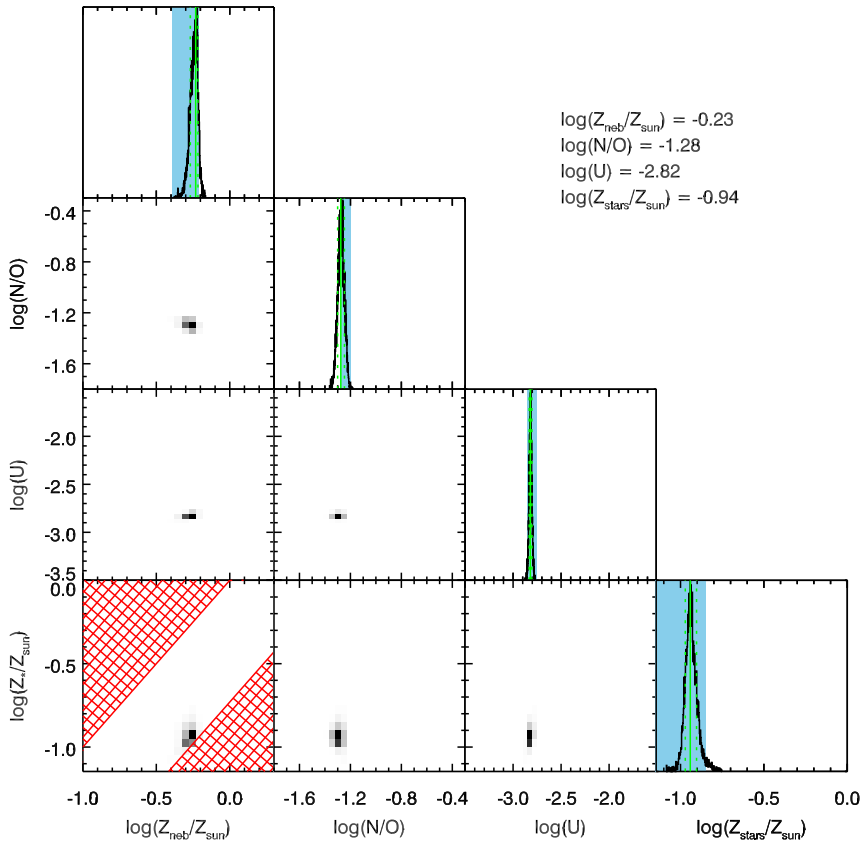

Figure 4.6: The MCMC results for the LM1 composite spectrum, shown in the same manner as Figure 4.3. The blue shaded regions indicate the values for each quantity and the corresponding uncertainties reported by S16.

4.3.3.1 The LM1 Composite Spectrum

We also test our method using measurements from the rest-optical composite spectrum presented by S16, where we were able to estimate O/H, N/O, U, and Z_* using a number of independent cross-checks. The "LM1" composite from that analysis was constructed using MOSFIRE observations of 30 KBSS galaxies with $z = 2.40\pm0.11$. As described by S16, the J, H, and K-band spectra of the galaxies were corrected for differential slit losses between bands and shifted into the rest-frame according to the measured nebular redshift, with the normalization of each galaxy's spectra adjusted to account for small redshift differences among the sample. The final composite spectrum is a straight average of the individual shifted and scaled spectra, excluding regions near bright OH sky lines.

To make a fair comparison with the individual galaxies in our sample, for which only the strongest rest-optical nebular emission lines are typically measurable, we

use the measurements of [O II]$\lambda\lambda$3727, 3729, [Ne III]λ3869, Hβ, [O III]λ5008, Hα, [N II]λ6585, and [S II]$\lambda\lambda$6718, 6732 reported by S16. Although we reported a limit on [O III]λ4364 for the LM1 composite in S16, we choose not to include it here, as it was not observed in the spectrum of each individual galaxy in the LM1 sample and is generally not available for individual high-z galaxies. The MCMC results using only the strong-line measurements are shown in Figure 4.6 and show narrow and well-defined marginalized posteriors for each of the four model parameters.

The parameter estimates for the LM1 composite from our photoionization model method are very similar to the values reported by S16 (identified by shaded blue regions in Figure 4.6). In that paper, we were able to directly incorporate information about the photospheric absorption features observed in the non-ionizing UV composite spectrum in order to infer Z_*, and we also leveraged measurements of the auroral [O III]$\lambda\lambda$1661, 1666 lines in the rest-UV as an independent constraint on $Z_{\rm neb}$. In addition, the N/O inferred for the LM1 composite using two locally-calibrated empirical strong-line calibrations was found to be in excellent agreement with the N/O determined through comparisons of the LM1 measurements with photoionization models alone. Given the internal consistency of the analysis presented in S16, the agreement between the new photoionization model method results and the earlier estimates is reassuring.

We note that the inferred values of $\log(Z_{\rm neb}/Z_\odot)$, log(N/O), and $\log(U)$ for the LM1 composite spectrum discussed above are close to the most common values reported for individual galaxies in Figure 4.5, but that the value of $\log(Z_*/Z_\odot)$ we have estimated for the LM1 composite ($Z_*/Z_\odot \approx 0.11$) is somewhat lower than the peak of the distribution for individual galaxies. Although it is possible that the galaxies used to construct the LM1 composite are not characteristic of the full range in Z_* present in the full $z \simeq 2-2.7$ KBSS sample, fits to the UV spectra of individual KBSS galaxies also consistently favor $Z_*/Z_\odot \approx 0.07 - 0.14$ (e.g., Steidel et al., in prep.). This is lower than the interquartile range inferred using the photoionization model method, which relies only on emission line measurements. Some of the discrepancy likely arises from the fact that the constraint on $\log(Z_*/Z_\odot)$ from nebular emission lines is only on the required shape of the ionizing UV spectrum, rather than direct observations of photospheric line-blanketing in the non-ionizing UV spectrum.

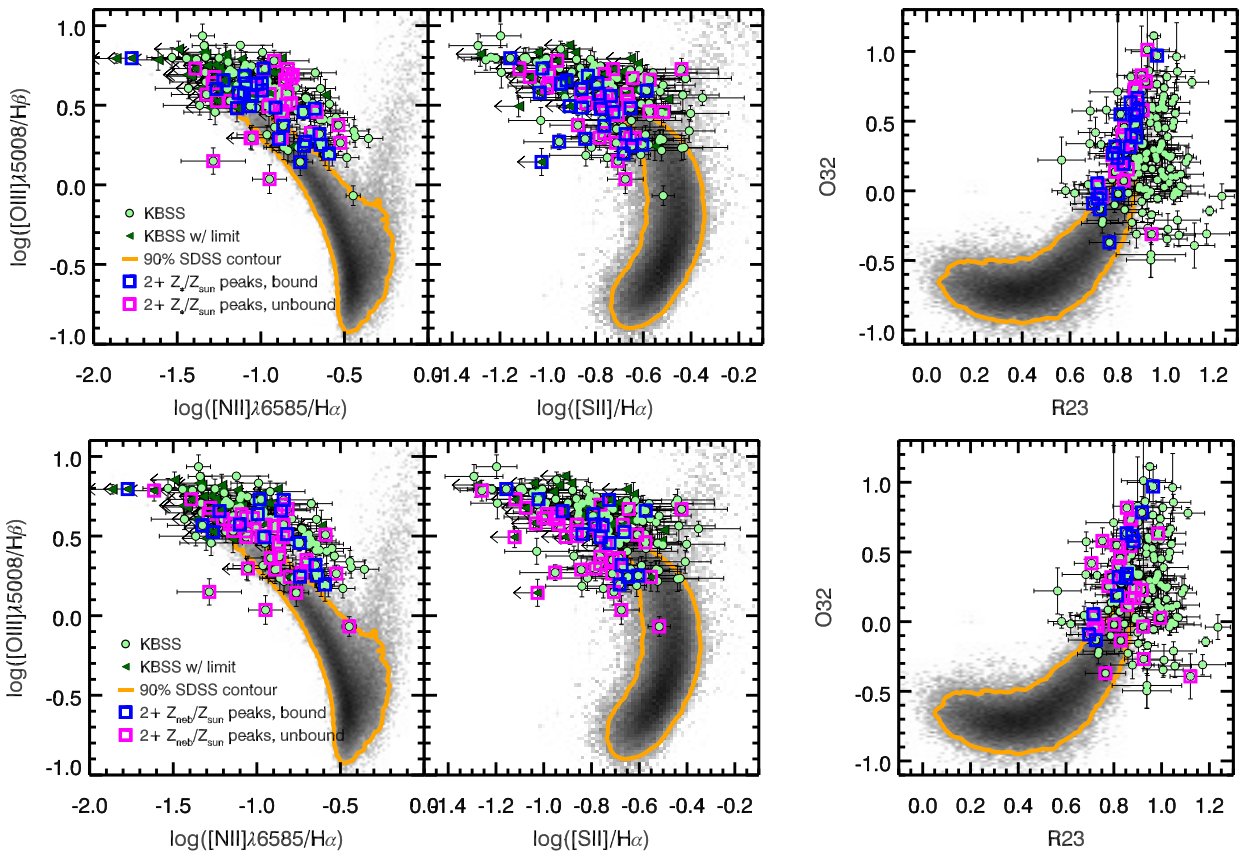

Figure 4.7: Three commonly-used 2D emission line ratio diagrams: the N2-BPT diagram (left column), the S2-BPT diagram (center column), and the dust-corrected O32-R23 diagram (right column). The locus of $z \sim 0$ galaxies from SDSS is shown in greyscale in each panel, with an orange contour enclosing 90% of the sample. The sample of $\langle z \rangle = 2.3$ galaxies from KBSS used in this chapter is shown by the green points with error bars; galaxies with 2σ upper limits on [N II] and [S II] are instead illustrated as darker green triangles. The top row shows the location of galaxies with multiple peaks in $\log(Z_{\rm neb}/Z_\odot)$, separated by whether the posterior is bound (blue squares) or unbound (magenta squares). The bottom row shows the location of galaxies with multiple peaks in $\log(Z_*/Z_\odot)$ in the same manner.

4.3.3.2 Multi-peaked Posteriors and Limits

Multipeaked posteriors are most frequently observed for $\log(Z_{\rm neb}/Z_\odot)$ and $\log(Z_*/Z_\odot)$. Figure 4.7 shows the location of galaxies with 2 or more peaks in the marginalized posteriors for these parameters in the N2-BPT, S2-BPT, and O32-R23 diagrams, highlighting differences in the spectra of galaxies with unbound posteriors (e.g., those with equal power shared among 2 or more peaks, identified by magenta squares) and those with bound posteriors (e.g., those with a single dominant peak or group of peaks, identified by blue squares). A few trends are common for both parameters, including the clustering on the left (low-R23) side of the galaxy locus in the O32-R23 diagram (shown in the right column). This region of parameter space is populated by photoionization model grid points with either low *or* high $Z_{\rm neb}$, whereas higher values of R23 at fixed O32 can only be achieved by combining moderate $Z_{\rm neb}$ with low Z_*.

Interestingly, galaxies with multi-peaked posteriors in $\log(Z_{\rm neb}/Z_\odot)$ or $\log(Z_*/Z_\odot)$ are well-mixed with the total sample in the N2-BPT diagram (left column in Figure 4.7), regardless of whether the posteriors are bound. The same is true for galaxies with bound multi-peaked posteriors in either parameter in the S2-BPT diagram (center column). Notably, however, galaxies with unbound multi-peaked posteriors in $\log(Z_*/Z_\odot)$ occupy a unique region of parameter space to the lower left of the ridge-line of KBSS galaxies in the S2-BPT diagram (with low [O III]/Hβ at fixed [S II]/Hα). In general, these galaxies do not exhibit multiple isolated peaks in $\log(Z_*/Z_\odot)$, but rather relatively flat posteriors with 2 or more local maxima spread over a range in $\log(Z_*/Z_\odot)$. Galaxies in this region of parameter space, as with those found at low-R23 and high-O32, are nominally consistent with a range in Z_*, thus requiring more information to break the degeneracy between possible solutions. In the future, we plan to incorporate constraints on the detailed stellar photospheric absorption features observed in the non-ionizing UV spectra of individual galaxies in KBSS, but note that such data is not typically available when trying to infer physical conditions from galaxies' rest-optical spectra.

There are 47 galaxies with marginalized posterior PDFs that reflect upper limits on log(N/O). These galaxies are not preferentially distributed in a specific location in the N2-BPT, S2-BPT, and O32-R23 diagrams, but over 97% of such galaxies have SNR < 2 measurements of [N II]λ6585, which was the significance threshold we adopted in S17. In contrast, only $\sim$ 11% of galaxies with bound posteriors in all four model parameters, including log(N/O), have SNR < 2 in their [N II]λ6585

measurements. A two-sample Kolmogorov-Smirnov (KS) test indicates that the distributions in [N II]λ6585 SNR for the two subsamples are significantly unlikely to be drawn from the same parent population. The distributions in SNR for the other strong lines are consistent with one another, with the exception of [O III]λ5008; galaxies with limits in N/O have significantly higher SNR detections of [O III]λ5008. Because the likelihood of having an upper limit on log(N/O) appears to result almost exclusively from a low SNR [N II]λ6585 measurement and have only a minor impact on the inferred values of the other model parameters, we choose to include such galaxies in the sample we consider for the remainder of the chapter.

Combining these constraints, the sample with useful estimates of their physical conditions of interest include the 103 galaxies with bound posteriors in all model parameters and an additional 36 galaxies with upper limits on log(N/O), for a total of 139 galaxies.

4.3.4 Trends with Galaxy Spectral Properties

It is interesting to consider whether galaxies with certain combinations of physical conditions are more likely to inhabit specific regions of the nebular diagnostic diagrams, resulting in trends in physical conditions along or across the galaxy locus in line-ratio space. For example, the locus of $z \sim 0$ star-forming galaxies from SDSS in the N2-BPT diagram is known to be a sequence in both gas-phase O/H (corresponding to $Z_{\rm neb}$) and U. However, when we investigate the presence of similar trends among $\langle z \rangle = 2.3$ galaxies (Figure 4.8), we find that although U is strongly correlated with position along the galaxy locus in the N2-BPT, the S2-BPT, *and* the O32-R23 diagram (middle panels), the trend with $Z_{\rm neb}$ in the N2-BPT or S2-BPT planes is noticeably weaker (top panels). The inferred value of $Z_{\rm neb}$ for $\langle z \rangle = 2.3$ galaxies appears to change *across* the galaxy locus rather than *along* it, which is especially notable in the O32-R23 diagram, where higher values of $Z_{\rm neb}$ are found on the low-R23 side of the locus. That the trends with $Z_{\rm neb}$ and U are essentially perpendicular to one another in the O32-R23 diagram suggests that a combination of these indices could be used to construct a strong-line diagnostic that simultaneously provides constraints on both O/H and U. This idea formed the basis of the earliest strong-line calibrations for R23 (e.g. Pagel et al., 1979; McGaugh, 1991) and has been proposed more recently by Shapley et al. (2015), who found that the local sequence of galaxies in the O32-R23 diagram increased monotonically in O/H as O32 and R23 declined. We explore the possibility of constructing such a diagnostic using the results for the KBSS sample in Section 4.4.

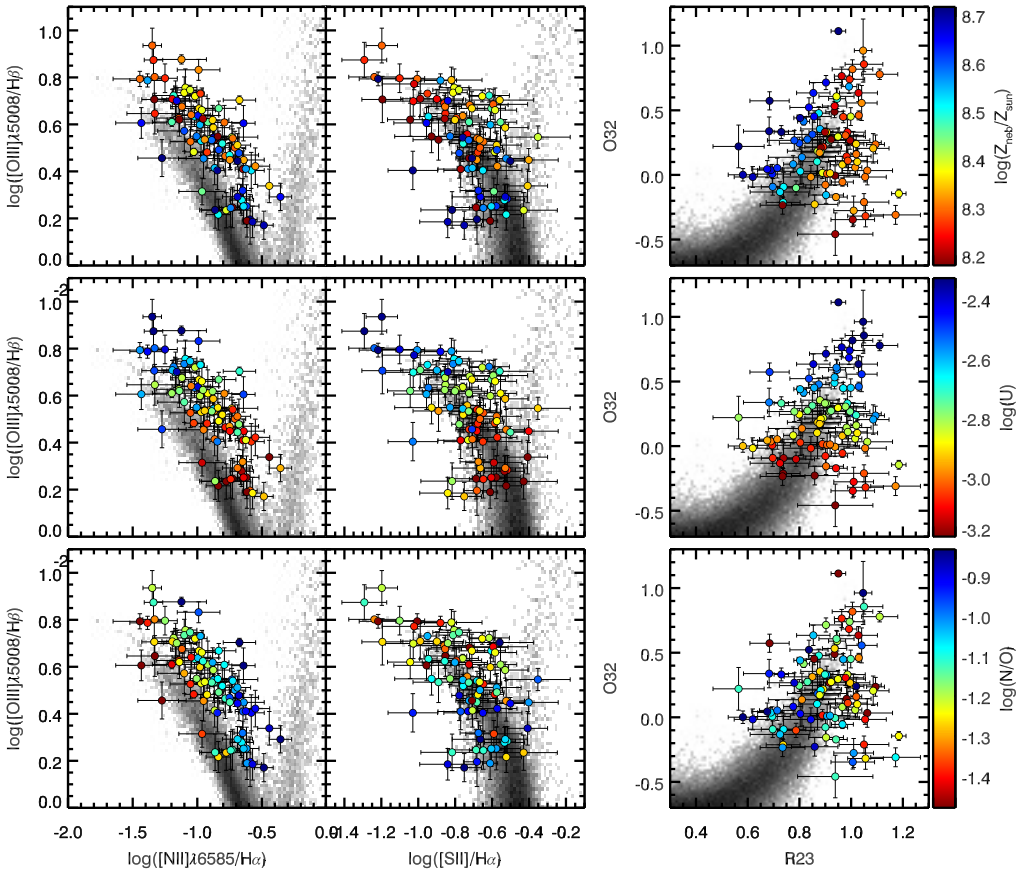

Figure 4.8: The N2-BPT (left column), S2-BPT (middle column), and O32-R23 (right column) diagrams, showing the trends with $\log(Z_{\rm neb}/Z_{\odot})$ (top row), $\log(U)$ (middle row), and log(N/O) (bottom row) for the KBSS sample described in Section 4.2, with $z \sim 0$ SDSS galaxies shown in greyscale for comparison. The KBSS points are color-coded by the inferred value of each parameter and highlight a few key correlations: $Z_{\rm neb}$ appears to change mostly across the galaxy locus in all three diagrams, whereas U decreases along the locus, toward low [O III]/Hβ and O32. Inferred N/O increases toward higher [N II]/Hα, but also weakly along the locus in the S2-BPT plane, toward lower [O III]/Hβ.

We also observe a strong correlation between galaxies' positions in the N2-BPT plane and the value of log(N/O) inferred from their nebular spectra (bottom left panel of Figure 4.8), with higher N/O corresponding to higher values of [N II]/Hα. This trend is also observed, although much less strongly, in the S2-BPT diagram, with higher N/O occurring in galaxies on the lower part of the locus. This is the opposite of the observed trend with U, which decreases in the same direction in the S2-BPT plane. This *may* suggest the presence of an inverse correlation between the ionization conditions and star-formation history as probed by chemical abundance patterns (at least, N/O) in high-z galaxies, but the orthogonal trend with $Z_{\rm neb}$ in the line ratio diagrams suggests that any such relationship may be qualitatively different from the strong anti-correlation observed between U and O/H at $z \sim 0$ (e.g., Dopita & Evans, 1986). We quantitatively investigate the correlations between inferred physical conditions, including ionization and metallicity, in Section 4.5.

For the galaxies with bound posteriors, we characterize their marginalized posteriors using four quantities: the MAP estimate for the model parameter, the width of the 68% HDI (hereafter Δ_{68}), the skewness, and the kurtosis excess. The skewness of a posterior, S, quantifies whether the distribution is left- or right-tailed and provides some insight regarding the constraints imposed on a given parameter in certain regions of parameter space. The kurtosis excess, K, measures the "peakiness" of the distribution (a normal distribution has $K = 0$); positive values indicate that the distribution contains more power in the peak relative to the tails, when compared with a normal distribution. As a posterior may have fat tails and still be relatively narrow, we use on Δ_{68} as our primary measure of precision.

Importantly, there appear to be no strong trends in Δ_{68}, S, or K for any model parameter in terms of the location of galaxies in the nebular diagnostic diagrams. This result implies that we are capable of recovering all high-z galaxies' physical conditions with similar precision, given a minimum set of strong-line measurements. The exception is galaxies falling below the galaxy locus in the S2-BPT diagram, where objects frequently have parameter PDFs with multiple strong peaks (as shown in Figure 4.7) and would likely benefit from additional constraints from rest-UV observations.

Figure 4.9 shows the distribution of the most precisely inferred parameter (i.e., the parameter with the smallest value of Δ_{68}, corresponding to the fractional error) for individual galaxies. For approximately $\sim 70\%$ of galaxies, $\log(U)$ is the parameter with the narrowest marginalized posterior, meaning that the nebular spectra of

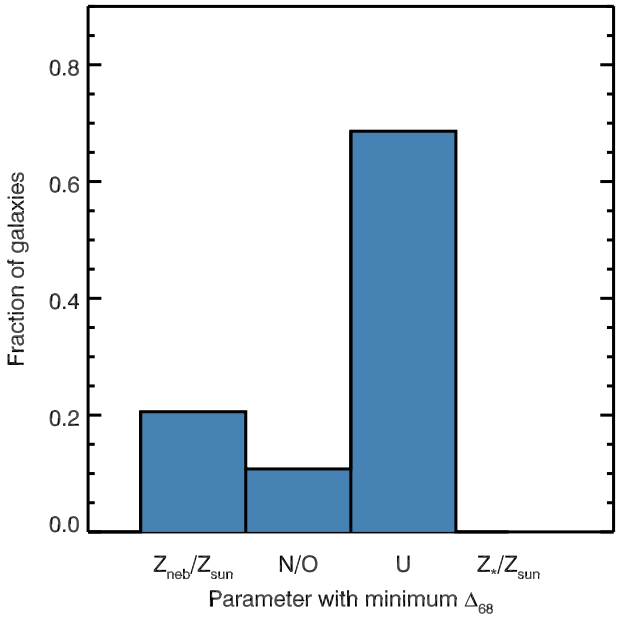

Figure 4.9: The distribution of the most precisely-inferred parameter for individual galaxies. In $\sim$ 70% of cases, $\log(U)$ is the the parameter with the narrowest 68% HDI (Δ_{68}), suggesting that the observed nebular spectrum responds most sensitively to changes in the ionization conditions and thus has the most power to discriminate between different ionization parameters. In contrast, $\log(Z_*/Z_\odot)$ is the most precise parameter for no objects, reflecting the relative indirectness of the constraints on the shape of the ionizing radiation obtained from nebular spectroscopy, especially when compared to direct observation of the non-ionizing rest-UV spectum.

individual galaxies are only consistent with a relatively limited range in U, but could be matched by a broader range in $Z_{\rm neb}$, N/O, or Z_* at a given U. In contrast, $\log(Z_*/Z_\odot)$ is the most precise parameter for no galaxies in the sample, consistent with our argument in Section 4.3.3.2 regarding the lack of robust constraints on the shape of the ionizing radiation when using only indirect observables, such as nebular emission lines.

Table 4.2 lists the Spearman coefficient (ρ) and p-value for the correlations between Δ_{68}, S, and K for each model parameter and the SNR of the Balmer decrement and the most commonly-measured strong emission lines. These results indicate that the precision of the model parameter estimates are sensitive to the quality of specific emission line features. Notably, Δ_{68} for $\log(Z_{\rm neb}/Z_\odot)$ correlates most strongly with the SNR of the Balmer decrement, but is also significantly correlated with the SNR of [O II]$\lambda\lambda 3727, 3729$ and [O III]$\lambda 5008$. The precision of inferred log(N/O) is strongly correlated with the SNR of [N II]$\lambda 6585$, [S II]$\lambda\lambda 6718, 6732$,

Table 4.2: Correlations between posterior shape and emission line SNR

Posterior quantity		Balmer decrement SNR		[O III]λ5008 SNR		[O II] SNR		[N II]λ6585 SNR		[S II] SNR	
		ρ	p	ρ	p	ρ	p	ρ	p	ρ	p
$\log(Z_{\rm neb}/Z_\odot)$	S	+0.15	0.1	+0.11	0.3	+0.04	0.7	−0.01	0.9	−0.17	0.1
$\log(Z_{\rm neb}/Z_\odot)$	K	+0.14	0.2	+0.14	0.2	+0.07	0.5	+0.26	7×10^{-3}	+0.33	8×10^{-4}
$\log(Z_{\rm neb}/Z_\odot)$	Δ_{68}	−0.51	3×10^{-8}	−0.46	1×10^{-6}	−0.43	1×10^{-5}	−0.28	4×10^{-3}	−0.28	4×10^{-3}
log(N/O)	S	−0.15	0.1	−0.07	0.5	−0.09	0.4	−0.14	0.2	−0.06	0.5
log(N/O)	K	−0.01	0.9	−0.23	0.02	−0.06	0.6	+0.56	1×10^{-9}	+0.25	0.01
log(N/O)	Δ_{68}	−0.50	1×10^{-7}	−0.12	0.2	−0.48	6×10^{-7}	−0.89	8×10^{-37}	−0.70	5×10^{-16}
$\log(U)$	S	−0.17	0.09	+0.12	0.2	−0.55	9×10^{-9}	−0.34	5×10^{-4}	−0.32	1×10^{-3}
$\log(U)$	K	−0.34	5×10^{-4}	−0.14	0.1	−0.46	3×10^{-6}	−0.18	0.07	−0.16	0.1
$\log(U)$	Δ_{68}	−0.68	5×10^{-15}	−0.58	2×10^{-10}	−0.57	2×10^{-9}	−0.31	2×10^{-3}	−0.37	1×10^{-4}
$\log(Z_*/Z_\odot)$	S	+0.11	0.3	+0.23	0.02	+0.01	0.9	−0.25	0.01	−0.01	1
$\log(Z_*/Z_\odot)$	K	+0.31	1×10^{-3}	+0.22	0.03	+0.11	0.3	+0.32	1×10^{-3}	+0.47	7×10^{-7}
$\log(Z_*/Z_\odot)$	Δ_{68}	−0.58	2×10^{-10}	−0.50	7×10^{-8}	−0.36	3×10^{-4}	−0.26	8×10^{-3}	−0.35	4×10^{-4}

[O II]$\lambda\lambda$3727, 3729, and the Balmer decrement, to a lesser degree. The value of Δ_{68} for $\log(U)$ is strongly correlated with the SNR of all the strongest emission line features, and Δ_{68} for $\log(Z_*/Z_\odot)$ is significantly correlated with the SNR of all but [N II]λ6585.

Collectively, these results have a number of implications for using strong emission line measurements to infer galaxies' physical conditions. First, the nebular spectrum of high-z galaxies is most sensitive to changes in the ionization conditions in the galaxies' H II regions. Consequently, ionization parameter, U, is the most easily and precisely determined quantity, given the observables that are typically available for high-z galaxies. Although there is certainly some ability to discriminate between the likely shape of the ionizing radiation (parameterized in our model by Z_*), our results also underscore that it is preferable to use more direct constraints, such as observations at rest-UV wavelengths, when available.

4.4 New Calibrations for Nebular Strong-Line Diagnostics

The photoionization model method we have introduced can easily be applied to the majority of high-z galaxy samples that currently exist. However, it is useful to test whether there are new calibrations for the commonly-used strong-line diagnostics (especially for N/O and O/H) that may be more appropriate for high-z samples than those based on samples at lower redshifts. Significant effort in the last several years has been dedicated to understanding the evolution of strong-line metallicity indices as a function of redshift (e.g., Jones, Martin & Cooper, 2015; Dopita et al., 2016; Kashino et al., 2017), with the prevailing wisdom being that calibrations based on "extreme" low-z samples of galaxies or H II regions are better suited for use at $\langle z \rangle = 2.3$ than those based on typical local galaxies. Although what is considered extreme varies, this assumption must be true to some degree, as all evidence suggests that typical $\langle z \rangle = 2.3$ galaxies have considerably higher degrees of nebular ionization and excitation than typical local galaxies. But it is also true that $\langle z \rangle = 2.3$ galaxies differ in their characteristic star-formation histories relative to galaxies at $z < 1$. Such differences will result in important variations in the chemical abundance patterns between high-z galaxies and even "extreme" low-z objects, which may, in turn, introduce systematic biases when diagnostics tuned to the latter are applied to the former.

In this section, we investigate the correlation between model-inferred physical conditions for individual galaxies in KBSS and strong-line ratios measured from their

nebular spectra. Such an exercise allows us to both comment on which parameters galaxies' spectra are most sensitive to and offer guidance regarding the utility of strong-line diagnostics at high redshift.

4.4.1 Ionization Parameter

The importance of the ionization state of the gas in H II regions in determining the resulting nebular spectrum is obvious: in order for the majority of the emission line features to be observed, H must be photoionized and then recombine; simultaneously, heavier elements such as N, O, and S must be singly- or doubly-ionized, then collisionally excited. The details of the observed collisionally-excited emission are set by T_e, which is in turn sensitive to the distribution of ionizing photon energies. Practically speaking, O is the only element with multiple ions whose commonly-observed transitions fall in the J-, H-, and K-band for galaxies with $z \simeq 2 - 2.7$[5], making the combination of [O III]λ5008 and [O II]$\lambda\lambda$3727, 3729 measurements a sensitive probe of the ionization conditions in high-z galaxies. Although [O I]λ6301 can be also be observed in the spectra of individual $z \simeq 2-2.7$ galaxies on occasion, emission from neutral O may not be spatially coincident with emission from ionized O, which requires at least an H-ionizing photon to be created. We discuss the challenges associated with observations of ions that trace low-ionization gas in Section 4.4.2 below.

As discussed in Section 4.3.1, we parameterize the ionization state of gas using the ionization parameter, $U = n_\gamma/n_H$. As it relates to O, higher values of U will result in more doubly-ionized O relative to neutral and singly-ionized O in the irradiated gas. In general, n_γ can be varied by changing the shape and/or the normalization of the ionizing radiation field, so measurements of U are most meaningful when details about the ionizing source are also known. In our method, we explicitly decouple these effects so that U reflects the required scaling of the ionizing radiation field, while the shape is set by the input BPASSv2 model.

Figure 4.10 shows the correlation between model-inferred $\log(U)$ and common strong-line indices for the sample of KBSS galaxies with bound posteriors in all model parameters and SNR > 2 for the line measurements used in the given indices (different for each panel). The definitions for O32, Ne3O2, and O3 are listed in Table 4.3, along with other commonly-used strong-line indices. Although all three indices shown in Figure 4.10 are strongly positively correlated with U, the correlation

[5]Doubly-ionized S has a low-lying transition at 9533Å, but this is only observable from the ground for galaxies with $z \lesssim 1.5$.

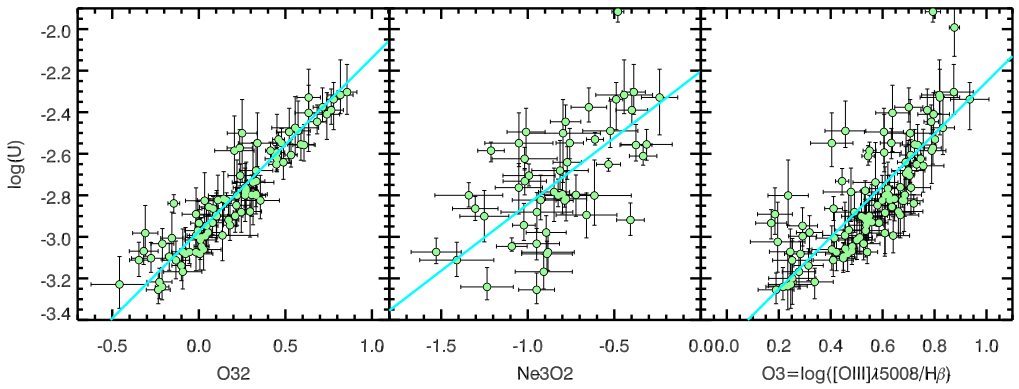

Figure 4.10: The correlation between model-inferred $\log(U)$ and common strong-line indices: O32, Ne3O2, and O3. The green points show the distribution of KBSS galaxies, limited to those with SNR > 2 for the emission lines used to calculate the strong-line indices. Unsurprisingly, O32 shows the strongest correlation and least scatter with $\log(U)$. Although not commonly used to infer $\log(U)$, O3 is also strongly correlated with ionization parameter. Ne3O2 exhibits large scatter, which could be attributed to the lower typical SNR for [Ne III]λ3869 measurements than for [O III]λ5008 or [O II]$\lambda\lambda$3727, 3729. The cyan lines show the best-fit linear relations determined from the KBSS results from our photoionization model method.

with O32 is the most significant (Spearman $\rho = 0.94$, $p = 5 \times 10^{-41}$) and has the least scatter about the best-fit linear relation (determined using the *MPFITEXY* IDL routine[6], Williams, Bureau & Cappellari, 2010), shown in cyan. The calibration based on KBSS galaxies is

$$\log(U) = -2.97 + 0.84 \times \mathrm{O32}, \tag{4.1}$$

Relative to the best-fit relation, the measurements have RMS scatter $\sigma_{\mathrm{RMS}} = 0.09$ dex and an estimated intrinsic scatter $\sigma_{\mathrm{int}} = 0.03$ dex. The same statistics for the correlations between $\log(U)$ and both Ne3O2 and O3 are reported in Table 4.3, corresponding to the following calibrations:

$$\log(U) = -2.20 + 0.64 \times \mathrm{Ne3O2} \tag{4.2}$$

$$\log(U) = -3.50 + 1.25 \times \mathrm{O3}. \tag{4.3}$$

It is perhaps somewhat disappointing that the correlation between Ne3O2 and $\log(U)$ is so poor, given the relatively tight locus in Ne3O2 vs. O32 observed for high-ionization $z \sim 0$ SDSS galaxies. Because [Ne III]λ3869 and [O II]$\lambda\lambda$3727, 3729 are close in wavelength, observing both emission features requires less observing time

[6] `http://purl.org/mike/mpfitexy`

for high-z galaxies, and uncertainties in dust extinction are reduced. However, based on the results for KBSS galaxies presented here, O3 (which has the same advantages) is *more* significantly correlated with $\log(U)$ and has less scatter about the best-fit calibration. Note that the calibrations presented here are only appropriate for objects with similar stellar populations as KBSS galaxies; this is especially important for O3, which is more strongly correlated with O/H in other samples with presumably softer ionizing radiation fields, including SDSS galaxies (Maiolino et al., 2008).

4.4.2 Nitrogen-to-oxygen Ratio

In contrast with U, N/O has a smaller effect on the overall nebular spectra from H II regions, as it primarily affects only emission lines of N. Still, as with U, there are clear and direct proxies for measuring N/O accessible in the rest-optical nebular spectra of galaxies. Due to similarities in the ionization potentials of N and O, the ionization correction factors are also relatively similar, meaning that N^+/O^+ corresponds roughly to N/O. As [N II]λ6585 and [O II]$\lambda\lambda$3727, 3729 are frequently detected in high-z galaxy spectra, N/O is one of the most accessible probes of the chemical abundance pattern in galaxies' interstellar medium (ISM).

The topic of N/O in galaxies has a long history, with a recent resurgence in interest, as samples of high-z galaxies with rest-optical spectra have increased in size and quality (e.g., Masters et al., 2014; Shapley et al., 2015; Masters, Faisst & Capak, 2016; Kashino et al., 2017; Kojima et al., 2017). In S17, we addressed the issue of N/O in KBSS galaxies, using N2O2 and a calibration based on a sample of giant extragalactic H II regions from Pil12. The 414 objects from that work have direct method measurements of N/H and O/H, which make them a useful comparison sample that we also choose to employ here.

Figure 4.11 shows the correlation between model-inferred log(N/O) and N2O2, N2S2 (another commonly-used probe of N/O), and N2 for KBSS galaxies (green points) and the Pil12 H II regions (orange squares), alongside the calibrations based on the Pil12 sample from S17 (red dashed lines) and the new calibrations determined based on the work presented in this chapter (cyan lines). As with the strong-line calibrations for U introduced above, we assess the usefulness of the strong-line ratios as proxies for N/O by calculating the strength and significance of the correlations, as well as the best-fit linear relation between N/O and the indices. The results of

Table 4.3: Correlations between strong-line ratios and model-inferred parameters

Index	Definition	Parameter	ρ	p	$\sigma_{\rm RMS}$ (dex)	$\sigma_{\rm int}$ (dex)
O32[1]	log([O III]$\lambda\lambda$4960, 5008/[O II]$\lambda\lambda$3727, 3729)	U	+0.94	5×10^{-41}	0.09	0.03
Ne3O2	log([Ne III]λ3869/[O II]$\lambda\lambda$3727, 3729)	U	+0.59	6×10^{-6}	0.22	0.20
O3	log([O III]λ5008/Hβ)	U	+0.80	2×10^{-23}	0.17	0.12
N2O2[1]	log([N II]λ6585/[O II]$\lambda\lambda$3727, 3729)	N/O	+0.79	3×10^{-18}	0.11	...
N2S2	log([N II]λ6585/[S II]$\lambda\lambda$6718, 6732)	N/O	+0.80	3×10^{-19}	0.11	...
N2	log([N II]λ6585/Hα)	N/O	+0.77	4×10^{-19}	0.12	...
		O/H	+0.29	5×10^{-3}	...	...
O3N2	log([O III]λ5008/Hβ)$-$ log([N II]λ6585/Hα)	O/H	-0.35	6×10^{-4}	0.16	0.11
R23[1]	log[([O III]$\lambda\lambda$4960, 5008+[O II]$\lambda\lambda$3727, 3729)/Hβ]	O/H	-0.47	5×10^{-7}	0.09	0.06

[1] Requires an extinction correction; we have adopted the Cardelli, Clayton & Mathis (1989) extinction curve.

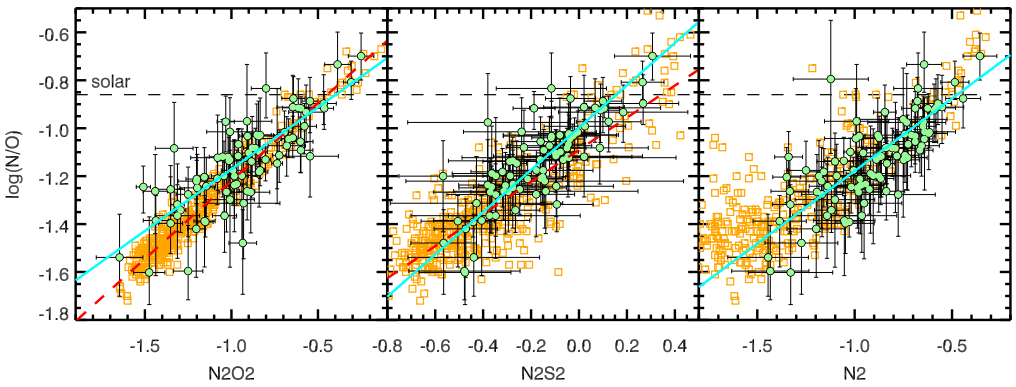

Figure 4.11: The correlation between model-inferred log(N/O) and common strong-line indices: N2O2, N2S2, and N2. As in Figure 4.10, the green points show the location of KBSS galaxies with SNR > 2 for the emission lines in the strong-line indices. For comparison, local H II regions from Pil12 are shown as orange squares. The dashed horizontal line shows the solar value from Asplund et al. (2009). The red dashed lines show the calibrations determined using a sample of local H II regions from Pil12, whereas the solid cyan lines show the calibrations determined from the KBSS sample.

these analyses are listed in Table 4.3[7], and the calibrations themselves are

$$\log(\mathrm{N/O}) = 0.55 \times \mathrm{N2O2} - 0.61 \tag{4.4}$$

$$\log(\mathrm{N/O}) = 0.94 \times \mathrm{N2S2} - 0.98 \tag{4.5}$$

$$\log(\mathrm{N/O}) = 0.57 \times \mathrm{N2} - 0.60. \tag{4.6}$$

All three indices have similarly significant correlations with N/O, as determined by their Spearman ρ and p values, and very similar RMS scatter relative to the new calibrations. We can take some guidance from the distribution of Pil12 H II regions, which exhibit similar behavior in the indices relative to N/O, but have smaller measurement errors. For the Pil12 sample, N2O2 (which is the most direct proxy for N/O) exhibits the smallest scatter relative to the best-fit relation based on the same sample (the red dashed line in the left panel of Figure 4.11); this suggests that N2O2 may also be the most accurate probe of N/O in high-z galaxies.

Although the calibrations based on the Pil12 sample are similar to those based on our new measurements for individual $\langle z \rangle = 2.3$ KBSS galaxies (especially for N2O2), we note that calibrations based on samples of local *galaxies* generally fare much worse in returning accurate estimates of N/O for high-z galaxies. Figure 4.12 shows the reason for this discrepancy. Although N2S2 and N2O2 have almost

[7]The intrinsic scatter, σ_{int} cannot be calculated for the N/O calibrations because measurement errors dominate the observed scatter in the correlations.

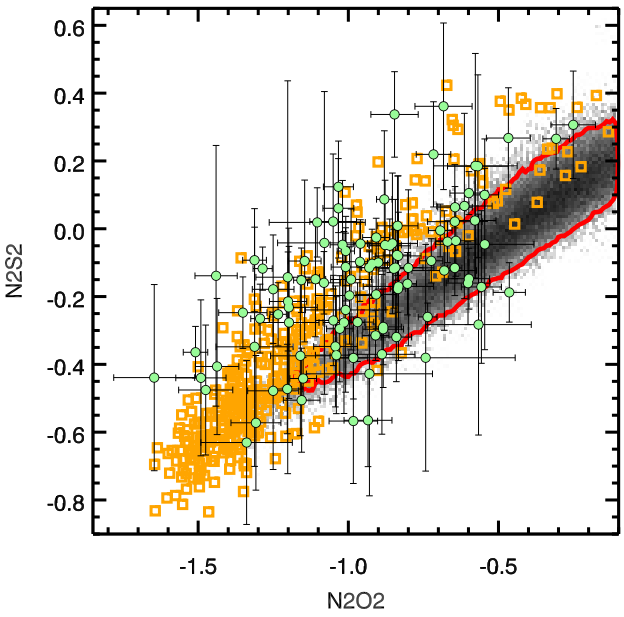

Figure 4.12: N2S2 vs. N2O2 for three samples of objects: $\langle z \rangle = 2.3$ KBSS galaxies (green points), individual $z \sim 0$ H II regions from Pil12 (orange squares), and $z \sim 0$ galaxies from SDSS (greyscale, with 90% of the sample enclosed by the red contour). As in Figure 4.11, KBSS galaxies and the Pil12 sample exhibit similar behavior, suggesting that N2O2 and N2S2 trace N/O in similar ways between the two samples. However, the locus of SDSS galaxies occupies a distinct region of parameter space, with somewhat higher N2O2 and N2S2 overall, but lower N2S2 at a given N2O2 than either the $\langle z \rangle = 2.3$ galaxies or $z \sim 0$ H II regions.

identical behavior relative to one another for KBSS galaxies (green points) and Pil12 H II regions (orange squares), the behavior of the same indices for $z \sim 0$ galaxies from SDSS (greyscale, with 90% of galaxies enclosed by the red contour) differs significantly, particularly at higher values of N2S2 and N2O2. Just as locally-calibrated strong-line methods for O/H that use the N2-BPT lines will return inconsistent estimates relative to one another for objects that fall significantly off the $z \sim 0$ N2-BPT locus, strong-line methods for N/O based on $z \sim 0$ galaxies will disagree for high-z galaxies.

This effect poses challenges to easily comparing N/O inferred using N2S2 and N2O2. Masters, Faisst & Capak (2016) argue that the N/O-M_* relation evolves slowly with redshift, with high-z galaxies exhibiting only slightly lower N/O at fixed M_* relative to local galaxies. Their inferences are based on results from Kashino et al. (2017), who examine the behavior of N2S2 with M_* for a sample of $z \sim 1.6$ galaxies from the FMOS-COSMOS program (Silverman et al., 2015) relative to

$z \sim 0$ galaxies from SDSS and find that the values of N2S2 observed in high-mass galaxies in their sample approach the N2S2 measured in high-mass SDSS galaxies. Based on these observations and the expectation that the mass-metallicity relation evolves more quickly with redshift (e.g., Erb et al., 2006a; Steidel et al., 2014; Sanders et al., 2015), Masters, Faisst & Capak (2016) claim that the slight observed decrement in N2S2 of the $z \sim 1.6$ FMOS-COSMOS galaxies relative to $z \sim 0$ SDSS galaxies reflects higher N/O values in high-z galaxies at fixed O/H relative to the N/O-O/H relation observed in the local universe. From our analysis of N/O in KBSS galaxies in S17, however, we show that the evolution in the N/O-M_* relation is roughly equivalent in magnitude to the inferred evolution in the O/H mass-metallicity relation, with $\langle z \rangle = 2.3$ galaxies exhibiting values of log(N/O) that are ~ 0.32 dex lower than $z \sim 0$ galaxies at fixed M_*. While we could not directly study the N/O-O/H relation for high-z galaxies in S17, we revisit the likelihood of elevated N/O in Section 4.5.2.

The behavior of N2S2 and N2O2 shown in Figure 4.12 offers some clues that may explain the discrepancy between our interpretation of the data and the interpretation favored by Masters, Faisst & Capak (2016) and Kashino et al. (2017). We can confidently assume that N/O increases with increasing N2S2 and N2O2 for all three samples. Nevertheless, it is apparent N2S2 does not increase as quickly with N/O in $z \sim 0$ galaxies as it does in $z \sim 0$ H II regions and $\langle z \rangle = 2.3$ galaxies. As a result, a comparison between N2S2, without first converting the index to N/O using the appropriate calibration, will underestimate N/O in $z \sim 0$ galaxies relative to $\langle z \rangle = 2.3$ galaxies. Conversely, it is possible that comparing N2O2 between $z \sim 0$ and $\langle z \rangle = 2.3$ galaxies (as we did in S17 by using the same calibration for N/O) may over-estimate the difference between the two samples, but N2O2 remains a far more direct tracer of N/O than N2S2.

The comparison between N2S2 and N2O2 shown in Figure 4.12 also highlights an intriguing and likely very meaningful result: $\langle z \rangle = 2.3$ galaxies appear to have nebular spectra that are much more similar to individual H II regions at $z \sim 0$ than to intregrated-light spectra of $z \sim 0$ galaxies. There are a number of reasons this might be the case, but as other authors (including Sanders et al., 2016; Kashino et al., 2017) have also suggested, the most straightforward explanation is that star-formation in $\langle z \rangle = 2.3$ galaxies takes place mostly in one, or a few, dominant H II regions, compared to typical $z \sim 0$ galaxies with similar M_*, where H II regions are more isolated with respect to one another. Thus, an integrated-light spectrum of

a local galaxy may potentially include contributions from gas outside H II regions (especially for neutral ions like O and low-ionization species like S^+, which do not require an H-ionizing photon to be created). In this context, the behavior of N2S2 for SDSS galaxies in Figure 4.12 makes more sense: if the [S II]$\lambda\lambda$6718, 6732 observed in SDSS galaxy spectra include contributions from this "diffuse ionized gas" in addition to the H II region emission, N2S2 will be depressed relative to high-z galaxies and individual H II regions at fixed N2O2.

4.4.3 Oxygen Abundance

Of perhaps greatest interest is the potential to provide new calibrations for strong-line diagnostics for O/H, which is generally the quantity one intends when referring to gas-phase "metallicity". The impact of the overall metallicity of ionized gas on the resulting nebular spectrum is more nuanced than the effects of ionization and differences in abundance *ratios*, like N/O. Metals, like O, are the primary coolants in low-density ionized gas, as they are able to convert kinetic energy in the gas into electromagnetic emission through collisionally-excited transitions. Yet, trends in emission line strength with O/H for transitions such as [O III]λ5008 are frequently complicated due to the competition between enrichment and gas cooling. The classic example is the double-valued behavior of R23, which increases with increasing O/H due to the larger number of O atoms present—until some critical value (usually near $12 + \log(\mathrm{O/H}) = 8.3$, but sensitive to the shape of the ionizing radiation field), at which point gas cooling due to metals dominates, and the observed value of R23 decreases again. Galaxies or H II regions with maximal values of R23($\approx 0.8 - 1.0$) must therefore have moderate O/H, as lower or higher values of O/H would result in a lower value of R23 being observed. This reasoning led us to conclude in S16 and S17 that most $\langle z \rangle = 2.3$ KBSS galaxies must be moderately O-rich, which we have now confirmed in this chapter (Figure 4.5).

For strong-line indices other than R23, including O3N2 and N2, part of the ability to estimate O/H comes from indirectly measuring N/O instead (by including [N II]λ6585) and relying on the existence a single, zero-scatter relationship between N/O and O/H. This implicit dependence on the N/O-O/H relation is what, until now, has prevented a direct investigation of the N/O-O/H relation at high-z (the subject of Section 4.5.2) and an independent analysis of O/H enrichment in the early universe, free from the biases introduced by relying on local calibrations.

We are now poised to develop new calibrations for O/H using the results from our

photoionization model method, but must first address the issue of abundance scales. To this point, we have reported the results of our photoionization model method in terms of $Z_{\rm neb}$. However, given the importance of O to the overall mass budget of metals in H II regions and, thus, to gas cooling and the nebular spectrum, it is reasonable to assume that $Z_{\rm neb}$ largely traces gas-phase O/H. As a result, we may convert $\log(Z_{\rm neb}/Z_{\odot})$ to the more commonly-used metric $12+\log({\rm O/H})$ by adopting a fiducial solar value. From Asplund et al. (2009), $12 + \log({\rm O/H})_{\odot} = 8.69$, so $12 + \log({\rm O/H})_{\rm KBSS} = \log(Z_{\rm neb}/Z_{\odot}) + 8.69$.

The O/H scale that results from this translation differs significantly from the abundance scale for diagnostics determined using T_e-based measurements of O/H, which are lower by ≈ 0.24 dex relative to measurements based on nebular recombination lines (see the discussion in Section 8.1.2 of Steidel et al. 2016; also Esteban et al. 2004; Blanc et al. 2015). Authors who have investigated this phenomenon report that the abundances resulting from recombination line methods are in fact closer to the *stellar* abundance scale than abundances from T_e-based methods that rely on collisionally-excited emission lines. In order to compare the O/H measurements for the local H II region sample introduced in the previous section, which are based on measurements of T_e, we must therefore shift the Pil12 abundances toward higher $12 + \log({\rm O/H})$ by 0.24 dex. It is not necessary to account for this difference when considering the abundance *ratio* N/O, as it affects inferences of both O/H and N/H.

Figure 4.13 compares the correlation between $12 + \log({\rm O/H})$ and the three most commonly-used strong-line indices for measuring O/H for both $\langle z \rangle = 2.3$ KBSS galaxies (green points) and the local H II regions from Pil12 (orange squares). Notably, R23 shows the strongest trend with $12 + \log({\rm O/H})$ for $\langle z \rangle = 2.3$ KBSS galaxies, with O3N2 and N2 with O3N2 showing markedly larger scatter. Table 4.3 lists the Spearman rank correlation coefficients and p-values for all three indices.

As with strong-line indices and N/O in Figure 4.11, the behavior of R23 with O/H appears very similar to that observed for the Pil12 H II regions, although the KBSS sample mostly populates the high-metallicity "branch." If we solve for a second-order polynomial calibration that describes the relation between $12 + \log({\rm O/H})$ and R23 for the KBSS sample (shown in cyan in the left panel of Figure 4.13), we find

$$12 + \log({\rm O/H}) = 8.22 + (0.81 - 0.83 \times {\rm R23})^{1/2}, \tag{4.7}$$

with the measurements exhibiting $\sigma_{\rm RMS} = 0.09$ dex and $\sigma_{\rm int} = 0.06$ relative to the calibration.

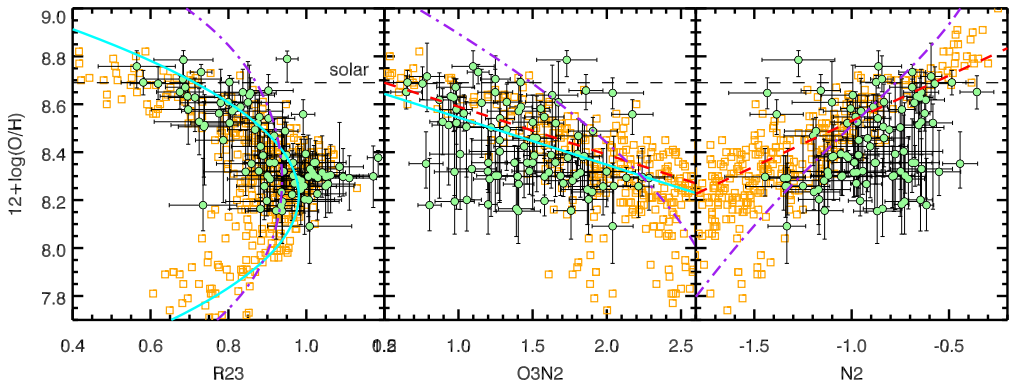

Figure 4.13: The correlation between 12 + log(O/H) and the most commonly-used strong-line diagnostics for O/H, shown in the same manner as Figure 4.11. The $\langle z \rangle = 2.3$ KBSS points are illustrated as green points with error bars, using the value of their model-inferred O/H. The $z \sim 0$ Pil12 sample is shown as orange squares, using O/H estimated using the direct method and shifted toward higher O/H by 0.24 dex to account for the difference in abundance scale, as described in the text. The red dashed lines show the calibrations based on the Pil12 sample from S17, and the purple dot-dashed lines represent the calibrations from Maiolino et al. (2008). Although all three indices are significantly correlated with O/H for the $z \sim 0$ objects, only R23 and O3N2 show significant correlations with O/H for KBSS galaxies. The new calibrations for R23 and O3N2 based on KBSS galaxies are shown in cyan.

This calibration is significantly different from the calibration for R23 provided by Maiolino et al. (2008), which we have shifted by 0.24 dex and shown as the dot-dashed purple curve. In that work, the authors used a superset of direct method and photoionization model measurements of O/H to construct a family of self-consistent strong-line diagnostics (the corresponding calibrations for O3N2 and N2 are also shown in the right panels). Although both the Maiolino et al. (2008) and KBSS calibrations reach a maximum value of R23 at nearly the same oxygen abundance (12 + log(O/H) $\approx$ 8.25) the KBSS calibration has a smaller latus rectum, with R23 varying more quickly as a function of O/H. We note, however, that $\sim$ 72% of $\langle z \rangle = 2.3$ KBSS galaxies have R23 > 0.8, where the index (regardless of calibration choice) becomes largely insensitive to changes in O/H. As a result, even our re-calibration for R23 is primarily useful for O-rich galaxies.

If we attempt to construct a calibration based on O32 *and* R23, in order to jointly account for the effects of O/H and U, we can reduce the scatter relative to the model-inferred O/H at high metallicities, as shown in Figure 4.14. Here, we have chosen a

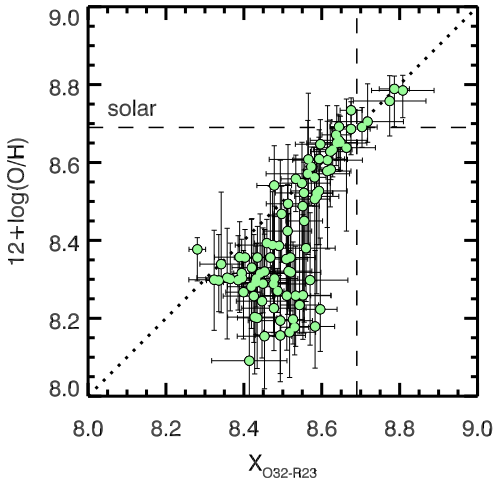

Figure 4.14: 12 + log(O/H) as a function of $X_{\rm O32\text{-}R23}$, a diagnostic combining O32 and R23, as described in the text. The dotted line shows the one-to-one relation. Although making use of both indices reduces scatter relative to the model-inferred O/H at high-metallicities, the calibration fails at $12+\log({\rm O/H}) \lesssim 8.6$. The point at which the calibration ceases to discriminate between metallicities is dependent on the exact formulation of the combined diagnostic, but is never useful for $12 + \log({\rm O/H}) \lesssim 8.4$.

diagnostic with the following form:

$$12 + \log({\rm O/H}) = X_{\rm O32\text{-}R23} = 9.04 + 0.50 \times {\rm O32} - 0.51 \times {\rm R23} + 0.26 \times {\rm O32}^2 \\ -0.12 \times {\rm R23}^2 - 0.50 \times ({\rm O32} \times {\rm R23}), \tag{4.8}$$

which is based on the sample of KBSS galaxies occupying the upper branch of the R23 relation, corresponding to $12 + \log({\rm O/H}) \geq 8.3$, and determined using a least-squares fit. For large values of O/H, this calibration has less RMS scatter than the R23-only calibration—but it fails for galaxies with $12 + \log({\rm O/H}) \lesssim 8.6$, greatly reducing its utility. It is likely that a separate O32-R23 calibration could be determined for galaxies on the low-metallicity branch in R23, but it is clear that inferring O/H for galaxies with R23 near the maximum using a simple strong-line diagnostic is more challenging.

Unlike R23, the behavior of O3N2 with O/H is markedly different for KBSS galaxies relative to the Pil12 H II regions, though the index is still significantly, albeit weakly, correlated with O/H. The best-fit linear calibration for the correlation is

$$12 + \log({\rm O/H}) = 8.74 - 0.20 \times {\rm O3N2}, \tag{4.9}$$

which has $\sigma_{\rm RMS} = 0.16$ dex and estimated intrinsic scatter $\sigma_{\rm int} = 0.11$ dex. This is almost twice as large as the scatter relative to the R23 calibration and could lead to O/H estimates for high-z galaxies that are significantly different from the true value.

The large scatter between N2 and O/H for KBSS galaxies is also notable and cautions against using the index as a diagnostic for O/H in high-z galaxies. Like O3N2, N2 has been favored in the past, largely because the index is less sensitive to dust

reddening and requires fewer emission line measurements and, thus, necessitates less observing time. However, given the large scatter observed for the KBSS sample, it is not possible to construct a new calibration for N2—and if a calibration based on the local sample (the red dashed line in the right panel of Figure 4.13) is used instead, our results imply that 12 + log(O/H) could be overestimated by up to ~ 0.4 dex for some high-z galaxies.

In conclusion, our analysis indicates that the most accurate and precise estimates of 12 + log(O/H) for $\langle z \rangle = 2.3$ galaxies result from using a photoionization model method such as the one described in this chapter. Although R23 (or a combined diagnostic using O32 and R23) is useful for galaxies with relatively high metallicities ($12 + \log(\mathrm{O/H}) \gtrsim 8.5 - 8.6$), there is significant added value in using the same emission line measurements to simultaneously estimate O/H, N/O, and U.

4.5 Intrinsic Correlations Between Galaxies' Physical Conditions

We have previously noted the similarity in the behavior of the nebular spectra of $\langle z \rangle = 2.3$ KBSS galaxies and individual local H II regions—especially as compared to $z \sim 0$ galaxies. It is likely that this agreement—or disagreement, in some cases—arises from similarities and differences in the underlying correlations between the physical conditions driving the observed spectrum. Thus, it is important to quantify the intrinsic correlations between these parameters to understand the ways in which the high-z galaxy populations differ from galaxies found in the present-day universe.

4.5.1 Correlations Between Model Parameters for Individual Galaxies

When performing linear regression of astronomical data, the measurement errors on the independent and dependent variables are often assumed to be independent. In the case that the measurement errors are actually correlated, however, the magnitude of the observed correlation will be overestimated if the measurement error correlation has the same sign as the intrinsic correlation between variables and underestimated in cases where the measurement error correlation has a different sign from the intrinsic correlation (Kelly, 2007). As a result, weak correlations where the measurement error correlation has the opposite sign may be unrecoverable unless the measurement errors *and* the covariance between measurement errors have been accounted for using a statistical model.

From the MCMC results shown in Figures 4.3 and 4.4, it clear that the model parameter estimates are correlated with one another for at least some fraction of the KBSS sample. In addition to knowing the correlation between model parameters

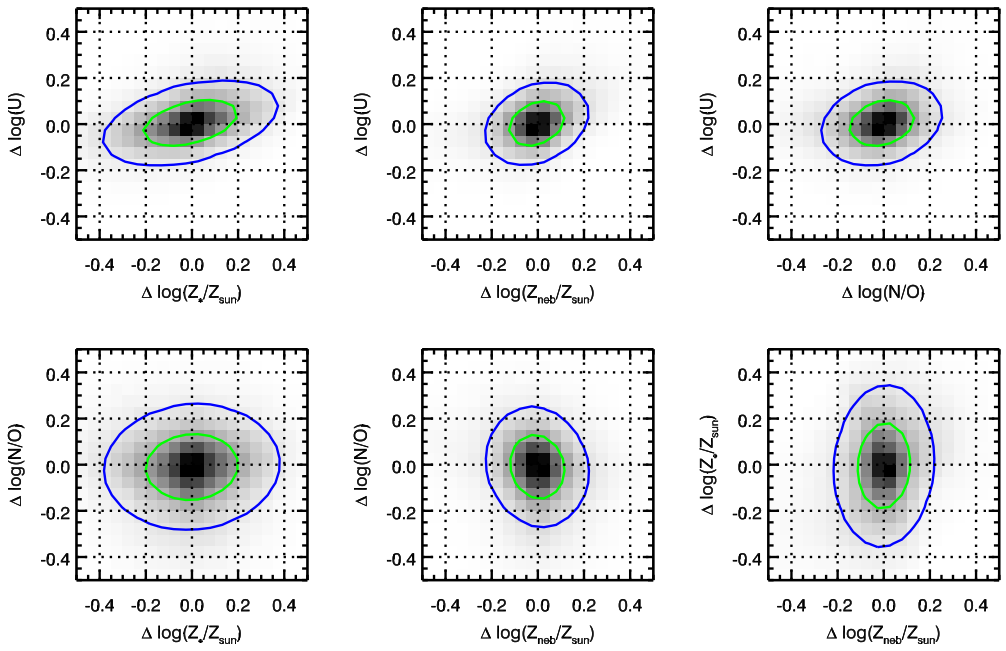

Figure 4.15: The average 2D posterior distributions for $\log(Z_{\rm neb}/Z_\odot)$, log(N/O), $\log(U)$, and $\log(Z_*/Z_\odot)$. The density maps are constructed by shifting the normalized 2D posteriors such that the MAP estimates for the parameters are at the origin and summing the posteriors for all objects with bound posteriors. The blue and green isodensity contours are drawn at 10% and 50% of the peak density, assuming the posteriors can be described by a bivariate Gaussian. The 2D posteriors illustrate the typical correlation between parameters as well as the relative precision of the parameter estimates. For example, $\log(U)$ is generally better constrained than $\log(Z_*/Z_\odot)$, but the parameters are highly correlated. In contrast, estimates of log(N/O) and $\log(Z_*/Z_\odot)$ exhibit less correlation with one another, on average.

for individual objects—important for recovering the intrinsic correlation between parameters for the entire sample—it is also interesting to understand the correlation between model parameters for an average galaxy, which can inform our intuition regarding galaxies' nebular spectra.

Figure 4.15 shows the average pairwise posteriors for the 4 model parameters, which have been constructed by shifting the normalized 2D posteriors for individual objects so that the peak of the distribution is located at the origin and summing the PDFs for all objects with bound posteriors. The green and blue contours highlight the shape of the posterior, assuming it can be described by a bivariate Gaussian function. The correlations between some model parameters are expected, including the strong correlation between U and $Z_*/Z_\odot$ (upper left panel), which parameterize the normalization and shape of the ionizing radiation, respectively. These results highlight the power of applying additional constraints, where available. For example,

Table 4.4: Correlations between model parameters for individual galaxies

Parameter 1	Parameter 2	Correlation
$\log(Z_*/Z_\odot)$	log(N/O)	+0.06
$\log(Z_{\rm neb}/Z_\odot)$	$\log(Z_*/Z_\odot)$	+0.07
$\log(Z_{\rm neb}/Z_\odot)$	log(N/O)	−0.10
log(N/O)	$\log(U)$	+0.22
$\log(Z_{\rm neb}/Z_\odot)$	$\log(U)$	+0.27
$\log(Z_*/Z_\odot)$	$\log(U)$	+0.41

Note: The linear correlation coefficient is determined from the covariance matrix derived from the 2D Gaussian fit to the average pairwise posteriors.

if we could impose a prior on Z_* from observations of the rest-UV spectra of the same galaxies (as we did for a composite spectrum in S16), our estimates of $\log(U)$ would be more precise because we would not need to marginalize over as large a range in Z_*.

In some cases, the correlations between inferred parameters run counter to our expectations for the correlations between the same parameters in the entire sample: N/O and $Z_{\rm neb}/Z_\odot$ are anti-correlated for a typical individual galaxy (bottom middle panel), whereas N/O and O/H (which is traced by $Z_{\rm neb}/Z_\odot$) are positively correlated for galaxy and H II region samples in the nearby universe. This result underscores the importance of accounting for the correlations between inferred parameters for individual objects when quantifying the intrinsic correlations between the same parameters in the full sample, which is the focus of the remainder of this section.

4.5.2 N/O-O/H Relation

In Figure 4.16, we show that $\langle z \rangle = 2.3$ star-forming galaxies exhibit N/O ratios at fixed O/H consistent with the range observed in local H II regions. The KBSS sample is shown as green points or green triangles (for galaxies with only upper limits on N/O), with the local sample from Pil12 represented by the orange contours; 82% of KBSS galaxies fall within the outermost contour, which contains 99% of the Pil12 objects, and there is good agreement in the distribution of N/O at fixed O/H between the samples. We note that the paucity of objects with $12 + \log(\mathrm{O/H}) < 8.2$ is likely the result of selection bias; galaxies with lower M_* than typical KBSS galaxies ($M_* \ll 10^9\ M_\odot$), such as the Lyman-α-selected galaxies from Trainor et al. (2016), are expected to populate this region of parameter space.

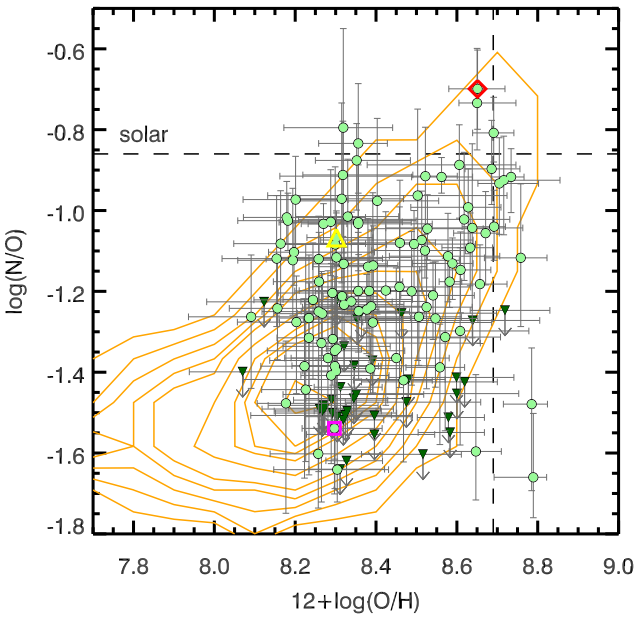

Figure 4.16: The N/O-O/H relation observed for $\langle z \rangle = 2.3$ KBSS galaxies, shown as green points; galaxies with only a limit on the inferred value of log(N/O) are shown as dark green triangles at the location corresponding to a 2σ upper limit. For comparison, the distribution of $z \sim 0$ objects from Pil12 is represented by the orange contours, with the outermost contour enclosing 99% of the sample. Most of the KBSS galaxies ($\sim$ 82%) fall within these contours and appear to follow the same trend as the local H II regions. Three galaxies with different combinations of N/O and O/H are highlighted by colored symbols: Q1442-RK119 (red diamond), Q1442-BX235 (yellow triangle), and Q0449-BX22 (magenta square). For comparison, the locations of these galaxies in common line-ratio diagrams are shown in Figure 4.17.

Like the $z \sim 0$ sources, $\langle z \rangle = 2.3$ galaxies show large scatter in N/O at fixed O/H. At 12 + log(O/H) = 8.3 ($Z_{\rm neb}/Z_{\odot} \approx 0.4$), the full range in observed log(N/O) is $\sim$ 0.8 dex, consistent with that observed among the Pil12 H II regions. Although N/O and O/H are formally significantly correlated for the local sample, a simple Spearman test indicates only a marginally significant correlation between the two parameters for KBSS galaxies ($\rho = 0.20$, $p = 0.02$). Given the significant anti-correlation between inferred N/O and O/H for individual galaxies (Figure 4.15, Table 4.4), however, a Spearman test is likely to underestimate the presence of a positive correlation between N/O and O/H for the KBSS sample. To address this issue, we use the IDL routine LINMIX_ERR to measure the strength of the correlation between N/O and O/H among the KBSS galaxy sample while accounting for both measurement errors and the covariance between measurement errors. The resulting linear correlation coefficient inferred for the $\langle z \rangle = 2.3$ N/O-O/H relation

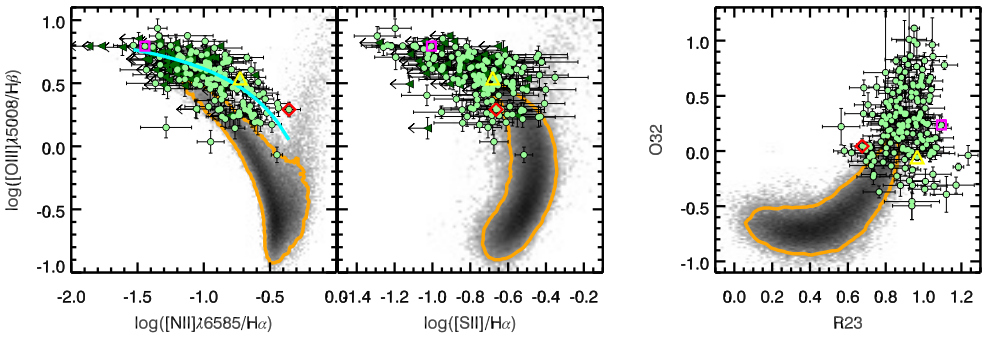

Figure 4.17: Three classic nebular diagnostic diagrams (the N2-BPT, S2-BPT, and O32-R23 diagrams), showing the location of the galaxies highlighted in Figure 4.16 in observed line-ratio space; the cyan curve in the left panel reflects the ridge-line of the $z \sim 2$ KBSS sample from S17. Q1442-RK119 (identified by the red diamond) has the highest N/O in the sample, and also shows the largest [N II]/Hα ratio. Q1442-BX235 (yellow triangle) and Q0449-BX22 (magenta square) have different inferred N/O but very similar O/H, but show significant differences not only in [N II]/Hα, but in all three line ratio diagrams. These results demonstrate the challenges associated with attempts to derive physical information from a single 2D projection of multidimensional line-ratio space.

is $\rho = 0.47$, with an overall 99.9% likelihood of a positive correlation between the parameters and an estimated intrinsic scatter of $\sigma_{\rm int} = 0.13$ dex.

The cause of this intrinsic scatter in N/O at fixed O/H is not immediately obvious, for either the $\langle z \rangle = 2.3$ sample or $z \sim 0$ objects. Some authors have found that local galaxies with higher N/O at a given O/H also have higher SFR (Andrews & Martini, 2013), but we find no strong evidence of a similar trend for the KBSS sample. To illustrate differences in the nebular spectra of high-z galaxies found in different regions of the N/O-O/H plane, we highlight three galaxies in Figure 4.16: Q1442-RK119, which has the highest value of N/O in the KBSS sample (red diamond); Q1442-BX235, near the upper envelope of the locus at more moderate O/H (yellow triangle); and Q0449-BX22, which has similar O/H to Q1442-BX235, but is near the low-N/O edge of the distribution (magenta square). The locations of these galaxies in the N2-BPT, S2-BPT, and O32-R23 diagrams are also noted in Figure 4.17. As expected for a galaxy with high N/O, Q1442-RK119 also has a very high value of N2 (the highest among the star-forming KBSS galaxies discussed in this chapter[8]). Further, in contrast to the two galaxies with more moderate O/H, Q1442-RK119 is found on the low-R23 side of the galaxy locus in the O32-R23 diagram, as expected.

[8]AGN at similar redshifts can have higher N2 values, which we reported for KBSS in S17. Coil et al. (2015) discusses the nebular properties of a more diverse sample of AGN from the MOSDEF survey, which extend to even larger N2.

A comparison between the locations of Q1442-BX235 and Q0449-BX22 demonstrates that an increase in N/O at fixed O/H does not correspond only to a horizontal shift in the N2-BPT diagram as one might naively expect; instead, Q1442-BX235 also exhibits lower [O III]/Hβ and O32 and higher [S II]/Hα. Together, these differences reflect a decrease in log(U) of 0.5 dex (at similar O/H to Q0449-BX22), which is clear when information from all three diagrams is incorporated (as in our photoionization model method) but more difficult to diagnose on the basis of the galaxies' locations in a single diagram.

4.5.2.1 Enhanced N/O and the N2-BPT Offset

In S17, we studied the distribution of N/O (inferred using N2O2) within the KBSS sample, without the aid of independent estimates of O/H. Based on our comparison between $\langle z \rangle = 2.3$ KBSS galaxies and $z \sim 0$ galaxies that likely share similar ionizing radiation fields, we concluded that although high-z galaxies may have somewhat higher N/O than local galaxies with the same O/H, this could not account for the entirety of the offset observed between typical $\langle z \rangle = 2.3$ galaxies and typical $z \sim 0$ galaxies in the N2-BPT diagram. Now, with self-consistent estimates of N/O and O/H in hand for a large sample of $\langle z \rangle = 2.3$ galaxies, we can revisit the question of whether N/O is enhanced in the most offset star-forming galaxies at high-z.

If we simultaneously solve for the best-fit linear relation between N/O and O/H for KBSS galaxies that fall above the sample ridge-line in the N2-BPT diagram (the cyan curve in the left panel of Figure 4.17) and those that fall below the ridge-line, we confirm an offset between the two samples of $\Delta \log(\mathrm{N/O}) = 0.13 \pm 0.05$ dex, with the most offset KBSS galaxies exhibiting significantly higher N/O at fixed O/H than KBSS galaxies that appear more similar to typical galaxies in SDSS. We note that this difference cannot account for the total offset between the KBSS subsamples in the N2-BPT diagram (≈ 0.34 dex, S17), reaffirming our conclusion from S14 and S17 that high-z galaxies must also have harder ionizing radiation fields at fixed O/H relative to typical local galaxies. The harder spectra, which we have argued are due to more Fe-poor stellar populations, account for the remainder of the offset that cannot be explained by the modest N/O enhancement we find here.

4.5.3 U-O/H and U-Z_* Relations

Several authors have found evidence for an anti-correlation between ionization parameter and O/H in low-z samples (e.g., Dopita & Evans, 1986; Dopita et al., 2006;

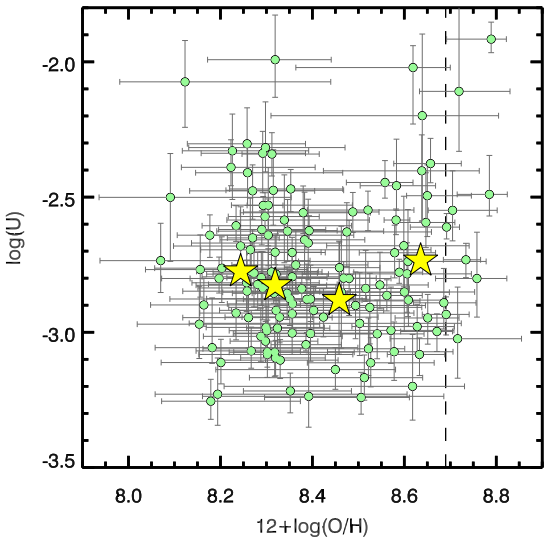

Figure 4.18: Ionization parameter as a function of gas-phase O/H for 138 $\langle z \rangle = 2.3$ KBSS galaxies. The yellow stars represent the median value of $\log(U)$ in equal-number bins of $12+\log(\mathrm{O/H})$. The dashed vertical line represents the solar value of $12+\log(\mathrm{O/H})_\odot = 8.69$. There is no obvious relationship between the two model-inferred parameters for the high-z sample. Even after accounting for measurement errors and covariance between measurement errors, the probability of an anti-correlation is only 75%, with a likely linear correlation coefficient of $\rho = -0.09$.

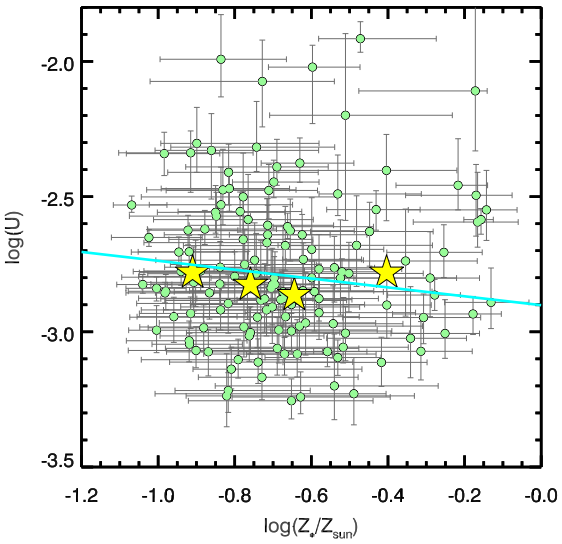

Figure 4.19: Ionization parameter as a function of stellar metallicity, which traces Fe/H, for the same galaxies shown in Figure 4.18; here, the yellow stars show the median value of $\log(U)$ in equal-number bins of $Z_*/Z_\odot$. Accounting for measurement errors reveals evidence of a stronger and more significant anti-correlation than observed between U and O/H. We calculate a 90% probability of a negative correlation, with a linear correlation coefficient of $\rho = -0.16$. The best-fit linear relation corresponding to this correlation is shown as a cyan line in the figure.

Pérez-Montero, 2014), but evidence for a similar trend among high-z galaxies is less abundant. Sanders et al. (2016) offer a thorough exploration of the behavior of O32 with galaxy properties in $\langle z \rangle = 2.3$ MOSDEF galaxies, noting the strong observed anti-correlation between O32 and M_* and suggesting that an anti-correlation between ionization parameter and metallicity at high-z might also exist, given the existence of a mass-metallicity relation. Onodera et al. (2016) estimate q ($\equiv Uc$) and O/H for a sample of $z \gtrsim 3$ galaxies using strong-line methods and recover a strong anti-correlation, but note that it arises largely because both parameters are estimated using the same line ratio. Although Kojima et al. (2017) use T_e-based estimates of O/H instead of relying on strong-line methods, they find that most of the $z \sim 2$ galaxies in their sample are not consistent with the observed U-O/H relation at $z \sim 0$.

We find little evidence for a correlation between U and O/H in the KBSS sample, even after accounting for measurement errors and the correlation between the inferred parameters for individual galaxies (Figure 4.18). Our results imply that there is only a 75% probability of an intrinsic anti-correlation between U and O/H, with a very weak linear correlation coefficient ($\rho = -0.09$). Given our sample selection, the range in O/H observed in typical KBSS galaxies does not extend to very low metallicities, which could impede our ability to recover a weak, but significant anti-correlation. It is also possible that our definition of U, which is a free parameter that does not incorporate differences in geometry or the shape of the ionizing radiation field, obscures the intrinsic relationship between the total ionizing flux and O/H which has been found at $z \sim 0$, often using somewhat different definitions for ionization parameter.

Still, although unexpected in the context of the local universe, the absence of a strong anti-correlation between U and O/H, coupled with the sensitivity of high-z galaxies' nebular spectra to differences in U (Figure 4.10), does offer an explanation for the relative difficulty in determining O/H from the same nebular emission features (Figure 4.13). Even though our analysis suggests that $\langle z \rangle = 2.3$ KBSS galaxies follow the same N/O-O/H relation as observed in the local universe and that N/O can be accurately and precisely determined for high-z galaxies using common strong-line diagnostics (Figure 4.11), measuring O/H will remain a challenge if it is not also strongly correlated with U (as it appears), especially given the large scatter observed in the N/O-O/H relation.

In addition to the issues of selection bias and model construction we have already highlighted, there may be a physical reason to expect the behavior of U and O/H in

high-z galaxies seen in Figure 4.18. Dopita et al. (2006) assert that the underlying astrophysical cause for an observed U-O/H anti-correlation is the effect of increasing metallicity on the opacity of stellar atmospheres, which will (1) increase the number of ionizing photons absorbed by the stellar wind and (2) more efficiently convert luminous energy flux to mechanical energy needed to launch the wind. However, O/H does not trace enrichment in Fe (which is the primary source of the opacity in stellar atmospheres and is responsible for driving stellar winds) at high-z in the same manner as in the majority of local galaxies, so the absence of a strong anti-correlation between U and O/H is not surprising, especially when the expected correlation is in fact between U and Z_*. Figure 4.19 shows the correlation between U and Z_*, as observed in the KBSS sample. After accounting for measurement errors, we find a 90% probability of an anti-correlation, with a linear correlation coefficient of $\rho = -0.16$. The corresponding best-fit linear relation is shown in cyan and has the form:

$$\log(U) = -2.91 - 0.19 \times \log(Z_*/Z_\odot). \tag{4.10}$$

Our understanding of the intrinsic correlations between U and other parameters will benefit from expanding high-z samples to include a larger range in O/H and Z_*, if present, but it seems clear that the paradigm based on our understanding of the local universe is insufficient. Fortunately, with samples like KBSS, it is now possible to study the high-z universe independently of calibrations based on low-z galaxy populations.

4.5.4 O/Fe in High-z Galaxies

Just as we translated $\log(Z_{\rm neb}/Z_\odot)$ into $12 + \log(\mathrm{O/H})$, we may also directly approximate [O/Fe] for KBSS galaxies using the inferred values of stellar and gas-phase metallicity from the model: $[\mathrm{O/Fe}] \approx \log(Z_{\rm neb}/Z_\odot) - \log(Z_*/Z_\odot)$. This ratio roughly traces the relative contributions of Type Ia and CCSNe, which contribute the majority of the Fe and O, respectively, to the overall enrichment of the ISM in galaxies. Figure 4.20 shows the distribution of [O/Fe] for the same KBSS galaxies shown in Figure 4.5, including galaxies with limits on N/O. The interquartile range in inferred [O/Fe] for this sample is $0.25 - 0.53$, somewhat lower than the value we inferred in S16 for a composite spectrum of KBSS galaxies ([O/Fe]$\sim 0.6 - 0.7$) and also lower than the maximal [O/Fe] expected for purely CCSN enrichment ([O/Fe]≈ 0.73 Nomoto et al., 2006). Still, the range in [O/Fe] found in the KBSS subsample shown in Figure 4.20 is significantly super-solar, reinforcing the need for stellar models that explore non-solar abundance patterns, particularly in O and Fe.

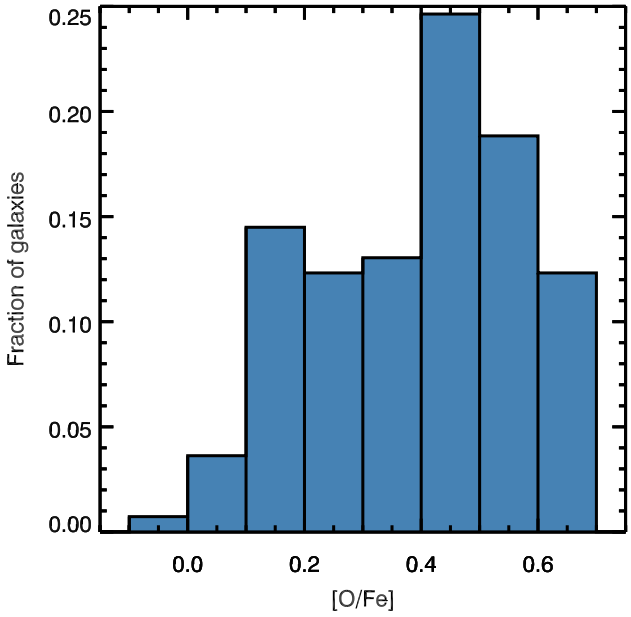

Figure 4.20: The distribution of [O/Fe] for the galaxies shown in Figure 4.5, including galaxies with limits on N/O. For these galaxies the interquartile range is [O/Fe]= $0.25-0.53$, which is somewhat lower than the value inferred for a composite spectrum of KBSS galaxies by S16. Still, these galaxies demonstrate that a significant portion of high-z galaxies exhibit abundance patterns that are indicative of enrichment primarily by CCSNe, modulo uncertainties in supernova yields and the importance of prompt Type Ia SNe.

Because we are using the values of $Z_{\rm neb}$ and Z_* derived from the marginalized posteriors, [O/Fe] < 0 is allowed, even though this region of parameter space is forbidden in the MCMC. We choose to estimate [O/Fe] in this manner—rather than from the MCMC itself—in order to avoid marginalizing over dispreferred solutions for the galaxies with multiple peaks in their posterior PDFs. We will be able to more robustly estimate [O/Fe] in future work that incorporates constraints on the Fe line-blanketing in stellar atmospheres observed in the rest-UV spectra of KBSS galaxies.

4.6 Summary and Conclusions

We have introduced a photoionization model method that self-consistently accounts for the primary astrophysical drivers of high-z galaxies' nebular spectra, using observables that are commonly available for most samples. Applying this method to 203 $\langle z \rangle = 2.3$ galaxies from the KBSS, we find that:

- The majority of $\langle z \rangle = 2.3$ galaxies are moderately O-rich, with an interquartile

range in 12 + log(O/H) = 8.29 − 8.55 ([O/H] = [−0.40, −0.14], Figure 4.5). The same galaxies have significantly sub-solar Fe enrichment, with an interquartile range of [Fe/H]= [−0.84, −0.54].

- There are strong correlations between commonly-used line-ratio indices and both U (which is the parameter measured most precisely for individual galaxies) and N/O (Figures 4.10 and 4.11). We have presented new calibrations for these quantities (Equations 4.1 and 4.4), which can be used to estimate U and N/O in high-z galaxies or any galaxies with similar stellar populations.

- The nebular spectra of high-z galaxies resemble more closely those of local giant H II regions than the integrated-light spectra of galaxies at $z \sim 0$ (Figure 4.12).

- Of the commonly-used strong-line indices employed for estimating O/H, R23 shows the strongest correlation with gas-phase O/H in high-z galaxies (Figure 4.13). However, $\sim$ 72% of high-z galaxies in the KBSS sample have values of R23 near the "turnaround", making R23 a useful diagnostic only for O-rich systems (Equation 4.7). In addition, a calibration based on R23 and O32 does not perform significantly better than R23 alone (Figure 4.14).

- The physical parameters inferred from galaxies' nebular spectra are often highly correlated with one another (Figure 4.15, Table 4.4), which can complicate studies of the intrinsic relationships between the physical conditions in galaxies. It is therefore necessary to account for both measurement errors and covariance between measurement errors in determining the true correlation between parameters, as we have done in Section 4.5.

- High-z galaxies exhibit the same range in N/O at fixed O/H as observed in a sample of local H II regions (Figure 4.16). For both samples, N/O varies by up to a factor of $2 - 3$ at a given O/H, particularly near the transition between the primary plateau and secondary N enrichment.

- We do not recover a strong anti-correlation between U and either O/H or Z_*, contrary to observations of galaxies in the local universe (Figures 4.18 and 4.19). The lack of a strong correlation between these quantities makes it more difficult to infer O/H from high-z galaxies' nebular spectra, which are much more sensitive to changes in U.

- Most high-z galaxies are consistent with super-solar O/Fe (Figure 4.20), indicative of ISM that has been enriched primarily by CCSNe. Given the evidence for substantially non-solar abundance patterns at high-z, it is increasingly important to have stellar models that better reflect the enrichment patterns in the early universe, rather than simply scaling solar relative abundances.

The unavoidable conclusion from these results is that the chemical abundance patterns in $z \simeq 2 - 2.7$ galaxies is significantly different from the $z \sim 0$ samples of galaxies which have necessarily driven the development of diagnostics for inferring galaxy physical conditions. Thus, in order to fully characterize galaxies that formed during this critical time in the universe's history—and, in turn, provide constraints on theoretical models of galaxy formation and evolution—it is imperative that we avoid making assumptions based on galaxies with significantly different enrichment histories. Although it is not realistic that every observation of individual high-z galaxies will allow for an independent analysis of the sort outlined in this chapter, it is clear that diagnostics based on galaxies with similar stellar populations and star-formation histories should be preferred over locally-calibrated methods. To address the need for such diagnostics, we have provided guidance on inferring U, N/O, and O/H in typical $z \sim 2 - 2.7$ star-forming galaxies, including re-calibrations of common strong-line diagnostics based on KBSS galaxies, although the development of flexible photoionization model techniques that can be used with any dataset is still needed (and the subject of ongoing work).

Finally, we note that the results of our photoionization model method also have important implications for constraining other galaxy scaling relations at high-z, including the mass-metallicity relation (MZR, e.g., Erb et al., 2006a). Although application of our method is briefly addresses in the following chapter, a detailed investigation of the MZR and other correlations between local conditions and bulk galaxy properties is the subject of a forthcoming paper (Strom et al., in prep.), where a more thorough discussion can be dedicated to what is both a critically important and nuanced topic.

Chapter 5

OUTRO

The work presented in this thesis confirms that galaxies at the peak of galaxy assembly exhibit spectral features distinct from most present-day galaxies, exemplified by the offset of the entire locus of high-z galaxies toward higher [O III]λ5008/Hβ at fixed [N II]λ6585/Hα relative to typical $z \sim 0$ galaxies from the Sloan Digital Sky Survey (SDSS, York et al., 2000). At the same time, $z \simeq 2 - 2.7$ galaxies from the Keck Baryonic Structure Survey (KBSS, Steidel, Rudie, Strom et al., 2014) appear consistent with the most extreme tail of the SDSS distribution in other diagnostic line-ratio diagrams. As discussed in Chapter 3, the combination of these observations is due to uniformly high degrees of ionization and excitation in high-z star-forming galaxies. Comparisons with photoionization models motivated by observations of the same galaxies' physical conditions (including electron density, n_e) and stellar populations (probed by their rest-UV spectra) reveal that these extreme ionization and excitation conditions arise from differences in the shape of the stellar ionizing spectra at fixed gas-phase oxygen abundance (O/H), most likely due to contributions from Fe-poor binary stars. The combination of Fe-poor stellar populations and moderately O-rich gas is necessary not only to reconcile the detailed observations of a composite spectrum of $z \simeq 2 - 2.7$ KBSS galaxies (Steidel, Strom, et al., 2016) *but also the properties of individual galaxies* spanning a large range in stellar mass (M_*) and star formation rate (SFR), as shown in Chapter 4.

5.1 Star Formation History as the Fundamental Property of Galaxies

The apparent ubiquity of super-solar O/Fe among high-z galaxies is one of the most important differences—and arguably the *most* important chemical difference—between galaxies at $z \simeq 2 - 2.7$ and those at $z \sim 0$. As argued in Chapter 3 (and also by Steidel, Strom, et al., 2016), the gas in galaxies with constant or rising SFRs and stellar population ages $\lesssim 1$ Gyr, like most high-z galaxies (Reddy et al., 2012), will reflect enrichment primarily from core-collapse supernovae (CCSNe). The resulting super-solar O/Fe will generate harder ionizing spectra at a given O/H compared to galaxies with lower O/Fe, including most $z \sim 0$ galaxies, which have more extended star formation histories.

These differences cannot be ignored, because—as demonstrated throughout this

thesis—the nebular spectra we observe in individual galaxies are sensitive to both the detailed shape of the ionizing radiation field (set largely by the Fe content of the massive stars, but also related to the ionization parameter) *and* the specifics of the gas cooling (driven by the gas chemistry, including O/H). As a result, nebular diagnostics designed to measure quantities like gas-phase O/H that are based on observations of one sample of galaxies will introduce systematic uncertainties if applied to galaxies whose star formation histories differ significantly from the "calibration" sample. Specifically, nebular diagnostics tuned to local galaxies should only be applied with extreme care—*if at all*—to high-z galaxies, due to significant differences in the characteristic star formation histories and, therefore, the prevailing α/Fe of galaxies at different redshifts.

With new, independent methods for self-consistently determining the physical conditions in high-z galaxies—such as the photoionization model method outlined in Chapter 4—it is now possible to avoid these systematic biases and study many individual galaxies at $z \sim 1-3$ in unprecedented detail. The results from such techniques lend renewed confidence to studies of high-z galaxy scaling relations, like the mass-metallicity relation (MZR), which in turn constrain theories of galaxy formation and evolution (c.f. Ma et al., 2016). Theoretical models must be able to reproduce the observed relations, not only using the boundary conditions provided by $z \sim 0$ galaxies, but also matching the evolution in galaxy properties as a function of redshift.

The observation that high-z galaxies exhibit lower O/H at fixed M_* relative to $z \sim 0$ galaxies (Figure 5.1) is frequently interpreted as an increase in overall enrichment in galaxies at later times, but is also a reflection of the decrease in galaxies' typical gas masses. Figure 5.2 shows the first results for the $z \sim 2.3$ MZR using photoionization model O/H estimates for the KBSS-MOSFIRE sample from Chapter 4. We find a weak, but marginally significant, relation with a linear correlation coefficient of $\rho = 0.25$ (estimated using *LINMIX_ERR*) and relatively large scatter ($\sigma_{\rm int} \approx 0.14$ dex). At present, it is unclear what is the best way to compare these results with estimates of O/H for local galaxies, given the uncertainty in abundance scales between different methods (an issue briefly discussed in Chapter 4).

Ionization parameter ($U = n_\gamma/n_{\rm H}$) and nebular excitation (traced by [O III]/Hβ) are also strongly anti-correlated with M_* in high-z galaxies, with more massive galaxies exhibiting significantly lower levels of nebular ionization and excitation. The correlation between U and M_* (Figure 5.3) is, in fact, one of the most significant

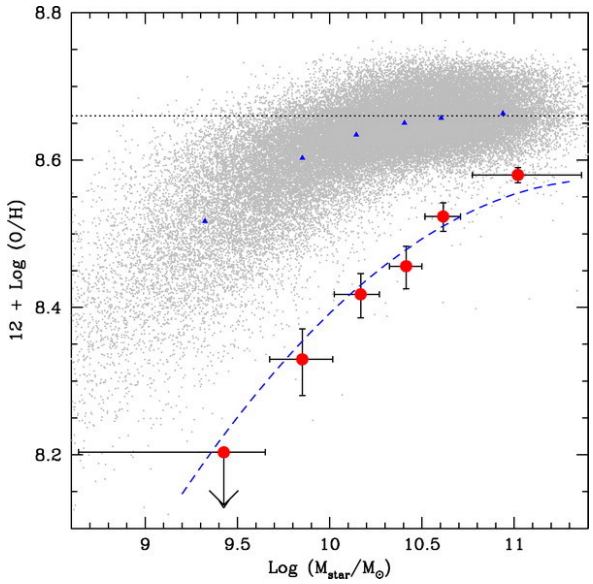

Figure 5.1: The mass-metallicity relation (MZR) for $z \sim 0$ galaxies (grey dots) compared to the relation measured from composite spectra of $z \sim 2$ rest-UV color-selected galaxies in bins of stellar mass (red points); the small blue triangles indicate the mean metallicity of $z \sim 0$ galaxies in the same bins. In both cases, O/H has been estimated using the N2 index, which the results from Chapter 4 suggest is more strongly correlated with N/O (and U, to a lesser degree) than with O/H. Figure reproduced from Erb et al. (2006a).

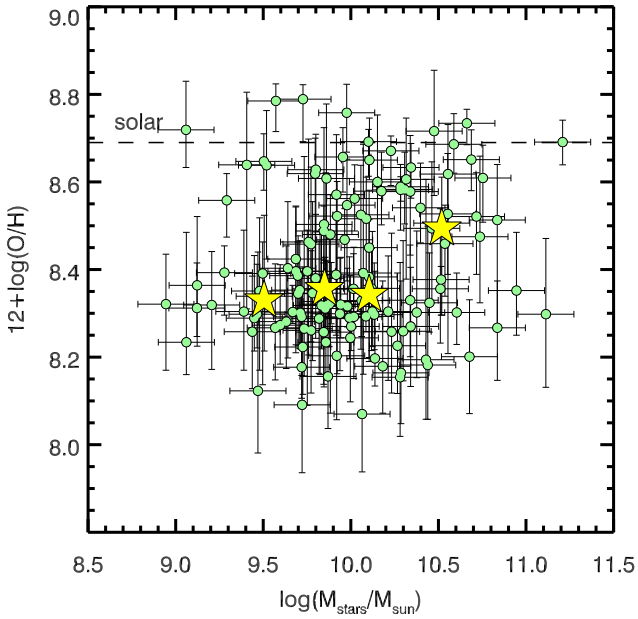

Figure 5.2: The MZR for 135 $z \simeq 2 - 2.7$ KBSS galaxies with O/H inferred using the photoionization model method introduced in Chaper 4 (green points). The median values of 12+log(O/H) in equal-number bins in M_* are illustrated by the yellow stars. This is the first time that O/H has been measured in a large number of high-z galaxies without relying on a locally-calibrated diagnostic. We find a marginally significant positive correlation with relatively large intrinsic scatter, $\sigma_{\rm int} \approx 0.14$ dex.

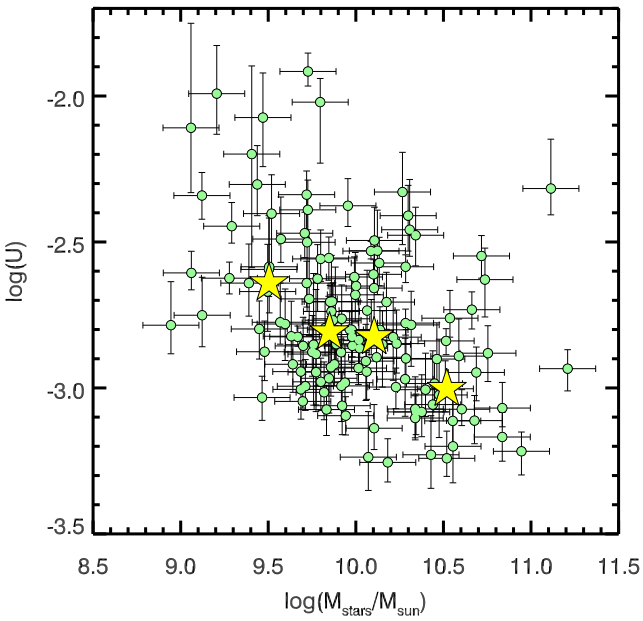

Figure 5.3: The mass-ionization relation for 135 $z \simeq 2 - 2.7$ KBSS galaxies with model-inferred ionization parameters (in green), showing the strong anti-correlation between U and M_*. As in Figure 5.2, median values of $\log(U)$ in equal-number bins in M_* are illustrated by the yellow stars. The Spearman coefficient is $\rho = -0.40$ with $p = 1 \times 10^{-6}$. Because most KBSS galaxies are consistent with similar electron densities, $n_e \approx 300\,\mathrm{cm}^{-3}$, this trend suggests that the density of ionizing photons is a strong function of M_*. The correlation between the detailed astrophysics in galaxies' H II regions and their global properties is a natural consequence of variations in their star-formation histories.

correlations observed between the conditions in galaxies' interstellar medium (ISM) and an integrated galaxy property (Spearman $\rho = -0.40$, $p = 1 \times 10^{-6}$). This result mirrors the relation observed between [O III]/Hβ and M_* shown for $z \sim 2.3$ KBSS galaxies in Chapter 3 (which is actually *more* significant). The strength of these correlations may explain why studies of the high-z MZR based on strong-line indices (which are in fact most sensitive to U, as shown in Chapter 4) appear much more significant than the relation shown in Figure 5.2[1]. Rather than measuring O/H in high-z galaxies, such studies may instead be probing the ionization and excitation conditions in their ISM.

[1] Additionally, the M_* estimates favored up to this point for KBSS galaxies (and, indeed, most other high-z galaxy surveys) rely on stellar population synthesis models with solar Fe enrichment and solar abundance patterns. Such models have now been ruled out conclusively at $z \sim 2 - 3$, in part due to the work contained in this thesis. As these differences may introduce systematic biases in estimating M_* for high-z galaxies, a final analysis of the $z \sim 2.3$ MZR must await new, self-consistent SED fitting methods that employ stellar population models that reflect the chemical enrichment seen at these redshifts.

In any case, it is not immediately clear why *any* local gas conditions—including ionization and excitation—in H II regions should be sensitive to the bulk properties of the host galaxy. The most straightforward explanation is that these correlations, as well the super-solar O/Fe ratios observed in high-z galaxies, are manifestations of trends in galaxies' star formation histories—which connect integrated star formation on large scales with the properties of the gas and stars on small scales through galaxies' chemical abundance patterns. In the context of studies of local dwarf galaxies, whose detailed star formation histories can be recovered by using the chemical signatures of individual stars as a kind of clock (see Tolstoy, Hill & Tosi, 2009, and references therein), this interpretation is more obvious. In the case of high-z galaxies, we can only study trends in chemical abundance patterns across populations of galaxies, rather than among stars contained within a single galaxy, an effort that will undoubtedly be aided greatly by comparisons with cosmological simulations.

From an observational perspective, exploring the importance of star formation history in determining galaxy scaling relations requires data for galaxies spanning *the full range* of plausible star formation histories at a given redshift. Evolved galaxies with declining or truncated star formation histories are a particularly interesting sub-population at $z \sim 1-3$, as they will contain an admixture of nucleosynthetic products from both Type Ia SNe and CCSNe and therefore exhibit nebular spectra distinct from (the more common) younger galaxies. The analysis in Chapter 2 suggests that KBSS may be biased against such galaxies relative to other surveys that use complementary selection techniques. Still, from the observations of red star-forming galaxies within the KBSS sample, we already know that these galaxies occupy a unique region of nebular parameter space where the photoionization model results described in Chapter 4 are more likely to be double-peaked, requiring additional information to break the degeneracy between potential solutions. It is also possible that the models based on typical $z \sim 2.3$ KBSS galaxies, with constant or rising star-formation histories, may not be appropriate for explaining more evolved galaxies at the same redshifts.

Just as attempts to force high-z galaxies to fit the paradigm established using observations of $z \sim 0$ galaxies led to systematic biases in measuring galaxy properties, applying the conclusions based on typical high-z galaxies directly to galaxies with different characteristic star formation histories may only cause further confusion. In order to independently constrain the physical conditions in red, star-forming galax-

ies without relying on models tuned either to typical high-z star-forming galaxies or low-z galaxies—that are likely fundamentally different in other ways—detailed observations of the rest-optical spectra of a representative sample of more evolved galaxies are required. This need is even more pressing for galaxies at $z \sim 1.5$ (where most RK galaxies in KBSS are found), as the fraction of galaxies with declining star-formation histories will increase toward lower redshifts as the overall level of star formation in the universe also begins to decline.

5.2 Emission Galaxies Throughout Cosmic Time

Over the next several years, the analysis of galaxy spectra currently possible at $z \sim 0$ with SDSS and at $z \sim 2.3$ with surveys like KBSS will become viable at virtually all redshifts, with large surveys of $0.5 \lesssim z \lesssim 2$ galaxies being planned with the Prime Focus Spectrograph (PFS, Tamura & PFS Collaboration, 2016) on Subaru and the Multi-Object Optical and Near-infrared Spectrograph (MOONS, Cirasuolo & MOONS Consortium, 2016) on the VLT. At higher redshifts, the *James Webb Space Telescope* (*JWST*) will open new discovery spaces for studying some of the earliest galaxies in the universe with instruments like the Near-Infrared Spectrograph (NIRSpec) and the Mid-Infrared Instrument (MIRI). In order to directly connect observations of galaxy populations at different redshifts, it will be crucial to account explicitly for differences in galaxies' star formation histories, which impact our ability to extract astrophysical information from their spectra. This thesis provides a basis for developing such a framework.

As a case study, we note that for galaxies at $z > 3$, ground-based facilities no longer have access to Hα, [N II]λ6585, and the [S II]$\lambda\lambda$6717, 6731 doublet in their rest-optical spectra; by $z \sim 6$, the same portion of galaxies' spectra is redshifted beyond 2.5 μm and can only be observed from space. Studies of $z \gtrsim 6$ galaxies have thus far focused entirely on observations of their rest-UV spectra, which remain accessible to ground-based spectrographs at the red end of the optical bandpass (7000 – 9000Å) and in the Y and J NIR bands (e.g Ando et al., 2006; Stark et al., 2015). Following the commissioning of *JWST* in 2019, it will be possible to obtain complementary rest-optical spectroscopy for statistical samples of such galaxies in Band III (2.0 – 5.3 μm) with NIRSpec (see Figure 5.4).

In addition to providing the practical advantage of access to joint observations in the rest-UV and rest-optical, $z \sim 5 - 6$ galaxies are representative of a unique time in cosmic history. At the end of the Epoch of Reionization, the age of the universe

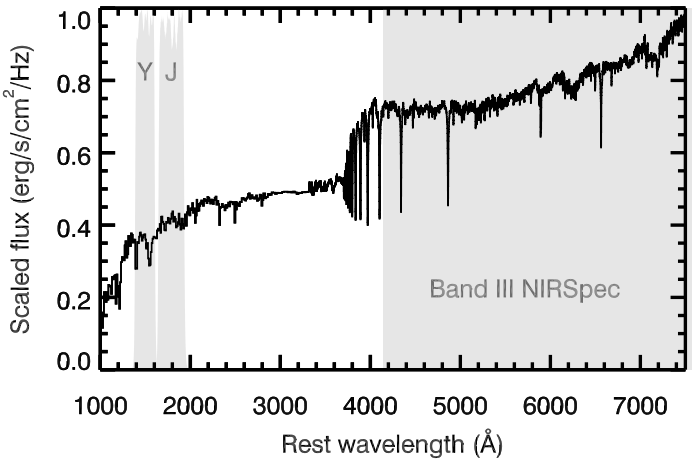

Figure 5.4: The stellar SED of a $z = 6$ galaxy, illustrating the regions accessible to joint ground- and space-based infrared observations. For galaxies at similar redshifts, rest-UV spectra can be observed using existing ground-based NIR spectrographs and the rest-optical spectra will be accessible in the near-future using *JWST*/NIRSpec.

was only $\sim$ 1 Gyr, making it likely that all galaxies at that time exhibit chemical abundance patterns that reflect CCSNe yields, similar to the galaxies studied as part of this thesis.

Appendix A

QUICK-START GUIDE TO *MOSPEC*, AN INTERACTIVE ANALYSIS TOOL FOR NIR SPECTROSCOPY FROM MOSFIRE

The IDL-based analysis tool *MOSPEC* was designed specifically for interacting with pipeline-reduced, two-dimensional (2D) spectra, with an emphasis on near-infrared (NIR) spectroscopy of faint emission line galaxies with MOSFIRE, such as those that compose the majority of the Keck Baryonic Structure Survey (KBSS) sample. Developed as a command line tool similar to the *SPLOT* task in IRAF, *MOSPEC* allows the user to extract one-dimensional (1D) spectra of any object on-the-fly, characterize observations of bright stars that are used to measure the image quality and flux zeropoint for MOSFIRE masks, and measure redshifts and emission line fluxes for individual galaxies (including serendipitous observations). The emission line catalogs for KBSS-MOSFIRE galaxies assembled using *MOSPEC* form the basis of the work presented in this thesis and were also used in a number of other publications over the last several years (including Steidel et al., 2014; Trainor et al., 2015; Turner et al., 2015; Steidel et al., 2016; Trainor et al., 2016; Turner et al., 2017). This appendix provides a quick-start guide to *MOSPEC* for new users.

A.1 Interactive User Display

MOSPEC is launched from the IDL command line using the following syntax:

```
IDL> MOSPEC, file, [/all, /small, /large, /nocal, /nomodel, cpoly=]
```

Figure 1.1 shows an example of the initial display for a 2D spectrum that has not been previously analyzed. The object name and current file are identified at the top of the window, with the corresponding 2D spectrogram displayed near the bottom. A boxcar extraction aperture centered on the predicted position of the science target (taken from the MOSFIRE mask design information in the file header and bracketed by the horizontal green lines) is used to determine the initial 1D spectrum, which is plotted in white, with the corresponding 1σ error spectrum shown in red.

A new extraction aperture can be interactively defined by pressing 't' with the cursor positioned on a well-defined emission line in the 2D spectrum (or anywhere for an object with significant continuum emission), which will prompt the user to select the desired range in pixels along the slit (Figure 1.2). Apertures defined this way will use boxcar-weighting to sum the sky-subtracted 2D spectrum over the requested

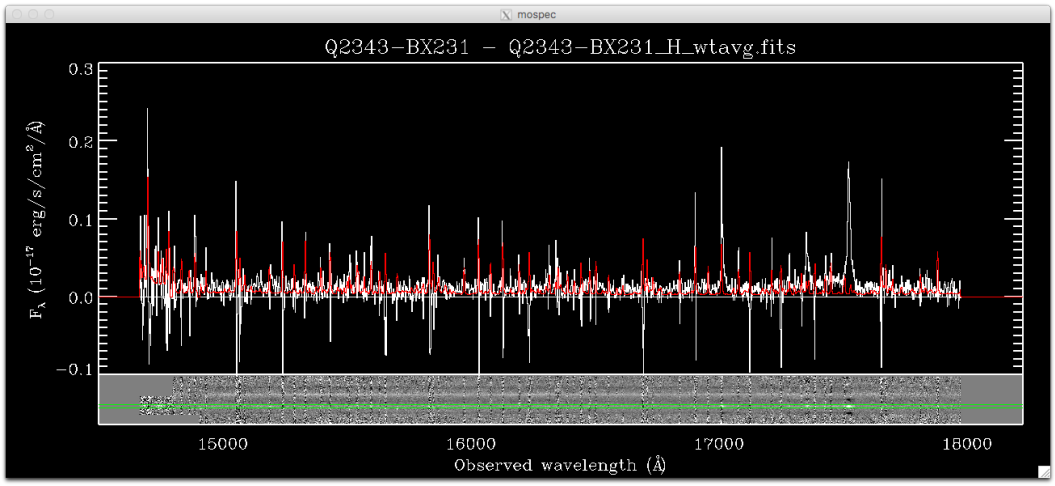

Figure 1.1: An example of a 2D spectrum viewed in *MOSPEC*. The weight-averaged *H*-band 2D spectrum of galaxy Q2343-BX231 is shown near the bottom of the window, with the 1D spectrum extracted using the default aperture (highlighted by the horizontal green lines) shown above; the corresponding error spectrum is shown in red.

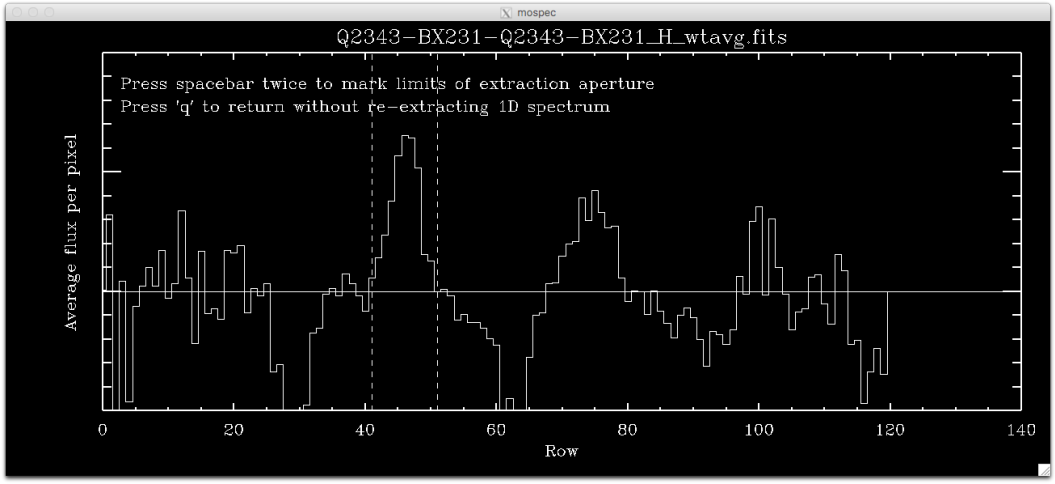

Figure 1.2: The extraction aperture selection window called using the ‘t’ command in *MOSPEC*. The 2D spectrum is collapsed in the dispersion direction in the region near the cursor, and the average flux in the spatial direction is displayed. The current aperture is shown by the vertical dashed lines, and the user is prompted to select the desired range in pixels, if different. Note that the ‘t’ command assumes boxcar weighting in all cases; optimal extraction may be selected using the ‘o’ command.

range of pixels, with the 1σ error spectrum taken to be the square root of the summed 2D variance spectrum.

In some cases, optimal extraction (Horne, 1986) may be preferred to maximize the S/N per pixel in the 1D spectrum. Optimal extraction applies a weighting function in the spatial dimension to down-weight the contributions from rows that contain less flux from the science target, which reduces the statistical noise while maintaining photometric accuracy. The weighting function can be constructed in a number of ways, depending on the spatial profile[1]. For unresolved sources like stars, a Gaussian approximation works well, but may not be appropriate for extended objects with complicated morphologies. In *MOSPEC*, optimal extraction can be implemented by using 'o' instead of 't', which will prompt the user to decide between a Gaussian fit to the spatial profile or the empirical spatial profile. For objects with only faint emission lines, the spatial profile is often too noisy to construct a weighting function confidently; as a result, boxcar weighting is generally preferred for the analysis of KBSS-MOSFIRE galaxies.

Once a 1D spectrum has been extracted, the user may interact with it in a number of ways; Table A.1 provides a summary of the available commands. The 'e' command extracts the currently-displayed (observed frame) 1D spectrum without fitting the emission lines, which may be desired in the general case and is also useful for the spectra of bright stars. The procedure for fitting an emission line spectrum (with or without significant continuum) is described in the following section.

A.2 Emission Line Modelling

In addition to extracting 1D spectra from the 2D pipeline products, *MOSPEC* is also capable of measuring the redshifts, line widths, and emission line fluxes for distant galaxy spectra. To initiate the fitting procedure, the user invokes the 'f' command with the cursor at the location of a well-defined emission line in the 1D spectrum and identifies the rest-wavelength of the feature. After performing the fit, *MOSPEC* will print the best-fit combination of parameters assuming the default model to standard output and display the fit in the graphics window (Figure 1.3).

An estimate of the object's redshift is determined from the peak of the line identified during the call to the fitting procedure, and the final fit is performed on the continuum-substracted spectrum using the IDL routine *MPFITEXPR* (Markwardt, 2009). The continuum level is measured by either (1) fitting a polynomial function

[1] A boxcar extraction aperture is equivalent to using a uniform weighting function along the slit.

Table A.1: *MOSPEC* commands

Key	Action
a	set zoom: type once in lower left corner of desired region and once again in the upper right corner; type twice in the same spot to unzoom
b	move to previous object
c	clear all changes to spectrum and redraw with original aperture guess
d	determine image quality using current spectrum (best used with stellar spectra)
e	extract and save current 1d spectrum
f	calculate simultaneous fit to the continuum and strong emission lines
g	write line fluxes and fit parameters to mospec.log
i	identify emission lines using the default list or lines.dat (requires a redshift)
j	mark emission line and provide its rest wavelength to return redshift
k	remove emission line location from spectrum header
l	choose a range of lines to define the aperture (e.g., '60 70')
m	print the MASKS header keyword, if available
n	move to next object
o	optimally extract spectrum using spectrum near cursor to define the weighting profile
p	print figure of current object to file
q	quit
r	redraw the spectrum with current zoom, smoothing, masking, and line list
s	smooth spectrum (must choose a value from 1-9)
t	view the trace selection window
u	mask or unmask noisy regions
v	mark cursor position as location of emission line center
w	switch between rest and observed wavelength
x	pause the IDL routine; to restart program, type '.c'
z	apply a redshift solution to the spectrum
,	zoom out by a factor 2 in flux
.	zoom in by a factor 2 in flux
/	show points that would be masked in stack_1d
?	help

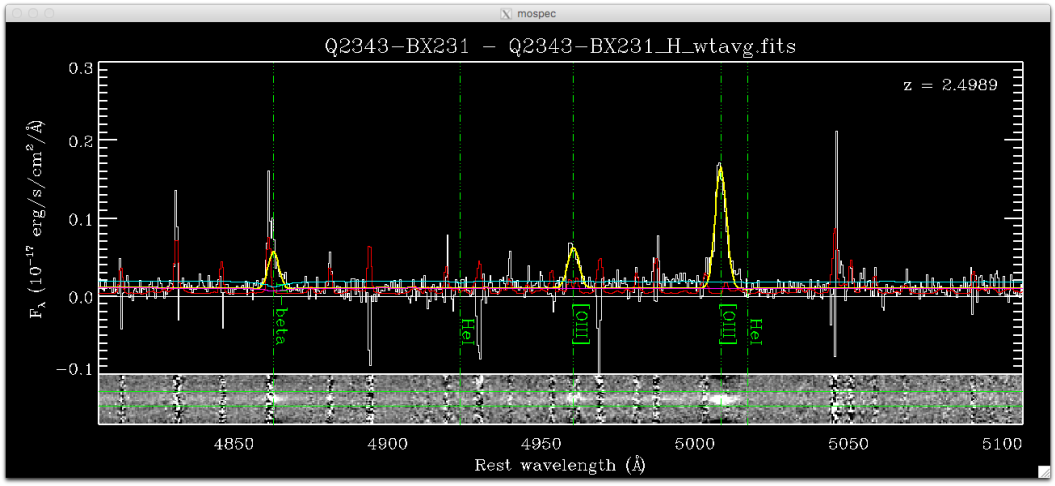

Figure 1.3: An example of emission line fitting in *MOSPEC*, showing a zoomed-in version of the *H*-band spectrum from Figure 1.1, centered on the region around Hβ and [O III]$\lambda\lambda$4960, 5008. The galaxy has been fit using the standard emission line model, with the result shown in yellow and commonly-measured emission line features identified by the vertical green lines. The cyan line shows the best-fit SED model corresponding to Q2343-BX231, and the scaled version used for estimating the continuum in the fitting procedure is shown in magenta (the ratio between these is the "SED slit correction"). The redshift determined from the emission line fit is printed in the upper-right corner.

to the spectrum between emission lines (with a default degree of one, corresponding to a line) or (2) scaling a reddened high-resolution stellar population synthesis model (matching the full spectral energy distribution, or SED, of the object) to the observed continuum. Where the latter method is possible (as it is for 90% of KBSS-MOSFIRE galaxies), the effects of stellar Balmer absorption are accounted for automatically. The Balmer absorption corrections to Hα and Hβ are quantified by comparing the full fit with a fit determined by using a model continuum that linearly interpolates between the continuum on either side of regions around the Balmer features.

The default emission line model assumes a single redshift (z) and Gaussian line profiles with a single line width (σ, in km s^{-1}) for all lines in a single NIR band. Further, the ratios of the nebular [O III]$\lambda\lambda$4960,5008 and [N II]$\lambda\lambda$6549,6585 doublets are fixed at 1:3 and the ratios of the density-sensitive [O II]$\lambda\lambda$3727,3729 and [S II]$\lambda\lambda$6718,6732 doublets are restricted to be within 20% of the range of physically allowed values, which is 0.43 – 1.5 for [S II]λ6718/[S II]λ6732 (Tayal & Zatsarinny, 2010; Mendoza & Bautista, 2014) and 0.35 – 1.5 for [O II]λ3729/[O II]λ3727 (Kisielius et al., 2009). Adopting these constraints allows the fitting procedure to recover emission line fluxes even for lines which are coincident with strong OH

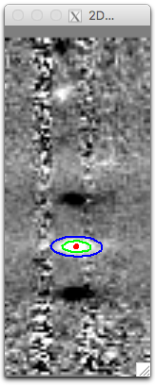

Figure 1.4: The results from fitting a 2D bivariate Gaussian model to the [O III]λ5008 line from the 2D spectrum of Q2343-BX231 shown in Figures 1.1 and 1.3. When a spectrum is fit with *MOSPEC*, the emission line identified by the user is also fit in 2D, to both determine whether the line exhibits evidence of a rotation curve and provide a more robust determination of the vertical profile along the slit. The peak of the line is marked by the red point, with contours highlighting 50% (green) and 10% (blue) of the peak value.

emission. So long as a portion of the line is not obscured by the OH feature in the dispersion direction, the constraints on z, σ, and normalization from other lines in the spectrum (and, importantly, the other line in the doublet) frequently allow a good fit to be determined.

It is also possible to assign a fixed z and σ to the fit. This is often desirable if a spectrum is of insufficient quality to simultaneously determine all of the parameters; for $z \sim 2$ KBSS-MOSFIRE galaxies with moderate-to-large values of σ, it can be especially challenging to fit the [O II]$\lambda\lambda$3727, 3729 doublet in low S/N J-band spectra, given the degeneracies between z, σ, and line flux. As a result, z is often fixed (using ':z <redshift>') to the value determined from the corresponding fit to [O III]λ5008 in the H-band spectrum of the same galaxy. Line width can be fixed using ':v <sigma in km s^{-1}>'.

MOSPEC estimates the total slit losses for objects in two ways. First, it compares the observed continuum level with the normalization of the best-fit SED model (which is set by the overall broadband photometry), resulting in the "SED slit correction". Second, it estimates the geometric slit loss due to a finite slit width by assuming the true object shape can be described by an azimuthally-symmetric 2D Gaussian. The radial profile is assumed to be equivalent to the Gaussian approximation of the spatial profile, as derived from a fit to the overall 2D line emission (Figure 1.4). *MOSPEC* then reports the "2D slit correction" as the ratio of the total volume contained in the model 2D Gaussian profile to the fraction within the rectangle defined by the slit width and user-defined extraction aperture. The fit to the emission line profile shown in Figure 1.4 can also used to flag objects with evidence of significant, spatially-resolved rotation, which will manifest as a tilt in the emission lines observed in the 2D spectrogram.

An example of the complete fitting procedure output is shown below, corresponding to the fit to the 1D spectrum in Figure 1.3. The emission line features are reported using their vacuum wavelengths, and the fluxes (not corrected for slit losses) have units of 10^{-17} erg/s/cm^2.

```
LINE       LAMBDA     FLUX                          SNR
H-gamma    4341.670   4.18e-01 +/- 5.08e-02       8.233
[OIII]     4364.435   3.60e-02 +/- 3.75e-02       0.960
HeI        4389.163  -2.92e-02 +/- 3.06e-02       0.952
HeI        4472.345  -3.25e-02 +/- 3.70e-02       0.878
HeII       4687.012   3.35e-03 +/- 3.17e-02       0.106
[ArIV]     4712.688  -1.18e-02 +/- 2.69e-02       0.438
[ArIV]     4741.486  -1.14e-01 +/- 2.87e-02       3.964
H-beta     4862.721   7.88e-01 +/- 4.20e-02      18.770
HeI        4923.304   9.87e-03 +/- 3.93e-02       0.251
[OIII]     4960.295   8.32e-01 +/- 1.62e-02      51.497
[OIII]     5008.239   2.50e+00 +/- 4.85e-02      51.497
HeI        5017.079  -3.43e-03 +/- 2.82e-02       0.122
Redshift: 2.4989  z_error: 8.6 km/s  Line width: 109.71 +/- 2.04 km/s
Tilt: 1.18 degrees CCW   SED Slitcor: 1.83   2D Slitcor: 1.33   Balmer cor: 1.12
```

Note that because the ratio of the [O III]$\lambda\lambda$4959,5008 lines is fixed, the S/N ratio for both lines is the same.

Once satisfied with the fit to the 1D spectrum, the user may print the results to a log file using the ‘g’ command, which also extracts the 1D spectrum as a separate FITS file, with pertinent model parameters (including the redshift) written to the header.

BIBLIOGRAPHY

Adelberger, K. L., Steidel, C. C., Shapley, A. E., et al., 2004, ApJ, 607, 226

Adelman-McCarthy, J. K., Agüeros, M. A., Allam, S. S., et al., 2008, ApJS, 175, 297-313, 297

Aihara, H., Allende Prieto, C., An, D., et al., 2011, ApJS, 193, 29, 29

Ando, M., Ohta, K., Iwata, I., et al., 2006, ApJ, 645, L9

Andrews, B. H., & Martini, P., 2013, ApJ, 765, 140, 140

Asplund, M., Grevesse, N., Sauval, A. J., & Scott, P., 2009, ARA&A, 47, 481

Baldwin, J. A., Phillips, M. M., & Terlevich, R., 1981, PASP, 93, 5

Bertin, E., & Arnouts, S., 1996, A&AS, 117, 393

Bian, F., Kewley, L. J., Dopita, M. A., & Juneau, S., 2016, ApJ, 822, 62, 62

Blanc, G. A., Kewley, L., Vogt, F. P. A., & Dopita, M. A., 2015, ApJ, 798, 99, 99

Blanton, M. R., & Moustakas, J., 2009, ARA&A, 47, 159

Brinchmann, J., Pettini, M., & Charlot, S., 2008, MNRAS, 385, 769

Bruzual, G., & Charlot, S., 2003, MNRAS, 344, 1000

Calzetti, D., Armus, L., Bohlin, R. C., et al., 2000, ApJ, 533, 682

Campbell, A., Terlevich, R., & Melnick, J., 1986, MNRAS, 223, 811

Cardelli, J. A., Clayton, G. C., & Mathis, J. S., 1989, ApJ, 345, 245

Chabrier, G., 2003, PASP, 115, 763

Cirasuolo, M., & MOONS Consortium, 2016, in Astronomical Society of the Pacific Conference Series, Multi-Object Spectroscopy in the Next Decade: Big Questions, Large Surveys, and Wide Fields, ed. I. Skillen, M. Barcells, & S. Trager, Vol. 507, 109

Coil, A. L., Aird, J., Reddy, N., et al., 2015, ApJ, 801, 35, 35

Cowie, L. L., Barger, A. J., & Songaila, A., 2016, ApJ, 817, 57, 57

Daddi, E., Cimatti, A., Renzini, A., et al., 2004, ApJ, 617, 746

Davis, M., Faber, S. M., Newman, J., et al., 2003, in Proc. SPIE, Discoveries and Research Prospects from 6- to 10-Meter-Class Telescopes II, ed. P. Guhathakurta, Vol. 4834, 161

Diaz, A. I., & Tosi, M., 1986, A&A, 158, 60

Dickey, C. M., van Dokkum, P. G., Oesch, P. A., et al., 2016, ApJ, 828, L11, L11

Dopita, M. A., & Evans, I. N., 1986, ApJ, 307, 431

Dopita, M. A., Fischera, J., Sutherland, R. S., et al., 2006, ApJ, 647, 244

Dopita, M. A., Kewley, L. J., Sutherland, R. S., & Nicholls, D. C., 2016, Ap&SS, 361, 61, 61

Edmunds, M. G., & Pagel, B. E. J., 1978, MNRAS, 185, 77P

Erb, D. K. 2006, "The properties of star-forming galaxies at $z \sim 2$: Kinematics stellar populations, and metallicities", PhD thesis (California Institute of Technology)

Erb, D. K., Shapley, A. E., Pettini, M., et al., 2006a, ApJ, 644, 813

Erb, D. K., Steidel, C. C., Shapley, A. E., et al., 2006b, ApJ, 646, 107

—, 2006c, ApJ, 647, 128

Erb, D. K., Steidel, C. C., Trainor, R. F., et al., 2014, ApJ, 795, 33, 33

Erb, D. K., Pettini, M., Steidel, C. C., et al., 2016, ApJ, 830, 52, 52

Esteban, C., Peimbert, M., García-Rojas, J., et al., 2004, MNRAS, 355, 229

Esteban, C., García-Rojas, J., Carigi, L., et al., 2014, MNRAS, 443, 624

Faber, S. M., Willmer, C. N. A., Wolf, C., et al., 2007, ApJ, 665, 265

Ferland, G. J., Porter, R. L., van Hoof, P. A. M., et al., 2013, RMxAA, 49, 137

Franx, M., Labbé, I., Rudnick, G., et al., 2003, ApJ, 587, L79

Garnett, D. R., 1992, AJ, 103, 1330

Gelman, A., & Rubin, D. B., 1992, Statistical Science, 7, 457

Giavalisco, M., Ferguson, H. C., Koekemoer, A. M., et al., 2004, ApJ, 600, L93

Hainline, K. N., Shapley, A. E., Greene, J. E., & Steidel, C. C., 2011, ApJ, 733, 31, 31

Hopkins, A. M., & Beacom, J. F., 2006, ApJ, 651, 142

Horne, K., 1986, PASP, 98, 609

Jensen, E. B., Strom, K. M., & Strom, S. E., 1976, ApJ, 209, 748

Jones, T., Martin, C., & Cooper, M. C., 2015, ApJ, 813, 126, 126

Juneau, S., Dickinson, M., Alexander, D. M., & Salim, S., 2011, ApJ, 736, 104, 104

Juneau, S., Bournaud, F., Charlot, S., et al., 2014, ApJ, 788, 88, 88

Kashino, D., Silverman, J. D., Sanders, D., et al., 2017, ApJ, 835, 88, 88

Kauffmann, G., Heckman, T. M., Tremonti, C., et al., 2003, MNRAS, 346, 1055

Kelly, B. C., 2007, ApJ, 665, 1489

Kennicutt Jr., R. C., 1998, ARA&A, 36, 189

Kennicutt Jr., R. C., Bresolin, F., & Garnett, D. R., 2003, ApJ, 591, 801

Kewley, L. J., Dopita, M. A., Sutherland, R. S., Heisler, C. A., & Trevena, J., 2001, ApJ, 556, 121

Kewley, L. J., & Dopita, M. A., 2002, ApJS, 142, 35

Kewley, L. J., & Ellison, S. L., 2008, ApJ, 681, 1183

Kewley, L. J., Dopita, M. A., Leitherer, C., et al., 2013, ApJ, 774, 100, 100

Kewley, L. J., Zahid, H. J., Geller, M. J., et al., 2015, ApJ, 812, L20, L20

Kisielius, R., Storey, P. J., Ferland, G. J., & Keenan, F. P., 2009, MNRAS, 397, 903

Kojima, T., Ouchi, M., Nakajima, K., et al., 2017, PASJ, 69, 44, 44

Köppen, J., & Hensler, G., 2005, A&A, 434, 531

Kriek, M., Shapley, A. E., Reddy, N. A., et al., 2015, ApJS, 218, 15, 15

Law, D. R., Steidel, C. C., Shapley, A. E., et al., 2012, ApJ, 745, 85, 85

Lehnert, M. D., Nesvadba, N. P. H., Le Tiran, L., et al., 2009, ApJ, 699, 1660

Liu, X., Shapley, A. E., Coil, A. L., Brinchmann, J., & Ma, C.-P., 2008, ApJ, 678, 758

Ma, X., Hopkins, P. F., Kasen, D., et al., 2016, MNRAS, 459, 3614

Madau, P., Ferguson, H. C., Dickinson, M. E., et al., 1996, MNRAS, 283, 1388

Madau, P., & Dickinson, M., 2014, ARA&A, 52, 415

Maiolino, R., Nagao, T., Grazian, A., et al., 2008, A&A, 488, 463

Markwardt, C. B., 2009, in Astronomical Society of the Pacific Conference Series, Astronomical Data Analysis Software and Systems XVIII, ed. D. A. Bohlender, D. Durand, & P. Dowler, Vol. 411, 251

Masters, D., McCarthy, P., Siana, B., et al., 2014, ApJ, 785, 153, 153

Masters, D., Faisst, A., & Capak, P., 2016, ApJ, 828, 18, 18

McGaugh, S. S., 1991, ApJ, 380, 140

McLean, I. S., Becklin, E. E., Bendiksen, O., et al., 1998, in Proc. SPIE, Infrared Astronomical Instrumentation, ed. A. M. Fowler, Vol. 3354, 566

McLean, I. S., Steidel, C. C., Epps, H. W., et al., 2012, in SPIE Conference Series, Vol. 8446

Mendoza, C., & Bautista, M. A., 2014, ApJ, 785, 91, 91

Nomoto, K., Tominaga, N., Umeda, H., Kobayashi, C., & Maeda, K., 2006, Nuclear Physics A, 777, 424

Oke, J. B., Cohen, J. G., Carr, M., et al., 1995, PASP, 107, 375

Onodera, M., Carollo, C. M., Lilly, S., et al., 2016, ApJ, 822, 42, 42

Osterbrock, D. E. 1989, Astrophysics of gaseous nebulae and active galactic nuclei

Pagel, B. E. J., Edmunds, M. G., Blackwell, D. E., Chun, M. S., & Smith, G., 1979, MNRAS, 189, 95

Penston, M. V., Robinson, A., Alloin, D., et al., 1990, A&A, 236, 53

Pérez-Montero, E., 2014, MNRAS, 441, 2663

Pérez-Montero, E., & Contini, T., 2009, MNRAS, 398, 949

Persson, S. E., Murphy, D. C., Smee, S., et al., 2013, PASP, 125, 654

Pettini, M., Shapley, A. E., Steidel, C. C., et al., 2001, ApJ, 554, 981

Pettini, M., & Pagel, B. E. J., 2004, MNRAS, 348, L59

Pilyugin, L. S., 2003, A&A, 399, 1003

Pilyugin, L. S., Vílchez, J. M., & Thuan, T. X., 2010, ApJ, 720, 1738

Pilyugin, L. S., Grebel, E. K., & Mattsson, L., 2012, MNRAS, 424, 2316

Price, S. H., Kriek, M., Brammer, G. B., et al., 2014, ApJ, 788, 86, 86

Reddy, N. A., Erb, D. K., Steidel, C. C., et al., 2005, ApJ, 633, 748

Reddy, N. A., Steidel, C. C., Erb, D. K., Shapley, A. E., & Pettini, M., 2006, ApJ, 653, 1004

Reddy, N. A., Steidel, C. C., Pettini, M., et al., 2008, ApJS, 175, 48

Reddy, N. A., Pettini, M., Steidel, C. C., et al., 2012, ApJ, 754, 25, 25

Richards, G. T., Strauss, M. A., Fan, X., et al., 2006, AJ, 131, 2766

Rudie, G. C., Steidel, C. C., Trainor, R. F., et al., 2012, ApJ, 750, 67, 67

Sanders, R. L., Shapley, A. E., Kriek, M., et al., 2015, ApJ, 799, 138, 138

—, 2016, ApJ, 816, 23, 23

Schenker, M. A., Ellis, R. S., Konidaris, N. P., & Stark, D. P., 2013, ApJ, 777, 67, 67

Searle, L., 1971, ApJ, 168, 327

Shapley, A. E., 2011, ARA&A, 49, 525

Shapley, A. E., Steidel, C. C., Erb, D. K., et al., 2005, ApJ, 626, 698

Shapley, A. E., Reddy, N. A., Kriek, M., et al., 2015, ApJ, 801, 88, 88

Sharples, R., Bender, R., Agudo Berbel, A., et al., 2013, The Messenger, 151, 21

Shivaei, I., Kriek, M., Reddy, N. A., et al., 2016, ApJ, 820, L23, L23

Silverman, J. D., Kashino, D., Sanders, D., et al., 2015, ApJS, 220, 12, 12

Skelton, R. E., Whitaker, K. E., Momcheva, I. G., et al., 2014, ApJS, 214, 24, 24

Skillman, E. D., Côté, S., & Miller, B. W., 2003, AJ, 125, 610

Skrutskie, M. F., Cutri, R. M., Stiening, R., et al., 2006, AJ, 131, 1163

Stanway, E. R., Eldridge, J. J., & Becker, G. D., 2016, MNRAS, 456, 485

Stark, D. P., Schenker, M. A., Ellis, R., et al., 2013, ApJ, 763, 129, 129

Stark, D. P., Richard, J., Charlot, S., et al., 2015, MNRAS, 450, 1846

Steidel, C. C., Adelberger, K. L., Shapley, A. E., et al., 2003, ApJ, 592, 728

Steidel, C. C., Shapley, A. E., Pettini, M., et al., 2004, ApJ, 604, 534

Steidel, C. C., Erb, D. K., Shapley, A. E., et al., 2010, ApJ, 717, 289

Steidel, C. C., Rudie, G. C., Strom, A. L., et al., 2014, ApJ, 795, 165, 165

Steidel, C. C., Strom, A. L., Pettini, M., et al., 2016, ApJ, 826, 159, 159

Strom, A. L., Steidel, C. C., Rudie, G. C., et al., 2017, ApJ, 836, 164, 164

Tacconi, L. J., Neri, R., Genzel, R., et al., 2013, ApJ, 768, 74, 74

Tamura, N., & PFS Collaboration, 2016, in Astronomical Society of the Pacific Conference Series, Multi-Object Spectroscopy in the Next Decade: Big Questions, Large Surveys, and Wide Fields, ed. I. Skillen, M. Barcells, & S. Trager, Vol. 507, 387

Tayal, S. S., & Zatsarinny, O., 2010, ApJS, 188, 32

Tolstoy, E., Hill, V., & Tosi, M., 2009, ARA&A, 47, 371

Trainor, R. F., Steidel, C. C., Strom, A. L., & Rudie, G. C., 2015, ApJ, 809, 89, 89

Trainor, R. F., Strom, A. L., Steidel, C. C., & Rudie, G. C., 2016, ApJ, 832, 171, 171

Turner, M. L., Schaye, J., Steidel, C. C., Rudie, G. C., & Strom, A. L., 2015, MNRAS, 450, 2067

Turner, M. L., Schaye, J., Crain, R. A., et al., 2017, MNRAS, 471, 690

van Dokkum, P. G., Labbé, I., Marchesini, D., et al., 2009, PASP, 121, 2

van Zee, L., Salzer, J. J., & Haynes, M. P., 1998, ApJ, 497, L1

Veilleux, S., & Osterbrock, D. E., 1987, ApJS, 63, 295

Vila Costas, M. B., & Edmunds, M. G., 1993, MNRAS, 265, 199

Vogt, S. S., Allen, S. L., Bigelow, B. C., et al., 1994, in Society of Photo-Optical Instrumentation Engineers (SPIE) Conference Series, Instrumentation in Astronomy VIII, ed. D. L. Crawford, & E. R. Craine, Vol. 2198, 362

Wake, D. A., van Dokkum, P. G., & Franx, M., 2012, ApJ, 751, L44, L44

Williams, M. J., Bureau, M., & Cappellari, M., 2010, MNRAS, 409, 1330

Wilson, J. C., Eikenberry, S. S., Henderson, C. P., et al., 2003, in SPIE Conference Series, Vol. 4841, 451

Wisnioski, E., Förster Schreiber, N. M., Wuyts, S., et al., 2015, ApJ, 799, 209, 209

Wuyts, E., Kurk, J., Förster Schreiber, N. M., et al., 2014, ApJ, 789, L40, L40

York, D. G., Adelman, J., Anderson Jr., J. E., et al., 2000, AJ, 120, 1579

Yuan, T.-T., Kewley, L. J., & Sanders, D. B., 2010, ApJ, 709, 884